
# THE CHALLENGES OF LOW-ENERGY SECONDARY ELECTRON EMISSION MEASUREMENT

**DISSERTATION**

**Matthew J. Vincie, Captain, USAF**
**AFIT-ENG-DS-19-D-007**

**DEPARTMENT OF THE AIR FORCE**
**AIR UNIVERSITY**

**AIR FORCE INSTITUTE OF TECHNOLOGY**

**Wright-Patterson Air Force Base, Ohio**

AFIT-ENG-DS-19-D-007

# THE CHALLENGES OF LOW-ENERGY SECONDARY ELECTRON EMISSION MEASUREMENT

DISSERTATION

Presented to the Faculty

Graduate School of Engineering and Management

Air Force Institute of Technology

Air University

Air Education and Training Command

In Partial Fulfillment of the Requirements for the

Degree of Doctor of Philosophy

Matthew J. Vincie, BSEE, MSEE

Captain, USAF

November 2019

AFIT-ENG-DS-19-D-007

# THE CHALLENGES OF LOW-ENERGY SECONDARY ELECTRON EMISSION MEASUREMENT

DISSERTATION

Matthew J. Vincie, B.S.E.E., M.S.E.E.
Captain, USAF

Committee Membership:

Tod V. Laurvick, PhD
Chair

Hengky Chandrahalim, PhD
Member

Richard G. Cobb, PhD
Member

ADEDEJI B. BADIRU, PhD
Dean, Graduate School of Engineering
and Management

## Abstract

The phenomena known as secondary electron emission was discovered over a century ago. Yet, it remains very difficult to model accurately due to the limited availability of reliable experimental data. With the growing use of computer simulations in hardware development, the need for accurate models has increased. This research focused on determining what factors may be causing measurement discrepancies and methods for increasing the accuracy of measurements. It was found that several assumptions are commonly invoked when these measurements are performed that may not always be consistent with reality. The violation of these assumptions leads to measurement bias that is contingent upon the apparatus and the voltages used during the measurement. This research showed that secondary electron yield measurements are sensitive to changes in the apparatus geometry, the current level, and the electron gun settings. New techniques, hardware, and models were developed in order facilitate greater measurement repeatability and accuracy.

*Ut Prosim*

# Acknowledgments

This research presented many challenges which could not have been overcome without the contributions of many. I will forever be grateful to those that aided in my success.

To Dr. Tod Laurvick, for always taking the time to listen to me, offering advice, and helping with software, contracting, and infrastructure issues. Thank you for your mentorship.

To my committee members, Dr. Richard Cobb and Dr. Hengky Chandrahalim, for your support and feedback throughout my research.

To Dr. James Sattler, for the procurement and installation of the secondary electron emission measurement apparatus used in this research.

To Mr. Brian Crabtree and the machinists of the AFIT Model Fabrication Shop, for fabricating the parts used in this research and providing advice throughout my research.

To Mr. Adam Fritzche, for your assistance with test equipment calibration and setup.

To Ms. Angela Hayden, for your assistance with contracting and test equipment.

To Mr. Richard Johnston, for your advice and assistance in sputtering gold on the fasteners of the modified sample puck.

To Mr. Michael Hill, for your help in procuring the materials necessary to complete this research.

To Mr. Greg Smith, for your support in the operation of the ultrahigh vacuum chamber used in this research.

To the staff of the Department of Electrical and Computer Engineering, for assistance with travel, finance, and academic requirements.

To my classmates, for all your support and humor throughout the past three years.

To my daughter, for the love and joy you have brought to my life.

To my wife, for your continual love, faithful support, and sacrifice. I could not have achieved this without you.

Matthew J. Vincie

# Table of Contents

# List of Figures

# List of Tables

# List of Abbreviations

Abbreviation Page

THE CHALLENGES OF LOW-ENERGY SECONDARY ELECTRON EMISSION MEASUREMENT

# I. Introduction

In 1902, German physicists L. Austin and H. Starke discovered the phenomenon known as secondary electron emission (SEE) [1]. They revealed that when a material is bombarded with high-energy electrons the material can become positively charged indicating that, in addition to reflecting the high-energy electrons, other electrons leave the material. Since this discovery, the phenomenon has proven beneficial in some cases while a nuisance in others. From the earliest attempts to characterize SEE and even today, measurements made of the same elements performed by different labs or even the same lab display discrepancies.

In 2005, Lin and Joy examined over 80 years of published secondary electron yield (SEY) data from over a hundred authors and stated

"*An examination of this data is discouraging, because it is evident that even for common elements (such as aluminum or gold) for which there are often a dozen or more independent sets of data available, the level of agreement is rarely better than 25% and often shows relative divergences of 100% or more. The result of this situation is that anyone seeking yield data to explain an observation or to validate a model can usually find multiple values spanning a large enough range to support or disprove any assertion.*" [2].

SEY is the ratio of the average number of electrons leaving a material (commonly called secondary electrons) to the average number of electrons impacting the material (commonly called primary electrons) and is a critical parameter when characterizing the SEE of a material. Figure 1 demonstrates the large variation in SEY values for aluminum at different primary electron energies based on the data compiled by Joy [3].

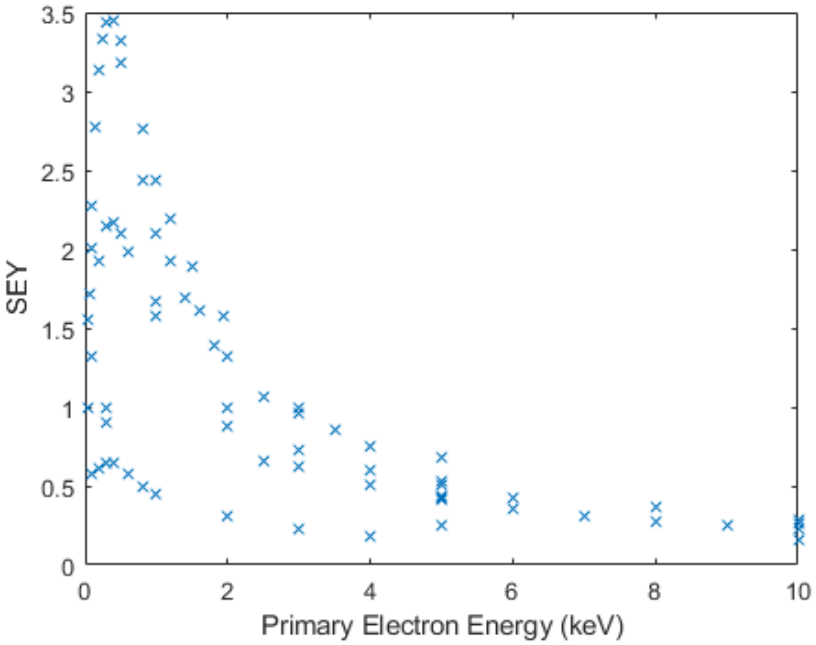


Figure 1: SEY versus primary electron energy for aluminum (derived from [3]).

More recently, Sattler found that SEY measurements performed on the same material using two different experimental apparatuses showed significant differences as shown in Figure 2 [4]. The discrepancies that are seen in SEE data and the scarcity of the data available make it difficult to accurately and completely model SEE.

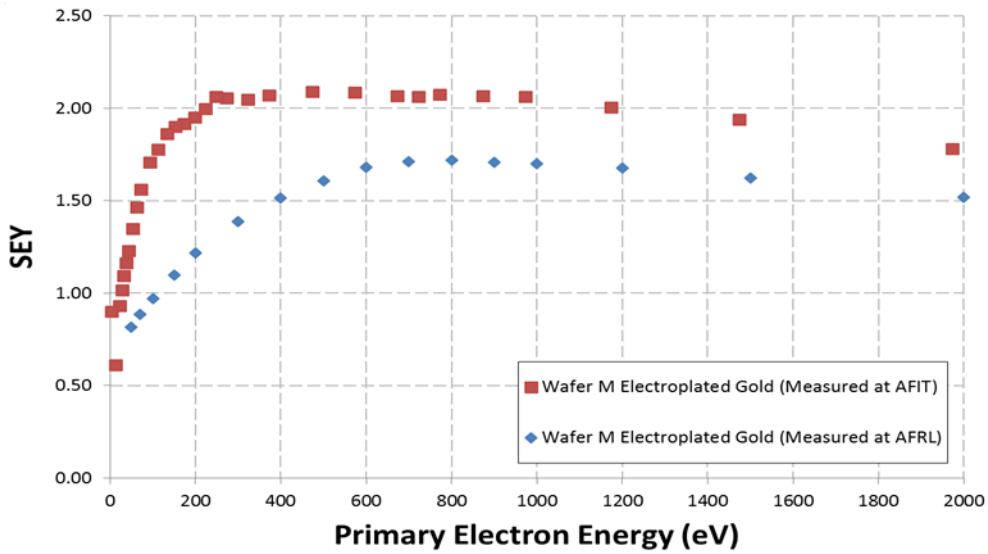


Figure 2: Plot of SEY data measured by Sattler for electroplated gold using two different apparatuses [4].

## 1.1 Research Goal

The ability to accurately model SEE is critical to the measurement of other physical phenomena, the development of technology, and the safe operation of spaceborne radio frequency (RF) systems. During the measurement of the photoelectric effect, thermionic emission, field emission, and other experiments involving free electrons, SEE is present and affects the results of the measurement. Normally, neglecting SEE effects will bias the measurement. To achieve a higher degree of accuracy requires that either the effects of SEE on the measurement are determined and subtracted out or the experimental apparatus is designed such as to reduce the impact of SEE on the measurement. The design of these apparatuses and other technologies which rely on mitigating SEE are enabled by accurate SEE modelling.

Recently, the phenomenon of SEE has experienced increased scrutiny due to its connection with multipactor. Multipactor is a cyclical process of electron multiplication through SEE in an alternating electromagnetic field. This phenomenon takes place in a vacuum where collisions with gas molecules are minimized. The occurrence of multipactor within an RF system can reduce the performance of the system and cause damage. In the space environment, damage to an RF system can render a satellite useless due to it being unable to transmit data resulting in a large financial loss to a space program. Furthermore, the failure of a defense satellite reduces the capability of our government to provide national security. For these reasons, the Aerospace Corporation has written the

*Standard/Handbook for Multipactor Breakdown Prevention in Spacecraft Components* which provide guidance for the test of RF components for use in space [5].

This guidance establishes a process to verify that an RF component or system will not experience multipactor breakdown when operating at or below maximum power [5]. In order to ensure that breakdown will not occur, the power at which multipactor occurs is first determined through analysis or testing, and then a safety margin is subtracted from this power to determine the maximum allowed power within the component. Simulation is considered a valid analysis method for determining the power at which breakdown occurs for devices with defined geometries [5]. This excludes devices that vary in geometry due to unit-to-unit production variations or the incorporation of tuning elements such as tuning screws. Simulation requires that SEE is modeled, and the accuracy of the SEE model is imperative in ensuring that the simulation yields accurate results. Currently, the guidance indicates that a bounding, worst-case SEY shall be used in simulation due to the variations in surface conditions that can occur over the life of a component. However, the guidance does not provide any indications on how to model the angular and energy distribution of the secondary electrons. Scott Rice and John Verboncoeur have shown that multipactor is extremely sensitive to the energy distribution of the secondary electrons [6]. Thus, it is necessary to accurately model both the SEY, energy distribution, and presumably the angular distribution (though the sensitivity of multipactor to the angular distribution is currently unknown) in order to yield accurate simulation results.

In conclusion, accurate models of SEE are required for the measurement of other physical phenomena, the development of more capable technology, and the safety of spaceborne RF systems. However, our ability to develop accurate models is hampered by

the discrepancies and limited availability of measured SEE data. The goal of this research is to identify the cause of the measurement discrepancies and provide guidance on methods for improving measurement accuracy.

### 1.2 Research Objectives

Since multipactor may occur when the SEY exceeds unity, it crucial to be able accurately measure and model SEY at energies near and below the energy where the SEY first exceeds unity, which is known as first crossover energy. Measurements of the SEY at these low energies have been referred to as low-energy SEY (LE-SEY) measurements [7]. These measurements come with many challenges due to factors such as the contact potential difference (CPD) between electrodes and the thermal spreading of the primary electron energy. As a result, these measurements are often criticized and debated. This research focuses on LE-SEY measurement due to its relevance to multipactor.

In order to the achieve the goal of this research, the following research objectives were established.

1) Determine factors which may lead to measurement discrepancies by performing a review of literature pertaining to the measurements of SEE. These factors will exclude discrepancies due to differences in sample composition.
2) Develop an experimental system capable of performing large numbers of measurements autonomously in order to establish repeatability of measurements and facilitate testing under numerous test conditions.
3) Develop a simulation model of the experimental system to facilitate analysis of experimental test results.

4) Preform measurements at different primary currents and compare results to determine how changes in current may affect SEY measurements.

5) Determine how the spacing between the electron gun and sample may affect SEY measurements.

6) Determine how the first crossover of the SEY curve is altered by changing the potential of the electron gun optics.

7) Determine how the electron gun's optics can be adjusted in order to reduce SEY measurement errors.

8) Preform SEY measurements on a magnetized sample to determine if the magnetic type I contrast effect can be used to reduce secondary emission from the vacuum chamber walls during SEY measurements.

These objectives with the exception of objectives 2 and 3 were chosen to answer specific research questions which are self-evident in the objectives and will not be restated. The accomplishment of these objectives will provide insight into the dependence of SEY measurements on changes in the configuration of the experimental apparatus and provide the knowledge needed to establish guidance for improving measurement accuracy.

### 1.3 Chapter Outline

This dissertation is divided into five chapters. The purpose of the first chapter was to briefly introduce SEE and multipactor and to establish the goal, motivation, and objectives for this research. The second chapter describes SEE and multipactor in greater detail and provides insight into the factors which cause measurement discrepancies. The third chapter describes the approach used in this research to fulfill the research objectives

and the development of the experimental system and simulation model. In the fourth chapter, the results from simulations and experimental measurements are analyzed. The fifth chapter provides guidance based on the conclusions draw from the previous chapters and recommendations for future research.

### 1.4 Summary

This chapter introduced the topics of SEE and multipactor and briefly described the difficulties involved in modeling SEE due the discrepancies and scarcity associated with measured SEE data. The importance of accurate SEE models in the development of technology and the safety of spaceborne RF systems was emphasized, and the goal of identifying the cause of the measurement discrepancies and providing guidance on methods for improving measurement accuracy was established. Eight objectives involving both experimentation and simulation were identified for reaching this goal. Lastly, an outline of the dissertation chapters was provided.

# II. Literature Review

This chapter provides a review of literature regarding SEE and multipactor. The first section provides a historical overview of the important discoveries, challenges, and inventions surrounding SEE and multipactor. The second, third, and fourth sections describe the different types of SEE measurement, the apparatuses involved, and the models used to simulate each aspect of SEE. The fifth section describes current commercial, multipactor software and the SEE models implemented in each. In addition, the multipactor software developed by the Air Force Office of Scientific Research (AFOSR) and the Air Force Research Laboratory (AFRL) is briefly discussed. The final section discusses the ongoing challenges to accurate SEE measurements.

## 2.1 Historical Overview

The following sections discuss the important findings and activities surrounding SEE and multipactor research followed by a brief summary.

### 2.1.1 SEE Discovery

German physicists L. Austin and H. Starke are recognized for the discovery of the phenomenon known as secondary electron emission [1]. Their research began as a study of the relationship between the number of reflected electrons and the primary electrons' incidence angle. However, during the course of their research, they discovered SEE along with several key relationships. Firstly, they observed that an isolated, metal reflector became positively charged when bombarded by high-energy electrons. This indicated to them that in addition to the usual electron reflection other negatively charged particles were released. Secondly, they believed that the emission of "negativer Elektricität" (translated

negative electricity) was a result of the emission of negatively charged particles whose velocities were of the same order of magnitude as the incident electrons. However, the scientific community now knows that these charged particles can have velocities distributed across several orders of magnitude depending on the incident velocity of the primary electron. Thirdly, they found that the emission decreased as the speed of the incident electron increased. Based on data obtained following their discovery, this is not completely true: the emission first increases as the speed of the primary electron increases before decreasing. Fourthly, they found that emission increases when the target surface is polished, which is consistent with data collected since their discovery. Fifthly, they concluded that emission increases as the density of the reflector increases. This conclusion however does not agree with data collected since their discovery, and it was determined that a correlation between emission and work function could just as easily be observed [8]. Efforts to correlate emission to other physical characteristics of materials have continued, but the results thus far have been inconclusive [2]. Lastly, they discovered that the emission increased with incidence angle, which is consistent with data collected since their discovery. They published these finding in 1902; and many of these findings remain relevant to this day. Throughout history, this phenomenon has also been called secondary emission and secondary electron radiation.

### 2.1.2 Classification of Secondaries

Shortly after the discovery of secondary electron emission, German physicist P. Lenard made the distinction between what he called “secondary electron radiation” and “Rückdiffusion” (translated re-diffusion) according to Bruining [9]. Lenard’s “secondary

electron radiation" are the electrons excited by the primary electrons (PE) and ejected from the material. They are now commonly called true secondary electrons (TSE). Lenard's "Ruckdiffusion" are the primary electrons which are backscattered from the material. This group is further divided into inelastically backscatter primary (IBP) and elastically backscatter primary (EBP). Figure 3 identifies the types of electrons involved in secondary electron emission. For clarity, the term "secondaries" when used in this text refers to all types of secondary electrons ejected from the target material. Throughout history, this term has been used inconsistently: sometimes referring true secondary electrons and other times referring to all emitted electrons. Lenard made this distinction because he found that there is a "slow" group of secondaries that have an approximately constant energy (~10 eV) regardless of the primary electron energy [9]. This "slow" group is commonly associated with TSE. Figure 4 shows a typical energy distribution for secondaries and identifies the relative position of each secondary electron type. Auger electrons will be discussed in a later section.

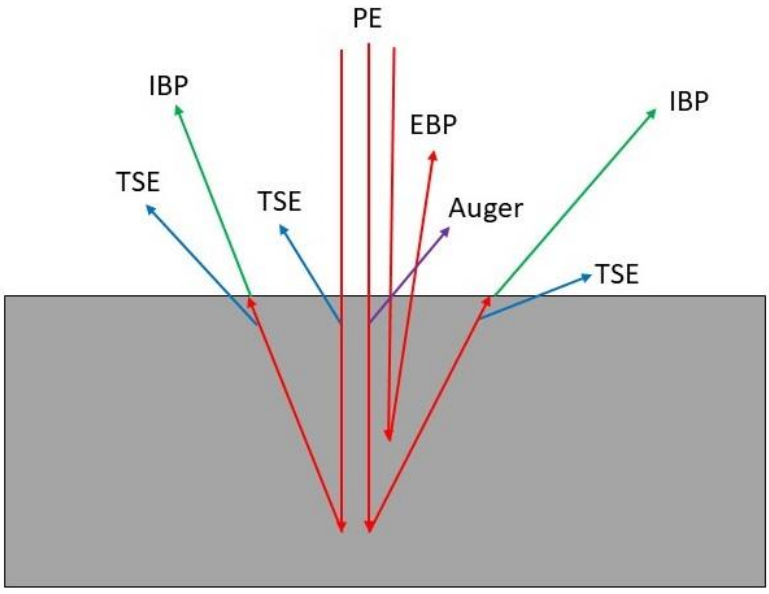


Figure 3: Diagram identifying types of secondaries generated during SEE.

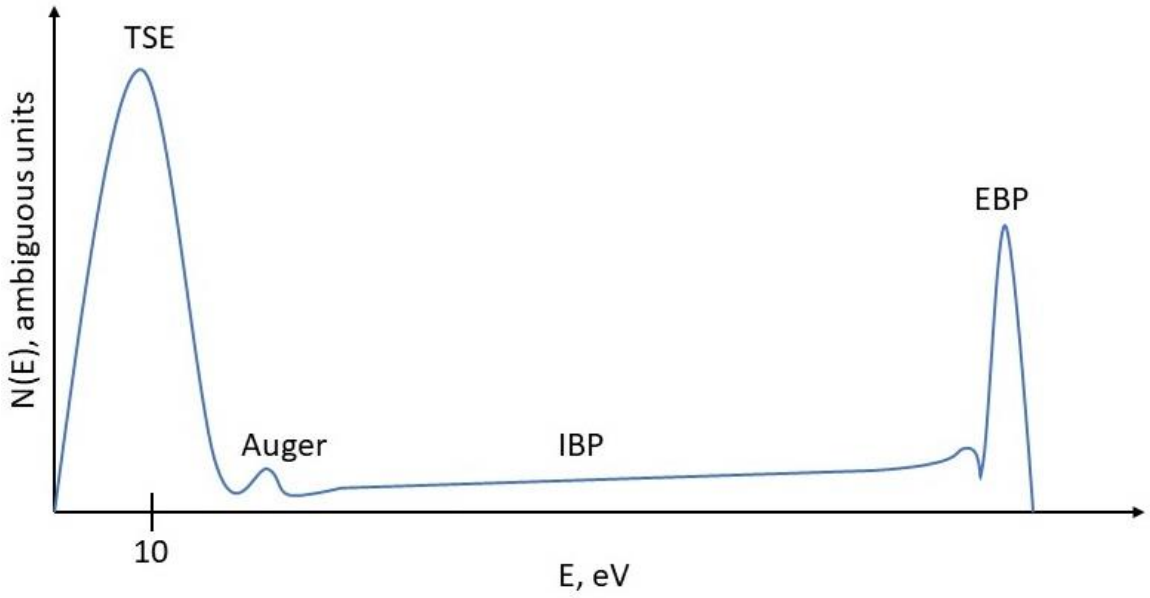


Figure 4: Secondary electron energy distribution with secondary electron types identified. N(E) is the distribution of secondary electrons with respect to energy and is normally shown in ambiguous units.

### 2.1.3 First Device to Harness SEE

In August of 1915, Albert W. Hull patented the dynatron while working for the General Electric Research Laboratory (Figure 5) [10]. This was the first device to make use of SEE. The dynatron is a vacuum tube device that functions as a negative resistance when appropriately biased [11]. It can be used in amplifier and oscillator circuits [11, 12]. In 1922, Hull referred to the electrode that emitted secondaries as the dynode. This term is still used today to describe electrodes that perform electron multiplication through secondary electron emission.

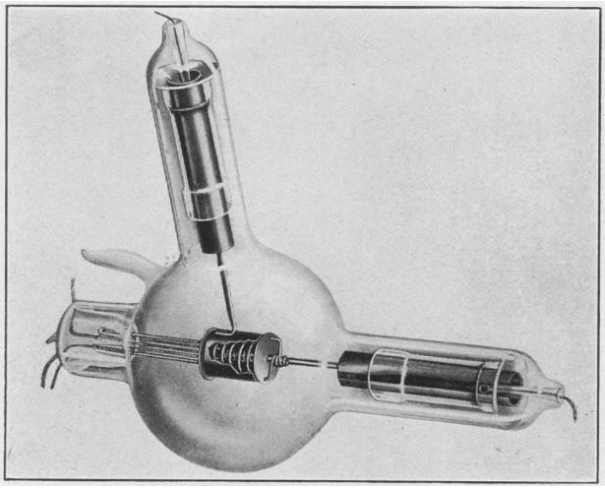

Figure 5: The dynatron [11].

### 2.1.4 Auger Electrons

In 1923, Austrian physicist Lise Meitner discovered Auger electrons though French physicist Pierre-Victor Auger is credited with the discovery [13]. When an inner shell electron of an atom is removed by a primary electron or photon, an outer shell electron emits energy and falls to fill the vacancy in the inner shell (Figure 6). The emitted energy can either escape the atom as a photon or be transferred to another electron which is then ejected from the atom. The ejected electron is known as an Auger electron.

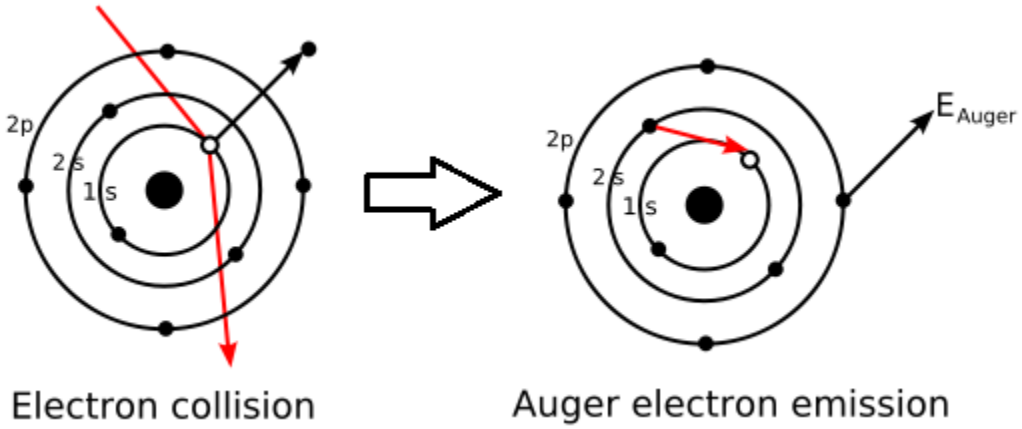


Figure 6: Schematic of Auger electron emission process [14].

Auger electrons are emitted with specific energies that are associated with the quantized energy levels of the atom and normally appear at a slightly higher energy than the TSE in the energy distribution (Figure 4). They constitute an extremely small portion of the secondary electron population (less than 1 in $10^4$) [15]. Consequently, they are not considered in the simulation of multipactor, vacuum tube devices, and many other simulations involving secondary electrons.

### 2.1.5 Electron Diffraction

In 1924, Louis de Broglie, based on the findings of Planck, Einstein, and Bohr, suggested that particles could act as waves having a wavelength associated with their momentum [16]. This relationship predicted that crystals when bombarded by electrons would exhibit diffraction following the Bragg diffraction condition, which had previously been applied to X-ray diffraction. In 1927, Davisson and Germer in the US and Thomson in Britain independently observed the electron diffraction pattern experimentally [16]. The diffraction pattern appears in the angular distribution associated with the EBPs. One way to observe the diffraction pattern is to use two electrically biased grids to filter out slower secondary electrons using a retarding potential (Figure 7). The remaining electrons are accelerated into a fluorescent screen for visual observation. Since a majority of the materials used in the construction of RF and vacuum tube devices are not crystalline and EBPs constitutes a small percentage of the secondaries, electron diffraction is commonly ignored in the simulation of these devices.

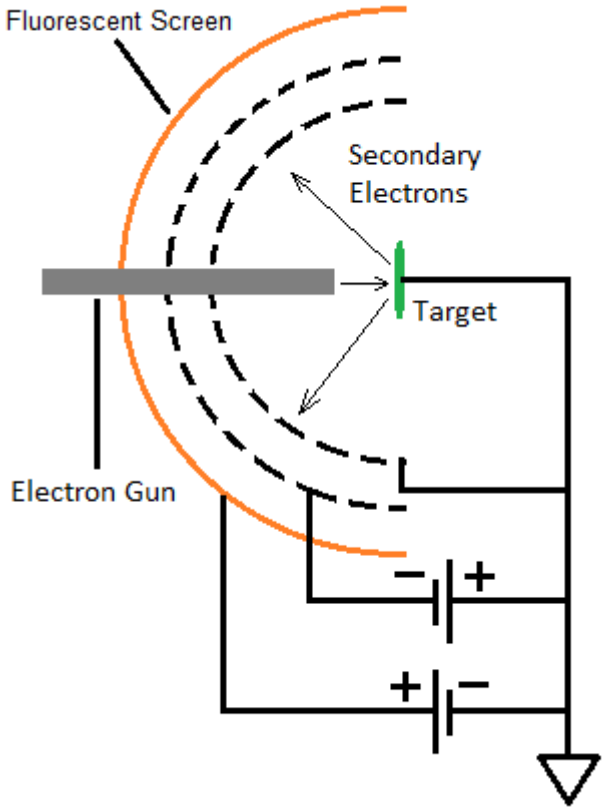


Figure 7: Diagram of low-energy electron diffraction (LEED) apparatus.

### 2.1.6 Vacuum Tube Distortion

In the late 1920's as vacuum tube electronics progressed, the phenomenon of SEE produced undesirable behavior in the tetrode [17]. During this time, Bernard Tellegen began researching ways to reduce SEE from the anode of the tetrode [17]. Methods such as coating the anode with carbon and cutting ridges into the anode reduced the emission but did not completely suppress irregularities in the tetrode's behavior [18]. By December of 1926, Tellegen solved the problem by placing an additional grid between the anode and the screen grid (Figure 8) [19]. The additional grid is called the suppressor grid. It is negatively biased with respect to the anode in order to force the slow-moving secondary electrons back into the anode. Since a large portion of secondaries are moving slowly, the

suppressor grid largely eliminated the undesirable behavior in the tetrode. The tetrode with the suppressor grid became known as the pentode.

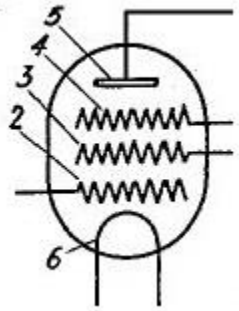


Figure 8: Diagram of Pentode [19]. 2—control grid; 3—screen grid; 4—suppressor grid; 5—anode; 6—cathode

### 2.1.7 Multipactor Discovery

In 1924, French physicist Camille Gutton is believed to be the first person that experienced the multipactor phenomenon during his research of low pressure glow discharge at high frequency; however, Gutton attributed the phenomenon to ions and failed to identify electrons and secondary electron emission as the underlying cause [20, 21, 22]. He along with his son, Henri Gutton, continued to study the glow discharge phenomena at high frequency but failed to make a connection between secondary electron emission and the observed phenomena [22, 23, 24].

The discovery of multipactor was not accidental: it was predicted, and a device was designed to make use of the phenomenon. In the early 1930's, Philo T. Farnsworth built a device to amplify weak electrical signals through the multiplication of electrons via SEE in an alternating electric field [25]. He referred to the device as a multipactor tube (Figure 9) [26, 27, 28]. These tubes did not find any lasting application; and, by the 1940's, the name was transferred from the tubes to the phenomenon on which they are based [28].

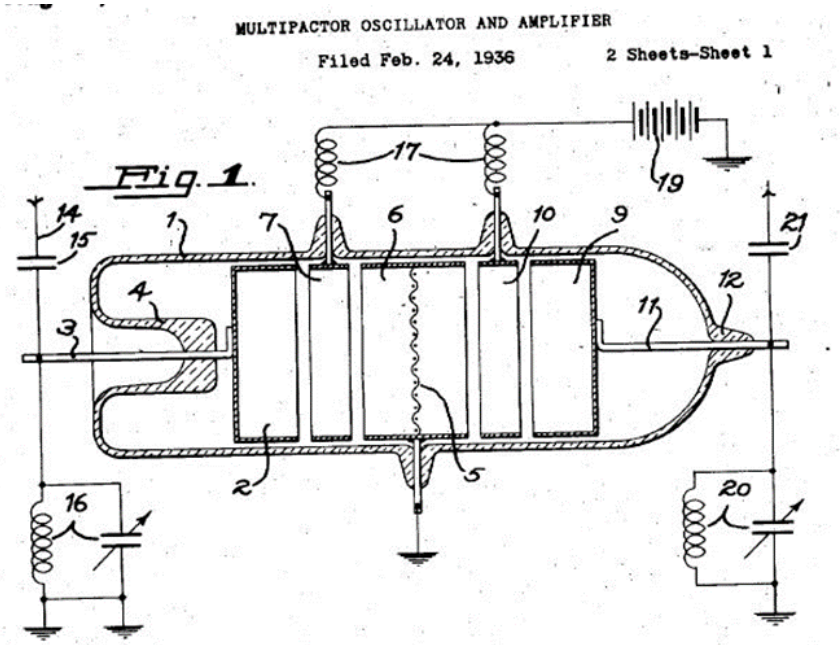


Figure 9: Farnsworth's Multipactor Tube [75].

Multipactor is a process of electron multipaction in an alternating electromagnetic field due to SEE. The multipactor phenomenon takes place within a vacuum where collisions with gas molecules are minimized. Common examples of multipactor include single-surface and two-surface multipactor. Single-surface multipactor commonly takes place at waveguide pressure windows. A free electron can appear near the dielectric window due to numerous emission processes (e.g. high energy space particles, photoelectric effect, field emission, etc.) (Figure 10a). The electromagnetic field, propagating towards the right in Figure 10, forces the electron into the dielectric. If the energy of the impacting electron is sufficient to generate more than one secondary electron, multiple electrons will be emitted from the dielectric surface leaving behind positive charge (Figure 10b). The emitted electrons are accelerated by the electromagnetic field and collide again with the dielectric window generating additional free electrons (Figure 10c). This process continues with

additional free electrons being generated during each impact. The dielectric window is heated during this process and may experience a catastrophic failure.

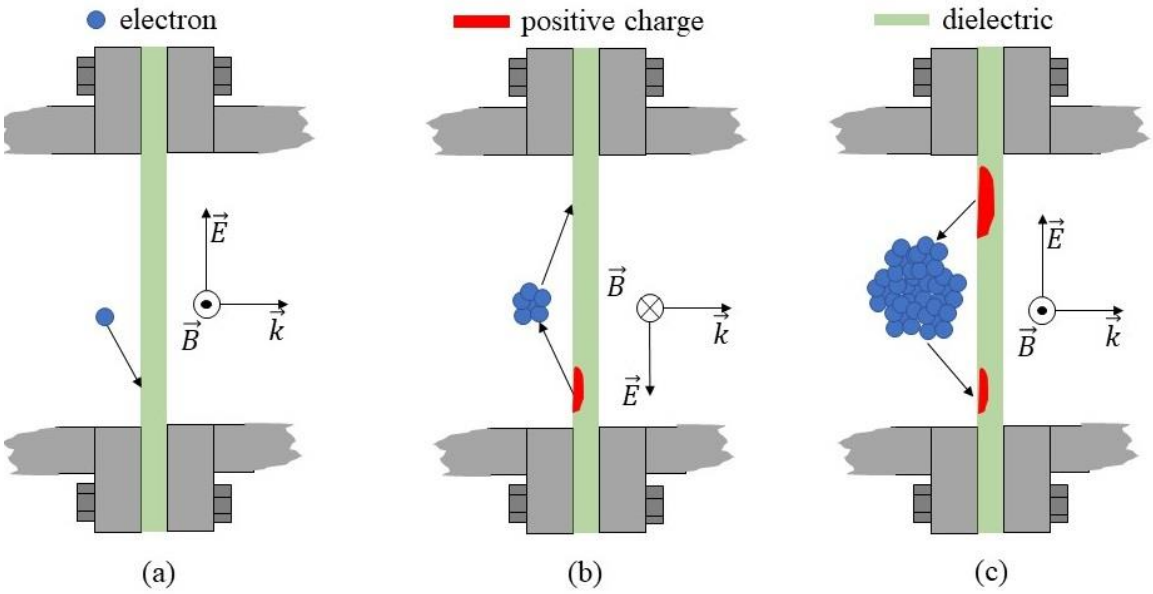


Figure 10: Single-surface Multipactor.

Two-surface multipactor is phenomenon exploited by Farnsworth's multipactor tubes. An alternating electric field between two parallel plates causes a free electron to be accelerated into one of the plates (Figure 11a). If the energy of the electron is sufficient to generate more than one secondary electron, multiple electrons will be emitted from the plate. The emitted electrons are then accelerated by the electric field and collide with the opposite plate (Figure 11b). This second collision multiplies the number of free electrons (Figure 11c). The electron multiplication process happens synchronously with the electric field leading to a buildup of electrons between the two places. The repeated impact of electrons with the plates heats the surface of the plates producing several possible effects: surface conditioning, emission of x-ray photons, damage to the plates, and outgassing of trapped gases. The outgassing of trapped gases is especially detrimental. The collision of electrons with gas molecules ionizes the gas molecules creating plasma. The plasma

absorbs much of the RF energy leading to further heating and energy loss. If left unattended, the component may experience a catastrophic failure. Furthermore, harmful x-ray radiation may be emitted during multipactor causing damage to surrounding electronics and living organisms [28].

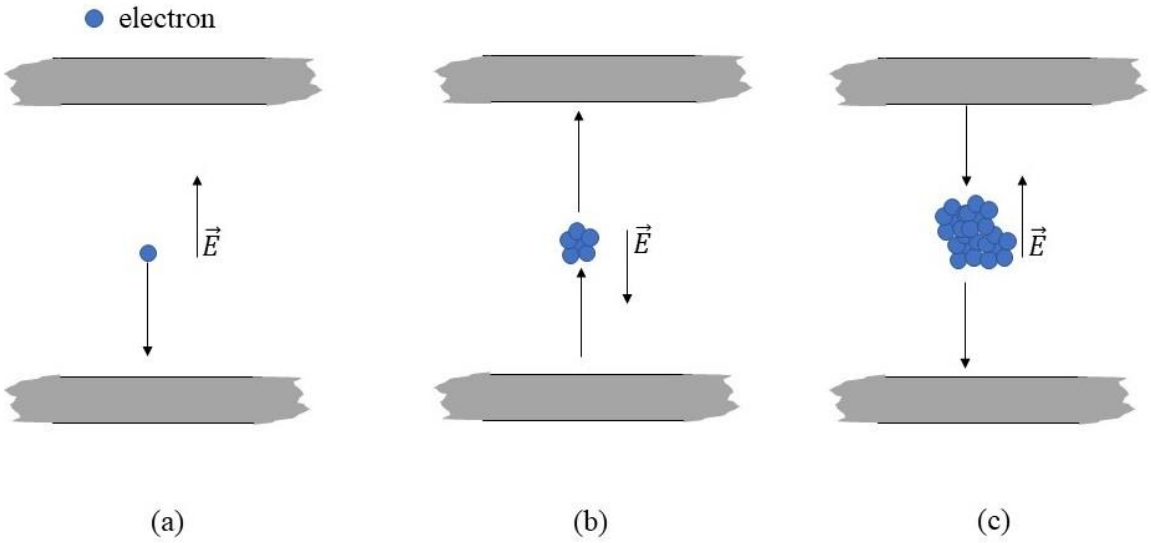


Figure 11: Two-surface Multipactor.

### 2.1.8 Multipactor Semi-empirical Modeling

During the 1930's, researchers began to propose theories for multipactor [20]. In order to make analytic solutions tractable, researchers made assumptions without having any physical basis and focused on simple geometries, such as parallel plates and single dielectric surfaces [20]. Some of these assumptions were:

1) the secondary electrons are emitted at a velocity of zero, a velocity that is proportion to a constant *k* times the primary electron velocity (the constant-*k* theory), or a velocity, *v*, that is constant (monoenergetic) regardless of the primary electron velocity (the constant-*v* theory) [20, 29]

2) the emitted velocity of the secondary electrons is normal to the surface [30]

3) electric field between the plates is uniform [30]

4) space charge effects are negligible [30]

5) magnetic field effects are negligible [30]

Based on the physics of SEE, the first two assumptions are incorrect. Nevertheless, by making these assumptions researchers were able to develop semi-empirical equations which they could fit to experimental data. These models were useful for constructing multipactor susceptibility curves for use by engineers but did not aid in understanding the underlying processes involved in multipactor [20].

Figure 12 shows the baseline multipactor threshold curve found in the *Standard/Handbook for Multipactor Breakdown Prevention in Spacecraft Components*. This curve was produced using Hatch and Williams susceptibility curves which are based on a parallel plate geometry. The peak RF voltage is the voltage at which multipactor breakdown occurs. The gap is the distance between the parallel plates, and the frequency is the frequency associated with the electromagnetic field. In order to avoid multipactor breakdown, a component should be operated in the region below the bold, black curve. Though these curves are based on a parallel plate geometry, they are routinely used to determine the multipactor breakdown threshold of non-parallel plate geometries.

When applied to non-parallel plate geometries, over-conservatism may exist [5]. This is due to the fact that the parallel plate assumption does not include electron loss mechanisms. When analysis is performed on realistic RF components, the opposing cavity walls are considered to be infinite parallel plates (Figure 13a). Since the features on the walls are not infinitely wide, electrons can escape from the sides of the features (Figure 13b-c). Due to this loss mechanism, the actual multipactor breakdown threshold may be

much higher than that predicted using susceptibility curves [5]. The accuracy of these models decreases when the opposing walls are not parallel and when the gap is large compared to the feature size [5]. Due to the limited applicability of the semi-empirical models, much of the design for multipactor-free systems was done through trial and error [31]. It would not be until the development of multipactor computer simulations that the breakdown thresholds of complex geometries could be more accurately predicted.

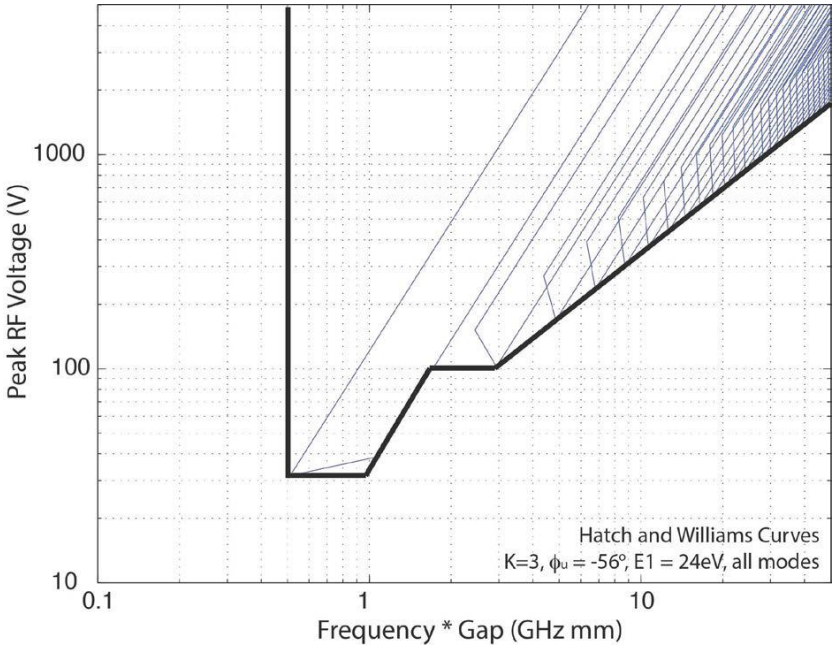


Figure 12: Baseline multipactor breakdown threshold [5].

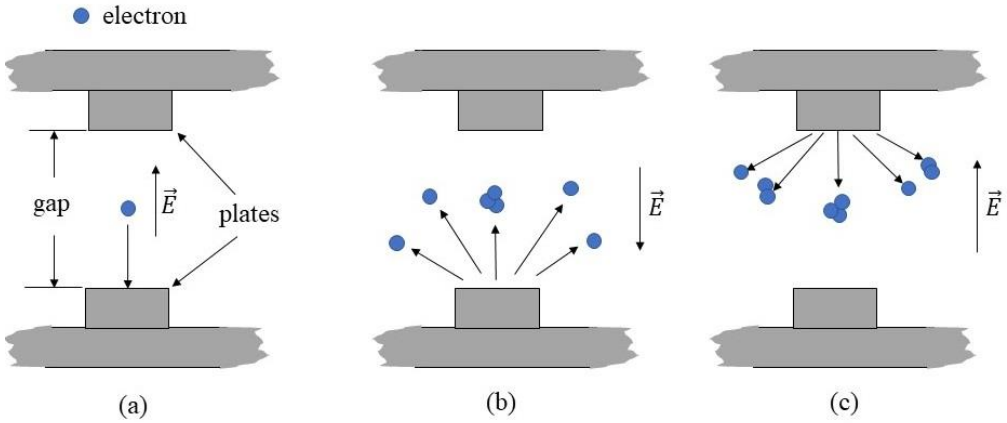


Figure 13: Electron loss mechanism. The features labelled “plates” are consider infinite parallel plates in the analysis using susceptibility curves.

### 2.1.9 Multipactor Simulation

To the author's knowledge, the earliest known multipactor computer simulation was developed by Stanford University in 1973 [20, 32, 33]. Using the simulation, the researchers were able to track numerous initial electrons and multiple generations of secondary electrons in two dimensions (Figure 14). From the simulation, the researchers discovered a non-resonant multipactor process as opposed to the then well-known resonant multipactor process [32]. In this simulation, the fields within the cavity were first calculated, and then initial electrons were introduced into the cavity. The simulation calculated the trajectories of individual electrons though numerical integration until the electrons impacted the walls. A Monte Carlo algorithm based on experimental SEE data was then performed to determine the number of secondaries and their associated energies [32].

This simulation was a significant step forward in multipactor research. SEE data was finally integrated into multipactor analysis, and more complex geometries could now be analyzed. The unfortunate disadvantage associated with this type of simulation is that each electron must be tracked. During multipactor, the number of free electrons can grow to more than a trillion within 50 to 300 RF cycles requiring excessive computer resources for tracking all the electrons [34, 35]. The need to simulate large numbers of particles was addressed by particle-in-cell simulations.

According to Kishek *et al.*, particle-in-cell (PIC) simulations began to be applied to multipactor in the 1990's [20]. Prior to being applied to multipactor, PIC simulations had been applied to plasma research [36]. PIC simulations are applied to the plasma and multipactor phenomena due to the excessive computational requirement associated with

tracking individual particles. In order to reduce the number of particles being tracked, individual particles are grouped together into “superparticles” (also called macroparticles) which are then tracked [36].

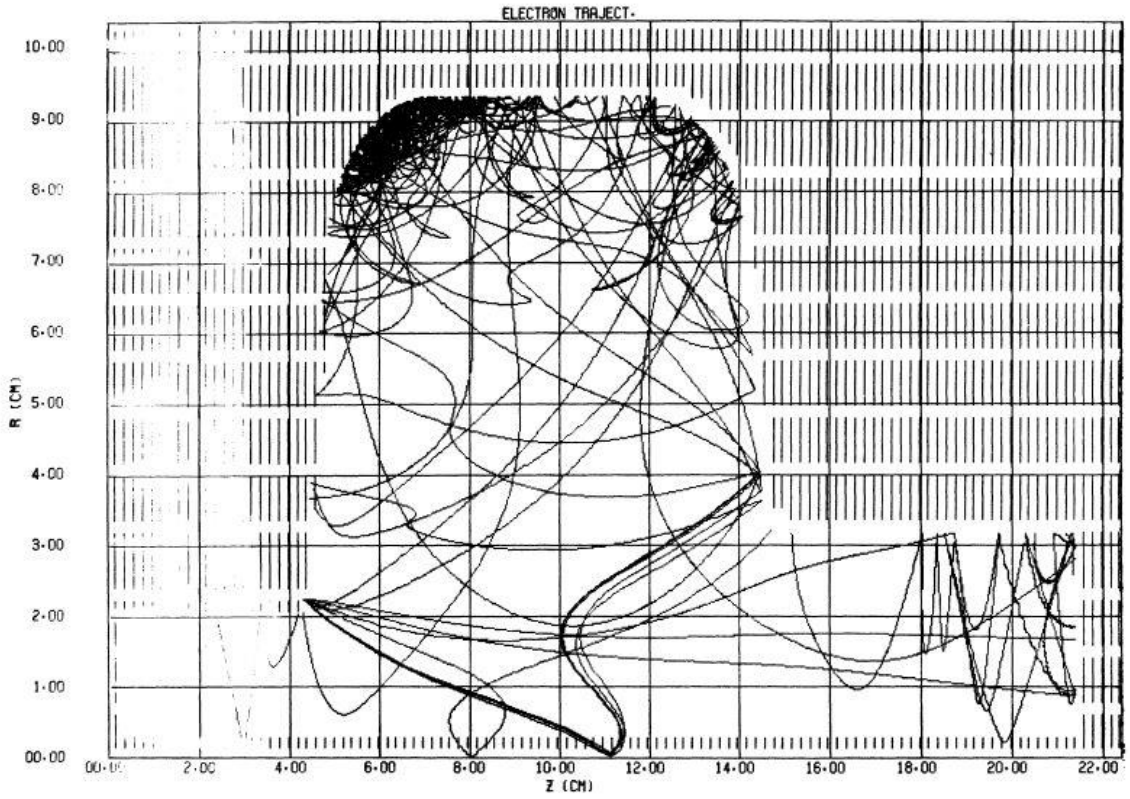


Figure 14: Typical computer plot of electron trajectories produced by the multipactor simulation program developed at Stanford University [32].

There are numerous PIC algorithms currently available; attempting to discuss each in detail would be futile. Generally, the algorithms follow the cycle of arithmetic operations shown in Figure 15 [36, 37, 38]. In Figure 15, the index $i$ references quantities associated with a superparticle, and the indices $j$, $k$, and $l$ reference the nodes of a 3-D spatial grid. For each time step, $\Delta t$, the algorithm performs four operations. First, based on the location of the superparticle in the user-defined spatial grid, the associated charge distribution of the superparticle, and the velocity distribution of the superparticle, a current and charge density

is assigned to either the nearest grid point or eight grid points surrounding the superparticle [36, 37].

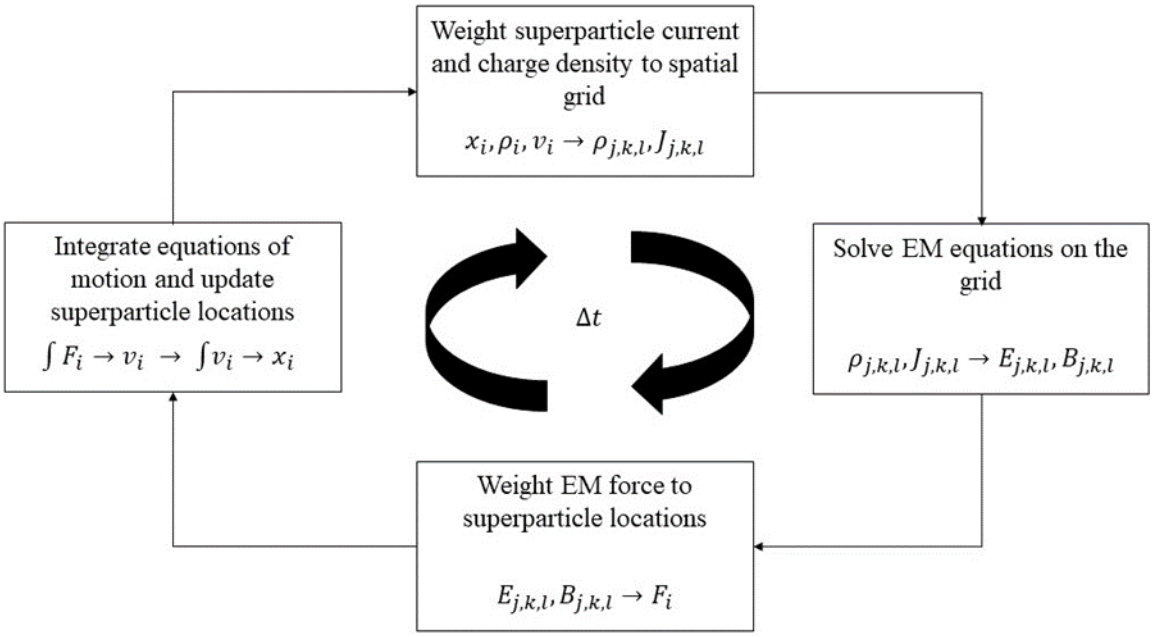


Figure 15: General flow of operations in PIC algorithms.

Due to the periodicity of the spatial grid, Maxwell's equation can then be solved using a Fast Fourier Transform (FFT) which yields the electric and magnetic field components at each spatial node [36]. Since the superparticles are not located at the nodes, a weighting scheme is used to determine the electric and magnetic field at the location of the superparticle and the resultant Lorenz force on the superparticle [37]. The new position and velocity of each of the superparticles is finally determined using either Newton's second law of motion or the relativistic equations of motion [36]. Additional operations are required to simulate SEE and the ionization events which occur in plasma.

### 2.1.10 SEE Measurement Difficulties

Despite the success seen in the development of vacuum tube devices, scientists struggled to make accurate measurements of SEE that were consistent across the scientific

community. The methods and equipment used in the measurement of SEE has gone through several important changes since the discovery of SEE. In 1938, Warnecke pointed out the variability of SEY caused by varying the duration and temperature of heat treatments [39]. Figure 16 demonstrates the sensitivity of the SEY of aluminum to heat treatments. A decade later, McKay indicated that probably the most important development since the discovery of secondary emission was the creation of "…extensive degassing treatment and careful high vacuum techniques" [8]. Around 1948, the electron gun became the predominated device for making SEY measurements [8]. Previously, the triode was also used in SEY measurements. According to McKay, the results obtained using an electron gun were more easily interpreted than the triode method [8], and Bruining wrote that the triode method was less accurate [40]. Despite the improvements that were made in the measurement of SEE, in 1951 Pomerantz and Marshall wrote,

"*The disagreement among the results of different experiments is such as to preclude many crucial comparisons which could cast light upon the nature of the mechanisms involved in the process of secondary emission*" [41].

Since the 1950's, vacuum technology has continued to improve, and two additional technologies were developed that have allowed scientists to make improved measurements. The first technology was modern surface analytical instruments. In the 1960's, these instruments became widely available and allowed scientists to characterize the chemical composition of their samples [42]. This knowledge gave scientists a better understanding of the factors that were affecting SEE and the ability to identify when contaminants had formed on their samples. The second technology was the cleanroom. In 1962, Willis Whitfield invented the cleanroom which allowed scientists to prepare samples with fewer

contaminants [43]. Together, these technologies have helped scientists reduce sample contamination and identify when sample contamination has occurred.

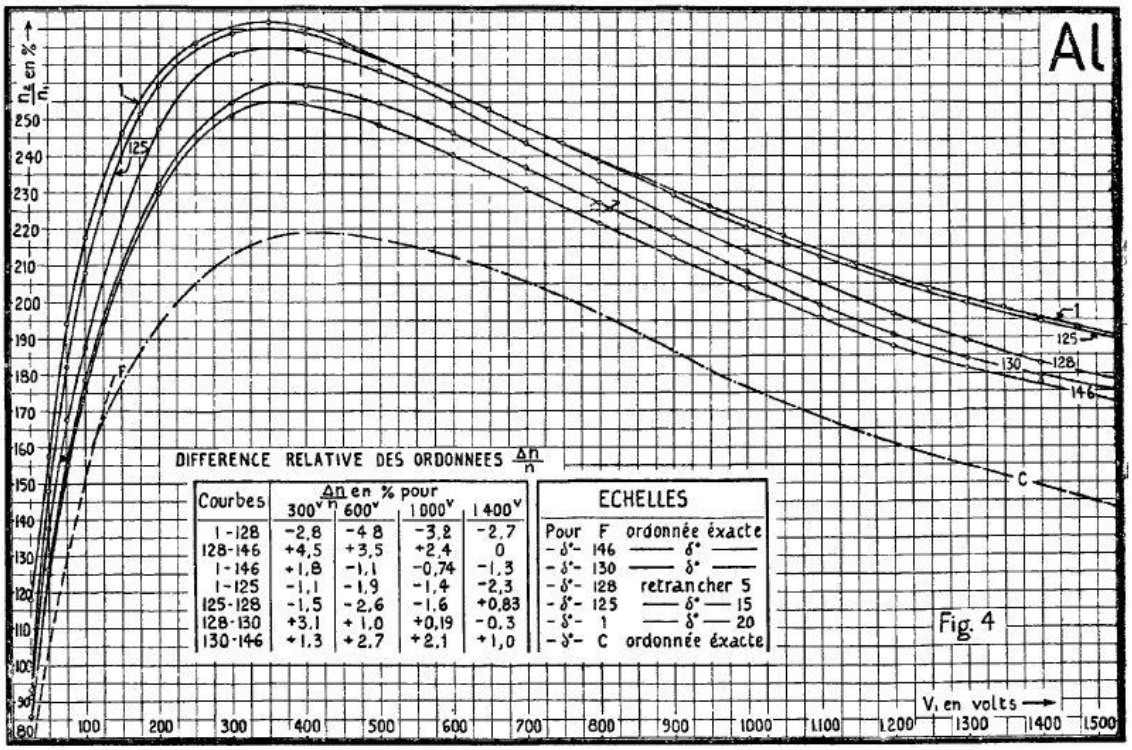

Figure 16: Secondary electron yield for aluminum following heat treatments [39]. Curve 1—24 hours after end of pumping. Curve 125—after 1.5 h of 440° C heating and 240 h after curve 1. Curve 128—after 1 h of 400° C heating following curve 125. Curve 130—after 2.5 h of 470° C heating following curve 128. Curve 146—after 1.5 h of 570° C following curve 130. Curve F—data from Farnsworth. Curve C—data from Copeland.

Nevertheless, inconsistencies in SEE measurements continued to occur. In 1981, a group of researchers performed Auger electron spectroscopy (AES) measurements on copper and gold using 28 different instruments [44]. These measurements are of the secondary electron energy distribution. This distribution contains peaks which are associated with Auger electrons and can be used to identify the elemental composition of a surface. Their results showed significant inconsistencies in both Auger electron energies and intensities. They concluded that a measurement standard was necessary to eliminate the inconsistencies. In 1991, the International Organization for Standardization formed

Technical Committee 201 which is responsible for AES measurement standards [45]. These standards provide a means for greater consistency among AES measurements; however, it is unknown to what extent these standards have been successful. Unlike AES measurements, SEY measurements and angular distribution measurements do not have a standard or committee responsible for standardization.

Even with technological advances, discrepancies with SEE measurements are still witnessed. An identical sample can yield two different results when measured by two different labs or even the same lab. These discrepancies appear as measurement biases rather than random measurement errors. Thus, averaging of the results does not guarantee that the true value of the SEE characteristic, such as SEY, will be obtained. The cause of these discrepancies and how to deal with them is at the center of this research.

### 2.1.11 Summary of History

The research areas of SEE and multipactor began as two separate fields of study. SEE was discovered in 1902. Physicist studied SEE with the objective of understanding the underlying mechanisms of SEE. Some of their important findings were the discovery of Auger electrons and electron diffraction. Meanwhile, engineers were designing vacuum tube devices that either relied on SEE for operation or required the mitigation of SEE. Multipactor research began in the 1930's with Farnsworth's invention of the multipactor tube. Researchers studying multipactor worked to perfect semi-empirical models which made unrealistic assumptions concerning SEE and focused on simple geometries in order to make analytic predictions of multipactor thresholds feasible. In the early 1970's, multipactor research began to implement the models obtained from SEE research in

computer-based multipactor simulations [20, 32, 33]. It is at this time that multipactor research began to really benefit from SEE research. Multipactor simulations produced more accurate results in predicting multipactor breakdown thresholds for complex geometries than the previous semi-empirical models [5]. With the implementation of PIC algorithms in the 90's, multipactor simulations could handle problems involving a large number of electrons [20]. Despite the advances in multipactor simulation, the underlying SEE models still contain unsubstantiated assumptions which lead to variability in simulation results. The struggle to produce more accurate SEE empirical models have been hampered by the difficulties associated with SEE measurements. The techniques and technology involved in these measurements have seen many advances over the past century; however, discrepancies in SEE measurements are still witnessed today. Figure 17 provides a brief timeline of important events in the history of SEE and multipactor research.

### 2.2 Secondary Electron Yield

The measurement of SEY is the simplest conceptionally of all the types of SEE measurement. The SEY is defined as

$$\mathrm{SEY} = \sigma = \delta = \frac{\mathrm{i_{sec}}}{\mathrm{i_{pri}}} \tag{1}$$

where σ and $\delta$ are the characters normally associated with SEY. The primary current, $i_{pri}$, is the current associated with the electrons that impact a sample. The secondary electron current, $i_{sec}$, is the current associated with the electrons emitted from a sample. These currents are normally measured using long integration times due to noise. Noise is generated by the random fluctuation in the emission of electrons from the cathode of the electron gun, known as shot effect, and by the SEE process [8, 15, 46].

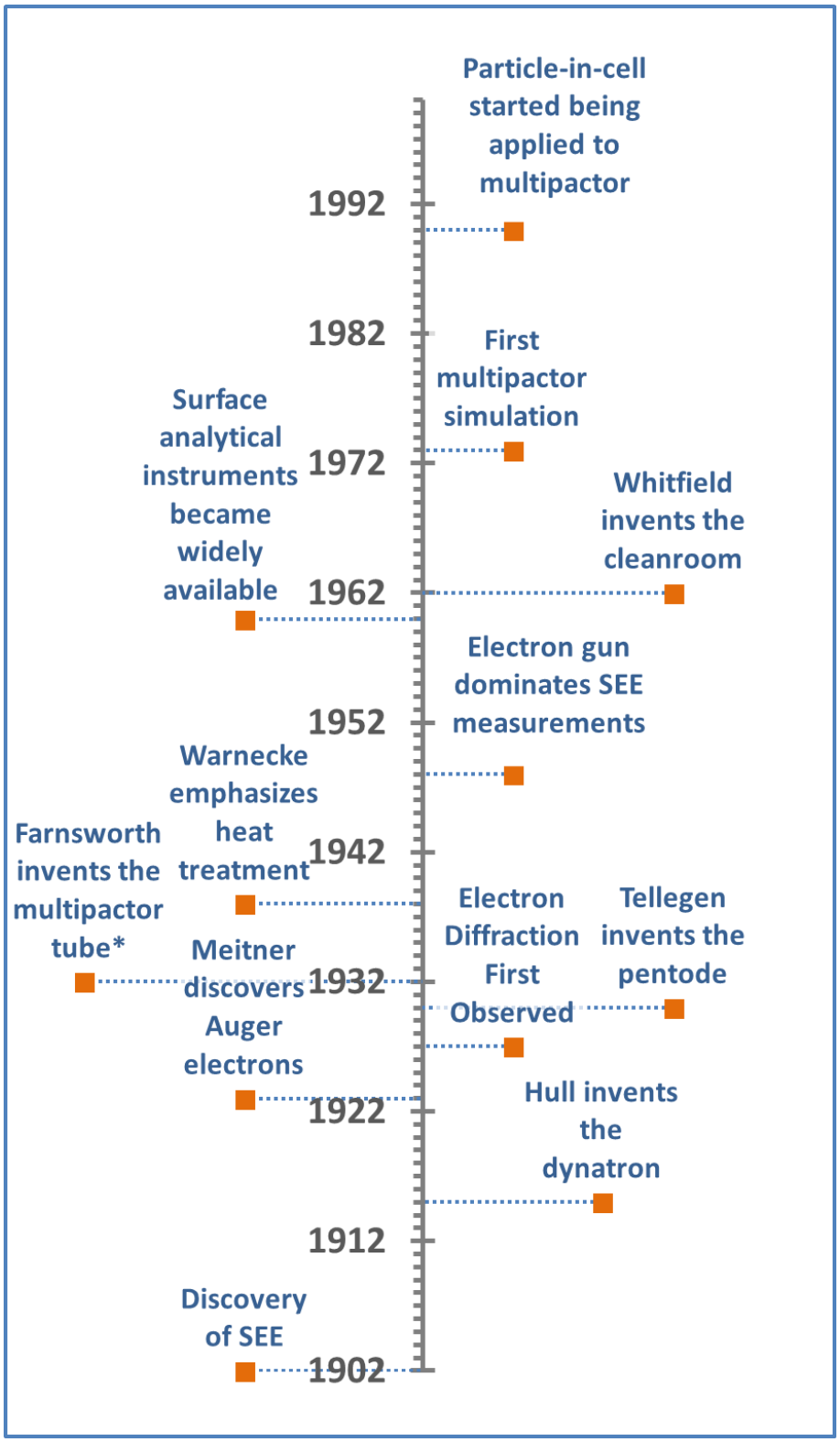


Figure 17: Timeline of SEE and multipactor events. *The multipactor tube was developed sometime in the early 1930's.

In addition to long integration times, digital filtering may also be used to further reduce noise. SEE measurements are often performed in ultrahigh vacuum (UHV) chambers in order to prevent the collision of electrons with gas molecules and reduce the number of absorbed molecules on the test sample.

### 2.2.1 Measurement Techniques

Figure 18 shows a diagram of a SEY measurement apparatus. This apparatus can take on numerous shapes and sizes, and some may not allow measurements of all the currents shown. In Figure 18, $i_c$ is current measured through the collector, and $i_s$ is the current measured through the sample. The primary electron current, $i_{pri}$, can be estimated by placing a Faraday cup at the opening of the electron gun. Alternatively, several researchers have estimated $i_{pri}$ by positively biasing the sample in order to attract most of the secondary electrons back to the sample [47, 48, 49, 50]. This estimated current for $i_{pri}$ will be designated $i_{pe}$ in this research. Note that the conventional current standard is not used; rather, current is in the direction of electron flow in order make the discussion of SEE more intuitive. This convention will be used throughout this research. With the measurement of these three currents, the SEY can be estimated in four ways as shown in Table 1. Each of the equations can be derived using Kirchhoff's current law (KCL). The first three of these equations allow the estimation of SEY with two measured currents. To the author's knowledge, estimation using the fourth equation has never been attempted, and the equation is only shown here for completeness.

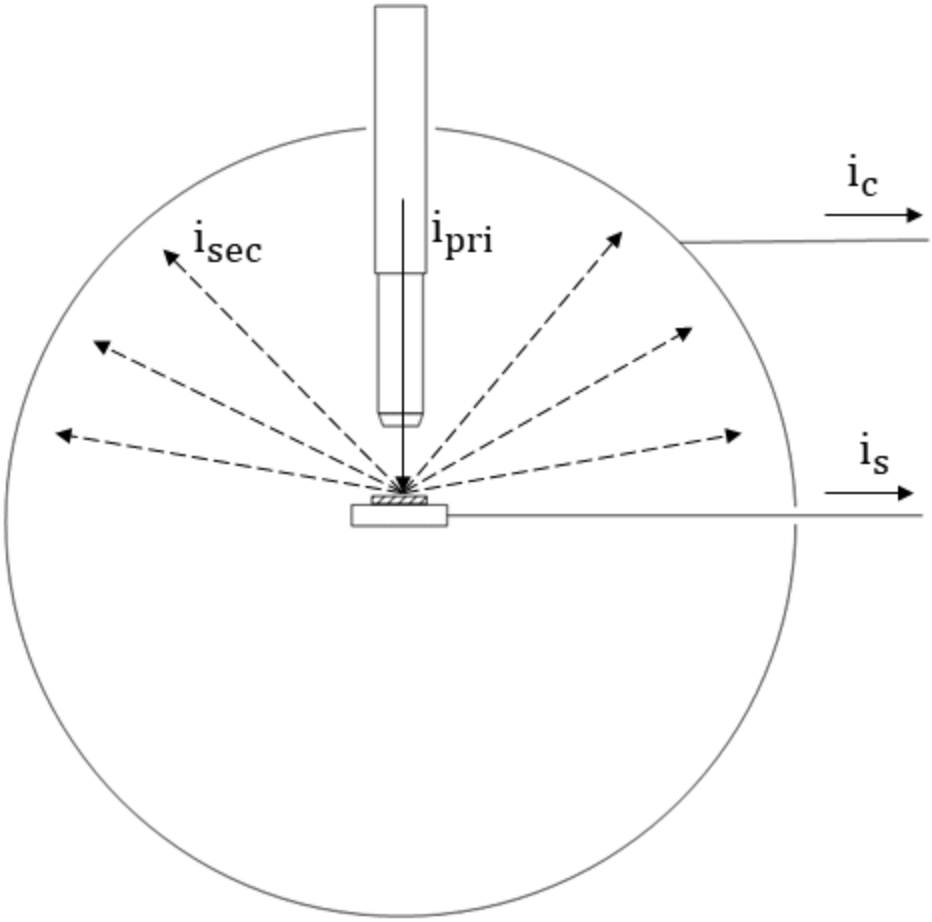


Figure 18: Diagram of SEY measurement apparatus.

Table 1: Equations for estimating SEY

| Measured Currents | Equation |
|---|---|
| $i_c$ and $i_{pe}$ | $\sigma_{est.1} = \frac{i_c}{i_{pe}}$ |
| $i_s$ and $i_{pe}$ | $\sigma_{est.2} = \frac{i_{pe} - i_s}{i_{pe}} = 1 - \frac{i_s}{i_{pe}}$ |
| $i_c$ and $i_s$ | $\sigma_{est.3} = \frac{i_c}{i_c + i_s}$ |
| $i_c$, $i_t$, and $i_{pe}$ | $\sigma_{est.4} = \frac{i_{pe} - i_s}{i_c + i_s}$ |

### 2.2.2 Application of Potential Bias

The secondary electrons generated by the collision of primary electrons with the sample surface go on to collide with the collector, electron gun, and other objects in the

chamber producing additional secondaries. Hachenberg and Brauer called these secondary electrons “tertiary electrons” [51]. Tertiary electrons will be used throughout this research when describing electrons that are neither the primary electrons nor the secondary electrons generated by the incidence of primary electrons. The tertiary electrons must be controlled in order to prevent measurement errors. There are three biasing techniques which are used to control the tertiary electrons.

The first technique is to create a static electric field surrounding the sample. This is typically done by negatively biasing the target because the collector in many cases is the wall of the chamber which is directly connected to earth ground for many chamber designs. The barrel of the electron gun is typically electrically connected to the chamber, so it is also held at ground potential. Figure 19 illustrates the direction of the electric field within the chamber. This electric field causes many of the tertiary electrons to be pulled back towards the collector preventing them from returning to the target. This is due to the fact that most secondary electrons are emitted with lower energies than the incident electrons.

The disadvantage with this technique is that the electric field is greatest between the end of the gun barrel and sample causing primary electron beam defocusing. This defocusing may cause slow primary electrons to miss the sample completely as illustrated in Figure 20. For all the equations shown in Table 1, the estimates for SEY will approach unity as the number of primary electrons missing the target increases. In this century, with the renewed interest in SEY measurements, repeat occurrences of the SEY approaching unity as the primary electron energy approaches zero have been reported in literature [4, 52, 53]. These reports are likely artifacts of the measurements. Andronov emphasized that previous SEY experiments made by several researchers had not shown this tendency

towards unity [52]. Furthermore, early theories indicated that the SEY would approach 5% or less, and H. A. Fowler and H. E. Farnsworth also provided evidence that the SEY tends toward 5% or less as the primary electrons' energy approaches zero using primary electron energies as low as 0.2 eV [54]. As the primary electron energy is decreased, it becomes increasing difficult to determine the number of primary electrons impacting the sample due to beam defocusing [55]. Careful attention must be exercised in order to perform accurate measurements with low-energy primary electrons. The beam defocusing caused by biasing the sample should be avoided by reducing the sample bias.

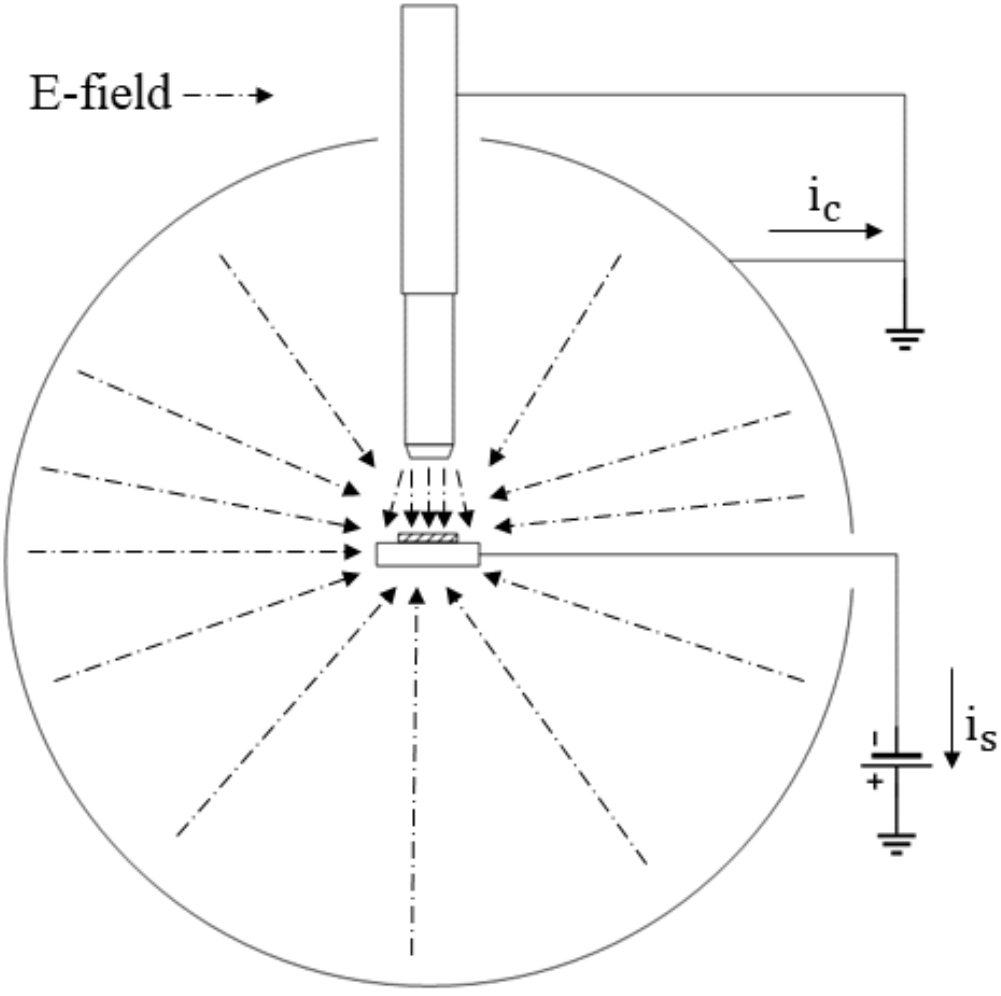


Figure 19: Illustration of the direction of the electric field for a biased target.

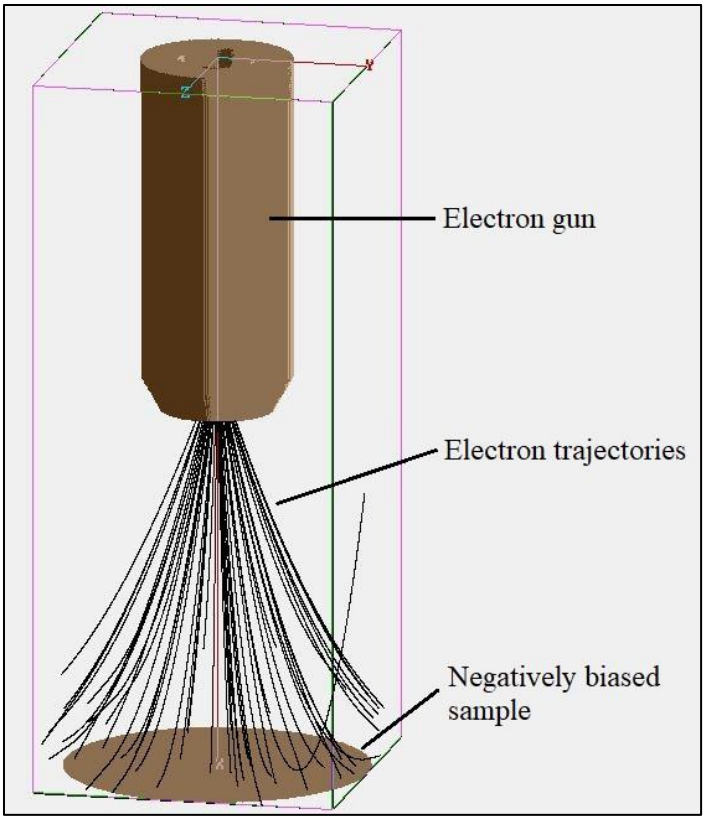

Figure 20: Illustration of primary electrons being deflected by a negatively biased sample.

In the second technique, the collector is positively biased with respect to the sample in order to retain the tertiary electrons at the collector. This technique is also subject to beam defocusing at low primary electron energies, which may require reducing the collector bias at low primary electron energies [56]. It requires a more complex apparatus than first technique due the addition of the collector.

The third technique is to have zero electric field surrounding the target while creating an electric field between a grid and collector (Figure 21). This technique is reminiscent of the suppression grid used in the pentode discussed in Section 2.1.6. The electric field between the collector and grid forces most of the tertiary electrons generated on the collector back into the collector. This configuration can also be used to measure the secondary electron energy distribution. The disadvantages with this configuration are the

complexity involved in its construction and that any tertiary electrons emitted on the side of the grid facing the sample can return to the sample uninhibited because no electric field exists in that region. In 1959, Hachenberg and Brauer provided a diagram of an apparatus using the same technique to return secondary electrons to the collector (Figure 22) [51]. To the author's knowledge, the use of grids is encountered far less often in the measurement of SEY than in the measurement of secondary electron energy distribution, such as in a LEED/Auger spectrometer or 4-grid retarding field analyzer [57].

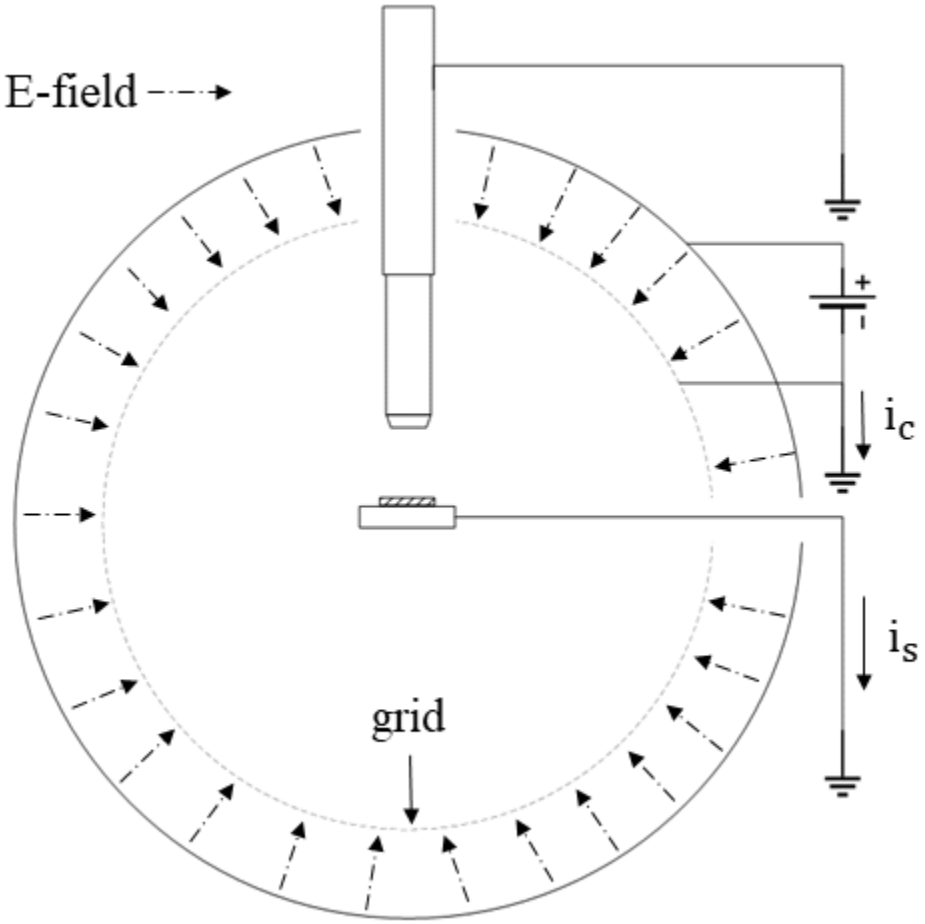


Figure 21: Illustration of the direction of the electric field between collector and grid.

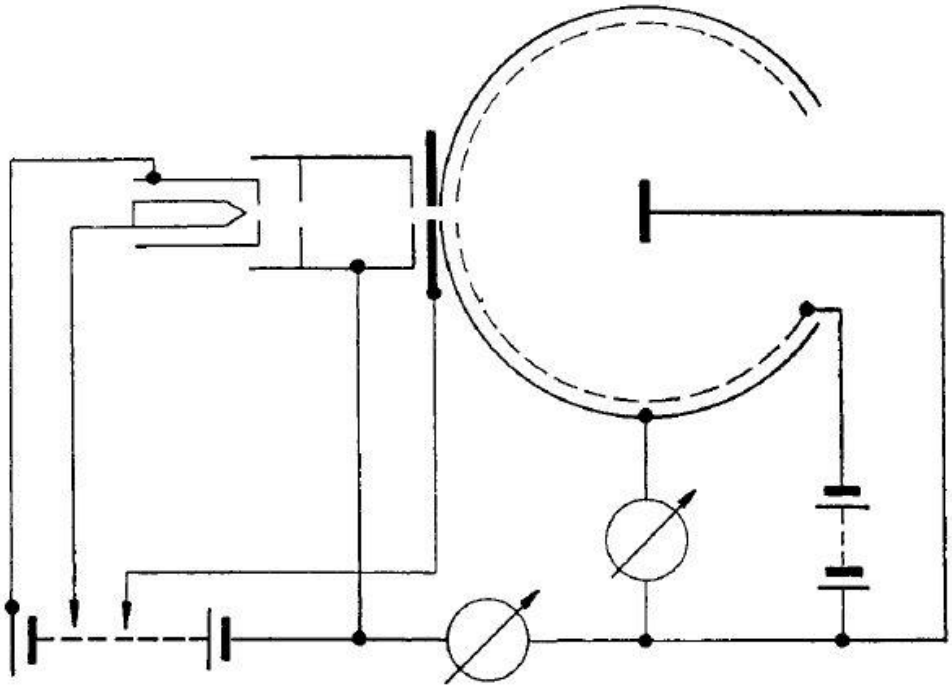

Figure 22: Diagram SEY measurement device provided by Hachenberg and Brauer in 1959 [51].

Pertinent to the discussion of biasing is the topic of CPD. It is also called Volta potential and was discovered by Alessandro Volta in 1797 [58]. When two metals with differing work functions are electrically connected, a CPD will exist if the metals have differing work functions. As illustrated in Figure 23, the Fermi level for the electron gun, $E_{F(gun)}$, is higher than the Fermi level for the target, $E_{F(target)}$, before an electrical connection is made between them. When an electrical connection is made, the Fermi levels must become equal in order for thermal equilibrium to be achieved. Because the work function for the gun, $\Phi_{gun}$, differs from the work function for the target, $\Phi_{target}$, a CPD, $V_{cpd}$, will exist between the gun and the target. Thus, an electrical field exist between the gun and the target which is capable of deflecting electrons.

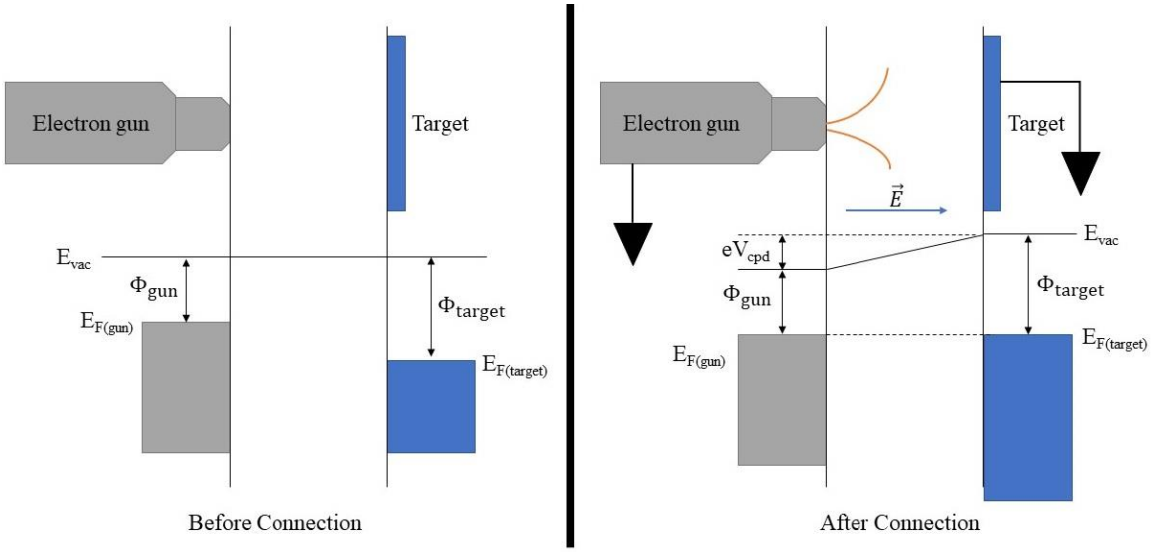


Figure 23: Illustration of CPD between electron gun and target. Orange curves are exaggerated electron deflections caused by the retarding field of the CPD.

CPD affects all types of SEE measurement [51, 52, 54, 59, 60]. Since CPD is usually a couple volts at most, the trajectories of slow electrons are impacted the most [58]. Thus, the effects caused by CPD become especially apparent when attempting to make measurements using primary electrons with low energies [52, 54]. Since the work function of materials changes with surface contamination, the CPD within the measurement apparatus may change over time requiring careful recalibration [54]. Furthermore, the work function may vary for different patches on the surface of a polycrystalline surface given rise to the "patch effect" [54, 55, 61]. This effect causes the primary electrons to be deflected or reflected as they approach within microns of the surface and further complicates low-energy measurements [54, 55].

### 2.2.3 The Universal Curve

When the SEY is plotted with respect to primary energy, the trend shown in Figure 24 is observed. For the discussion of this section, only primary electrons impacting the

surface at normal incidence will be considered. The yield curve tends toward zero as the primary electron's energy, $E_p$, decreases to zero [52, 53, 54]. The yield first reaches unity at $E_1$, which is commonly called the first crossover energy. The yield then increases to the maximum yield, $\sigma_{max}$, at $E_{max}$. Continuing to increase $E_p$ decreases the yield, and the yield again reaches unity at the second crossover energy, $E_2$.

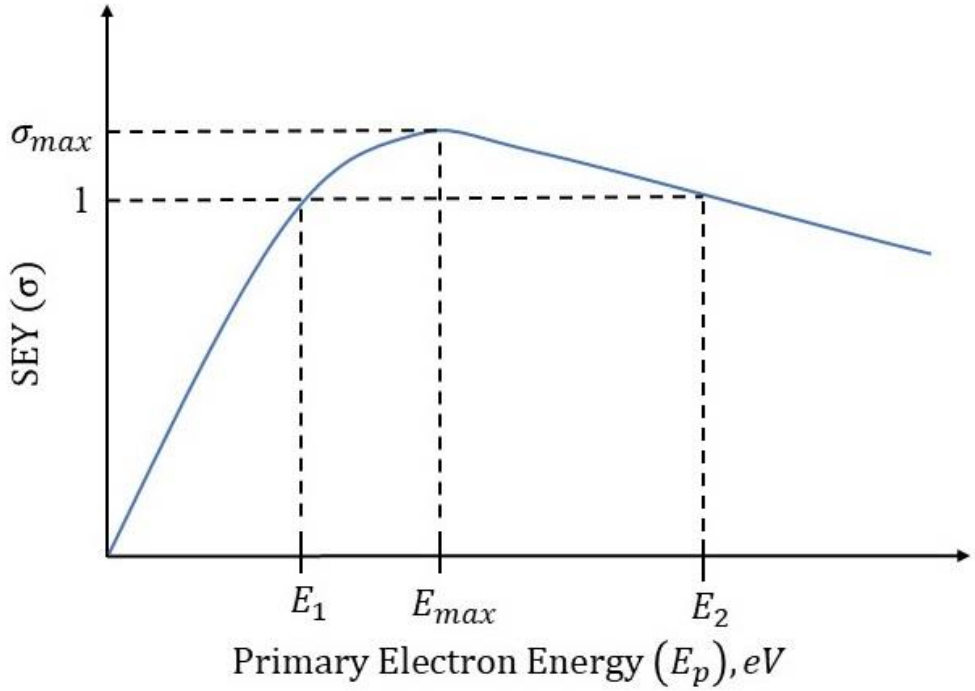


Figure 24: Typical plot of the SEY versus primary electron energy.

In 1950, Baroody was the first to identify that when $\sigma/\sigma_{max}$ is plotted versus $E_p/E_{max}$ for a large number of materials the data appears to follow the same curve (Figure 25) [62, 63]. This curve has been called the universal curve. When considering only one material, it is called a reduced yield curve [62].

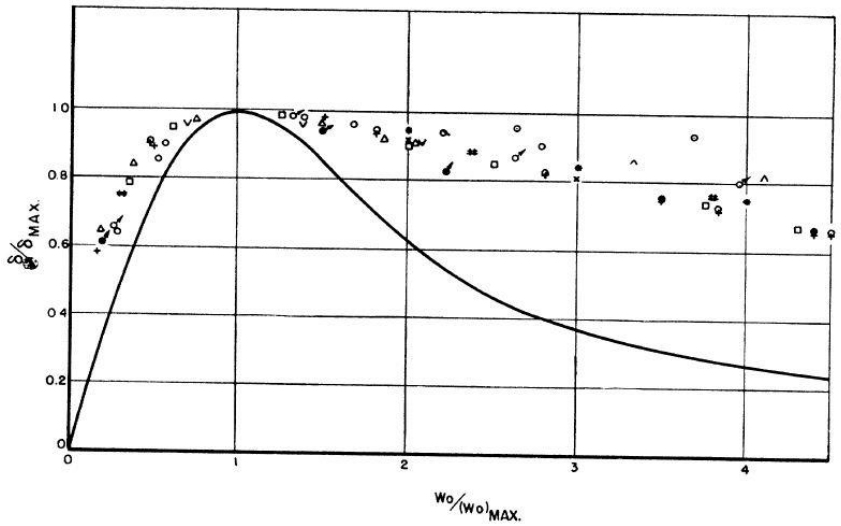


FIG. 1. Variation of secondary emission with primary energy. $\delta/\delta_{max}$ is the secondary emission coefficient divided by its maximum value, and $W_0/(W_0)_{max}$ is the primary energy divided by the energy for maximum emission. The points show experimental results for various materials, taken from small-scale published curves: + Cu, × Ni, ♀ Li, △ Ti, □ Mo, ○ Pt, ∨ Al, ♂ Mg, # Fe, ♂ Cb, ⊙ Rb, ∧ B, ✳ Ge, ♀ Si. The points approximate a single curve. The curve, based on Eq. (24), is qualitatively similar to the experimental curve.

Figure 25: Baroody's original plot of $\sigma/\sigma_{max}$ versus $E_p/E_{max}$ (labelled Wo/(Wo)$_{MAX.}$) [63]. The line drawn on the graph is based on Baroody's semi-empirical model.

In general, the reduced yield curves of metals follow the universal curve allowing their SEY characteristics to be specified using only $\sigma_{max}$ and $E_{max}$. However, the SEY curves for insulators show a strong divergence away from the universal curve at energies greater than $E_{max}$ [19].

### 2.2.4 Material Dependency

Due to the large variations appearing in SEY measurements, it is difficult to draw any in-depth conclusions about the relationship between SEY and other material properties. In general, it appears that materials consisting of single elements exhibit a lower yield than those made of compounds [41, 51]. Additionally, insulators typically produce a far greater yield than conductive materials, but they are subject to surface charging effects [8, 9, 64].

For primary energies below $E_1$, the insulator becomes negatively charged until the primary electrons are unable to reach the target due to the repulsion created by the electric field. For primary energies between $E_1$ and $E_2$, the surface becomes positively charged, and the primary electrons receive additional acceleration when approaching the target. Positive

charging continues until the primary electrons reach the energy of $E_2$. For primary energies above $E_2$, the surface becomes increasing negatively charged until the surface is charged such that the primary electrons are decelerated to an energy $E_2$. For primary energies around $E_2$, the surface will oscillate between positive and negative charging. Due to this charging effect, the SEY of insulators is measured with short pulses of primary electrons [8, 9, 51, 64]. The insulator may also be heated between pulses in order to aid in the migration of electrons through the insulator [51]. More recently, Cazaux summarized the following methods of handling this charging: mobilizing the electrons through UV radiation, heating the material to increase electron diffusivity, limiting the number of gun pulses per SEE measurement, and compensating for positive surface charging with a low energy electron flood gun [65, 66].

### 2.2.5 Temperature Effects

For clean metal surfaces, temperature has a negligible effect on the SEY provided the metal does not experience a phase transformation [9, 41, 62]. Metals with surface contaminants, such as absorbed gases, however may experience SEY variations due to changes in the gas density with temperature [8, 67]. In metals, the number of secondaries produced is limited by the interaction of secondaries with conduction-band electrons [62, 68]. Increasing the temperature of a metal increases the thermal energy of conduction-band electrons; however, it has a negligible effect on the yield due to the energy of the secondaries being much larger than the thermal energy [9].

The SEY of insulators is generally temperature dependent [9, 8]. Absorption of secondaries in insulators is primarily due to electron-phonon and electron-impurity

interactions due to the lack of conduction-band electrons [68]. The secondaries experience much less energy loss from these interactions leading to a much higher SEY for insulators [68]. These interactions are not believed to change significantly with temperature, and the temperature dependency of SEY is most likely due to changes in the conductivity of the insulator which affects charging [8, 9]. Bunney wrote that there are indications of an inverse relationship between temperature and SEY in insulators though McKay wrote that some insulators are temperature independent [8, 67].

### 2.2.6 Surface Effects

Since the discovery of SEE, it has been known that surface roughness has a significant effect on the SEY [1]. Rough surfaces have a lower SEY than smooth surfaces. McKay wrote,

"*This is qualitatively explained by postulating that a rough surface can be likened to a series of holes or wells. A secondary electron, produced at the bottom of such a well, may be trapped by the sides of the well and hence will not be emitted from the surface*" [8].

Porous materials also have a lower SEY than nonporous materials. Bruining *et al*. compared the porous material to a surface rich in labyrinths from which it was "…almost impossible for secondaries to escape" [69].

If the material is a single crystal, the different faces of the material have been shown to produce small differences in SEY [51]. Thus, when measurements are made on single crystals, the crystal face involved in the interaction must be recorded. For polycrystalline materials, differences in the SEY across the surface of the material may appear negligible if the primary electron beam strikes multiple crystals during each measurement. Jonker made a similar remark about the angular distribution of secondary electrons from a

polycrystalline material: he stated that the effects on the angular distribution would be negligible provided that the primary electrons struck a large number of crystals [70].

Surface contaminants may either increase or decrease the SEY. Prolonged bombardment of primary electrons tends to produce surface carbon contaminants which lowers the SEY and is known as the "conditioning effect" [71]. On the other hand, oxidation can cause the SEY to increase or decrease. A monatomic layer of oxygen will form an "electrical double layer" which will increase the work function and reduce the yield [8]. However, if a thick layer of oxide forms on the surface, the yield will be greatly altered and likely increase [8].

### 2.2.7 Angle of Incidence Effects

For polycrystalline and amorphous materials which are nonporous and have smooth surfaces, increasing the incidence angle with respect to normal incidence increases both $\sigma_{max}$ and $E_{max}$ [8, 41]. TSE are generated closer to the surface when the incidence angle is increased, which increases the probability of the TSE escaping the surface rather than being absorbed [8, 72]. Porous materials, such as soot, however have shown much less dependence on incidence angle [62, 72]. Dekker presumed that the reduction in dependence was due to "…the possibility of interception of emitted electrons" [62]. However, Bruining indicated that for the rough, porous surface of soot the incidence angle is not well defined [72]. The data measured and plotted by Bruining is shown in Figure 26.

For single crystals, the dependence of SEY on incidence angle is not well understood. As shown in Figure 27, minima and maxima exist when plotting SEY with respect to incidence angle. The angular position of these maxima does not depend on the

energy of the primary electrons, which would be expected if the variation in SEY was due to diffraction [73].

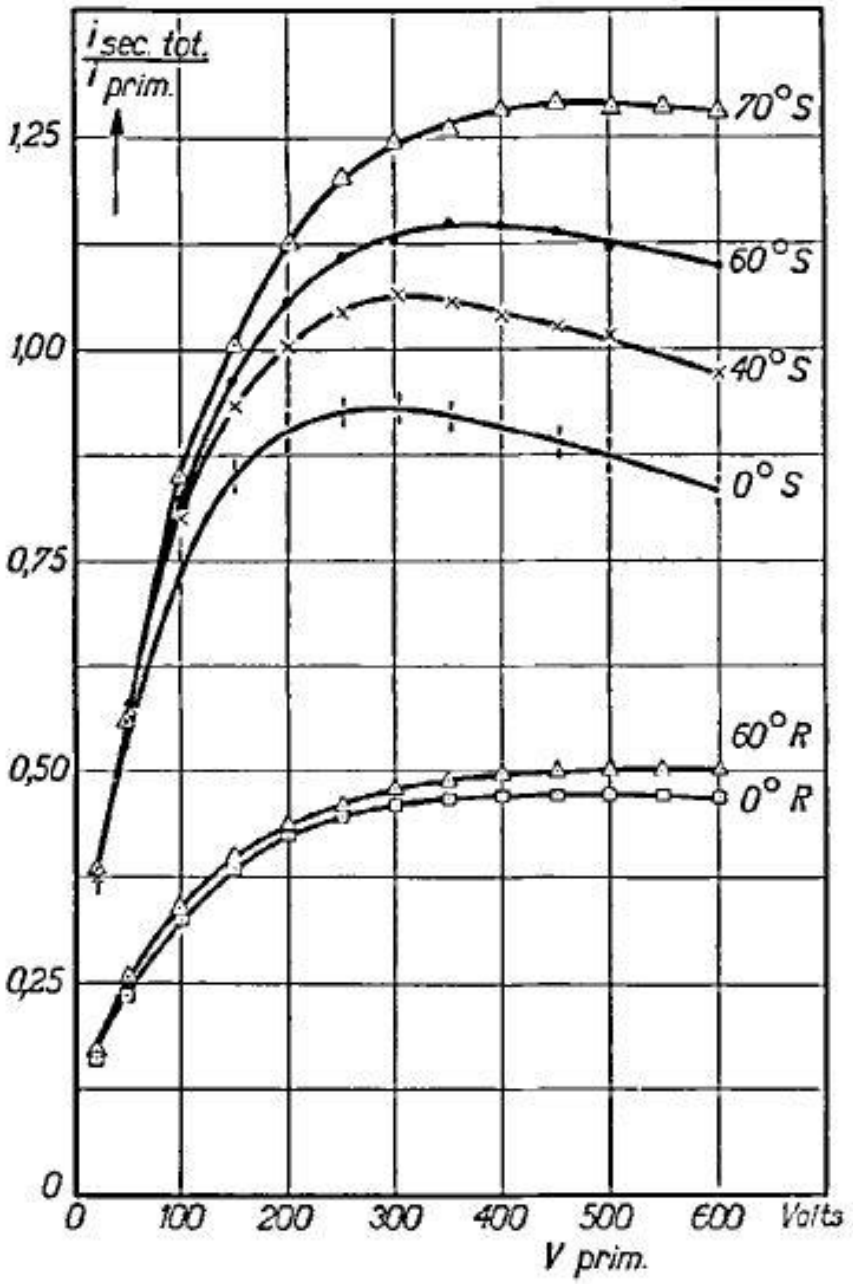


Figure 26: SEY as a function of the accelerating voltage of the primary electrons for different incidence angles [72]. The “S” and “R” next to each curve indicates a smooth nickel surface and rough, porous carbon surface respectively.

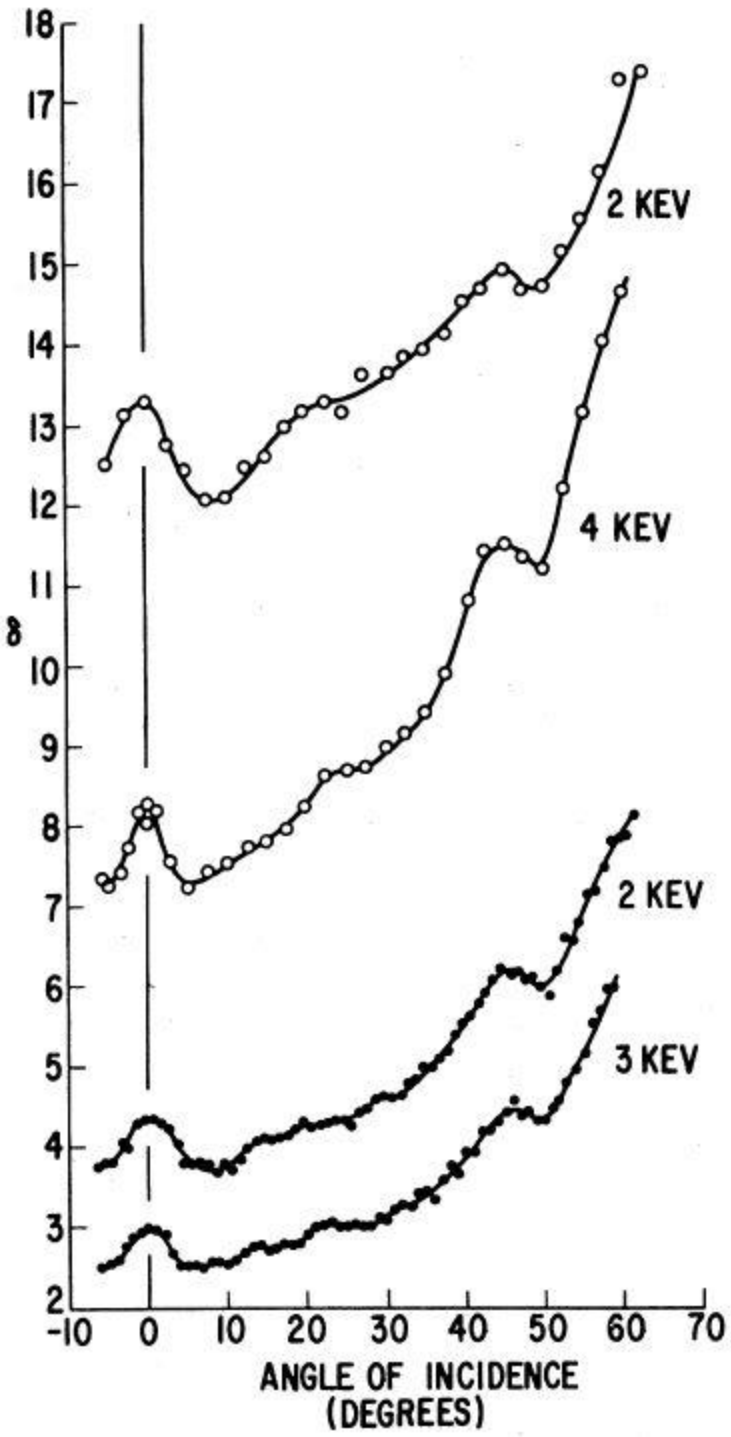


Figure 27: SEY versus incidence angle for different primary electron energies [73]. The curve containing open circles corresponds to data obtained for MgO, and the curve containing solid circles corresponds to data obtained for LiF.

### 2.2.8 Effects of Primary Current Level

McKay indicates that many investigators under widely differing conditions of primary current have found that SEY is independent of the primary current [8]. Bunney also indicated that theoretical analysis confirms that the SEY is independent of the primary current [67]. However, the measurement of SEY at low primary electron energies is known to be affected as current increases due to the buildup of space charge within the apparatus [7, 8, 51]. Since many of the secondary electrons have relatively low energies, an increase in space charge above the emitting surface may occur when the primary electron current is increased [74, 75]. This can reduce emission causing the measured SEY to be less than the actual SEY [75]. Furthermore, large currents may lead to surface heating which could cause changes in the surface composition leading to variations in the SEY.

### 2.2.9 Models

Physicists have developed many semi-empirical models in an attempt to characterize SEY: Baroody [63], Bruining [9], Dekker [62], Dionne [76], Lye and Dekker [77], Marshall [78], Salow [79], Wooldridge [80], and Dekker and van der Ziel [81]. This list is not comprehensive. Some of the models follow a classical approach while other follow a quantum mechanical approach. They predict the general behavior of SEY for materials though they often deviate from experimental data. In addition, most, if not all, require calibration using experimental SEY data [64]. The models are based on simplifying assumptions in order to make analytic solutions tractable; however, Devooght *et al*. wrote that the main problem with the early theories was the lack of justification for the assumptions [82].

Attempts have been made to correlate work function, density, and atomic shell filling to $\sigma_{max}$. Though $\sigma_{max}$ has been shown to increase with work function, it is believed that this behavior is more likely due to underlining factors which vary with the work function [8, 41]. A correlation between density and $\sigma_{max}$ can just as easily be observed [8]. Sternglass made the discovery that $\sigma_{max}$ varies along each horizontal line of the periodic table from alkalis to multivalent metals [51, 83]. This indicates that SEE is dependent on bound atomic electrons in addition to electrons in the valence and conduction bands [83]. In 2005, Lin and Joy again found that SEY data for numerous materials seemed to correlate with atomic shell filling; however, they could not make a final conclusion because they needed additional experimental data to fill the gaps that existed in their available SEY data [2]. To the author's knowledge, physicists have not reached a conclusion on the relationship between $\sigma_{max}$ and shell filling.

As engineers began incorporating multipactor simulations into the development of RF components, models of SEY were necessary in the performance of these simulations. Vaughan recognized this need and developed a phenomenological model to determine the SEY based on the energy and incidence angle of the primary electrons [84, 85]. Vaughan's model is applied in multipactor simulation programs, such as FEST3D®, ICEPIC, and CST® [37, 86, 87]. Vaughan's model requires only four parameters to characterize a material: two factors related to the smoothness of the surface, $\sigma_{max}$ at normal incidence, and $E_{max}$ at normal incidence [6, 84, 85]. Physicists and engineers continue make adjustments to Vaughan's model in order to find better agreement with experimental data [6, 88].

In 2002, Furman and Pivi developed a phenomenological, probabilistic model that is designed to be mathematically self-consistent [89]. In order to be self-consistent, the probabilistic model was designed such that:

"*(1) when averaging over an infinite number of secondary-electron events, the reconstructed $\delta$ and $d\delta/dE$ are guaranteed to agree with the corresponding input quantities; (2) the energy integral of $d\delta/dE$ is guaranteed to equal $\delta$; (3) the energy of any given emitted electron is guaranteed not to exceed the primary energy; (4) the aggregate energy of the electrons emitted in any multielectron event is also guaranteed not to exceed the primary energy*" [89].

$\delta$ is again the SEY, and $d\delta/dE$ is the one of several ways to represent the secondary electron energy spectrum. In addition to providing a model for SEY, this model also specifies the energy distribution of the secondaries [89]. In contrast, Vaughan's model only specifies the SEY [84, 85]. However, this model generally requires 44 parameters, and there is not a unique set of parameters that define a specific material [6, 89].

The aforementioned models developed by Vaughan, Furman, and Pivi were developed for the simulation of devices that are orders of magnitude larger than the sub-nanoscale surface features which lead to variations in the SEY across a surface. The Furman and Pivi model is used more often by the particle accelerator community, while Vaughan's model is used more often by the RF community [6]. Attempting to use models that capture the sub-nanoscale variations is not computationally feasible in the simulation of much larger devices; however, there is interest in modeling SEE at the sub-nanoscale level for electron probe microanalysis, electron microscopy, and electron spectroscopy, which is addressed with Monte Carlo (MC) electron trajectory simulation methods [90].

MC simulations began to be applied to charged particles in the 1950's [91]. In these simulations, an electron's trajectory through a material is determined based on the

probability of different events occurring (e.g. elastic collision, inelastic collisions, and ionization events) and the sampling of random numbers [91]. Plotting the simulated trajectories for many electrons provides an overall picture of the SEE interaction taking place within the material as shown in Figure 28. Though the results of MC simulations provide useful insight, they are not based on first principles and require calibration using experimental SEE measurements [2, 90, 92]. Due to inconsistencies that are observed in SEE measurements, it is difficult to determine which set of SEE data to use in calibration. David and Lin provided a method for identifying and correcting errors in measured SEY data using the universal yield curve [2]. However, even with these corrections, the accuracy of MC simulations remains limited by the accuracy and availability of measured SEE data.

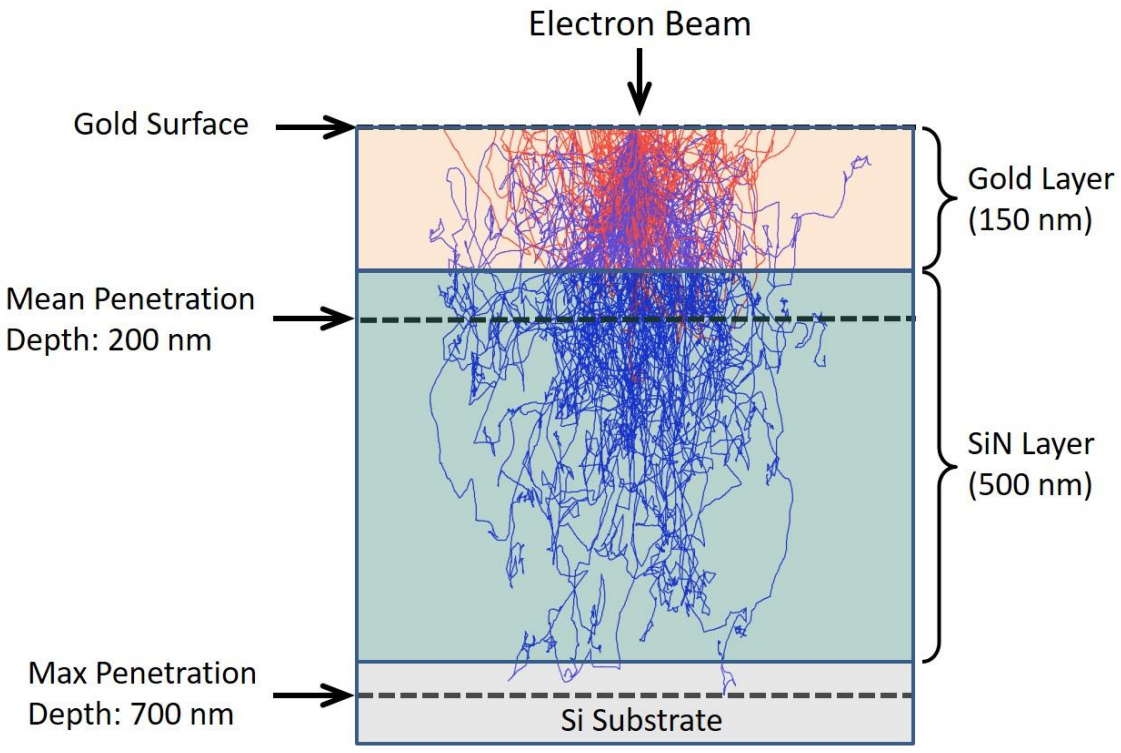


Figure 28: Simulated trajectories of 10,000 electrons for 20-keV primary electrons [4].

### 2.2.10 Mitigation

For many researchers today, much effort has been placed on developing materials with the goal of mitigating SEE. This mitigation can be achieved in several ways: applying a surface coating, performing a surface conditioning process, heating the surface while in a vacuum, sputter cleaning the surface, or surface roughening. To the author's knowledge the first time that surface coatings were used to reduce SEE in order to enhance an electronic devices performance was the vacuum tube device known as the tetrode.

During the development of the tetrode, SEE from the anode was identified as causing undesirable distortion in the tube's I-V characteristic (Figure 29) [9, 18]. To reduce the anode's SEE, a layer of porous carbon was applied to the anode. This reduced the distortion though the tetrode's performance is still less ideal than the pentode [18]. However, when transmitting high power, high frequency signals, the tetrode with its coated anode has superior performance over the pentode [9]. This is just one example of the application of a surface coating to reduce SEE.

A surface coating is an additional layer of material added to the surface of a bulk material. An example of this would be depositing a layer of lithium ($\sigma_{max} = 0.59$) on copper ($\sigma_{max} = 1.53$) so that the SEE properties of the surface are that of lithium which has a lower yield [2]. Provided the surface coating is thick enough, the surface will exhibit the SEE properties of the coating; otherwise, in the case of thin films, the surface exhibits neither the SEE properties of the bulk material or coating material and undesirable behavior such as the Malter effect may exist [9]. Porous coatings with conductivity will in general reduce SEE [8, 62]. On the other hand, porous coatings involving insulators, such as MgO, will

greatly enhance SEE above that of nonporous, insulative coatings due to electric field effects [62, 93].

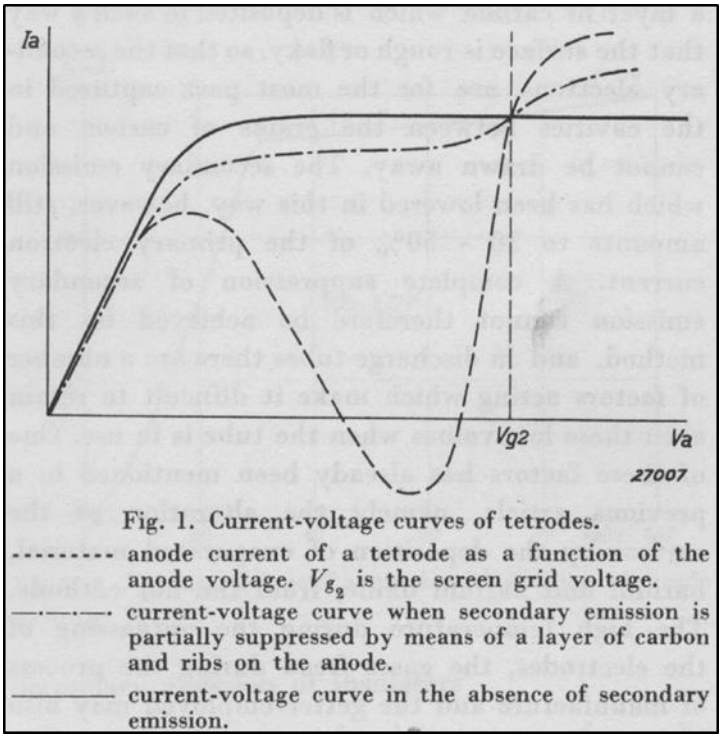


Fig. 1. Current-voltage curves of tetrodes.
--------- anode current of a tetrode as a function of the anode voltage. $V_{g_2}$ is the screen grid voltage.
—·—·— current-voltage curve when secondary emission is partially suppressed by means of a layer of carbon and ribs on the anode.
——— current-voltage curve in the absence of secondary emission.

Figure 29: Comparison of Tetrode I-V Characteristics [18].

Surface “conditioning”, “cleanup”, or “scrubbing” is the process of intentionally inducing multipactor breakdown in a controlled manner in order to reduce SEE [94, 95, 96]. In this process, the surface is repeatedly bombarded by electrons. Fundamentally, the process may be performed using a beam of electrons from an electron gun in a procedure called “electron conditioning” [97]. There are two popular theories as to why this process reduces SEE. The first theory is that prolonged exposure to electron bombardment drives absorbed gases out of the surface thereby decreasing SEE [94, 95]. The second theory is that the electron bombardment causes a gradual buildup of a carbon layer on the surface [71, 96, 98]. In some situations, either or both of the theories could be true. Nevertheless, conditioning does not always reduce the SEE of a surface. In the case of aluminum, it has

been shown to increase SEE by increasing oxide growth [97]. In short, the variations in SEE due to conditioning are caused by changes in the surface chemistry, and these changes may be observed by using surface analytic instruments [96, 97, 98].

A surface may also be heated to temperature near the melting pointing while in a vacuum in order to promote outgassing of absorbed contaminants. This process is known as heat treating the surface and was discussed in Section 2.1.10. Alternatively, the absorbed contaminants may be removed by sputter cleaning the surface with an inert gas. For example, Gonalez *et al.* showed that the SEY of silver, gold, and copper could be significantly reduced by sputter cleaning with argon (Figure 30) [99].

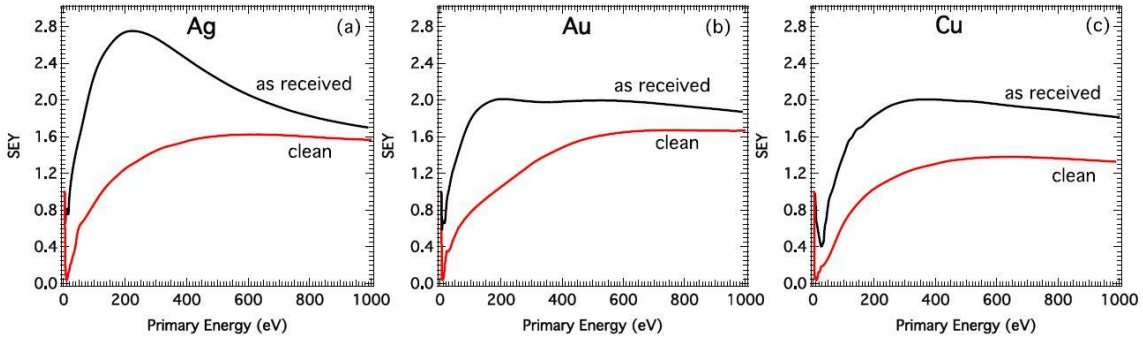


Figure 30: Comparison of the SEY of silver, gold, and copper before and after sputter cleaning with Ar+ ions [99].

Since the discovery of SEE, it was known that a rough surface has a lower SEY than a smooth surface. A rough surface can be produced in two ways. This first way is to remove material from the bulk material through cutting, sanding, etching, etc. The second way is to deposit a rough surface layer onto the bulk material's surface. The deposited layer may or may not have a lower SEY than the bulk material. Either way of roughening the surface comes with the challenge of contamination which could cause the SEE to increase instead of decrease.

Vaughan wrote that surface treatments for the mitigation of SEE are likely to degrade over time. However, it is unknown which type of surface treatment he was referring to because he never specified [77]. Indeed, there are numerous ways in which a surface can be treated as previously discussed in this section. In addition, Kishek *et al*. referred to surface coatings and surface treatments separately and then repeated Vaughan's supposition without providing any additional information [4]. It can be surmised that any surface will undergo changes over time and that the rate at which the changes occur will be dependent on both the material composition of the surface and environment to which it is exposed. Additionally, the SEE may either increase due to gas absorption or decrease over time due to the buildup of a carbon layer. Thus, it cannot be simply stated that surface treatments will degrade over time. The degradation of a surface treatment must be assessed on a case-by-case basis.

The implementation of surfaces treated for SEE mitigation may increase losses within an RF device due to the increases in surface resistivity [100, 101]. Thus, surfaces designed for SEE mitigation must be tested to determine if the surface resistance is acceptable. Furthermore, the losses within a device can be decreased by only placing the possibly more resistive, low-SEE surfaces where needed. The surfaces of the device must also be tested to ensure that harmful, localized heating does not occur in the location where a low-SEY surface has been implemented.

### 2.3 Secondary Electron Energy Spectrum

According to McKay, the secondary electron energy distribution, also called energy spectrum, is more difficult to experimentally measure and theoretically explain than SEY

[8]. The measurement of the spectrum requires the mitigation of spurious electromagnetic fields, Earth's magnetic field, and space charge effects in addition to correcting for CPD [8, 51, 7]. Typically, when discussing the energy distribution, researchers will refer to plots such as that shown previously in Figure 4. However, Figure 31 provides a more accurate picture of the distribution curve and the changes which take place when the primary electron energy is altered. Figure 31 was generated using a retarding electric field which collects secondary electrons emitted in almost all directions from the sample surface.

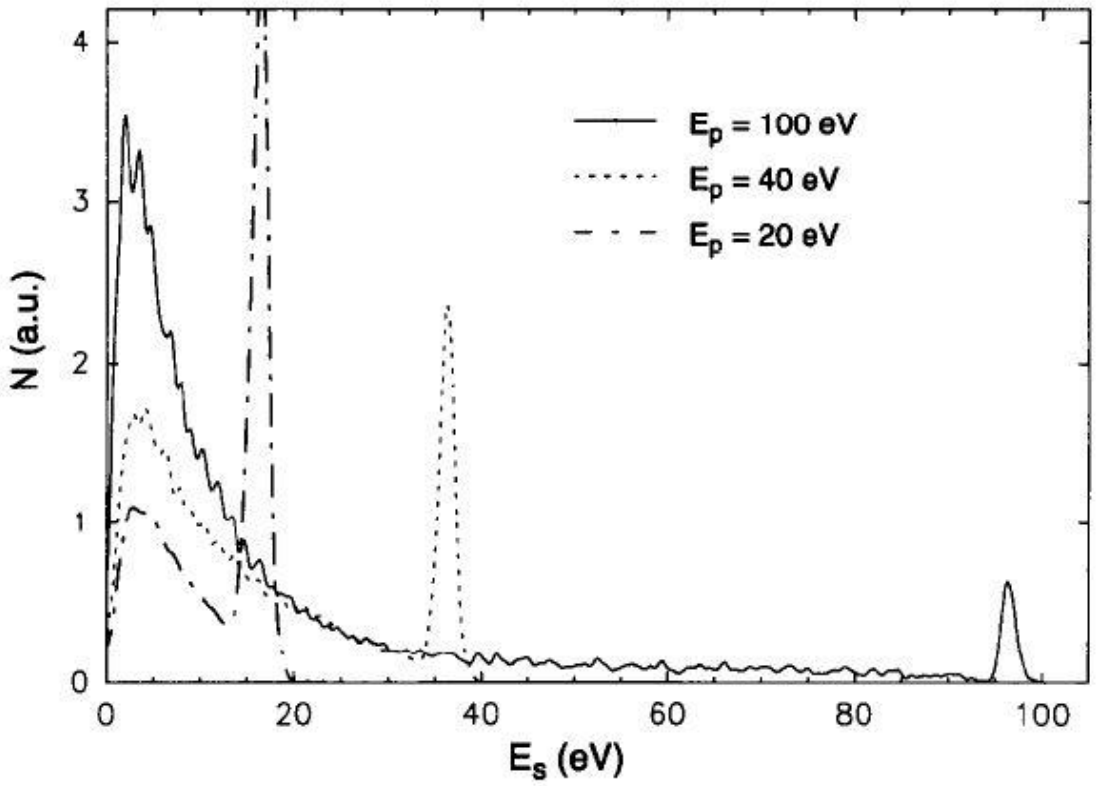


Figure 31: Secondary electron energy spectra for different primary energies [102].

The TSE are commonly designated as the secondary electrons with energies below 50 eV, while the IBP are designated as the secondary electrons with energies between 50 eV and the energy of the EBP, seen as a narrow peek at the right end of the spectrum. The discrimination between TSE and IBP is completely arbitrary [41, 62]. IBP can exist with

energies less than 50 eV. As the primary electron energy approaches zero, the peaks associated with TSE and IBP merge into a single peak, and the primary electrons have insufficient energy to create TSE [55]. The electrons which are emitted from the surface are backscattered primary electrons. Very little is known about the dependence of the secondary electron energy spectrum on material composition and surface condition. The following two sections will discuss the techniques for measuring the spectrum and modeling of the spectrum for simulation purposes.

### 2.3.1 Measurement Techniques

The measurement of the secondary electron energy spectrum is generally made in one of four ways: using a retarding electric field, using a deflecting electric field, using a transverse magnetic field, or using a longitude magnetic field. Each technique measures secondary electrons emitted at different angles from the surface and has advantages and disadvantages. This section discusses each technique and illustrates the apparatuses involved. A table summarizing these techniques is provided at the end of the section. For simplicity, the effects of CPD will not be included in this discussion.

Figure 32 provides a simplified illustration of the apparatus used to measure the secondary electron energy spectrum using a retarding electric field. H. E. Farnsworth used a similar apparatus without the suppression grid to measure the spectra of copper, iron, nickel, and silver in 1952 [59]. The suppression grid prevents most tertiary electrons emitted from the collector from returning to the target. The grid is biased to a lower potential than the target in order to repel secondary electrons from the grid and subsequently the collector. Ideally, the grid should be spherical in shape, and the target

should be relatively small so that the electric field between the grid and collector points radially outward [8]. Only secondaries with energies greater than $-eV_g$ , where $e$ is the charge of an electron and $V_g$ is the potential at the grid with respect to ground, will be able to reach the collector. Increasing $V_g$ decreases $i_{cg}$ monotonically as shown in Figure 33. By numerically differentiating $-i_{cg}$ with respect to $-eV_g$ and scaling the ordinate as desired, the spectrum as previously shown in Figure 31 is obtained [8, 102, 103].

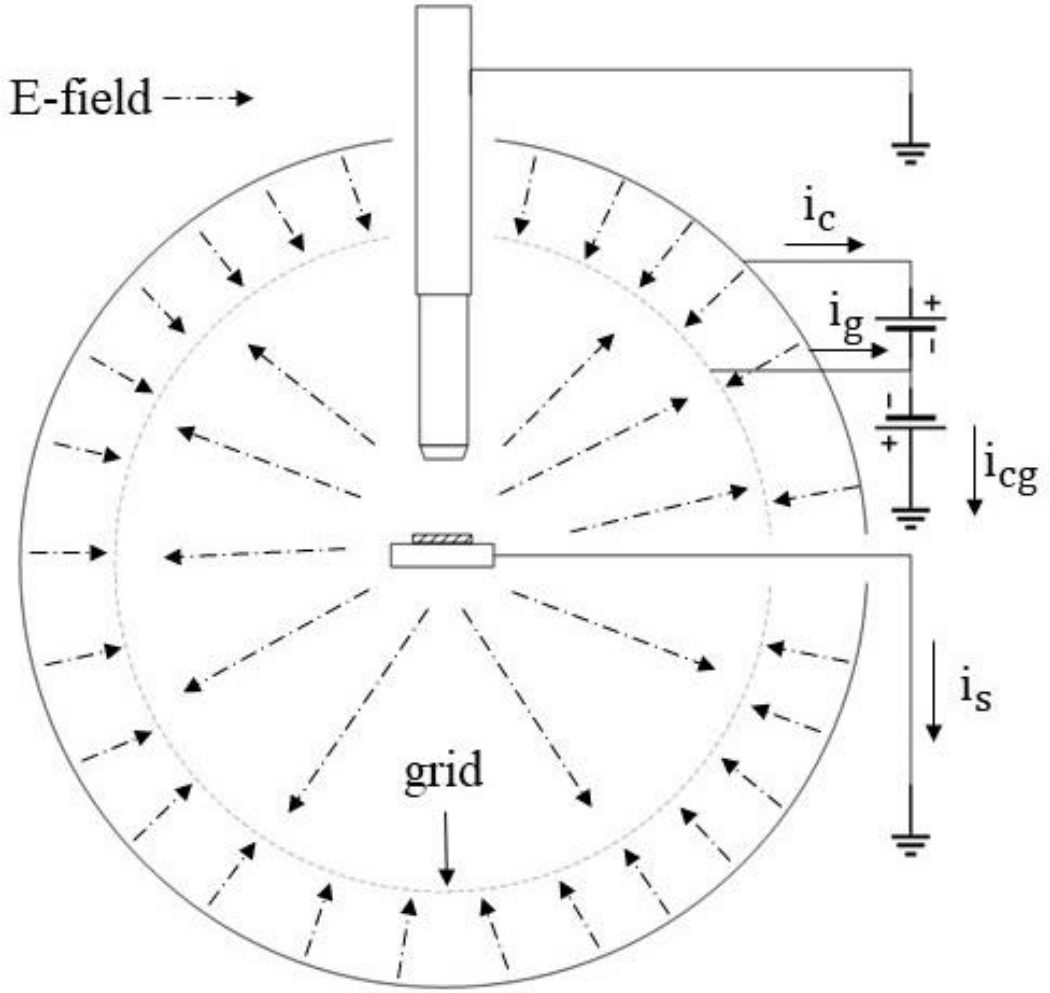


Figure 32: Device for measuring the secondary electron energy spectrum by means of a retarding electric field between target and grid.

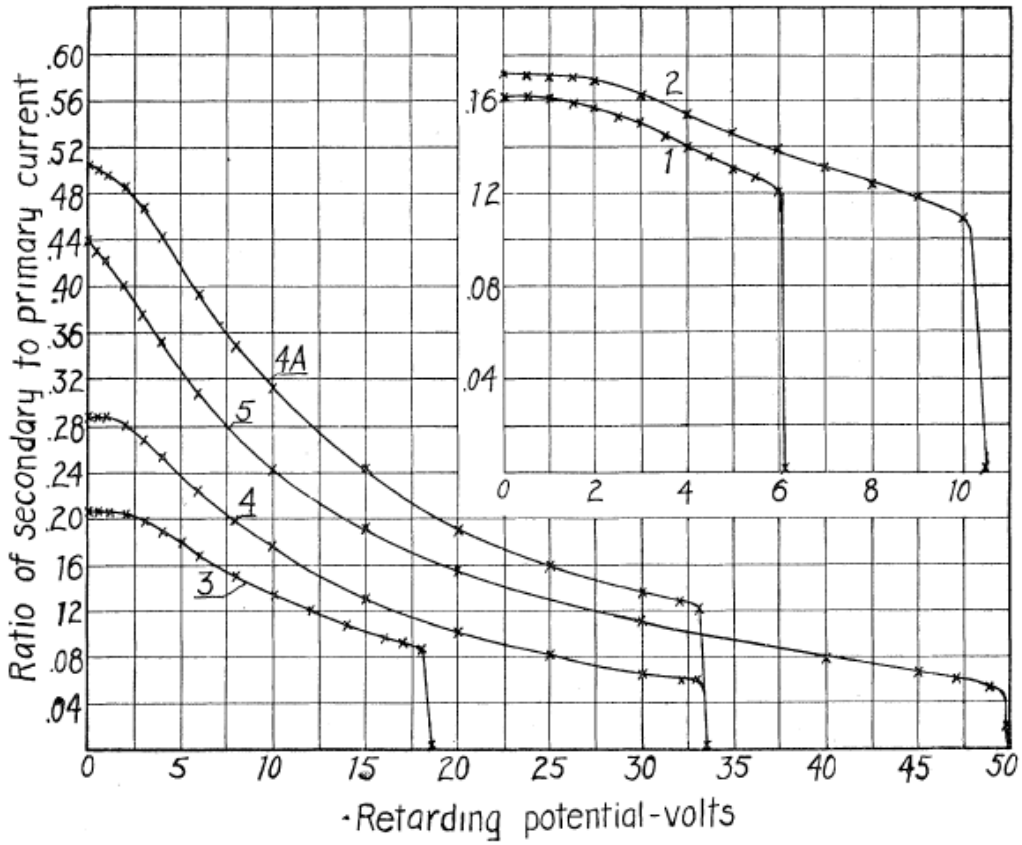


Figure 33: Ratio of secondary to primary current versus retarding potential for nickel [59]. Curve 1 is for 6.2-eV primary electrons. Curve 2 is for 10.4-eV primary electrons. Curve 3 is for 18.6-eV primary electrons. Curve 4 is for 33.5-eV primary electrons. Curve 5 is for 50.0-eV primary electrons. Curve 4A is for 33.5-eV primary electrons before the sample was heat treated. All other curves were measured after heat treatment.

The electric potential of other objects in the UHV chamber may prevent the electric field from pointing radially outward at all locations between the target and grid, and additional grids can be added to the chamber in order to reduce the distortion in the electric field. The innermost gird is held at ground potential in order to create a field-free region between the innermost grid and the target as shown in Figure 34.

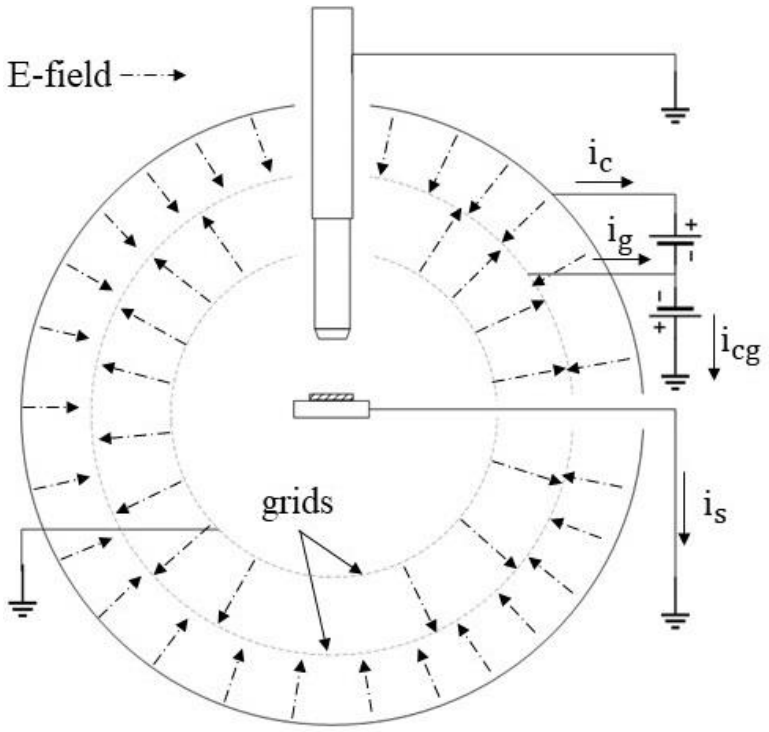


Figure 34: Device for measuring the secondary electron energy spectrum by means of a retarding electric field between grids.

There are a couple disadvantages with this technique. First, numerical differentiation amplifies any noise that may appear in the measured current data. Numerical differentiation can be avoided by applying a small sinusoidal potential to the retarding grid in order to measure the slope of the curves shown in Figure 33 [57]. However, this method requires either a third additional grid in order to avoid capacitive coupling between the collector and retarding grid or an external circuit which nulls the current produced by the capacitive coupling [57]. This method is commonly used in AES and requires a measurement apparatus of greater complexity than those using numerical differentiation only. Secondly, secondary electrons and tertiary electrons from the grids are forced back to the sample leading to a region of space charge in front of the sample. This space charge

region may slow down primary electrons as they approach the sample and secondary electrons leaving the sample. This effect may be mitigated by reducing the primary current.

An advantage with this technique is that secondary electrons are collected from almost all emission angles simultaneously. This is important because it is not uncommon for simulations to use a single model to define the energy distribution for all the secondary electrons leaving a surface regardless of emission angle [89]. Thus, the data measured using this technique is more suited for these models. Another advantage with this technique is that a relatively large current is measured due to the secondary electrons being collected from almost all emission angles which allows this technique to have potentially the highest signal-to-noise ratio (SNR) of all the techniques.

The next technique is to use a deflecting electric field as shown in Figure 35. In this method, the electrons leave the target and travel through a slit. The electrons then pass through an electric field and are deflected based on their energies [103]. The deflecting plates may also have a rounded geometry rather than being flat [104, 105]. Lower energy electrons will be deflected more than higher energy electrons leading to an angular separation of the electrons based on energy. The current associated with each energy can be measured by moving the opening of the collector or by altering the deflecting field.

A disadvantage with this technique is that the energy spectrum is only associated with secondary electrons emitted at the specific angle that aligns with the slit near the target. Thus, this information cannot be applied to models which are describing the energy distribution of all the secondary electrons. Another disadvantage is that this technique measures relatively small currents leading to a lower SNR. Lastly, another disadvantage is that tertiary electrons generated on surfaces surrounding the target are free to return to the

target due to the lack of an electric field. However, this effect can be mitigated by using a suppression grid.

An advantage with this technique is reduced space charge near the sample because secondary and tertiary electrons are not repelled back to the sample as with the previous technique. Another advantage is that this technique can be used to collect secondary electrons from almost all emission angles by rotating the energy analyzer. The exception being the solid angle occupied by the electron gun and primary electron beam. Additionally, numerical differentiation is not required making the energy spectrum less noisy than the retarding electric field method. Lastly, no restrictions are placed on the orientation of the electron gun as is the case when using a magnetic field to measure the energy spectrum.

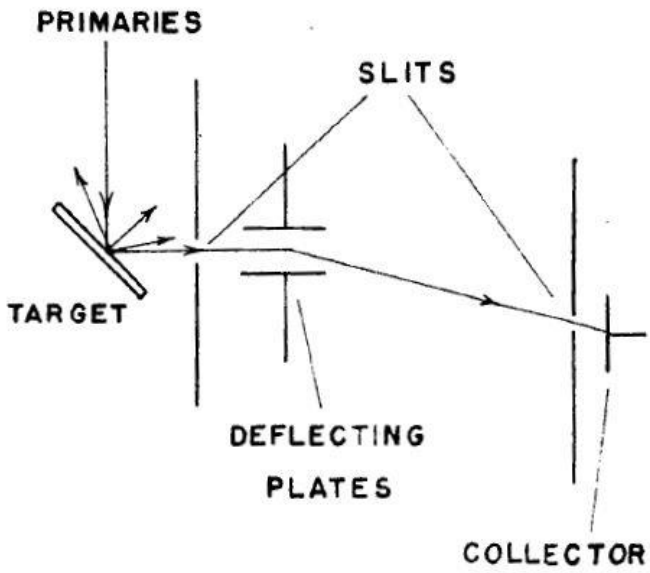


Figure 35: Simple model of device used to measure the secondary electron energy spectrum using a deflecting electric field [103].

Another technique for measuring the spectrum is to use a transverse magnetic field as shown in Figure 36. Like the previous technique, the electrons leave the target and travel

through a small opening into the energy analyzer. Only electrons with the appropriate velocity for a specific magnetic field intensity can pass through the analyzer and be collected within the cage [8, 103]. The magnetic field is adjusted in order to select the secondary electron velocity to be measured. In Figure 36, the magnetic field points into the page in order for the electrons to follow in the trajectory shown. It should be noted that the primary electrons must travel parallel to the magnetic field to avoid deflection [51]. Thus, the actual placement of the electron gun would be above or below the page for the instrument shown in Figure 36; however, this diagram, along with many other diagrams portraying this instrument, is limited by the constraints of two-dimensional drawings.

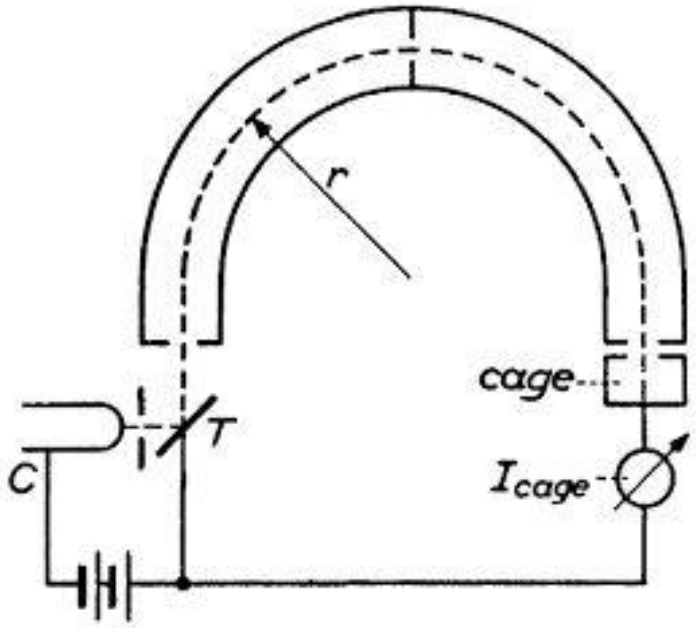


Figure 36: Diagram of an instrument for measuring the secondary electron energy spectrum using a transverse magnetic field [9]. C—cathode. T—target. r—radius of analyzer.

A disadvantage with this technique is that the energy spectrum is only associated with secondary electrons emitted at the specific angle that aligns with the opening of the energy analyzer. Lastly, another disadvantage is that the centerline of the electron gun's

barrel must remain oriented normal to the plane in which the energy analyzer lies in order to avoid the deflection of the primary electrons by the magnetic field. This greatly limits the possible combinations of primary electron incidence angles and secondary electron collection angles. The advantages with this technique are that the possibility of a space charge built-up in front of the target is greatly reduced because secondary and tertiary electrons are not repelled back to the sample and numerical differentiation is not required in determining the energy distribution.

The technique of using a longitudinal magnetic field to measure the secondary electron energy distribution was developed by German physicist Rudolf Kollath [9, 105, 106]. The instrument developed by Kollath is shown in Figure 37. This instrument is designed around the principle that electrons emitted from a point source at the same energy and at the same angle to a homogeneous magnetic field will focus to an image point [9, 67]. The distance of the image point from the source is directly proportional to the velocity of the secondaries and inversely proportional to the magnetic field [9, 67]. The image point appears at the opening of the collector, and the energy of the secondaries which enter the collector is selected by adjusting the magnetic field.

A disadvantage with this technique is that the electrons are not collected from a single emission angle or almost all emission angles. This complicates efforts when trying to model the energy spectrum. In addition, the possible combinations of primary electron incidence angles and secondary electron collection angles are greatly limited due to the construction of the device and the use of a magnetic field. Another disadvantage is that the magnetic field guides many of the secondary electrons back into the electron gun leading to a possible space charge buildup within the electron gun. The advantages of this technique

are that numerical differentiation is not required and that relatively large currents are measured. Thus, the SNR using this technique is greater than that of the deflecting electric field and transverse magnetic field techniques [8, 103].

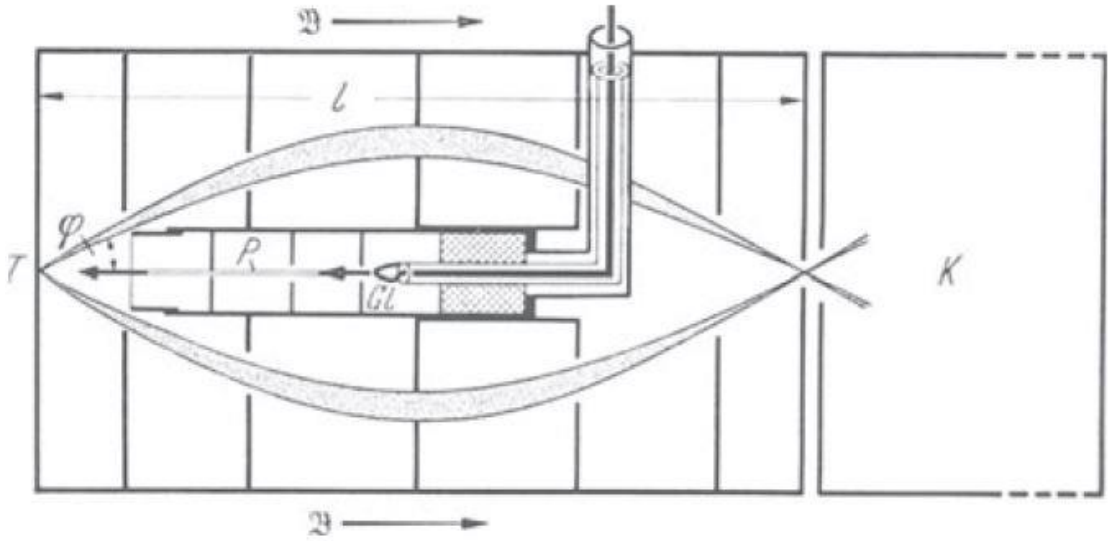


Figure 37: Schematic of the instrument used by Kollath to measure the secondary electron energy spectrum using a longitudinal magnetic field [105]. GL—electron gun; T—target; K—Collector; P—primary electrons; $\mathscr{B}$—magnetic field.

Table 2 summarizes the differences associated with each energy spectrum measurement technique. It is important to observe the differences in these measurement techniques when attempting to build SEE models. The technique used to acquire secondary electron energy spectrum may not always appear with the published measurement results requiring additional research to determine the technique used. Given the complex nature of the spectrum, it is much more difficult to model than the SEY.

### 2.3.2 Models

A Maxwellian distribution is often fit to the TSE portion of the energy spectrum although the distribution does not correspond directly to a Maxwellian distribution, and there is no physical connection between them [8, 51, 107]. In addition, Van der Ziel

indicated that energy spectrum of TSE could be approximated as a half-Maxwellian energy distribution with an equivalent temperature corresponding to a few electronvolts [108]. Furthermore, Scholtz *et al*. have shown that a Gaussian distribution provides a better fit to the TSE portion [102]. These distributions however are only valid for $E_p$ > 20 eV. Below an $E_p$ of 20 eV, the TSE and EBP portions of the energy spectrum begin to appreciably overlap. In 1966, Birdsall *et al*. indicated that curve fitting was the most reasonable way forward for defining the energy spectrum [46]. To the author's knowledge, the Furman and Pivi model currently provides the best fit for the energy spectrum data [89]. However, ensuring that the model fits experimental data for multiple incidence angles and primary electron energies is difficult, and the Furman and Pivi model has been observed to deviate from experimental measurements as shown in Figure 38.

Table 2: Comparison of Secondary Electron Energy Spectrum Measurement Techniques

| | Retarding E-field | Deflecting E-field | Transverse Magnetic | Longitudinal Magnetic |
|---|---|---|---|---|
| Possibility of Space Charge Buildup | High | Low | Low | High |
| Numerical Diff. | Yes, unless using small sinusoidal potential | No | No | No |
| SNR | High | Low | Low | Medium |
| Measured Emission Angles | Almost all simultaneously | Single angle from target to analyzer opening | Single angle from target to analyzer opening | Several angles simultaneously |
| Angular Combinations of Incident and Collection Angles | Multiple incident angles possible | Multiple incident and collection angles possible | Limited by requirement for e-gun to be normal to the plane of the magnetic analyzer | Greatly limited by device construction and e-gun placement in magnetic field |

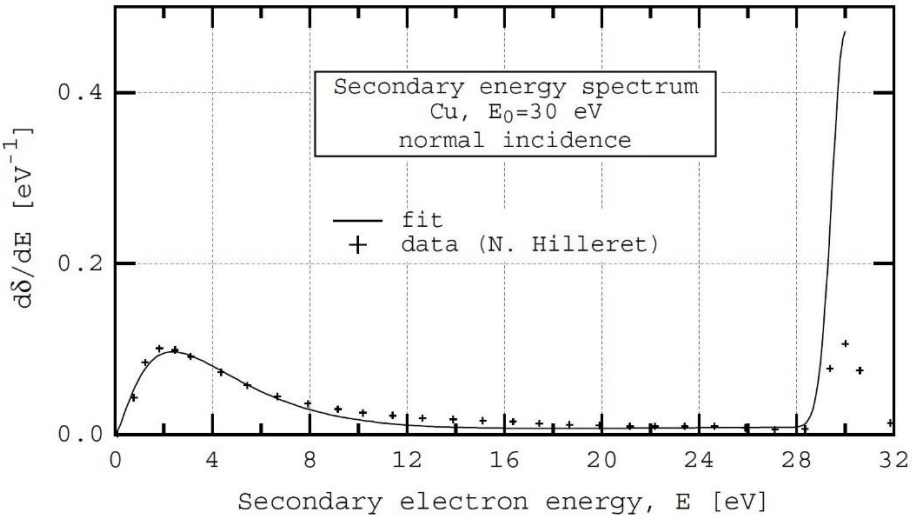


Figure 38: Comparison of a measured secondary electron energy distribution for copper to a fitted curve created using the Furman and Pivi model [109] . The primary electrons for this data were normally incident on the surface with a 30-eV energy.

### 2.4 Angular Distribution of Secondaries

The angular distribution is the most difficult aspect of SEE to measure due to the complexity of the instrument involved [110]. Prior to 1959, only Jonker had performed this type of measurement [51, 111]. The angular distribution is measured for specific energy groups, such as the secondary electrons with energies between 0 and 20 eV. Jonker performed his measurements using three groups which he called the slow secondary electrons, secondary electrons with moderate velocity, and rapid reflected electrons (Figure 39).

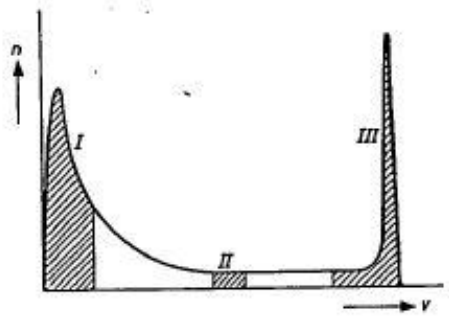


Figure 39: Jonker's secondary electron energy groups [110]. *I*—slow secondary electrons; *II*—secondary electrons with moderate velocity; *III*—rapid reflected electrons.

For the slow and moderate groups of secondaries emitted from a smooth, polycrystalline nickel target, Jonker found that the distributions followed roughly a cosine distribution (Figure 40). For all of his measurements, the trajectory of the primary electrons and the captured secondary electrons were in the same plane due to the mechanical constraints of his apparatus. Jonker was unable to measure the angular distribution within 10 degrees of either side of the electron gun due to the obstruction caused by the electron gun. He interpolated the missing part of the distribution "…as well as possible" using a dashed line (Figure 40) [110]. To this day, the appearance of the missing 20 degrees of the angular distribution is only speculated.

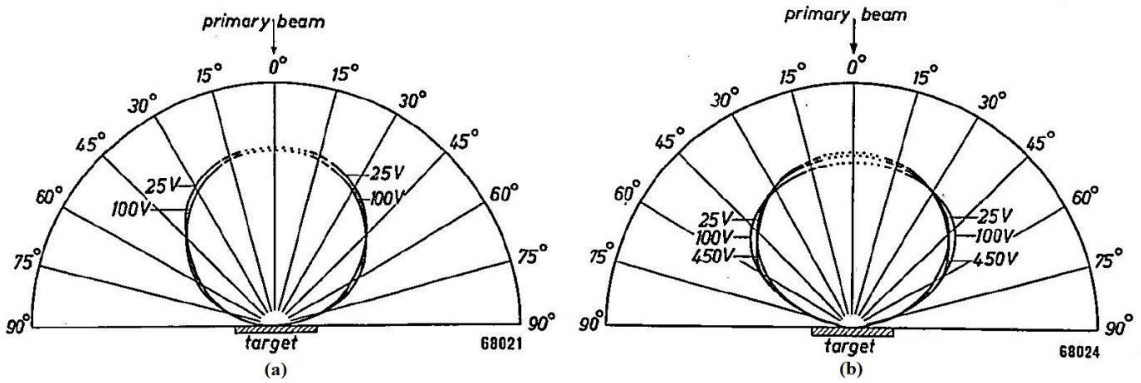


Figure 40: Angular distribution of the moderate (a) and slow (b) secondary electrons for a smooth, polycrystalline nickel target with normal incidence and different accelerating potentials [110].

The angular distribution for the rapid secondaries shows a pronounced deviation from the cosine distribution (Figure 41). These secondaries have a greater tendency to be emitted in a direction parallel to the primary electron beam incidence angle as shown in Figure 42.

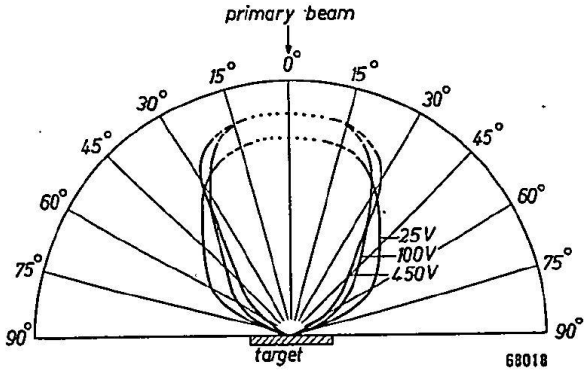


Figure 41: Angular distribution of rapid secondary electrons for a smooth, polycrystalline nickel target with normal incidence and different accelerating potentials [110].

The angular distributions of the slow and moderate groups show little deviation from the cosine distribution for various incidence angles [110].

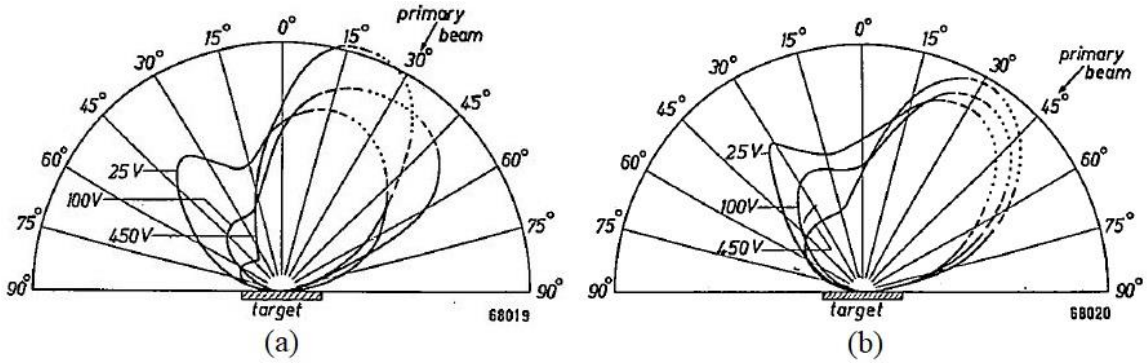


Figure 42: Angular distribution of rapid secondary electrons for a smooth, polycrystalline nickel target with 30° (a) and 45° (b) incidence and different accelerating potentials [110].

It is important to note that Jonker measured the current density at numerous angles not the joint probability density function defining the angular distribution of the secondary electrons. For example, if we assume that the current density for a group of secondaries follows a cosine function, then the current density is

$$\vec{J}(\theta_s, r) = \frac{i_m}{\pi r^2} cos(\theta_s)\hat{r} \text{ for } 0 \leq \theta_s \leq \pi/2 \ \ and \ 0 \leq \varphi_s \leq 2\pi \tag{2}$$

$$\vec{J}(\theta_s, r) = 0 \text{ otherwise} \tag{3}$$

so that when integrating $\vec{J}(\theta_s, r)$ over a hemisphere above the target, the integral yields $i_m$, the total current associated with the secondaries of a specific energy group, as shown:

$$\int_0^{2\pi}\int_0^{\pi/2} \frac{i_m}{\pi r^2} cos(\theta_s)\hat{r}\cdot\hat{r}r^2 sin\theta_s d\theta_s d\varphi_s = \frac{i_m}{\pi}\int_0^{2\pi}\int_0^{\pi/2} cos(\theta_s)sin\theta_s d\theta_s d\varphi_s = i_m \quad (4)$$

$\theta_s$ is the emission elevation angle with respect to the surface normal, $\varphi_s$ is the azimuthal angle associated with the emission, and $r$ is the radial distance from the location of emission. If we then assume that the joint probability density function also follows a cosine function, then the joint probability density function is

$$f_{\theta_s,\varphi_s}(\theta_s, \varphi_s) = (1/2\pi)cos\theta_s \text{ for } 0 \le \theta_s \le \pi/2 \ and \ 0 \le \varphi_s \le 2\pi \quad (5)$$

$$f_{\theta_s,\varphi_s}(\theta_s, \varphi_s) = 0 \text{ otherwise} \quad (6)$$

so that integrating $f_{\theta_s,\varphi_s}(\theta_s, \varphi_s)$ yields 1, as shown:

$$\int_0^{2\pi}\int_0^{\pi/2} (1/2\pi)cos\theta_s \, d\theta_s d\varphi_s = \frac{1}{2\pi}\int_0^{2\pi}\int_0^{\pi/2} cos\theta_s \, d\theta_s d\varphi_s = \frac{1}{2\pi}(2\pi) = 1 \quad (7)$$

This is the probability that a secondary electron will be emitted at an elevation angle between 0 and π/2 and azimuth angle between 0 and 2π, which constitutes all angles in the hemisphere above the target surface. The problem arises when one attempts to determine the current associated with electrons leaving the target over a specific range of angles by performing the following integration using the joint probability density function as in the following equation:

$$i_m \int_{\varphi_{s.min}}^{\varphi_{s.max}}\int_{\theta_{s.min}}^{\theta_{s.max}} (1/2\pi)cos\theta_s \, d\theta_s d\varphi_s \quad (8)$$

This integration is not equivalent to the integration of current density over a specific range of angles, which is

$$\int_{\varphi_{s.min}}^{\varphi_{s.max}} \int_{\theta_{s.min}}^{\theta_{s.max}} \frac{i_m}{\pi r^2} cos(\theta_s)\hat{r} \cdot \hat{r} r^2 sin\theta_s d\theta_s d\varphi_s \tag{9}$$

These two integrations will yield differing results. In order to yield consistent results, the following joint probability density function must be used instead.

$$f_{\theta_s,\varphi_s}(\theta_s, \varphi_s) = (1/\pi)cos\theta_s sin\theta_s = (1/2\pi)sin2\theta_s \tag{10}$$
$$\text{for } 0 \leq \theta_s \leq \pi/2 \ \ and \ 0 \leq \varphi_s \leq 2\pi$$

$$f_{\theta_s,\varphi_s}(\theta_s, \varphi_s) = 0 \text{ otherwise} \tag{11}$$

Figure 43 compares this probability density function to the previous. The $\varphi_s$ dimension is not shown due to lack of any variation in $f_{\theta_s,\varphi_s}(\theta_s, \varphi_s)$ with respect to $\varphi_s$. It is apparent that these two distributions are very different. In order for simulation models to be consistent with Jonker's results, the probability density function describing the angular distribution must be consistent with Equations 10 and 11. To the author's knowledge, this nuance is not emphasized in other literature.

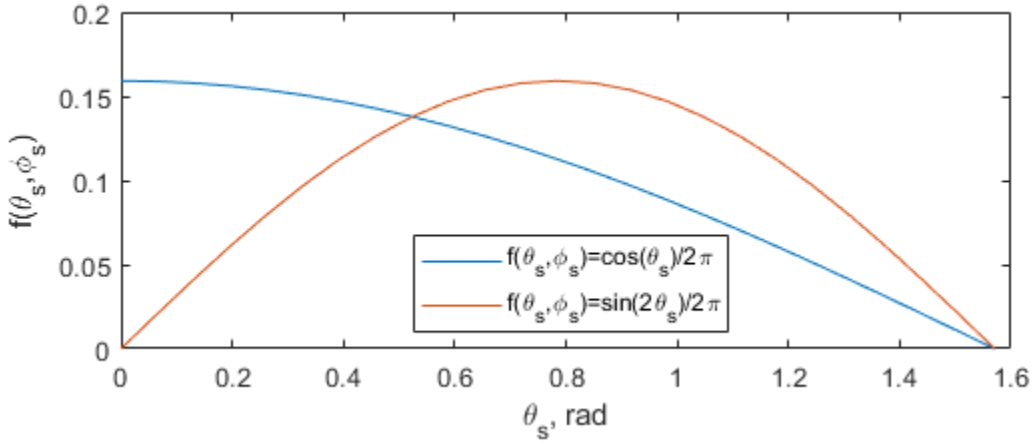


Figure 43: Comparison of joint probability density functions for the angular distribution of the secondary electrons.

### 2.4.1 Measurement Techniques

The measurement of the angular distribution requires an apparatus in which the incidence of the primary electron beam can be set and the angle of the secondary electron collection varied. It is commonly measured using a retarding electric field or a deflecting electric field due to the constraints associated with using a magnetic field. There are two techniques for making measurements using a retarding electric field.

The first technique is to remove secondary electrons below a specific velocity before they reach a collector. Jonker was the first to implement this technique using two concentric spheres (Figure 44) [112]. In order to perform this measurement accurately the retarding electric field must point radially outward. Jonker could not ensure that the electric field would be pointed radially outward in the region surrounding the target given the geometry of the target and electron gun, so he made this region a field-free region by placing the target, electron gun barrel, and inner sphere at the appropriate electric potential based on CPD considerations. He then surrounded the inner sphere by a concentric outer sphere which was negatively biased with respect to the inner sphere in order to retard secondary electrons leaving the inner sphere through the slit *N* in Figure 44. A few of the electrons would have sufficient energy to overcome the retarding field and enter an opening into the outer sphere that led to a collector. The collector was connected to an ammeter to allow measurement of the current entering the collector. The design and construction of Jonker's apparatus is rather complex compared to other devices used for SEE measurement (Figure 45). To the author's knowledge, Jonker was the only researcher to ever use this technique.

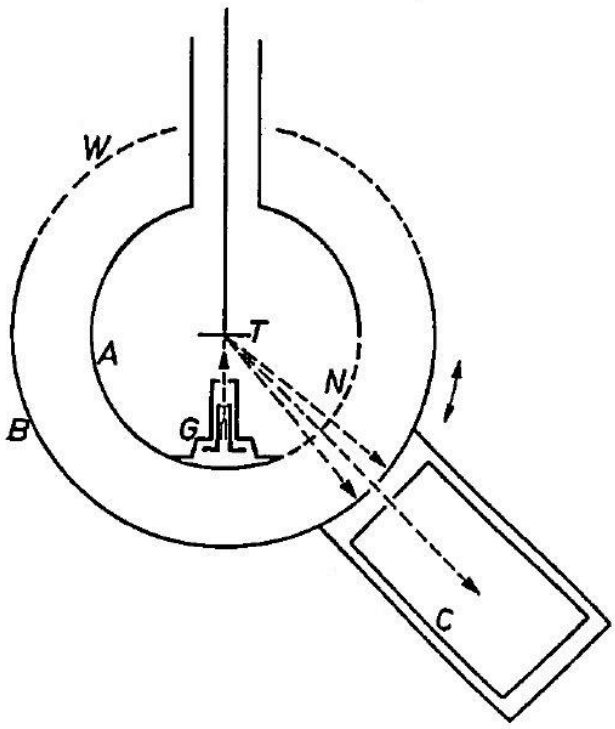


Figure 44: Schematic of Jonker's apparatus for measuring the angular distribution [112].
*A*—inner sphere with slit *N*; *B*—outer sphere with slit *W*; *G*—electron gun; *T*—target; *C*—collector.

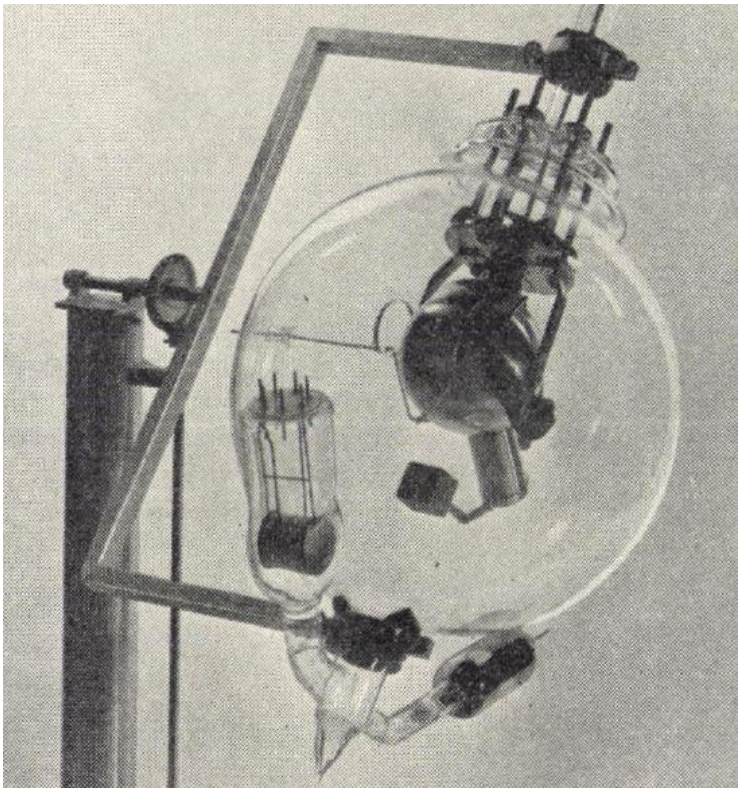

Figure 45: Picture of Jonker's apparatus for measuring the angular distribution [110].

The second technique is to allow secondary electrons to pass through a field-free region and enter an energy analyzer. An example of this is the apparatus developed by Burns (Figure 46). The secondary electrons would be emitted from the target and travel a straight path from the target through the field-free region into the opening of the "electron collector" [111]. Today, we refer to Burns' "electron collector" as a retarding field analyzer (RFA) because a retarding electrostatic field is used to separate electrons based on kinetic energy [113].

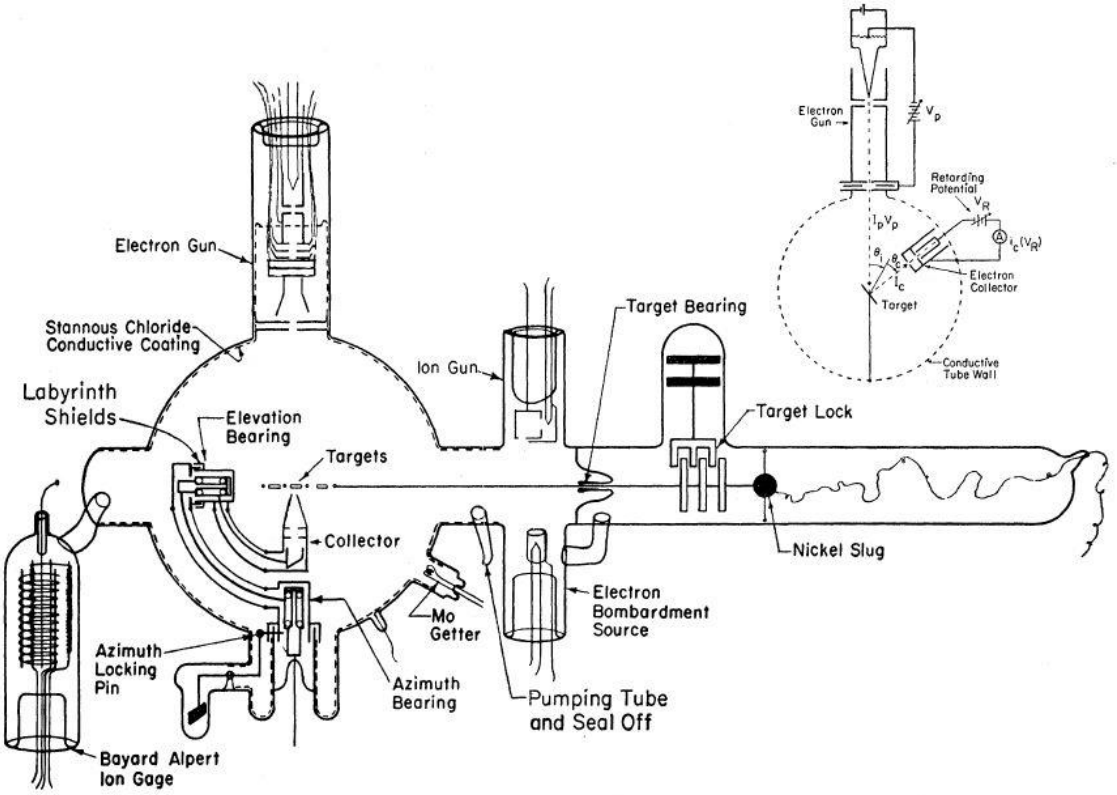


Figure 46: Schematic of Burns' apparatus for measuring the angular distribution [111].

An energy analyzer using a deflecting electrostatic field, such as a cylindrical electrostatic analyzer, may be used instead of an RFA. However, this analyzer measures the current associated with the secondary electrons having a specific energy rather than within a specific energy range. Nevertheless, one may numerically integrate the currents

measured using a deflecting electrostatic field with respect to the secondary electron energy over the desired energy range to obtain the same result as the RFA. Likewise, the measurements of an RFA may be numerically differentiated to obtain the results obtained using a deflecting electrostatic field.

### 2.4.2 Material Dependence

Currently, the exact relationship between other material properties and the angular distribution is unknown. However, some general trends can be observed for the angular distributions of polycrystalline, crystalline, and porous materials. The angular distribution for a polycrystalline material was previously discussed at the beginning of this section. This angular distribution will now be compared to a porous material and then a crystalline material.

Jonker measured the angular distribution of porous soot in order to better understand the SEE behavior of soot within a vacuum tube device [112]. He found that most of the secondary electrons from the slow, moderate, and rapid groups are always emitted in the direction of the electron gun (Figure 47). This is in stark contrast to the approximately cosine distribution observed for the slow and moderated groups of secondary electrons emitted from smooth polycrystalline nickel [110]. Furthermore, he observed that the shape of the angular distribution for each of the groups remains approximately the same and rotates as the incidence angle varies. This is also different from what was found for polycrystalline nickel, which did experience a appreciable change in the shape of the distribution for the rapid group as the incidence angle was varied. Lastly, the angular distribution of polycrystalline nickel showed an increase in the number of rapid

electrons at an angle near the specular reflection angle. For soot, this increase is not observed. Jonker compared his observations to moist grasslands illuminated by the sun where the greatest intensity of light is seen surrounding the shadow cast by the observer's head [112].

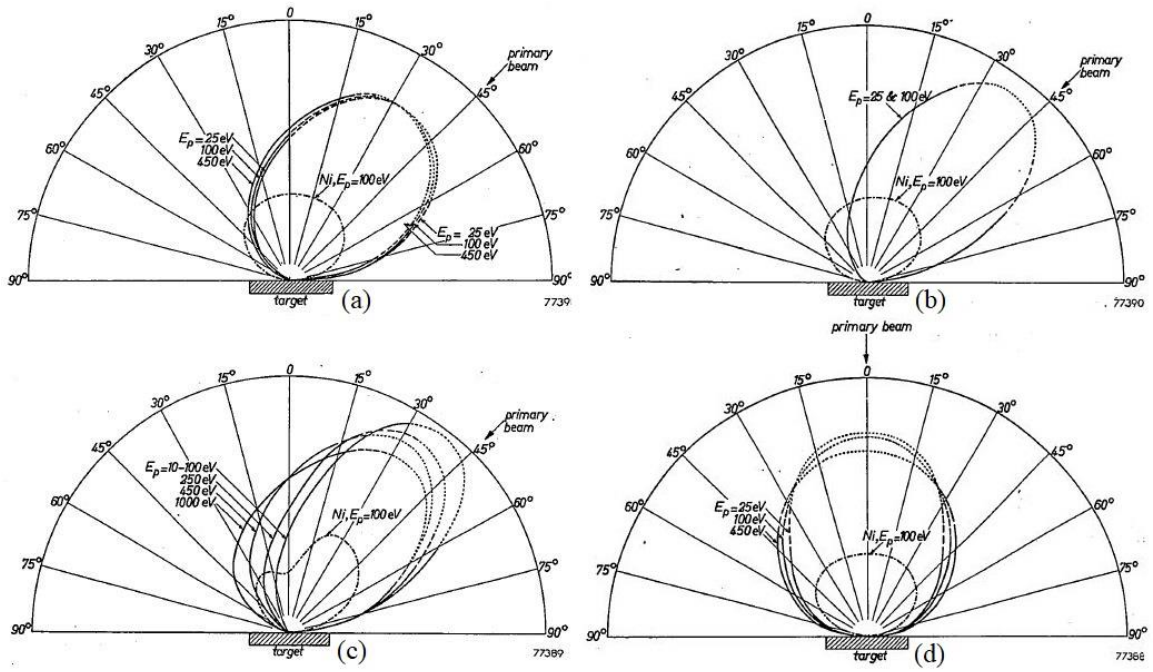


Figure 47: Angular distribution measured by Jonker for porous soot for different accelerating potentials and incidence angles [112]. (a) Slow, (b) moderate, and (c) rapid groups of secondary electrons for 45° incidence; (d) slow group of secondary electrons for normal incidence.

The angular distribution for crystalline materials is far more complex than the previously mentioned distributions. The distribution contains maxima and minima superimposed on an approximately cosine distribution (Figure 48) [111]. Burns stated that the angular distribution cannot to explained by the "…diffraction of internal secondaries either by Bragg planes in the crystal or by the surface lattice" and found the results to be consistent with quantum-mechanical collisions provided conservation of momentum is properly accounted for [111]. In order to model this angular distribution accurately for the

simulation of much larger scale devices, a much more complex model than the cosine distribution is necessary. It may be possible that periodic surface structures, such as groves, trenches, cones, or pores, will also exhibit a complex angular distribution; however, the author has been unable to ascertain any experimental evidence regarding this subject.

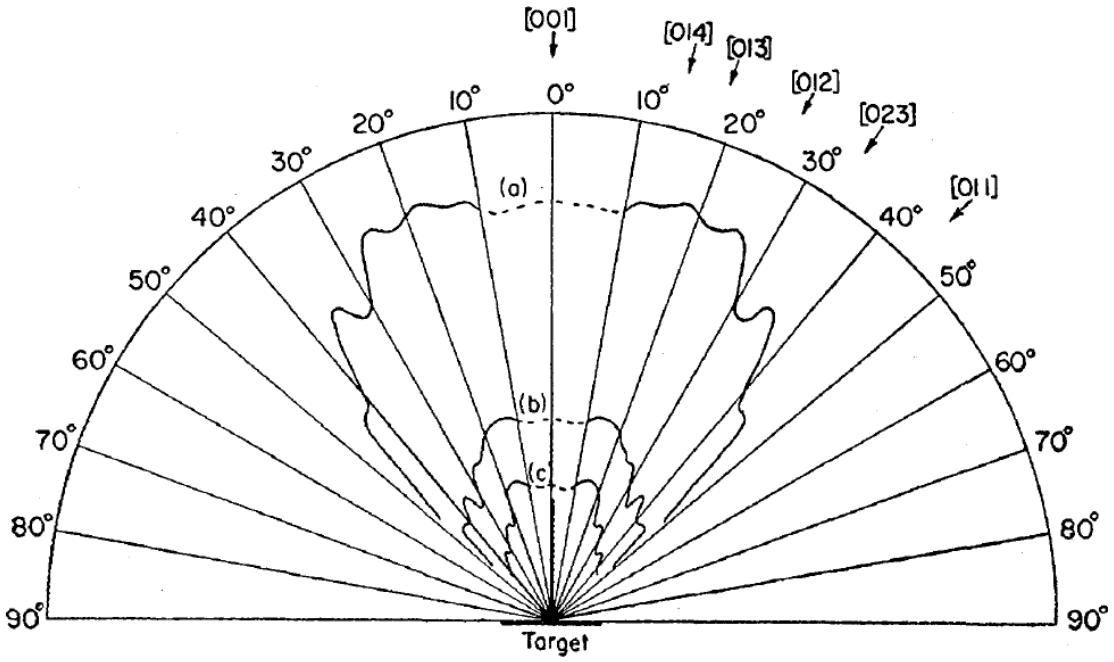


Figure 48: Angular distribution of secondary electrons from [001] face of copper crystal with 250 eV primary beam at normal incidence [111]. (a) 0 to 10 eV secondaries; (b) 10 to 20 eV secondaries; (c) 20 to 40 eV secondaries.

### 2.4.3 Models

Vaughan's model does not provide an angular distribution, and the Furman and Pivi model uses a $\cos^{\alpha}\theta_s$ probability density for the angular distribution, where $\alpha$ is a parameter determined by the simulation user and is normally set to 1 [84, 85, 89]. Based on the author's observations, it is common to assume that the angular distribution follows a cosine probability density based on Jonker's measurements for polycrystalline nickel or that all

secondary electrons are emitted normal to the surface. The angular distribution appears to be the most underdeveloped aspect of SEE modeling.

## 2.5 Multipactor Simulation Software

There are numerous software programs developed to simulate multipactor. Many of these programs are developed by universities and used for academic research [114, 115]. The most widely used commercial software for multipactor simulation are CST STUDIO SUITE®, FEST3D®, and Vsim®. The CST STUDIO SUITE® was developed by Computer Software Technology (CST®) and is part of SIMULIA which is brand owned by Dassault Systèmes® of France [87]. This software simulates multipactor by first solving for the EM fields within a RF component using the CST Microwave Studio® module of the CST STUDIO SUITE®. The EM field data are then imported into the CST PARTICLE STUDIO® module. This module contains the PIC algorithm used for the simulation of SEE and electron dynamics. For SEE modeling, this module uses one of the following: the Furman and Pivi model [89], Vaughan's model [84, 85], or imported SEY data containing impact energies and corresponding SEY values [87].

FEST3D®, which stands for Full-wave Electromagnetic Simulation Tool 3D, is produced by Aurora Software and Testing (AURORASAT™), S.L. of Spain [116]. FEST3D® contains a "high power" module which allows multipactor and corona breakdown level determination. In addition, FEST3D® also contains a stand-alone module called SPARK3D, which can also perform multipactor and corona breakdown analysis. SPARK3D can import EM field data from several electromagnetic simulation tools: FEST3D®, ANSYS® HFSS™, CST®, and FEKO [117]. Both modules use a "full 3D

electron tracker" as opposed to a PIC algorithm [116]. Both modules also use Vaughan's model for SEE simulation or imported SEY data containing impact energies and corresponding SEY values with the additional option of including the number of elastically reflected primaries [118, 119, 117]. In September of 2016, CST® announced their acquisition of AURORASAT™ [120]. FEST3D® and SPARK3D are now offered as an option of the CST STUDIO SUITE® or as stand-alone programs [121].

VSim® is a multiplatform, multiphysics software developed by the Tech-X® Corporation of Boulder, Colorado [122]. VSim® utilizes the VORPAL® computation engine in order to perform electromagnetic and particle simulations. VORPAL® uses a PIC model based on the PIC algorithms from Hockney and Eastwood [123] and Birdsall and Langdon [124, 125]. It has three methods of simulating SEE [126]. The first method implements the phenomenological model developed by Dionna [76]. The second method uses the Furman and Pivi probabilistic, phenomenological model [89], and the third method utilizes imported SEY data containing impact energies and corresponding SEY values. Tech-X® currently serves numerous laboratories and defense corporations, including the AFRL [122].

For the last 20 years, AFRL, with the support of the AFOSR, has used and developed a PIC code to aid in the development of high-power microwave devices [127]. The code is called Improved Concurrent Electromagnetic Particle-In-Cell (ICEPIC) and was initially developed by Richard Procassini from a particle code authored previously by Procassini and Bruce Cohen [128]. ICEPIC is developed for parallel processing across multiple CPUs [127, 129]. It does this by splitting the simulation domain into "rectangular prism spatial regions" and assigning each region to a CPU [130]. In addition, it implements

a more complicated PIC cycle than the conventional cycle shown in Figure 15 in order to keep each CPU busy (Figure 49).

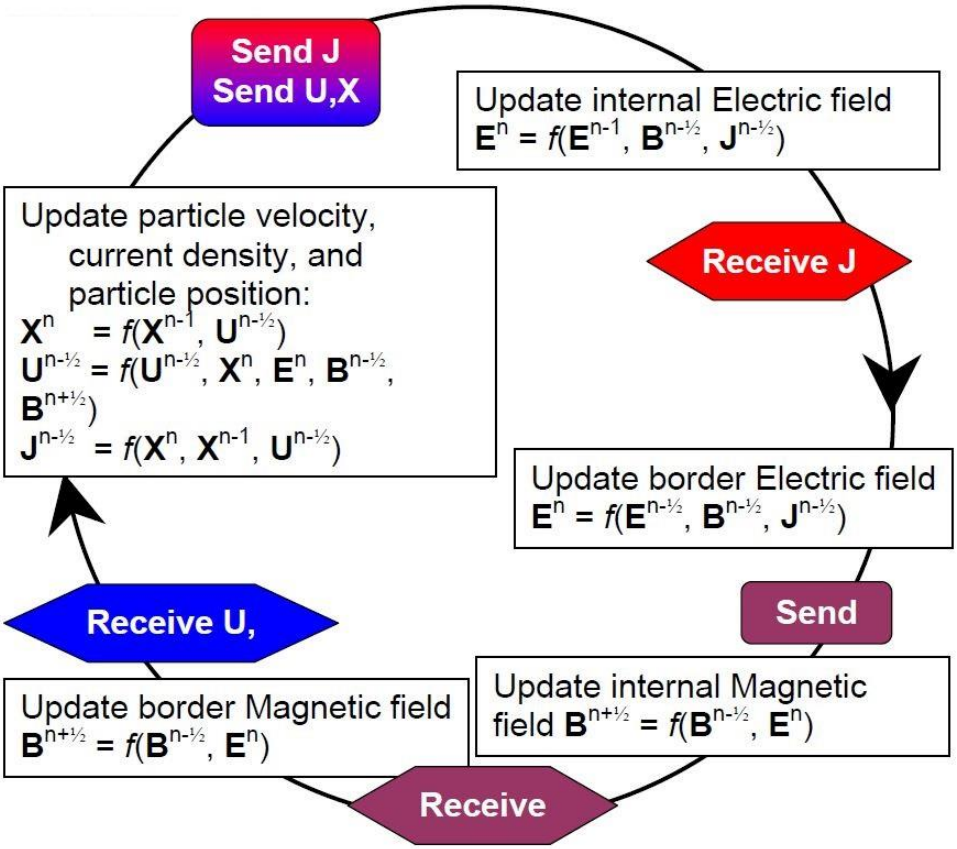


Figure 49: Flow of operations in the parallelized PIC loop used by ICEPIC [130].

In 2004, C. Fichtl *et al*. added a SEE capability to ICEPIC in order to simulate multipactor at waveguide pressure windows [131]. ICEPIC uses Vaughan's model for SEE simulation [37, 38, 131]. In 2009 and 2013, ICEPIC was used by two students within the Air Force Institute of Technology (AFIT) physics department for the simulation of multipactor breakdown at a waveguide pressure window [37, 38]. Since the publications of these students, no additional reports regarding multipactor simulation using ICEPIC appear to have been published.

## 2.6 The Challenges to Accurate Measurement

Based on the literature review, the measurements of SEE involve numerous assumptions which may or may not be consistent with reality in all situations, and it is difficult to determine when these assumptions have been violated. They are often made in SEE literature without directly stating that the assumptions have been made, and it is assumed that the reader understands all the underlying assumptions. When these underlying assumptions are violated, the results of the measurement become biased. Depending on the extent to which these assumptions are violated, a large number of inconsistent results may be observed in data collected by different researchers. For this discussion, the focus will be on SEY measurements; however, many of these assumptions are also applied to other types of SEE measurements. Each of the assumptions commonly made for SEY measurements will now be discussed along with their impact on the accuracy of the measurement.

### 2.6.1 Assumption 1

The first assumption is that the measured SEY at one location on a sample's surface is applicable to the entire surface. However, the SEY commonly varies between locations on a surface. It is this property that allows the scanning electron microscope to operate. The variation of the SEY at each point along the surface gives rise to the contrast seen in the images produced by a scanning electron microscope (SEM). When experimenters attempt to measure the SEY for a surface, the results of the measurement are dependent on where the primary electron beam impacts the surface. For example, a researcher performs a SEY measurement with the primary electron beam focused at location 1 in Figure 50. In

this measurement, many of the secondary electrons emitted at the bottom of the pit will be absorbed by the surrounding walls of the pit leading to a SEY measurement that is lower than would be measured for a flat surface. If the researcher moves the primary electron beam to location 2, many of the secondary electrons generated within the peak will escape due to their close proximity to the surface on all sides of the peak. Thus, the researcher will measure a higher SEY than would be found for a flat surface. These two locations represent the extremes for an SEY measurement created by the geometry of the surface. Similar results would be measured if the locations were different in other ways, such as contaminated versus uncontaminated or differing crystal faces. In order to ensure that the measurements are applicable to the entire surface, measurements may be performed at several locations and averaged. In addition, the diameter of the primary electron beam may be increased to expose a larger region of the surface to electrons during each measurement.

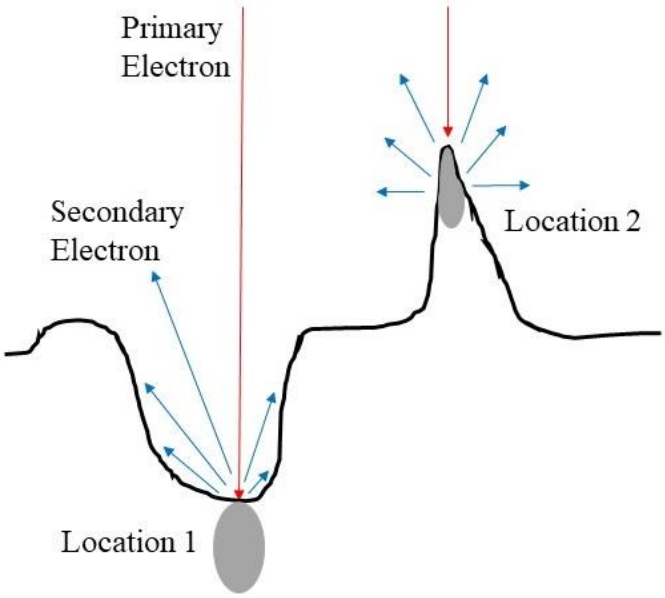


Figure 50: Illustration comparing secondary electron emission when a primary electron impacts in a pit versus on a peak.

### 2.6.2 Assumption 2

The second assumption is that the effects of CPD are negligible. If CPD is considered non-negligible, the SEY curve must be shifted based on the CPD between the cathode of the electron gun and the sample. This shift is normally a few eV at most since CPD is typically less than a couple volts. Thus, it is often considered negligible. However, when performing measurements for primary electron energies less than 1 eV, the CPD must be considered; otherwise, the accuracy of the experimental results is doubtful and subject to criticism [54]. The CPD must be periodically remeasured since the work functions of the cathode and sample may vary over time with changes in surface composition.

The CPD can be determined using three different methods. In the first method, the work functions of the cathode and sample are first determined, and then the CPD is calculated using these work functions. The disadvantage with this approach is in the difficulty associated with determining the work functions. Additional equipment is required in the vacuum chamber in order to measure the work functions in situ. Furthermore, the electron gun may require modification to allow the work function of the cathode to be measured. Removing the sample and cathode from vacuum chamber to perform work function measurements increases the risk for contamination leading to inaccurate work function measurements, and performing the removal and reinstallation periodically is not feasible in most situations.

In the second method, the CPD may be measured directly using the Kelvin probe method [54]. This approach requires the distance between any two electrodes for which the CPD is being measured to vary. A vibrating probe may be used to determine the CPD between the probe and sample and the CPD between the probe and cathode. The CPD

between the cathode and sample can then be calculated from CPDs measured using the probe. This method also requires additional equipment within the chamber and possibly a redesign of the electron gun.

In the final method, the CPD is determined based on the cutoff of the primary electron beam when the sample is negatively biased with respect to the electron gun [54]. This method does not require any additional equipment within the chamber. However, the primary electron energy distribution must be known, and assumptions must be made regarding the SEY at low primary electron energies in order to use this method. Though the CPD between the cathode and sample is responsible for the shift of the SEY curve along the energy axis, CPDs also exist throughout the vacuum chamber and within the electron gun, which may impact the measured SEY. These CPDs alter the electric fields from those based solely on measured potentials, and ignoring them when performing simulations leads to incorrect calculations of the electron trajectories.

### 2.6.3 Assumption 3

The third assumption is that each characteristic of the primary electrons can be defined with a single numerical value rather than a distribution. Thus, all the primary electrons are assumed to impact the sample surface at the desired incidence angle. In practice, this is impossible to achieve. At high primary electron energies, it is possible to have all the electrons strike the surface at nearly the same incidence angle. At low primary electron energies, however, it is difficult or nearly impossible to have the electrons strike the surface at the same angle, and the electrons strike the surface following a wide

distribution of incidence angles. This is due to the fact that the primary electrons are not emitted from the same location on the cathode and with the same momentum.

Furthermore, the primary electrons are also assumed to strike the target with the same energy. However, the primary electrons are emitted from the cathode following a distribution of energies. Therefore, it is not possible to have all the primary electrons arrive at the sample with the same energy. The energy spread of the primary electrons may be reduced by sending the electrons through an energy analyzer before entering the focusing optics of the electron gun [54]. However, this comes at increased complexity and cost. Alternatively, the type and temperature of the cathode may be chosen to reduce the energy spread. The true SEY curve can only be determined by the deconvolution of the measured SEY curve with the energy distribution of the primary electrons [7]. The challenge however is accurately determining the energy distribution of the primary electrons.

### 2.6.4 Assumption 4

The fourth assumption is that space charge is negligible. As previously discussed, the SEY is a ratio that is independent of the primary electron current. Therefore, for any primary electron current used in a SEY measurement, the SEY must remain the same. This can only be achieved if no electrons interact with each other. When the electrons are moving quickly and the current density is small, electron interactions are minimized. However, when electrons are moving slowly and/or the current density increases, electron interactions increase and the measurement bias due to space charge may become significant [74, 75, 132]. For this reason, SEY measurements involving low energy primary electrons are most susceptible to space charge effects. Since the SEY is independent of current, the

ratio between any two currents measured in the vacuum chamber must be constant regardless of the primary electron current. The deviation of any ratio from a constant value is an indication of a space charge accumulation. This is predicated on the belief that differences in the energy distribution of electrons emitted from the cathode are negligible for different primary electron currents.

### 2.6.5 Assumption 5

The fifth assumption is that Earth's magnetic field is negligible. The trajectories of the electrons are dependent on the properties of the magnetic field within the chamber; and, since this varies with geographic location, its effect on the accuracy of SEY measurements will also vary. As the energy of an electron decreases, the magnetic field has an increasing effect on the trajectory of the electron. Depending on the magnetic field, this may cause primary electrons to miss the sample, and secondary electrons to spiral back into the sample, which leads to measurement bias. To reduce the magnetic field within the chamber, the chamber may either be surrounded by a material with high permeability, such as mu-metal, or Earth's magnetic field may be negated by a second magnetic field produced by permanent magnets or electromagnets (e.g. Helmholtz coils).

### 2.6.6 Assumption 6

The sixth assumption is that the primary electron current can be accurately measured using a Faraday cup or by positively biasing the sample. This involves two underlying assumptions. The first being that all electrons leaving the electron gun can be captured by the Faraday cup or biased sample. The extent to which this can accomplished is dependent on the design of the cup or SEE properties of the sample in addition to the

applied bias. The second assumption is that the current measured by the Faraday cup or biased sample is equal to the primary electron current that will arrive at the sample. When the sample is negatively biased to prevent tertiary electrons from returning to the sample and the primary electrons have low energies, many of the electrons, which were captured by the Faraday cup or biased sample, may not reach the sample. This leads to an error in the determination of the primary electron current and consequently the SEY.

### 2.6.7 Assumption 7

The seventh assumption is that the measurement results are solely due to the SEE interaction taking place on the sample's surface involving primary and secondary electrons and all other interactions occurring in the vacuum chamber are assumed negligible. These other interactions include SEE and photoemission taking place in locations other than the sample's surface. The extent to which this assumption is valid is difficult to determine and is subject to the design of the experimental apparatus and the test conditions. Researchers have attempted to quantify the extent to which this assumption is valid and its effect on the accuracy of SEY measurements by comparing simulation and experimental results [56, 133]. They found that the accuracy of their measurements degraded as the primary electron energy was reduced from ~4% at 1 keV to ~20% at 5 eV [56]. Unfortunately, very little research is available regarding the quantification of measurement accuracy in SEY measurements.

## 2.7 Summary

This chapter provided a historical review of SEE and multipactor and discussed many of the challenges involved with the measurement of SEE. In addition, the different types

of SEE measurement (i.e. SEY, energy distribution, and angular distribution) were discussed along with the models associated with each type of measurement. The underdevelopment of SEE models, especially in areas of energy distribution and angular distribution, was highlighted. An overview of multipactor simulation software was provided, and the SEE models used by each software was identified. Finally, based on the evidence available in the literature, it was determined that the discrepancies observed in SEE measurements can be attributed to the violations in the seven commonly made assumptions. This determination satisfies the first objective of this research. Determining when these assumptions are violated and how to avoid violating these assumptions is the emphasis of this research.

# III. Methodology

As discussed at the end of Chapter II, the extent to which the assumptions are violated affects the accuracy of the SEE measurements. Determining the extent to which these assumptions are violated cannot be determined by experimentation alone given the nature of assumptions and requires an iterative process of experimentation, modeling and simulation, and theoretical refinement. This iterative process has been described by the Office of Nuclear Energy and is portrayed in Figure 51 [134].

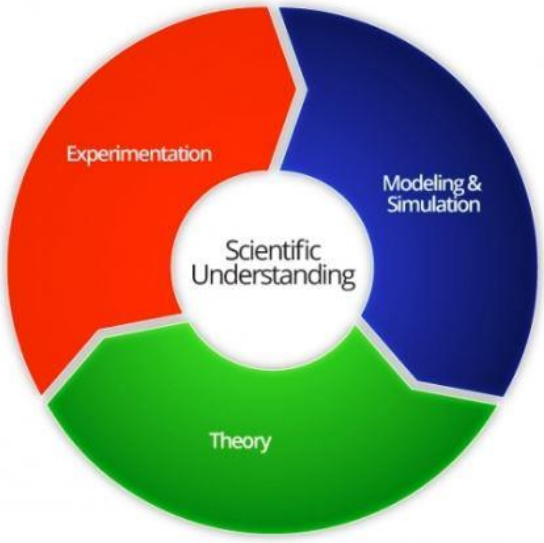


Figure 51: Iterative process of experimentation, modeling and simulation, and theory in improving scientific understanding [134].

Originally, this research set out to fully implement this process. However, due to amount of time consumed in the development of the experimental system and problems with the simulation software, the scope of this research was reduced. Nevertheless, this process was implemented to a limited extent in this research. This research focused on SEY measurements due to hardware constraints and was divided into four tasks. The first task was to develop a measurement system capable of performing a large number of

measurements autonomously. This included verifying that the measurements performed by the system under the same conditions were repeatable. This task was necessary due to the time associated with the performance of SEY measurements and the large number of test conditions involved in this research. The following section describes this task in greater detail. The second task was the development of a simulation model of the experimental system to provide insight in physics taking place during experiment SEY measurements. Section 3.2 discusses how the simulation model was developed and calibrated based on experimental measurements. The third task was to perform measurements under numerous conditions to determine how these condition affect SEY measurements. Chapter IV analyzes the results of these measurements with the aid of the simulation model. The final task was to formulate guidance for improving SEE measurements based on conclusions drawn from the research. This guidance is provided in Chapter V along with recommendation for future research.

### 3.1 Development of Experimental System

Before a study of how measurement condition affect SEY measurements could be undertaken, it was first necessary to establish the repeatability of measurements and develop an autonomous system for performing large numbers of measurements under differing test conditions. Over the course of several months, the measurement system evolved as knowledge of the system increased and problems with the hardware were identified. This section provides a summary of how and why both the hardware and measurement method were updated to perform measurements with greater repeatability and with less human involvement.

### 3.1.1 Chamber Modification Cancelled

In the originally proposed research, the UHV chamber was to be modified to contain a collector and suppression grid, which would allow measurements of the secondary electron energy distribution and for a field-free region around the target during SEY measurements. However, a solution for installing the collector and grid into the current UHV chamber was not achievable due to complexity created by the spherical shape of the chamber. Thus, this research was confined to SEY measurements, and the pursuit of a more capable SEE measurement system is delayed until a more suitable UHV chamber is procured.

Figure 52 displays the configuration of the UHV chamber used in this research. In this figure, $i_F$ is the current measured by the Faraday cup circuit, and $i_s$ is the current measured by the sample circuit. The Faraday cup is mounted on a swivel that allows it to rotate. The conventional current standard is not used in this diagram. Throughout this document, the Faraday cup is in the closed position when it is situated underneath the electron gun. It is in the open position when it is situated off to the side of the electron gun as shown in Figure 52.

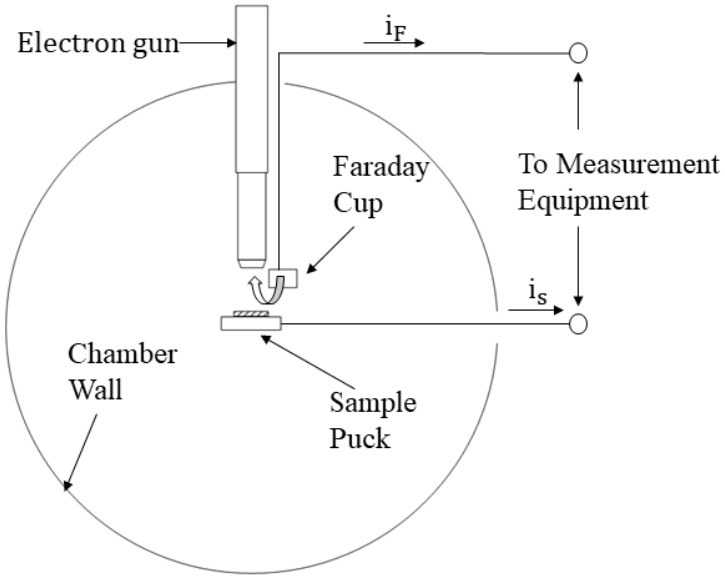


Figure 52: Diagram of UHV chamber used in this research.

### 3.1.2 Circuit Implementation

Before experimentation began, the circuitry for the measurement system had to be fabricated. The originally proposed circuit, shown in Figure 53, required modification due to the low impedance of the voltmeter. This low impedance caused more current to flow through the ammeter which required the ammeter to operate in a higher current range and increased the associated noise. By moving the location of the voltmeter, as shown in Figure 54, the ammeter was able to operate in a lower current range and with less noise. In addition to moving the location of the voltmeter in the circuit, two separate junction boxes were used which allowed more flexibility during testing. The Faraday cup and sample were separately connected to two circuits that are identical to that shown in Figure 54.

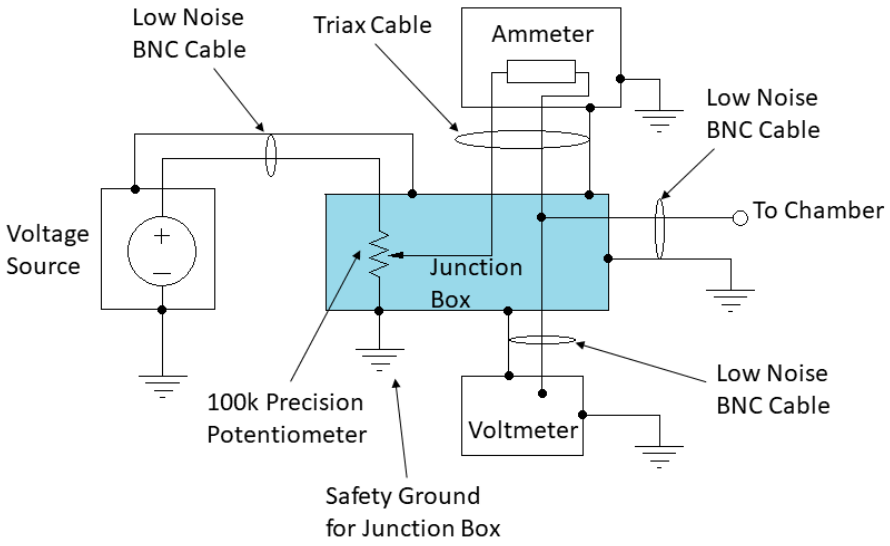


Figure 53: Proposed configuration for voltage source and measurement equipment.

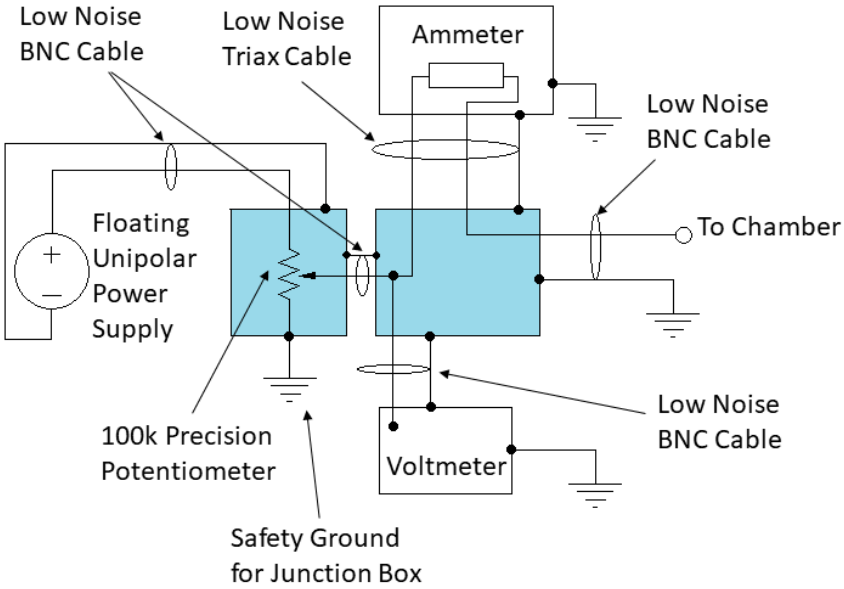


Figure 54: Updated configuration for voltage source and measurement equipment.

Potentiometers were used in order to prevent reverse currents, which may be created during SEE measurements, from damaging the power supply. Reverse currents cause the power supply to act as a power sink potentially damaging the power supply. Furthermore, if batteries are used, the reverse current will charge the batteries which could lead to leakage or explosion. The use of potentiometers in conjunction with increased power

supply voltages prevented reverse currents from entering the power supply. The junction box containing the precision potentiometer would later be replaced by a junction box containing a low-noise resistor, which will be discussed in a later section.

The cables used in the implementation of the circuit were each fabricated from the Keithley Model 4803 low noise cable kit and Keithley Model 237-ALG-2 low noise triax cables. These cables contain a graphite lubricant that reduces the electrical noise created by the triboelectric effect [135]. The triboelectric effect is induced by mechanical vibrations produced by the vacuum pumps of the UHV chamber. Keeping the cables short and away from parts of the system prone to vibration mitigated the noise in the system created by the triboelectric effect.

The ammeters in the circuit were Keithley Model 6514 electrometers, and the voltmeters were Agilent 34410A multimeters. During the early stages of research, the calibration certifications on the instruments had expired, and the measured results were only used to qualitatively characterize the system. The instruments were recalibrated before any data was collected for quantitative comparison.

In order to perform noise characterization and compare voltages and currents over time, the instruments were synchronized using an Agilent 33250A signal generator. Custom cables were fabricated in order to trigger the Keithley electrometers and Agilent multimeters, and a LabVIEW program was written to configure the instruments. The instruments stored measurements within their internal buffers rather than attempting to transmit the measured data over GPIB to the attached computer in real-time. This allowed measurements to be made at a faster rate albeit the measurements had to be downloaded after the measurements had concluded. Only the Keithley electrometers provided data with

timestamps. However, since the instruments are synchronized, it is safe to assume that the timestamps given by the Keithley electrometers can be applied to the voltage measurements made by the Agilent multimeters. More details regarding the configuration of the timing system can be found in Appendix A.

### 3.1.3 Noise Mitigation

With the circuit implementation complete, the noise characteristics of the system were examined while the electron gun remained off. During the examination of the system, three noise contributing sources were identified. The first source of noise was the leakage resistance within the sample manipulator, which was first identified by Sattler [4]. The leakage resistance is modelled with the resistor, $R_b$, in Figure 55.

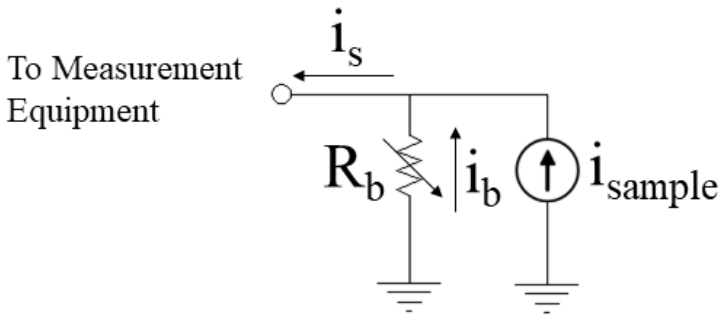


Figure 55: Circuit model containing leakage resistance.

Figure 55 does not follow the conventional current standard. In this figure, $i_{sample}$ is the net current through the sample puck when the electron gun is on, and $i_b$ is the current through the leakage resistance. During characterization, it was observed that the leakage resistance continued to decrease as sample puck was rotated on the manipulator. This increased the amount of current flowing through the electrometer connected to the sample requiring it to operate in a higher current range and greatly increased the noise in the circuit. Based on correspondence with the manufacture of the sample manipulator, the decrease in leakage

resistance is caused by the dielectric ball bearings of the sample puck holder collecting metal from the outer and inner race of the bearing. This leads to a loss in resistance over time due to both the rotation of the sample and the jarring motion created by clipping in the sample puck into the sample puck holder. During measurements, the sample puck was immobile, and it was expected that the leakage resistance would remain constant. However, when a bias was applied to the sample, the leakage current appeared to slowly increase with time as shown in Figure 56. This increase in current may be due to an increase in the ball bearing temperature caused by ohmic heating leading to the generation of more charge carriers within the dielectric ball bearings.

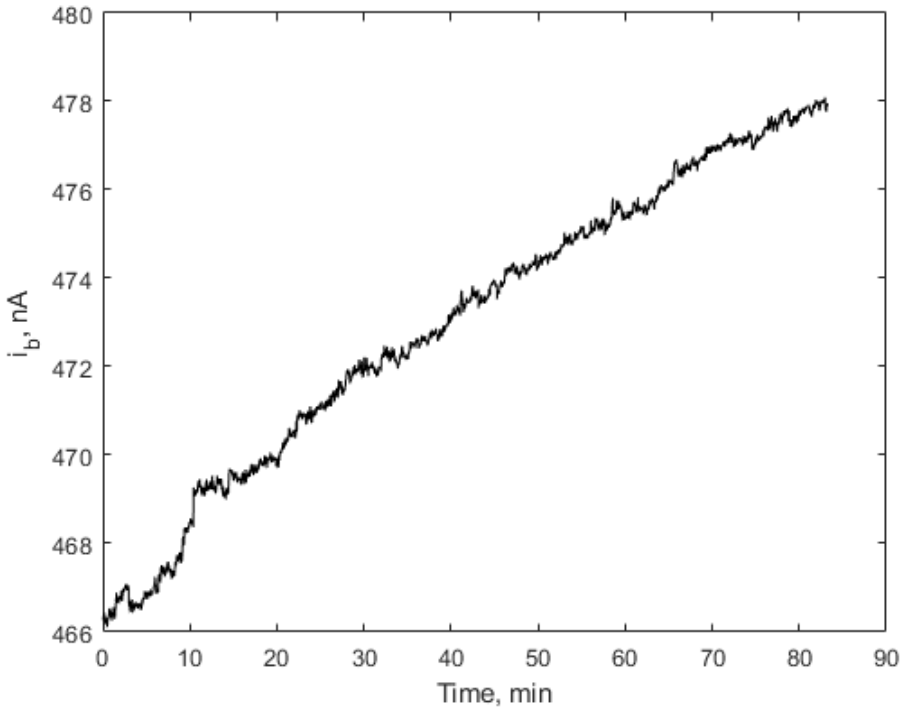


Figure 56: Current through bearings with the sample biased to 100 V.

The second noise source was caused by the electrostatic coupling between the system and operators working in the lab. Operators working in the lab were required to wear boot covers to prevent the spreading of contaminants into the cleanroom environment. However,

these boot covers contributed to a buildup of static electricity on the operator. The system was carefully grounded throughout and metal foils were place across all dielectric openings on the UHV chamber. All unused BNC feedthroughs into the chamber were connected to ground using BNC grounding plugs which prevented electrostatic coupling with objects outside the chamber and prevented the feedthroughs from building up a static charge due to their exposure to electrons within the chamber. However, this did not fully mitigate the coupling problem, and when an operator was moving in the vicinity of the equipment the current fluctuations shown in Figure 57 were induced. Thus, operators were required to wear a grounded wrist strap when operating near the system which eliminated the fluctuations.

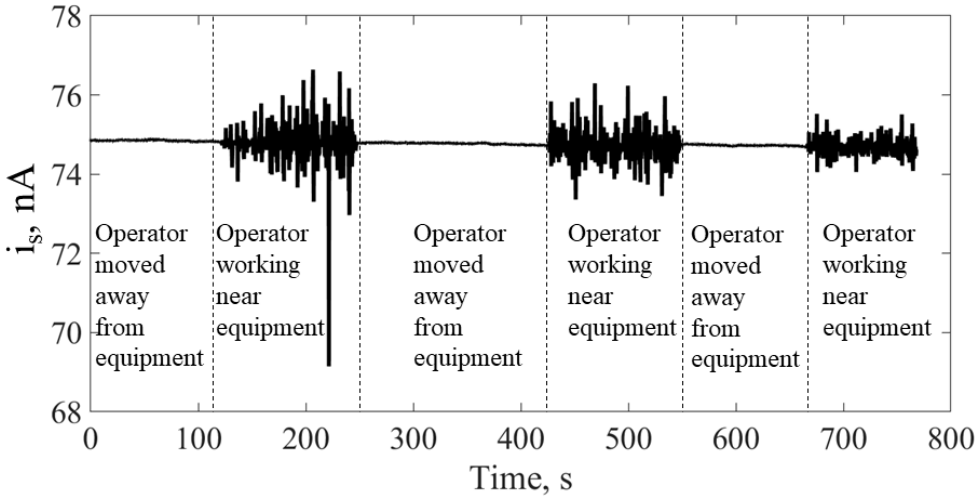

Figure 57: Fluctuations induced by an ungrounded operator.

The third noise source was associated with the temperature control system for the sample puck. The sample puck is designed to be heated via radiative heating by resistive coils situated beneath the sample puck. The temperature of the sample was monitored using a thermocouple that makes contact with the underside of the sample puck. The leads of the thermocouple were connected into the temperature control system. Ideally, the temperature

control system would measure the voltage difference across the leads while drawing negligible current. However, measurements revealed that this current was not negligible and would cause the electrometer to report different current values for different range settings as shown in Table 3.

Table 3: Erroneous measurements caused by temperature control system.

| Measured leakage current when temperature control system is disconnected, nA | Measured leakage current when temperature control system is connected, nA | Measurement Range |
|---|---|---|
| 35 | 2.8 | 200 nA |
| 35 | 230 | 2 μA |
| 35 | 30 | 20 μA |
| 35 | 30 | 200 μA |

The problem was not observed when connecting the thermocouple into a battery powered Fluke multimeter. The manufacturer of the sample manipulator suggested that this problem was not observed with Fluke multimeter because the multimeter is completely isolated from ground because it is battery-powered. However, the electronics within the temperature control system are not completely isolated from ground which allows an interaction to occur between the electrometer and the temperature control system leading to the erroneous current measurements. In addition, the temperature control system uses a K Type thermocouple extension wire without ground shielding creating electrostatic coupling problems between the wire and operators working nearby. This problem cannot be corrected by wearing a ground strap due to the fact that a potential difference between the thermocouple wire and ground exists whenever the sample is electrically biased. Based on these finding, the temperature control system remained disconnected from the system throughout the rest of the research. Furthermore, it was assumed that the temperature

measured on the walls of the vacuum chamber were equal to the sample puck's temperature.

### 3.1.4 Integration Time and Sampling Period

The multimeters and electrometers are designed to perform measurements using integrating analog-to-digital converters. In theory, these measurements are made by integrating the desired electrical signal over a selected integration time and dividing the result of the integration by the integration time (i.e. a time average). These measurements are repeated based on the selected sampling period as shown in Figure 58. The instruments are programmed for a specific integration time while the sampling period is controlled by the signal generator. The processing time varies with the current being measured. Thus, the sampling period had to be carefully considered because it is possible for the sampling period dictated by the signal generator to be too short for the instruments to complete processing before the next measurement begins. When this happens, the instruments continue to make measurements, but the measurements become asynchronous.

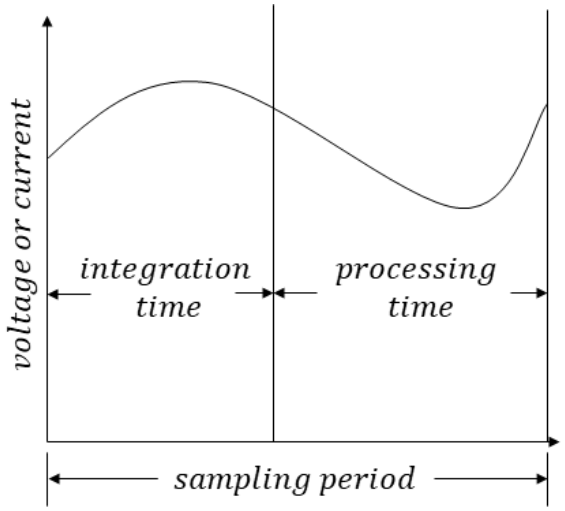


Figure 58: Diagram of sampling scheme.

The electrometers allow integration times up to 10 power line cycles (PLC) while the multimeters allow integration times up to 100 PLC. Tests were performed at 0.2, 1, and 10 PLC to determine the noise and sampling period associated with each integration time. The measurements remained synchronous for the following sampling periods: 100 ms for 0.2 PLC, 500 ms for 1 PLC, and 1 s for 10 PLC. The sampling period can be increased from those listed; however, decreasing the sampling period below that listed may produce asynchronous measurements. The noise analysis results to be discussed in the following paragraphs were performed using the aforementioned sampling periods, and each data point was derived from a sample set of 2500 measurements, which is the maximum number of measurements the electrometer can store in its buffer.

Figure 59 shows the standard deviation associated with voltage measurements made using different integration times for several voltage biases. The voltage measurements for both the Faraday cup and sample circuits appear identical. Thus, the results for only the sample circuit are shown. The measurements made at 10 PLC provided the lowest standard deviation. The measurements made at the 0 V setpoint were performed by disconnecting the power supply from the circuit and shorting the connection to ground. This significantly reduced the noise for the 0.2 and 1 PLC integration times, which indicates that the power supply may be contributing significantly to the noise. Placing a shunt capacitor at the power supply output may reduce this noise. However, this will increase the settling time of the circuit and was not pursued in this research.

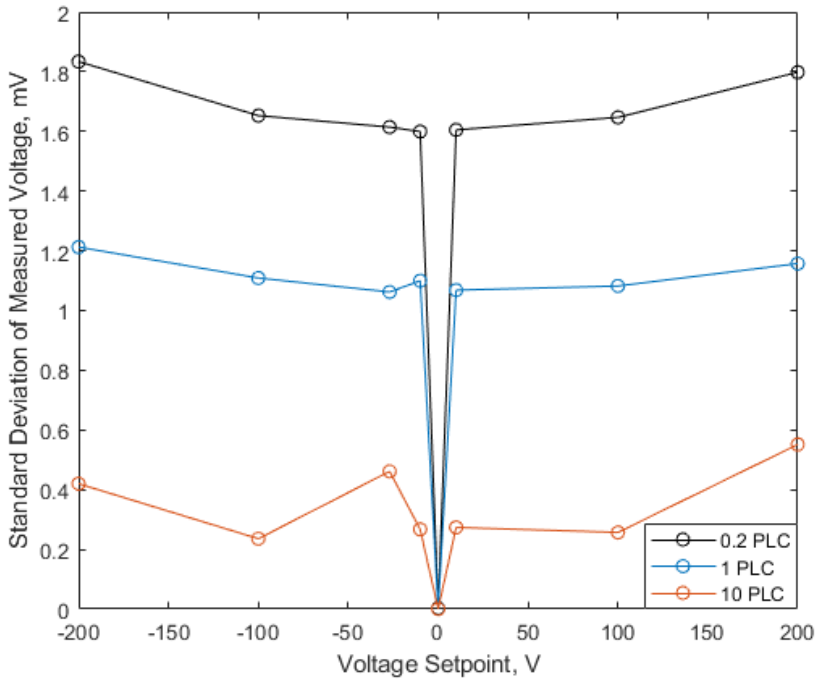


Figure 59: Standard Deviation of voltage measurements at several voltage setpoints.

Figure 60 shows the standard deviation of current measurements made on the Faraday cup circuit for different integration times and voltage biases. The 10 PLC integration time again provided the lowest standard deviation, and the standard deviation was drastically reduced for 0.2 and 1 PLC at the 0 V setpoint.

Figure 61 shows the mean and standard deviation of current measurements made on the sample circuit for different integration times and voltage biases. These data are from measurements made after the sample puck was redesigned and the feedthrough was replaced, which is discussed in a later section. At the 100V setpoint, the mean current measured by the electrometer connected to the sample puck was reduced by six orders of magnitude from the mean current previously measured with the ball bearing leakage in the circuit. Qualitatively, this data is similar to the results obtained before the replacement (i.e. The 10 PLC integration time always provided the least noise followed by 1 PLC then 0.2

PLC). The standard deviation was again drastically reduced for 0.2 and 1 PLC at the 0 V setpoint.

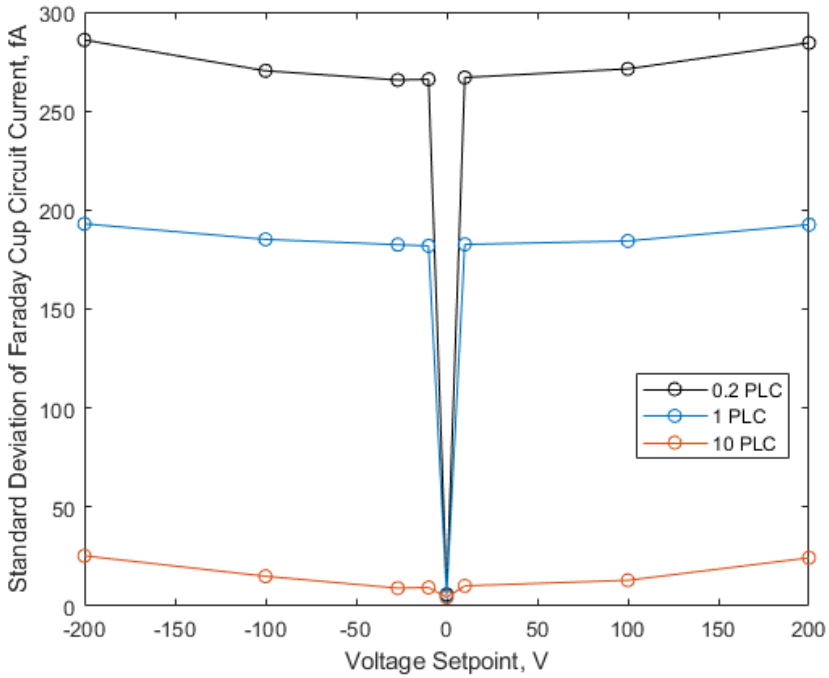


Figure 60: Standard deviation of Faraday cup current measurements at several voltage setpoints.

Using a longer integration time provides the least measurement noise, but it also reduces the rate at which measurements can be performed. With shorter integration times, it is possible to perform measurements at a faster rate and reduce the signal noise in post-processing using a digital filter, such as a moving average. However, this requires a greater amount of data storage for the measurements and the additional step of digital filtering during data analysis. For the data shown in Chapter IV, all measurements were taken with an integration time of 10 PLC and a sampling period of one second in order to reduce data storage and processing requirements.

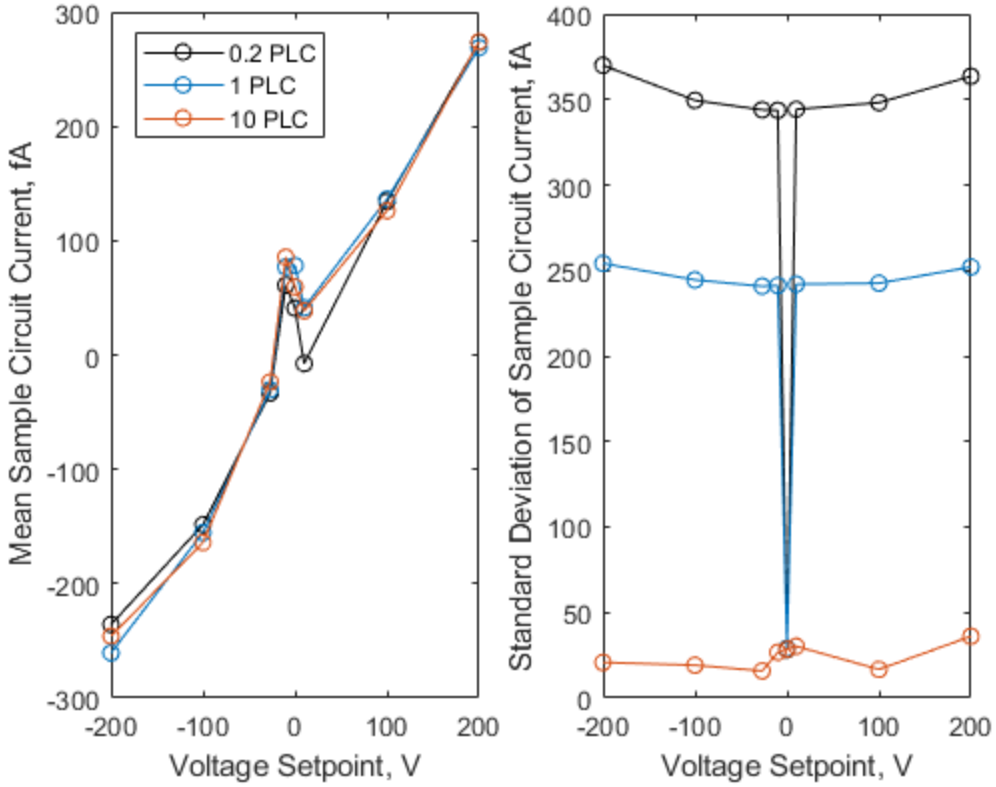

Figure 61: Mean and standard deviations of sample current measurements at several voltage setpoints.

### 3.1.5 Electron Gun Characterization

The electron gun used in the system is a Kimball Physics ELG-2A. The SIMION® simulation model for the electron gun is shown in Figure 62. It uses a thermionic cathode as a source of free electrons. The cathode consists of a tantalum disc attached to a heating element. When a voltage is applied across the heating element, the disc is rapidly heated causing a quick increase in the free electron current produced by the cathode as shown in Figure 63.

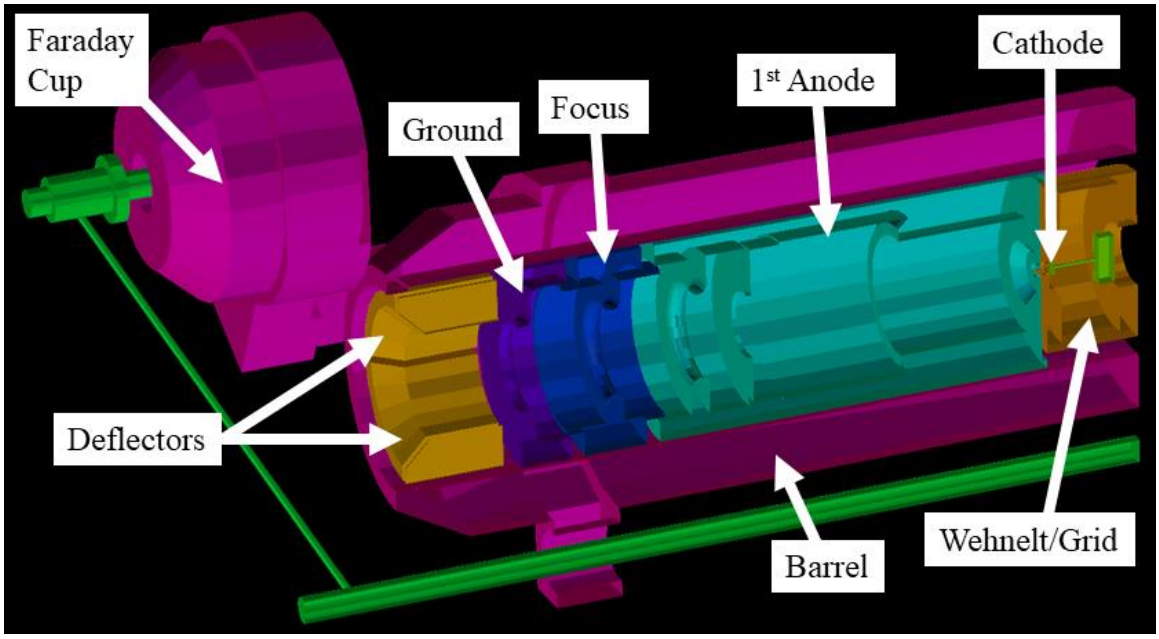

Figure 62: ELG-2A simulation model.

As the resistance of the heating element increases due to the increase in temperature, the power delivered to the cathode is reduced, and the output of the cathode begins to decline. Data collected over a 7-hour time period indicated that the current output would continue to monotonically decrease over time but the rate of decay sufficiently decreases after three hours such that measurements can made under the assumption that the cathode output is constant over a short time period. For all measurements performed using the electron gun, the cathode was allowed to heat for a minimum of 3 hours before beginning data collection.

It should be noted that the power supply for the electron gun has a feedback control system that is designed to measure and maintain a specific emission current from the electron gun. This system was never used in this research for several reasons. Firstly, the feedback control system cannot be used when the electron gun output is shut off between measurements using the electron gun's grid.

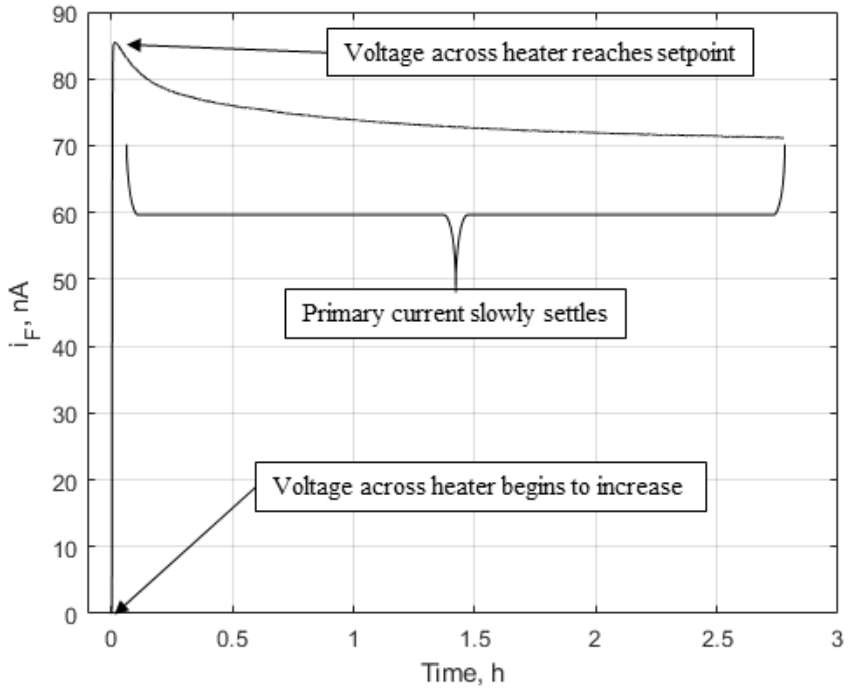

Figure 63: Electron gun warmup period.

Secondly, when the Faraday cup is swiveled under the opening of the gun barrel, secondary electrons are emitted from the Faraday cup back into the gun barrel. This leads to a drop in the measured emission current causing the feedback system to increase the voltage across the heating element. This scenario can also happen when secondary electrons are emitted from the sample back into the gun but to less extent because the secondary electrons created on the sample are not prohibited from spreading out into the chamber. Thirdly, the control system is stable to ±0.1% per hour of full scale (20μA) or ±20 nA per hour [136]. Furthermore, the lowest possible current setting is 10 nA. For reasons not yet discussed, measurements were typically made at about 10 pA, which is well below the operational limits of the feedback control system.

### 3.1.6 Beam Deflection by Biased Faraday Cup

While performing experiments to determine the primary electron beam spot size using a phosphor screen, it was observed that the electron beam was deflected towards the wire which connects the Faraday cup to the measurement circuit when the cup was positively biased. This wire is identified with a dashed, red line in Figure 64. The deflection increases for lower primary electron energies. In order to avoid this deflection for the low primary electron energies used in this research, the Faraday cup remained grounded for the data found in Chapter IV.

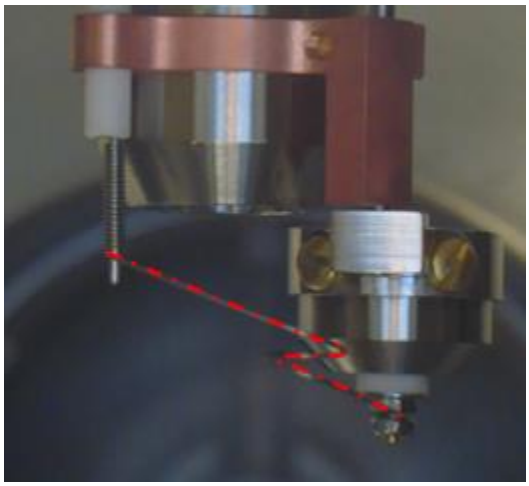

Figure 64: Wire connected to Faraday cup.

### 3.1.7 Leakage from the Faraday Cup

When the Faraday cup is in the closed positions, electrons are still able to escape from the narrow opening between the Faraday cup and the electron gun, which may lead to a measurable sample current. With the Faraday cup grounded and in the closed position, the sample received an approximately 1.5 nA current from the escaping electrons when the sample was biased to +100 V and the current leaving the cathode was approximately 89 nA. Increasing the positive bias of the Faraday cup decreases the number of electrons

escaping; however, it also causes the electrons to be deflected as they exit the end of the gun when the cup is in the open position as discussed in the previous section. In order to accurately measure the leakage resistance of the sample circuit, the Faraday cup must be either positively biased and in the closed position, or electrons must be prohibited from leaving the cathode by negatively biasing the grid. In addition, the only way to measure the leakage resistance of the Faraday cup circuit is to negatively bias the grid. Manually adjusting the grid potential is physically challenging when trying to also rotated the Faraday cup. Thus, for measurements made before the system was automated, the Faraday cup was positively biased, and the leakage current of the Faraday cup circuit was assumed negligible since it measures in the fA-range and the primary electron current used during these experiments was in the nA-range.

### 3.1.8 Burst Noise Detected

In early attempts to perform SEY measurements, the current from both the Faraday cup and sample were continuously measured and the Faraday cup was periodically rotated in front and away from the electron gun. Figure 65 shows the typical current signals from these measurements. The Faraday cup was positively biased in order to minimize the electrons escaping from the electron gun when the Faraday cup was in the closed position. During these measurements, unexpected transitions in the sample current started appearing during times when the Faraday cup was stationary as shown in Figure 66. As measurements continued, the current became increasing noisier and exhibited the characteristics of burst noise. The onset of this noise was quickened by increasing the sample bias. At the time of discovery, this noise was attributed to the leakage resistance associated with the dielectric

ball bearings. However, this noise was later also identified in the circuit connected to the Faraday cup indicating that this noise was not a result of the dielectric ball bearings as originally suspected.

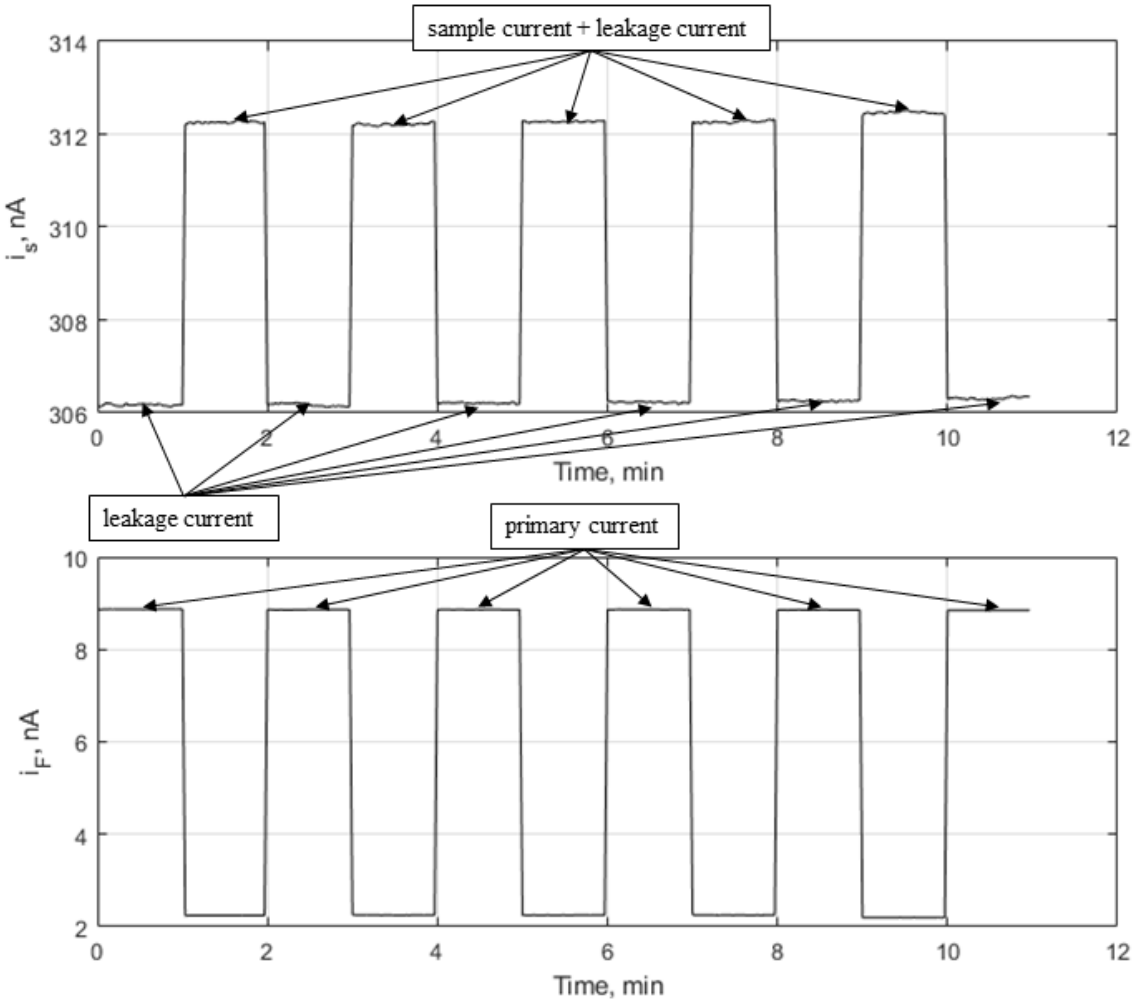


Figure 65: Current signals produced by periodically rotating the Faraday cup.

This noise may be due to the dielectric breakdown of insulating materials in the chamber after exposure to electrons from the electron gun and secondary electrons from the sample. The burst noise would worsen as measurements continued requiring the measurements to be temporarily discontinued to allow the burst noise to decrease. During the measurement

pause, the sample bias was removed, and the Faraday cup remained in the closed position in order to confine electrons within the electron gun. After waiting about 30 minutes, the sample was again biased, and the measurements were continued. Burst noise was not observed following the 30-minute waiting period. Thus, this waiting period was sufficient for allowing the burst noise to dissipate given the conditions of the measurement. Measurements continued until the burst noise again became significant or the measurements concluded.

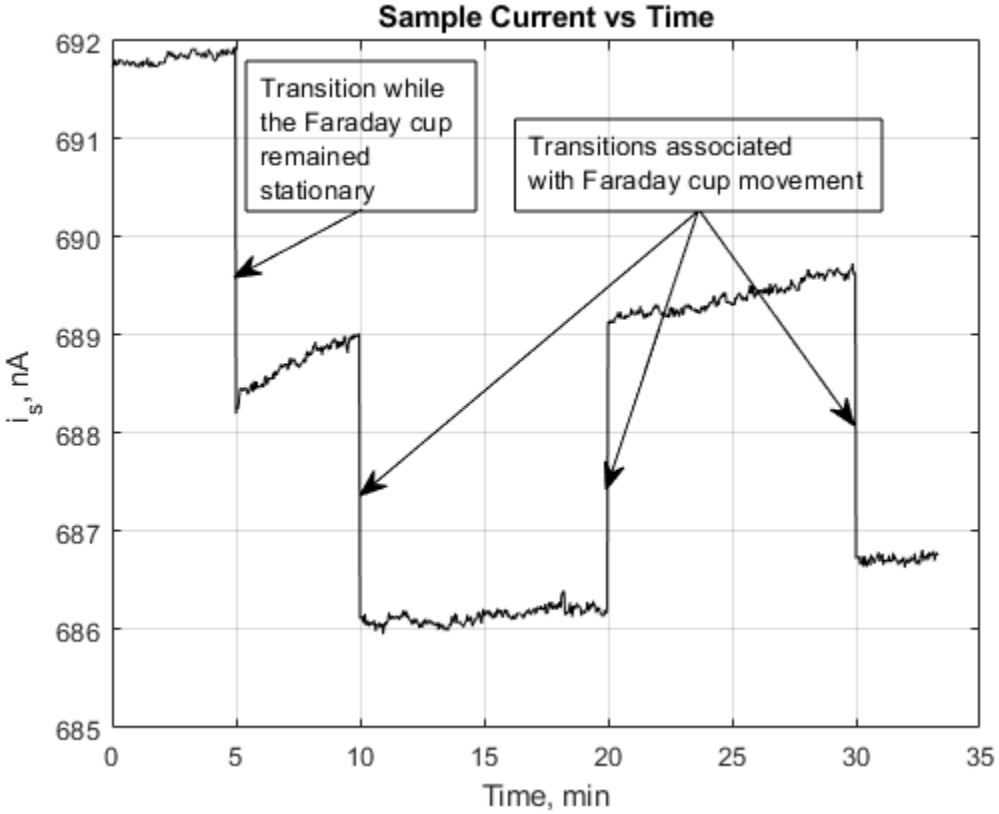


Figure 66: Unexpected transition in sample current.

### 3.1.9 Systematic Shift Observed in Measurements

Early measurements were conducted to determine the effect of using different primary currents and sample biases on SEY measurements. These measurements were

performed by maintaining constant electron gun settings and varying the sample bias. The Faraday cup was manually rotated back and forth producing current signals like those shown in Figure 65. At each of the transitions shown in Figure 68, a calculation of the ratio between sample current and primary current was performed after the leakage current associated with the dielectric ball bearings was subtracted. These ratios should maintain a nearly constant value for each sample bias. A MATLAB script was created to perform these calculations in addition to determining and ignoring transitions due to burst noise. Kalman filtering was also implemented in this script to further reduce the measurement noise. Each dataset contained 10 transitions which allowed 10 ratios to be calculated for each sample bias.

Figure 67 displays the results for measurements made at two different primary currents. The error bars shown on the figure represent three standard deviations. Normally, it is assumed that using a higher primary current will yield a lower standard deviation due to the increased SNR of the current signals. However, measurements made at several different sample biases proved this assumption incorrect and warranted a closer investigation of each calculated ratio.

Measurements were then performed using 20 transitions per dataset in order to increase the number of calculated ratios for comparison. Figure 68 shows the ratios calculated for each of the transitions of six separate datasets. For these measurements, the sample was grounded, and the Faraday cup was biased at +5 V. The primary electron current was about 100 nA. Each dataset shows a systematic decrease in the calculated ratio between the first and last transition of the set. This shift is the cause of the increased standard deviation, and the rate at which this shift occurs increases with the primary

current. In addition, the ratio measured at the beginning of each set was higher than that of the previous set. It was thought that the shift might be an artifact created by the Kalman filter. The filter was disabled, but the shift was still observed.

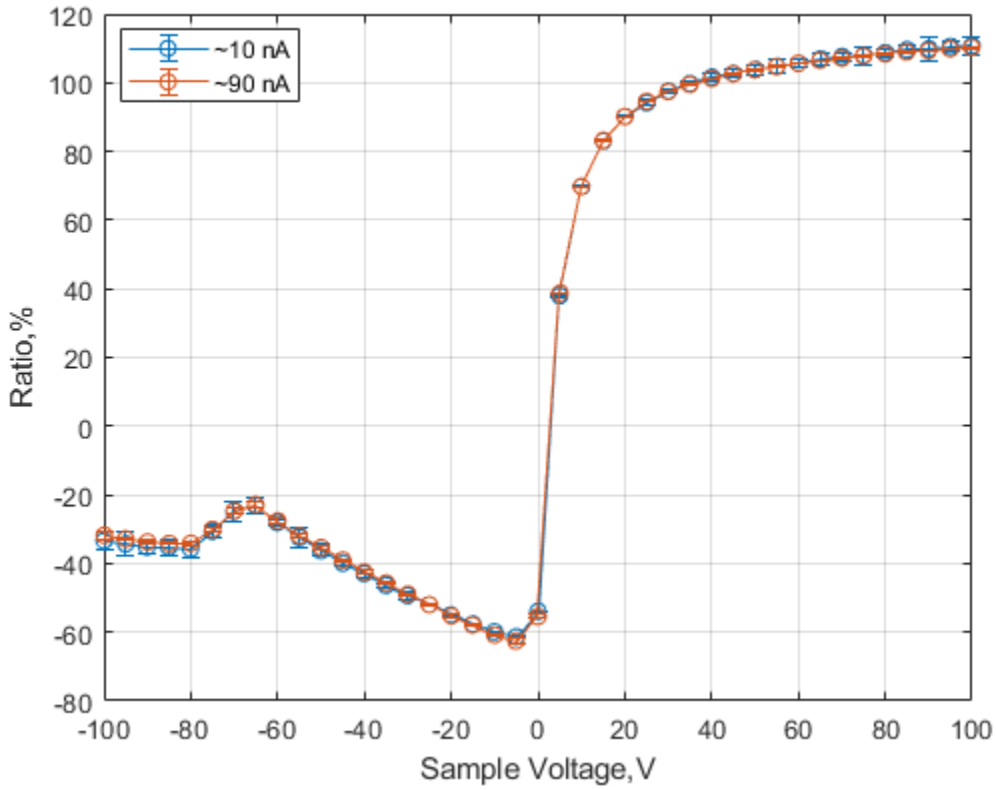


Figure 67: Ratio between sample current and primary current versus sample voltage.

The smallest primary current that could be used while maintaining a low standard deviation was about 8 nA due to the noise created by the leakage resistance associated with the ball bearings, and measurements with an 8 nA primary current still showed signs of this shift. Originally, it was believed that this shift was solely due to the charging of dielectric materials within the chamber; and, in order to reduce this charging, additional experiments were performed with the time the Faraday cup remained in the open position

reduced. The primary electron current used in these measurements was 8 nA. The results of these test still showed signs of this shift though to less extent as shown in Figure 69.

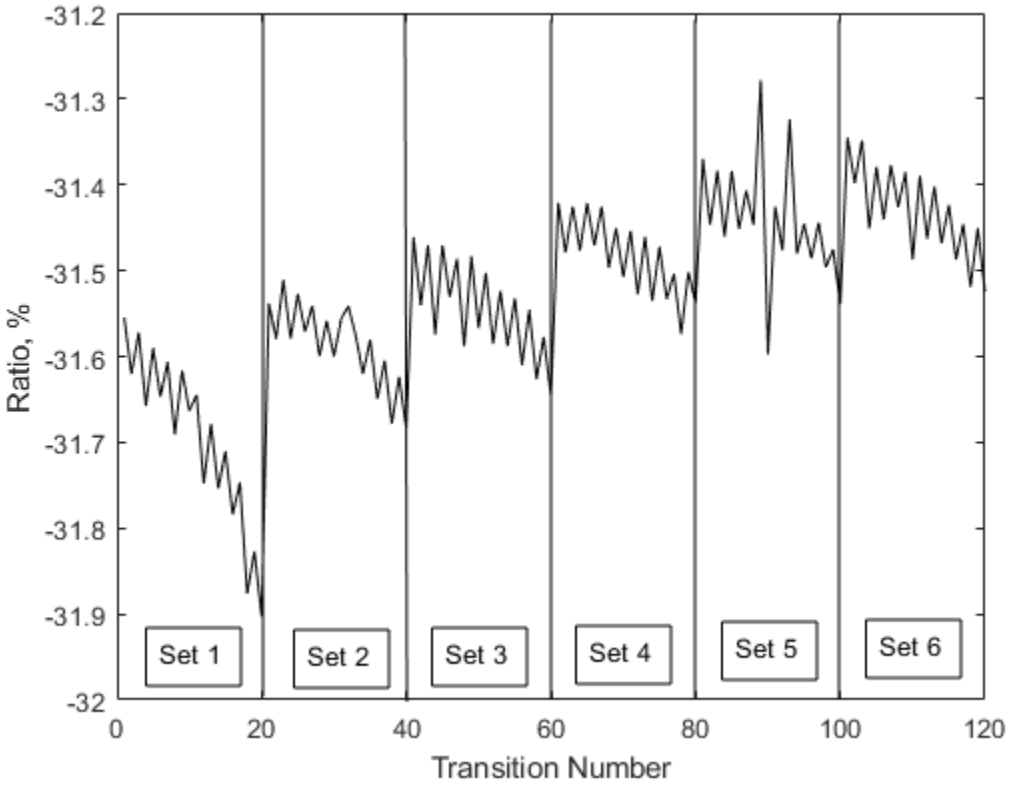


Figure 68: Ratios calculated from six separate datasets.

The legend indicates the amount of time the Faraday cup spent in the open and closed positions between transitions. Attempts to eliminate this shift were unsuccessful at 8 nA, so it was determined that the system would need to operate with a lower primary current which required circumventing the leakage resistance associated with the bearings.

### 3.1.10 Sample Puck Redesigned

In order to overcome the leakage resistance presented by the ball bearings, the manufacturer of the sample manipulator suggested splitting the sample puck into two

halves and placing a dielectric layer between the two halves as shown in Figure 70. The thermocouple makes contact with the underside of the upper half.

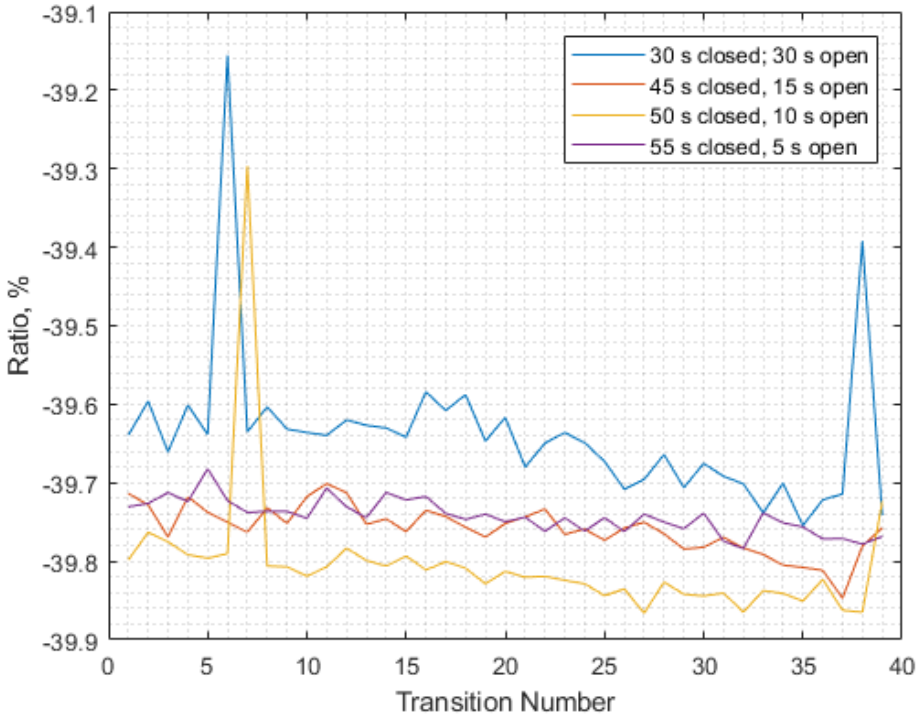


Figure 69: Ratios calculated for datasets containing 40 transitions.

The sample current was rewired to travel through the thermocouple to the voltage source and measurement equipment. The halves are held together by dielectric screws. Gold was deposited on the heads of the screws via sputtering in order to prevent the heads of the screws from building up charge when exposed to electrons from the electron gun. Washers composed of 316 stainless steel (316SS) were used with the fasteners in order to facilitate the testing of samples with various thicknesses.

The modified sample puck was created by the AFIT Model Fabrication Shop from 316SS which is slightly magnetic. This alloy of stainless steel normally has a relative

permeability near unity though it may vary slightly depending on the exposer of the material to different manufacturing processes, such as welding and annealing [137].

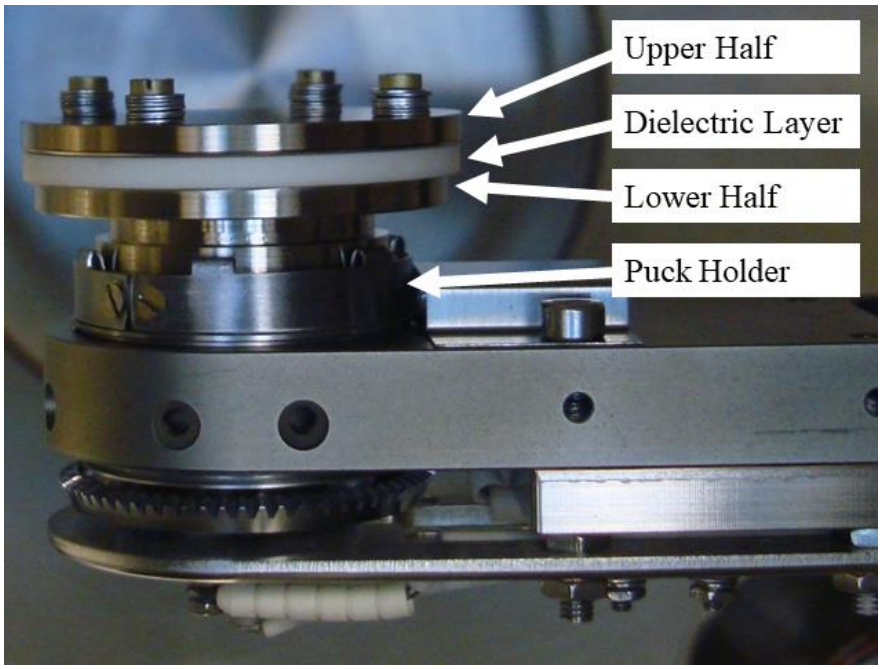


Figure 70: Redesigned sample puck.

The use of materials with relative permeabilities not equal to unity can lead to distortions in the magnetic field near the materials and is not ideal for SEE measurements. However, since the relative permeability of 316SS is near unity, the distortion effect is considered negligible for this research. Furthermore, slightly magnetic materials are used throughout the chamber: the electron gun is made from 316SS, and the chamber is made from a slightly magnetic stainless steel. The modified sample puck clips into the molybdenum sample puck holder. Due to the differing thermal expansion coefficients of molybdenum and 316SS, measurements using the modified sample puck are limited to room temperature in order to avoid damage to the sample manipulator.

### 3.1.11 Feedthrough Leakage Identified and Repaired

With the sample puck replaced, electrical characterization was again performed while the electron gun remained off. A +100V bias was applied to the sample circuit in order to measure the leakage current for the new circuit. After days, the sample current failed to stabilize and displayed the behavior shown in Figure 71. The cause of this unstable current was traced to the thermocouple feedthrough. This feedthrough had developed an electrical short to ground that varied significantly when force was applied to the pins of the feedthrough.

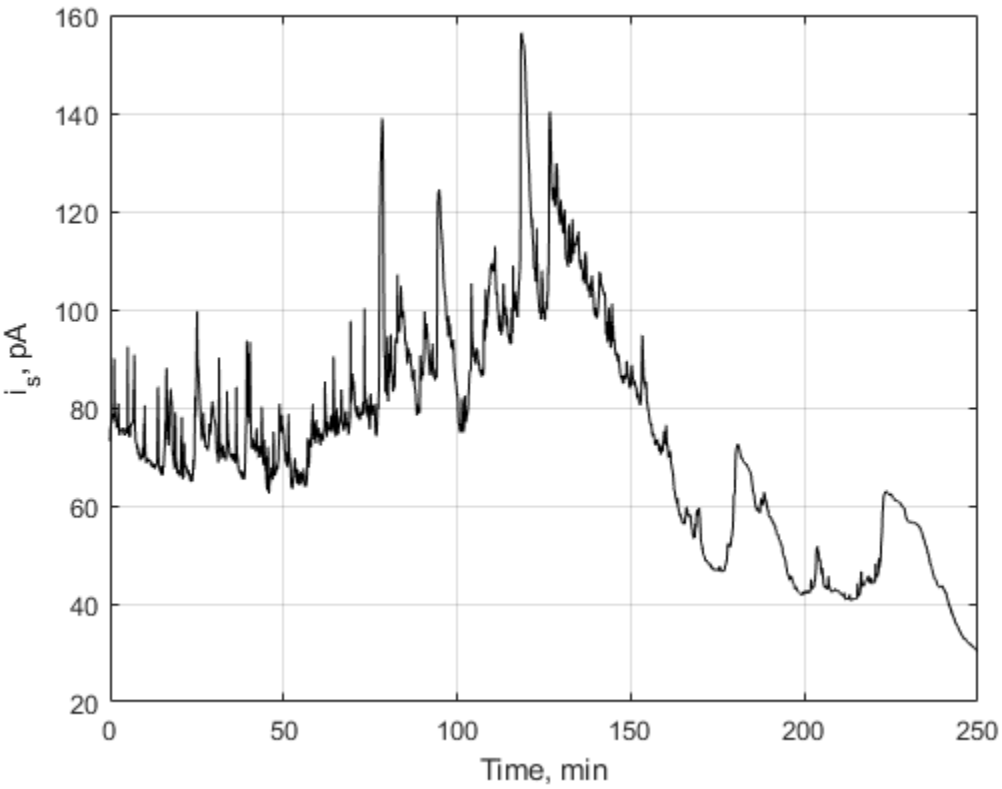


Figure 71: Variability of sample current due to feedthrough electrical short.

The original feedthrough which used a standard Type K mini plug was replaced by a sturdier, Mil-Spec feedthrough. Over the duration of a week, a bakeout procedure was

performed with +100 V applied to the sample. It was found that applying resistive heater tapes in the area near the new feedthrough allowed the leakage current associated with the sample circuit to be further reduced (Figure 72). The application of heater tapes in this area may have driven more contaminants away from this region during bakeout leading to a reduction in the leakage current. With the exception of placing heater tapes near the feedthrough, the bakeout procedure followed that prescribed by Sattler [4].

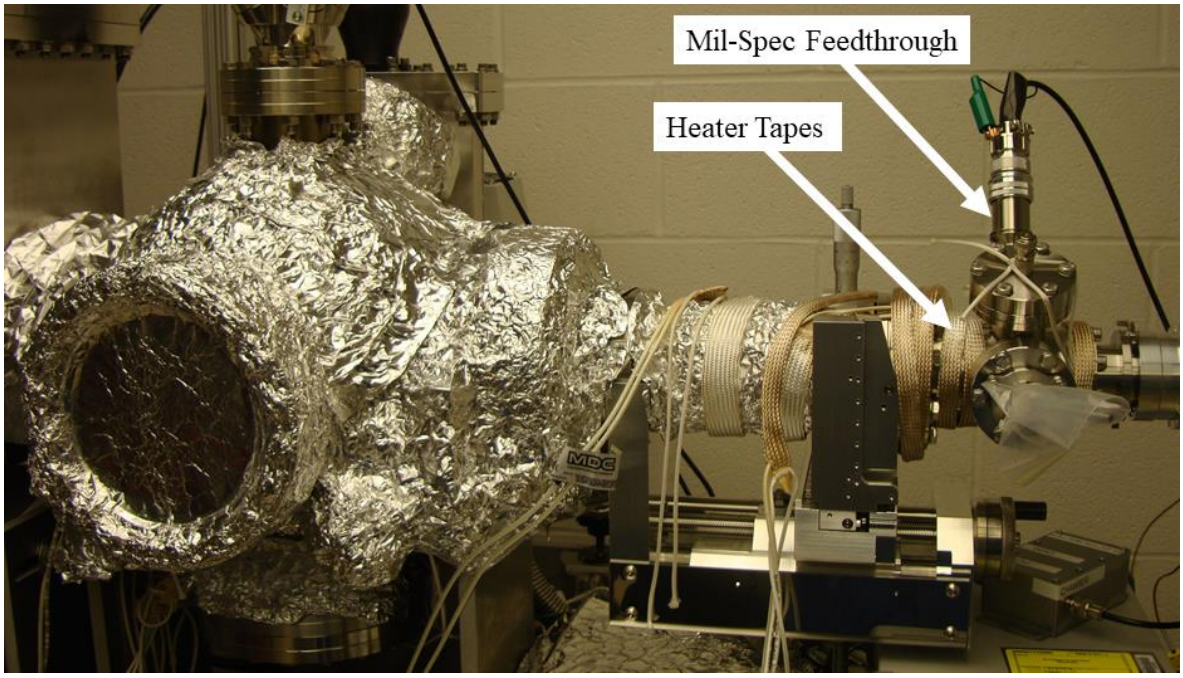


Figure 72: Heater tapes extended towards the end of sample manipulator.

### 3.1.12 Settling Time and Capacitive Coupling

When operating in the pA range, the sample and Faraday cup circuit require significantly more time for the currents to settle following bias changes than when operating in the nA range. Figure 73 shows both currents settling 60 minutes after the bias was switched from 0 V to +100 V. The time required for the current to settle increases as the difference between initial and final sample bias increases. For differences of 100 V or more, the system was given at least one hour to settle before measurements were

performed. For difference of 10 V or less, the system was given at least 15 minutes to settle before measurements were performed.

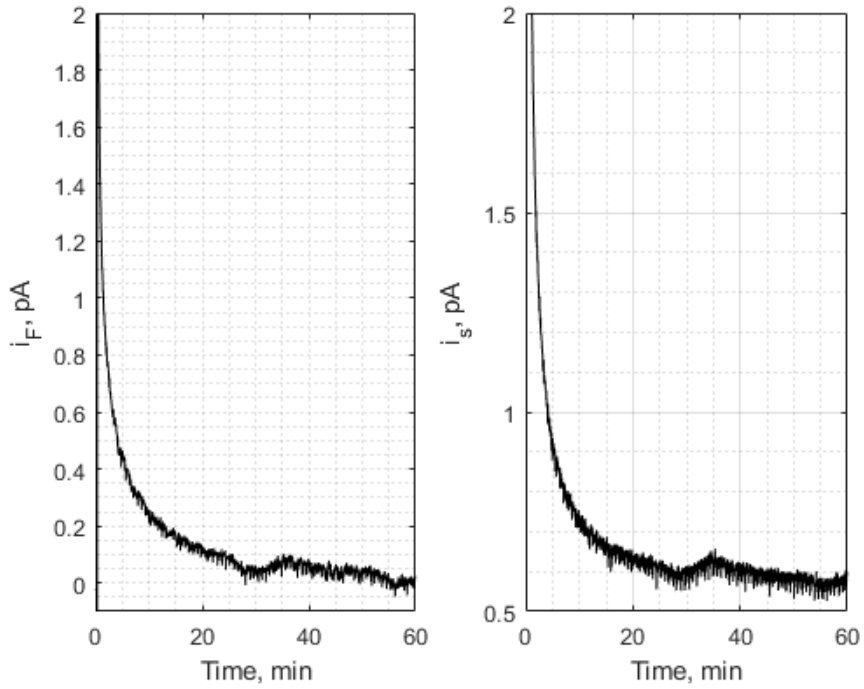


Figure 73: Sample current, $i_s$, and Faraday cup current, $i_F$, after +100V step input at time zero.

These long settling times are attributed to two capacitances. The first capacitance is associated with the circuitry outside the chamber. In order to reduce this capacitance, the length of the cables between instruments was reduced by positioning the instruments as near to the chamber as possible and by fabricating shorter cables. The second capacitance is associated with the wiring within the chamber. Altering this wiring requires redesigning the sample manipulator and electron gun, which is both a costly and time-consuming endeavor. Due to research constraints, this endeavor was not pursued. Minimizing the settling time further requires converting the entire system to triax, which would reduce the effective capacitance of the circuitry [135].

Though the sample circuit and Faraday cup circuit are not physically connected to one another, they are capacitively coupled with one another due to the close proximity of the Faraday cup and sample. This coupling can be observed when operation in the pA range. Figure 74 shows a transient in the sample current caused by a +100 V step input on the Faraday cup circuit at 12 seconds.

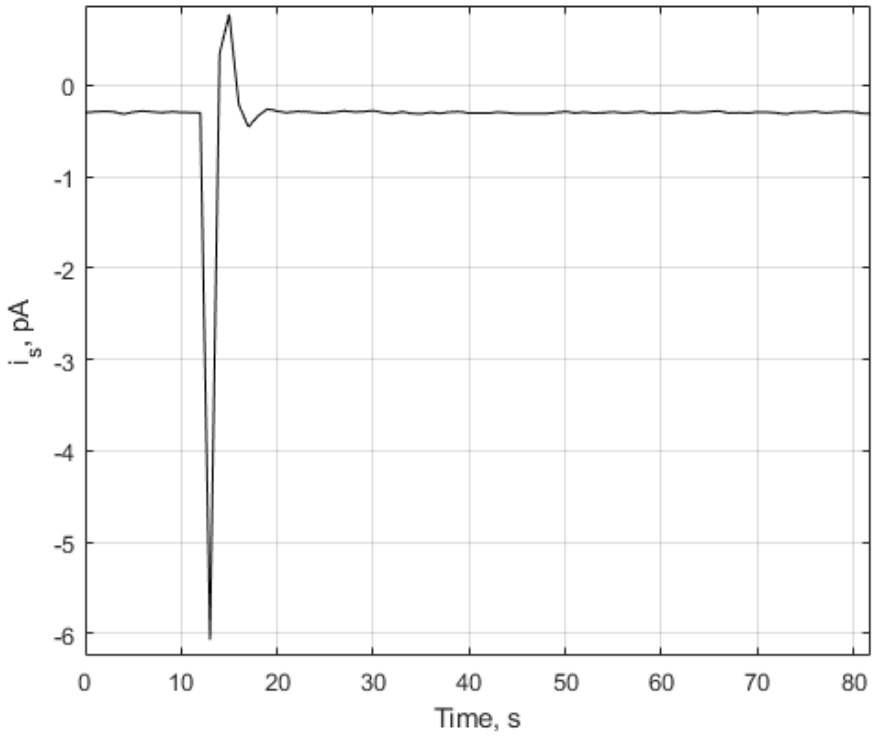


Figure 74: Transient response in sample current caused by +100V step input on Faraday cup circuit.

In addition, the Faraday cup is capacitively coupled to the optics within the electron gun. Because of this coupling, measurements must be delayed about 30 seconds after adjusting the potentials of the electron gun optics. Otherwise, the transient associated with the coupling will appear in the Faraday cup current measurements as shown in Figure 75.

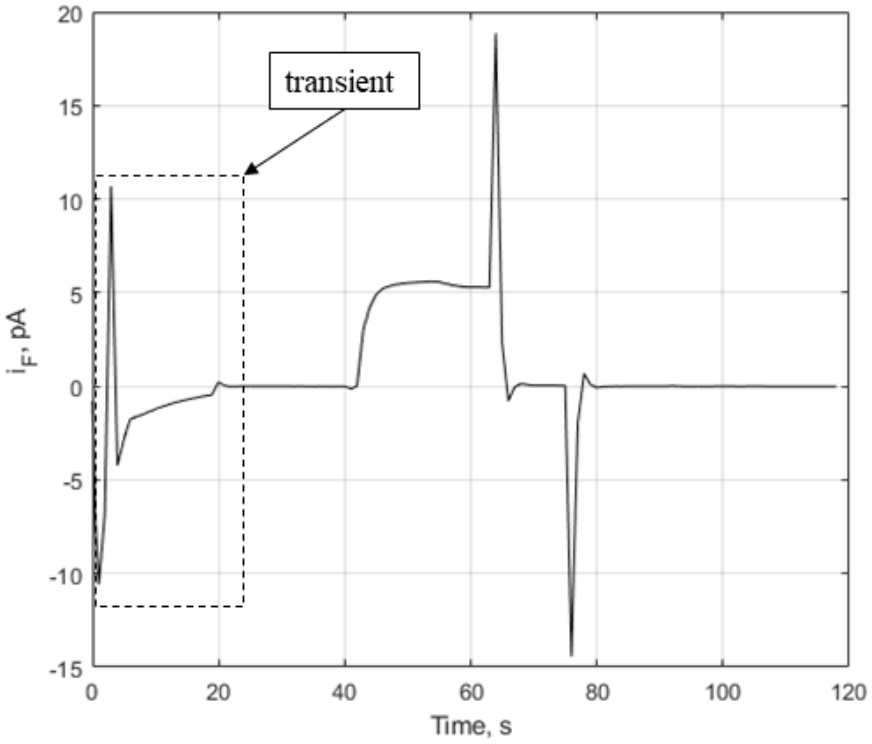


Figure 75: Transient in Faraday cup current caused by adjusting electron gun potentials.

### 3.1.13 System Automation

After having performed many experiments manually, it became apparent that performing measurements was both time-consuming and labor intensive. Additionally, it was physically impossible to adjust multiple pieces of equipment simultaneously, and the rate at which measurements could be performed was limited by both the equipment and operator. In order to perform the many measurements that remained in this research, the system was automated to perform all the task associated with measurements: actuating the Faraday cup, recording chamber temperature and pressure, recording and updating the settings of the electron gun, configuring and retrieving data from the instruments, controlling the function generator, and storing information regarding the sample type and location within the chamber. A single laptop running LabVIEW was programmed to

communicate with all the lab equipment using USB, RS-232, and GPIB connections as discussed in Appendices A and B. A simple actuator to rotate the Faraday cup was improvised using a servo and a LabJack USB DAQ as shown in Figure 76.

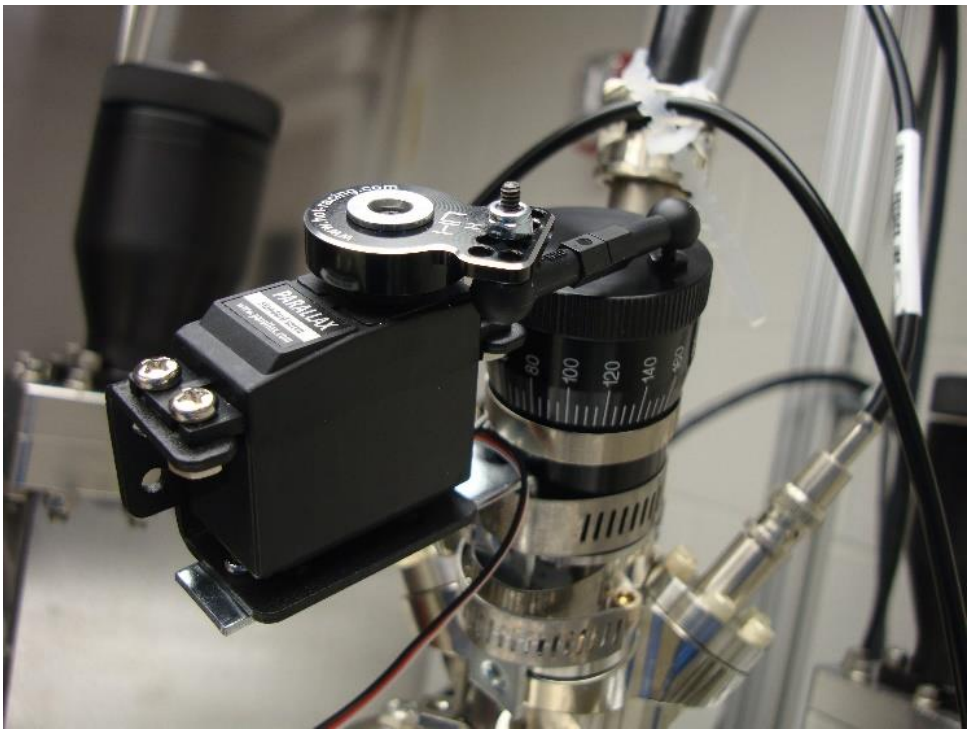


Figure 76: Actuator to rotate Faraday cup.

The potentiometers, which were previously discussed, were replaced by the low noise resistors shown in Figure 77. Figure 77 also shows a simplified model for one of the resistors within the measurement circuit. Based on this model, it was calculated that the power supply will not experience a reverse current when operating at its lowest voltage setting (1 mV) if $i_s$ or $i_F$ remains above -1 μA. If the bias is reversed on the power supply, $i_s$ or $i_F$ must remain below +1 μA. The resistors have a power rating of 600 mW which limits the permissible bias voltage to between -244 and +244 V. The bias of the sample and Faraday cup can now be completely controlled by the power supplies allowing for further automation and simpler control.

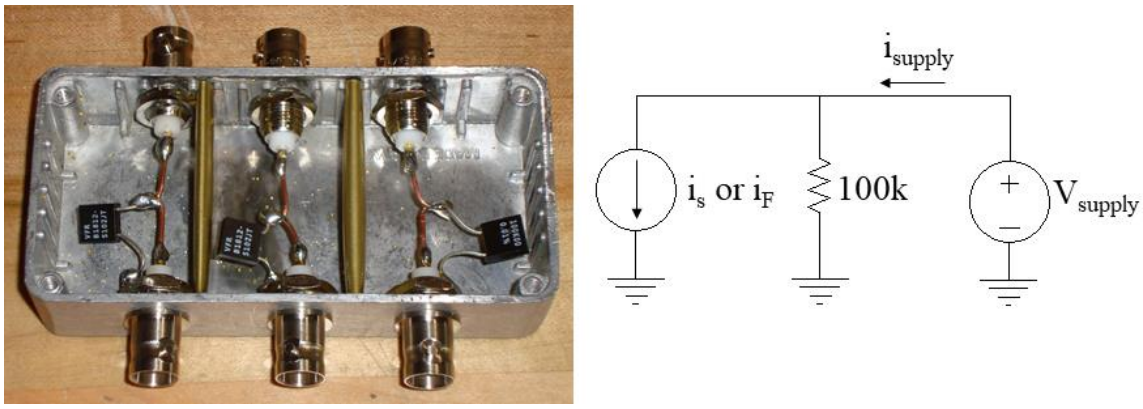

Figure 77: Low noise resistors (left); circuit model (right). Circuit model follows the conventional current standard.

### 3.1.14 Dose and Recovery Study

After all hardware modifications to the system were completed, tests were again performed to determine if the systematic shift discussed previously could be eliminated. During measurements, the chamber was intermittently exposed to a specific amount or dose of electrons by controlling the amount of time electrons are allowed to flow into the chamber and the cathode's current output. Previously, a majority of the electrons had been prohibited from entering the chamber by moving the positively biased Faraday cup to the closed position. With the automated system, the grid was biased to -50 V with respect to the cathode effectively prohibiting any electrons from leaving the cathode and entering the chamber, which will be referred to as the electron gun being off. When the bias was removed, electrons flowed freely from the cathode, which will be referred as the electron gun being on. Between doses, the chamber was allowed to recover from the previous dose.

These tests were performed using a timed sequence of events that produced the current signals shown in Figure 78. First, measurements started with the cup in the closed position, and the grid biased to -50 V with respect to the cathode. Second, the grid bias was adjusted to 0 V with respect to the cathode while the cup remaining in the closed position.

Third, the cup was moved to the open position. Finally, the measurements were halted while simultaneously the grid was biased to -50 V and the cup was returned to the closed position. The sampling period was one second, and each dataset required six minutes to acquire. After downloading the buffered data from the instruments, the system would begin performing measurements for the next dataset until the desired number of datasets were created. These measurements were made with the Faraday cup grounded and sample biased to +200 V. The current leaving the electron gun was around 12.5 pA. For all the measurements discussed in this section, the bias of the electron gun's 1$^{st}$ anode, focus, and cathode remained constant, and the deflectors were grounded.

To analyze data from the current signals, a MATLAB script was developed to extract data from the specific regions shown in red in Figure 78. Because the measurements were precisely timed, data could be extracted from multiple datasets using the same sample numbers. These regions were chosen to avoid transients in the current signals and ensure that the system had stabilized. The mean of each region of extracted data was then calculated and compared across multiple datasets as shown in Figure 79. Each dataset was acquired consecutively with dataset 1 being the first acquired and dataset 100 being the last. After the 46th dataset, five of the means began exhibiting large variations, which may be an indication of the burst noise behavior which was previously discussed. For each dataset, the ratio between $i_s$ for the cup in the open position and $i_F$ for the cup in the closed position was calculated after subtracting the appropriate leakage currents from $i_s$ and $i_F$. The ratio associated with each dataset is shown in Figure 80. Theoretically, this ratio should be a constant value. However, these ratios show a decrease by over 15% between datasets 1 and 20. The decreasing behavior is not repeatable, and the reason for this decrease is

unknown. Since these measurements were performed following the bakeout of the chamber, the decrease may be caused by electrons being redeposited on the exposed dielectric materials within the chamber causing a shift in the electrostatic field.

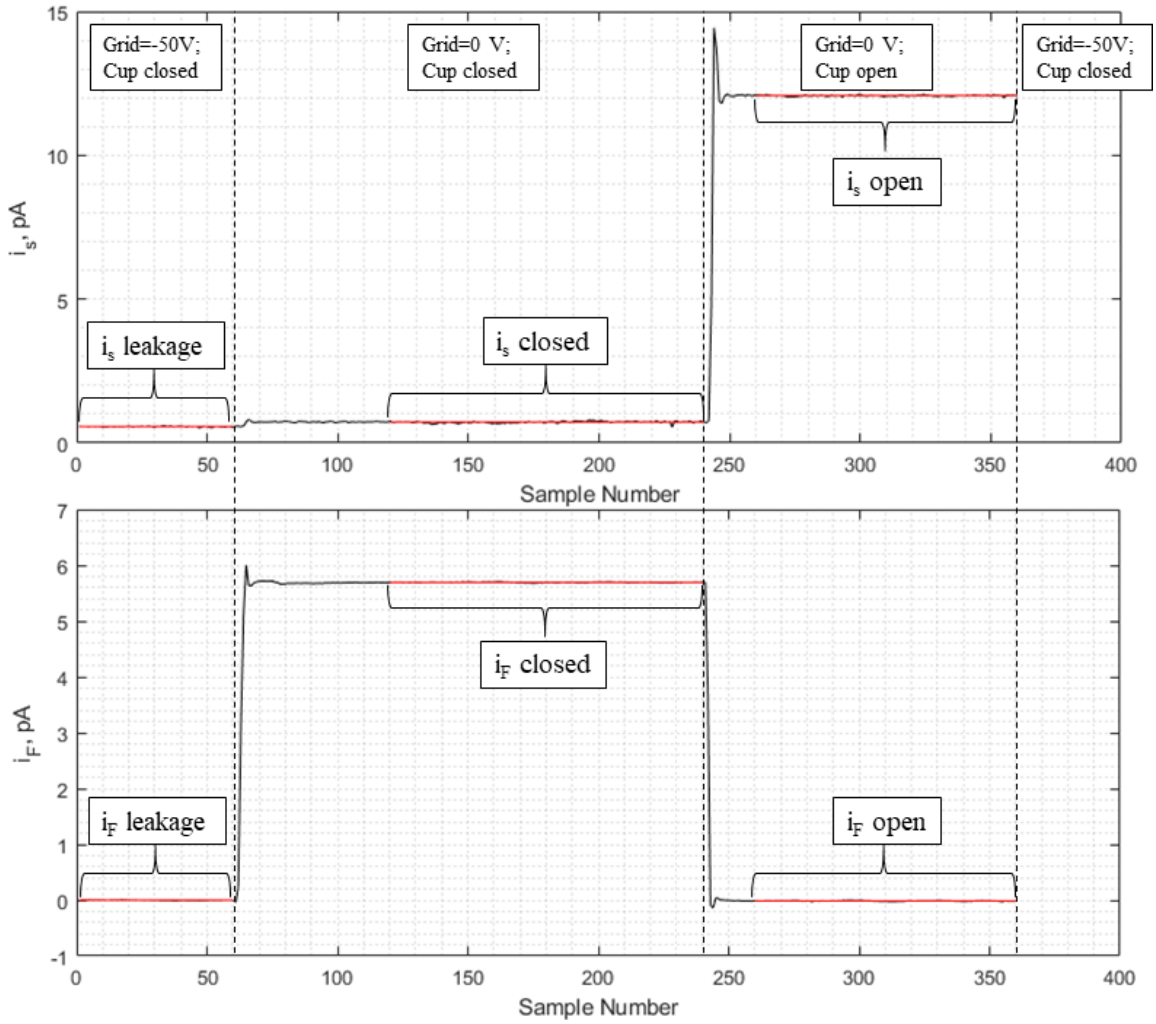


Figure 78: Current signals $i_s$ and $i_F$ generated using initial timing sequence.

Following the decrease, the ratio appears to stabilize and does not show signs of the previously discussed, systematic shift. After the 46th dataset, the ratios appear noisier than the ratios prior. For the datasets between 20 and 100, the mean of the ratios is 184.92% and the standard deviation is 0.46%.

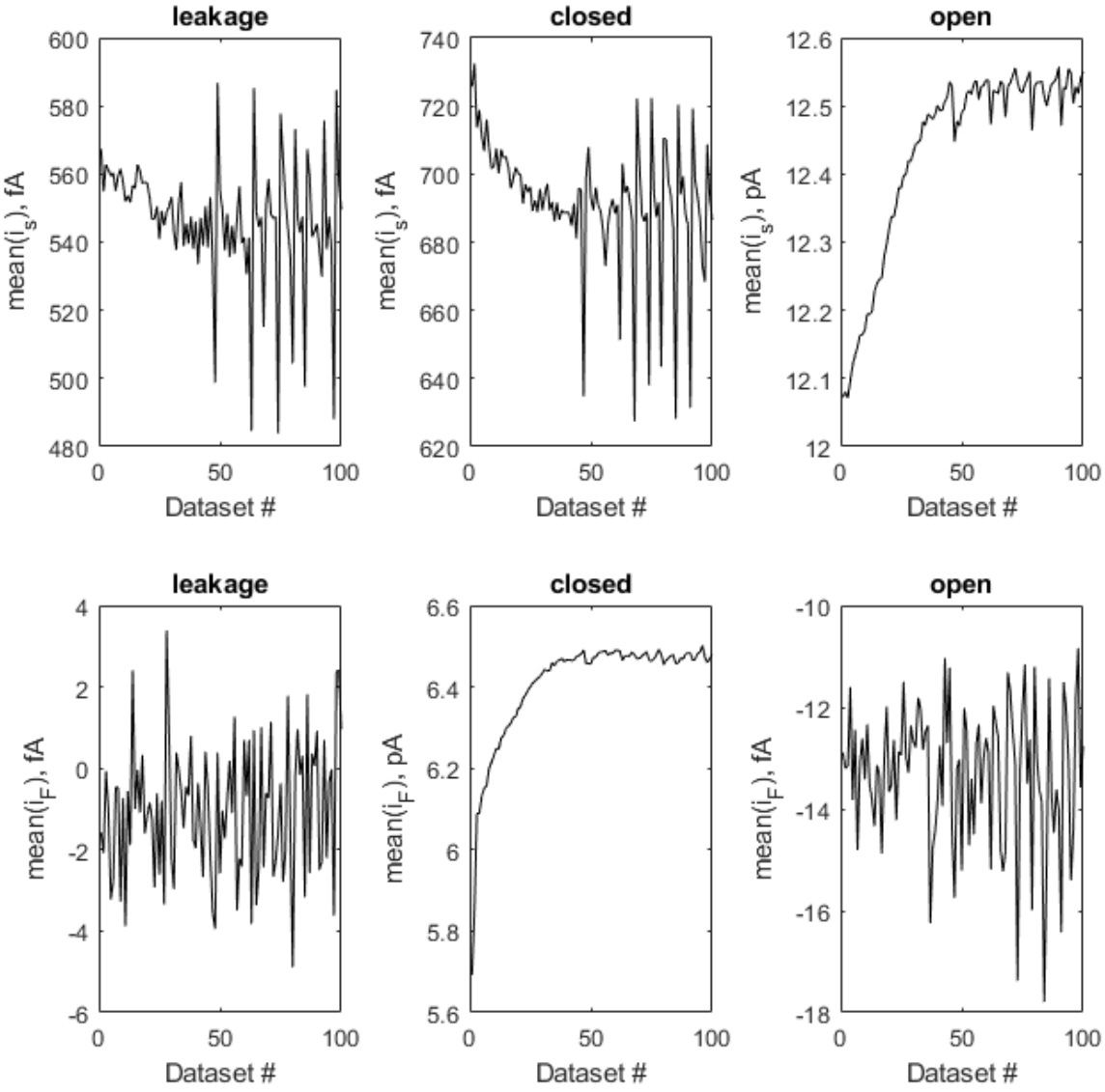


Figure 79: The mean of the extracted regions of $i_s$ and $i_F$ in Figure 78 for 100 datasets.

For these datasets, the electron gun was on for five minutes during each 6-minute dataset. The experiment was again performed using 6-minute datasets. However, the electron gun was on for 1.5 minutes of each dataset while the current was increased to 106 pA. Figure 81 shows the ratios between $i_s$ for the cup in the open position and $i_F$ for the cup in the closed position after subtracting the appropriate leakage currents from $i_s$ and $i_F$. The mean of these ratios is 180.15%, and the standard deviation is 0.27%. Note that this mean is less than the aforementioned mean of 184.92% by more than 17 times the standard

deviation. This represents a statistically significant variation to the ratio which was expected to be constant. This variation is an indication of possible space charge accumulation as discussed in Section 2.6.4. In order to ensure space charge effects are mitigated, the current emitted from the cathode must be minimized. This behavior is discussed in greater detail in Chapter IV.

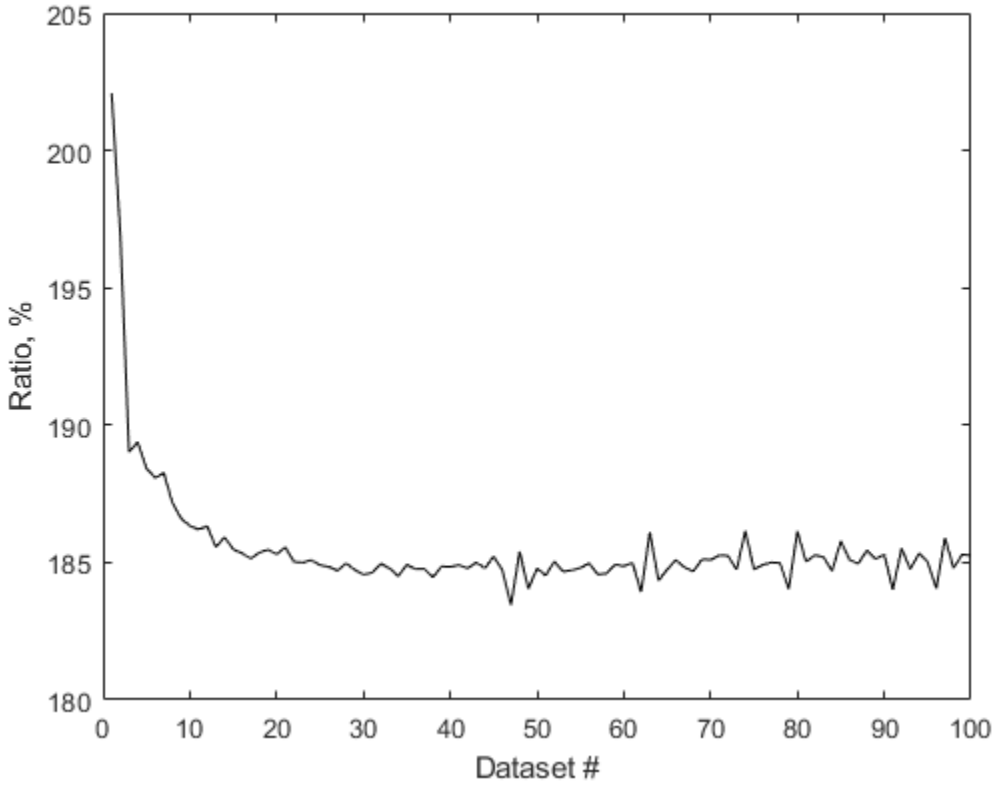


Figure 80: Comparison of ratios between $i_s$ for the cup in the open position and $i_F$ for the cup in the closed position.

The 6 minutes required to create each dataset was time prohibitive given the large number of measurements remaining to be performed in this research, so several experiments were performed in order to find a configuration that would reduce this time. The current leaving the electron gun was also reduced to approximately 12.8 pA to limit space charge effects. It was found that the datasets could be shortened to 2 minutes while

yielding a standard deviation comparable with the first datasets discussed. The ratios for 400, 2-minute datasets are shown in Figure 82 along with a histogram of the ratios. The mean of these ratios is 186.21%, and the standard deviation is 0.43% which the slightly smaller than 0.46% standard deviation of the first datasets.

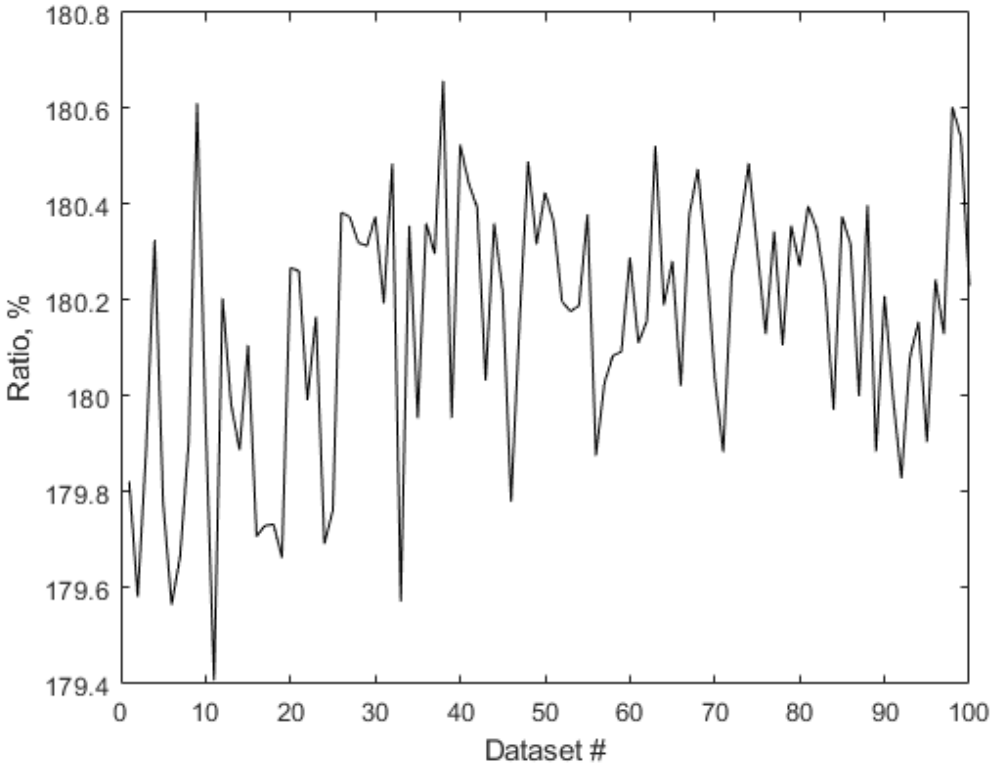


Figure 81: Ratios for 6-minute datasets acquired using ~106pA gun current with the gun on for 1.5 minutes in each dataset.

The timing sequence for the 2-minute datasets was altered from the initial timing sequence as shown in Figure 83. This timing sequence minimizes the dose of electrons the chamber receives in each dataset while allowing the system enough time to stabilize between each transient. For each dataset, the gun remains on for 36 seconds. Data was extracted from the regions marked in red in Figure 83. Measurements of the leakage currents are measured at the beginning and end of each dataset rather than only at the

beginning of a dataset. If the leakage current monotonically increases or decreases during a dataset, averaging the leakage current using data points at the beginning and end of the dataset provides a more accurate mean for the leakage current.

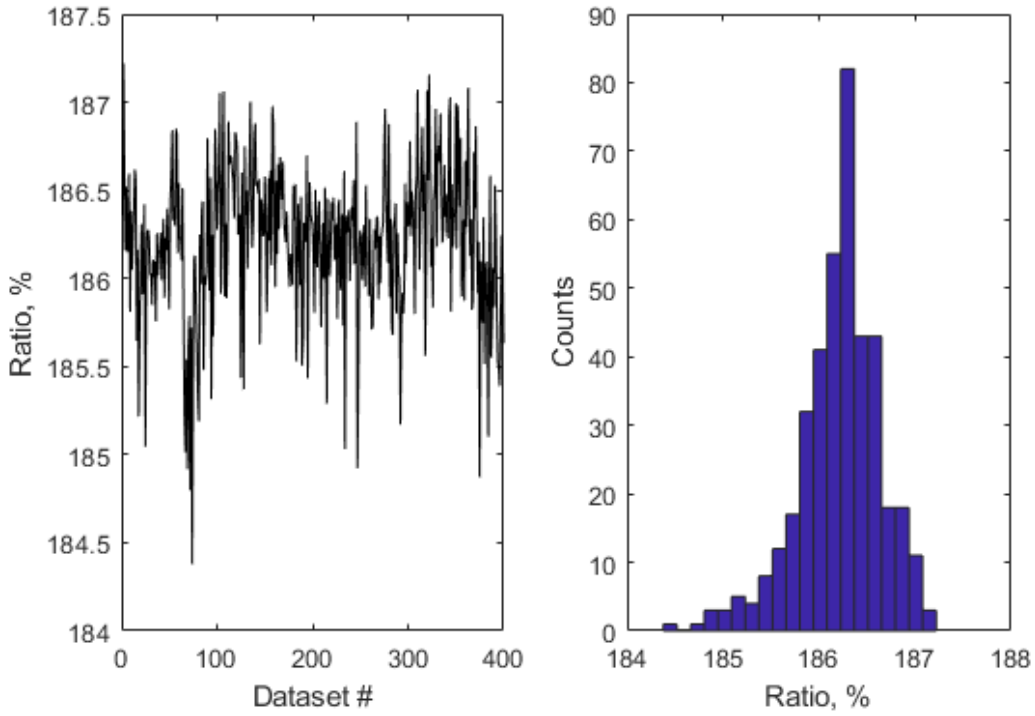


Figure 82: Ratios for 2-minute datasets acquired for a +200V sample bias.

Monotonic increases or decreases may be caused by not allowing enough time for the system to settle after changes in the sample or Faraday cup bias and as a result of exposing the chamber to electrons. Note that the first few samples of each dataset were ignored because they exhibited the transient behavior as shown in Figure 84. This transient behavior at the beginning of a dataset appeared often in the data collected throughout this research and was intentionally ignored when extracting data for calculation of the mean leakage currents. This behavior is a nuance associated with the measurement system.

For the previously discussed measurements, the sample was biased to +200 V. In order to determine if the timing sequence would yield a similar standard deviation for the

ratios when the sample was negatively biased, the measurements were again performed using the same timing sequence and electron gun settings with the sample biased to -195 V.

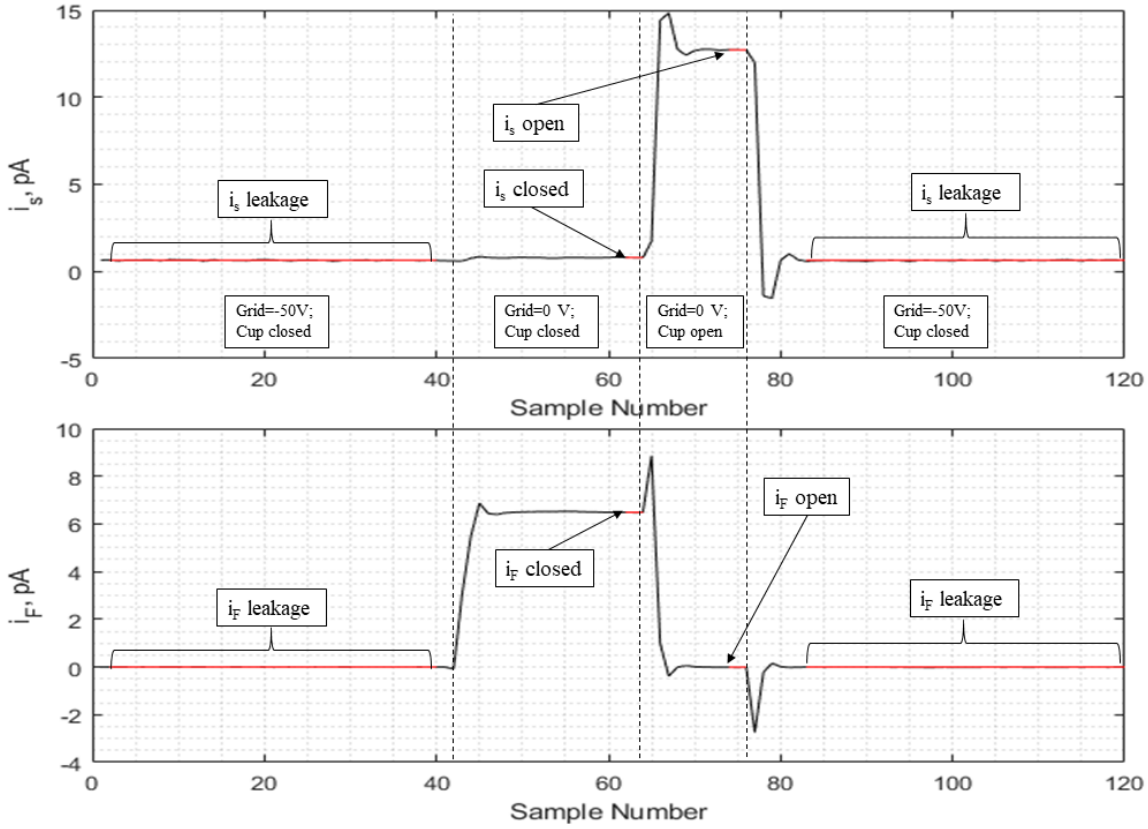


Figure 83: Current signals $i_s$ and $i_F$ generated using updated timing sequence.

When the sample is negatively biased, electrons are less confined to the sample than when the sample is positively biased. This allows more electrons to spread out into the chamber increasing the exposure of the chamber to electrons. The ratios for 500, 2-minute datasets are shown in Figure 85 along with a histogram of the ratios. The mean of these ratios is 1.47%, and the standard deviation is 0.46% which is nearly the same as the standard deviation measured when the sample was positively biased to +200 V.

The results of the 2-minute datasets for the sample biased to +200 V and -195 V did not show signs of the systematic shift discussed in Section 3.1.9, and the unexpected

transitions associated with burst noise were not observed in the sample or Faraday cup currents. Therefore, it was assumed that the 2-minute long timing sequence would also perform well for other electron gun settings and sample biases, and the timing sequence shown in Figure 83 was adopted for all the measurements discussed in Chapter IV, excepted where explicitly stated otherwise.

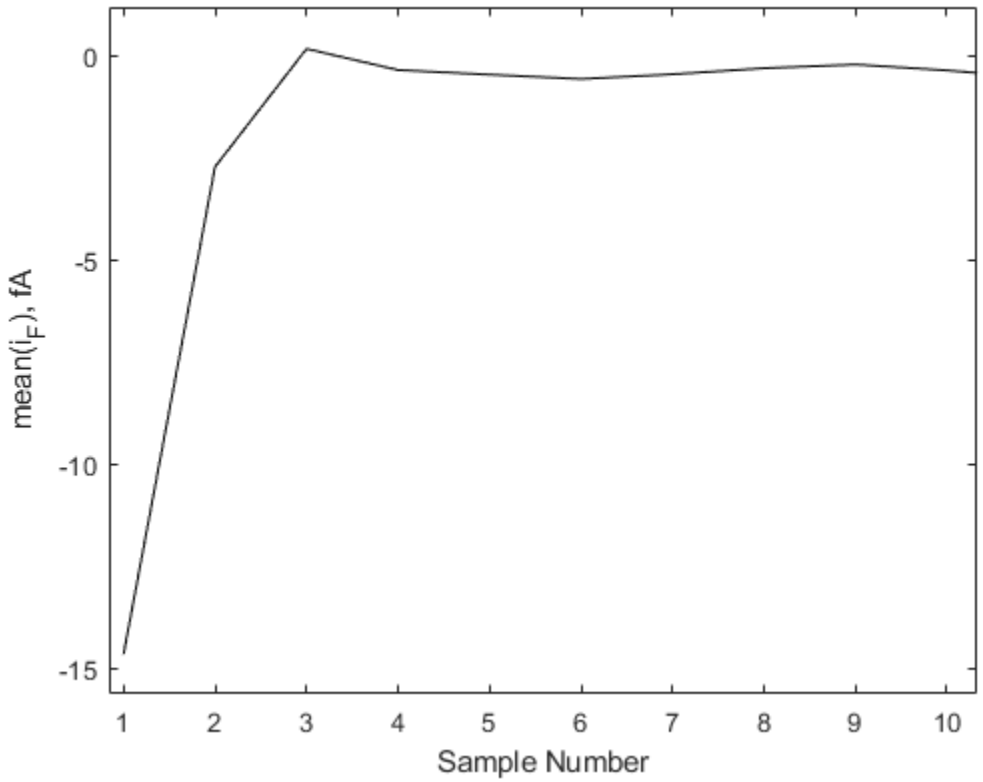


Figure 84: Plot of the average Faraday cup current, $i_{F,}$ of 374 datasets which shows the transient that appears during first 3 to 4 samples of every dataset.

As a final note, measurements were also performed with the sample biased to -195 V using the same timing scheme shown in Figure 83. However, the final phase of the timing scheme, when the grid is biased to -50 V and the cup is in the closed position, was extended by 3 minutes. This increased the recovery time between doses by three minutes. The system

was configured to perform measurements for 500 datasets; however, an error originating in the test equipment halted the measurements at the 374th dataset.

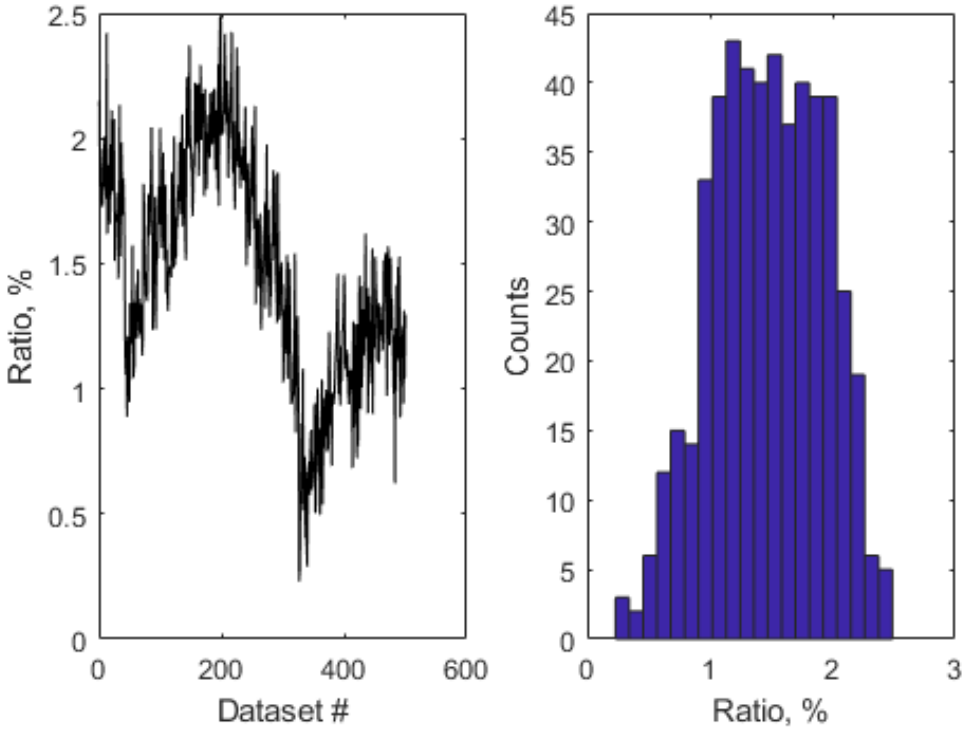

Figure 85: Ratios for 2-minute datasets acquired for a -195V sample bias.

The system was configured to perform measurements for 500 datasets; however, an error originating in the test equipment halted the measurements at the 374th dataset. The ratios from these datasets are shown in Figure 86. The mean of these ratios is 1.52%, and the standard deviation is 0.21%. This result indicates that it may be possible to further decrease the standard deviation of the ratios by increasing the recovery time albeit at the expense of longer acquisition times.

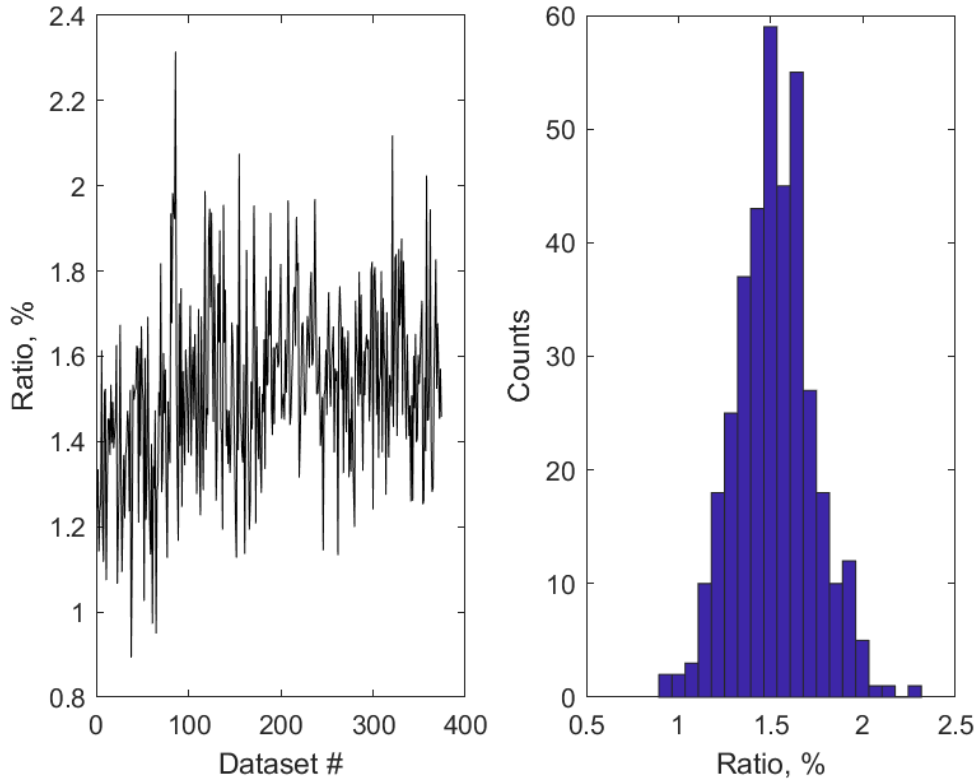

Figure 86: Ratios for 6-minute datasets acquired for a -195V sample bias.

### 3.1.15 Additional Data Collected During Each Dataset

The previous section focused on the currents which are measured by the system. However, 11 additional parameters are also measured during each dataset. These parameters were considered the inputs to an experiment. Whereas, the measured currents were considered the outputs of an experiment. The graph shown in Figure 87 contains these additional parameters and is representative of the graphs typically used for troubleshooting purposes during data analysis.

Seven of the parameters are associated with the electron gun: energy, source potential, grid potential, 1st anode potential, focus potential, emission current, and source current. As shown in Figure 88, the energy is the accelerating potential, $V_{EE}$, of the electron

gun multiplied by the charge of an electron. The source potential, $V_{ES}$, is the voltage across the heater for the cathode while the source current is the current through the heater.

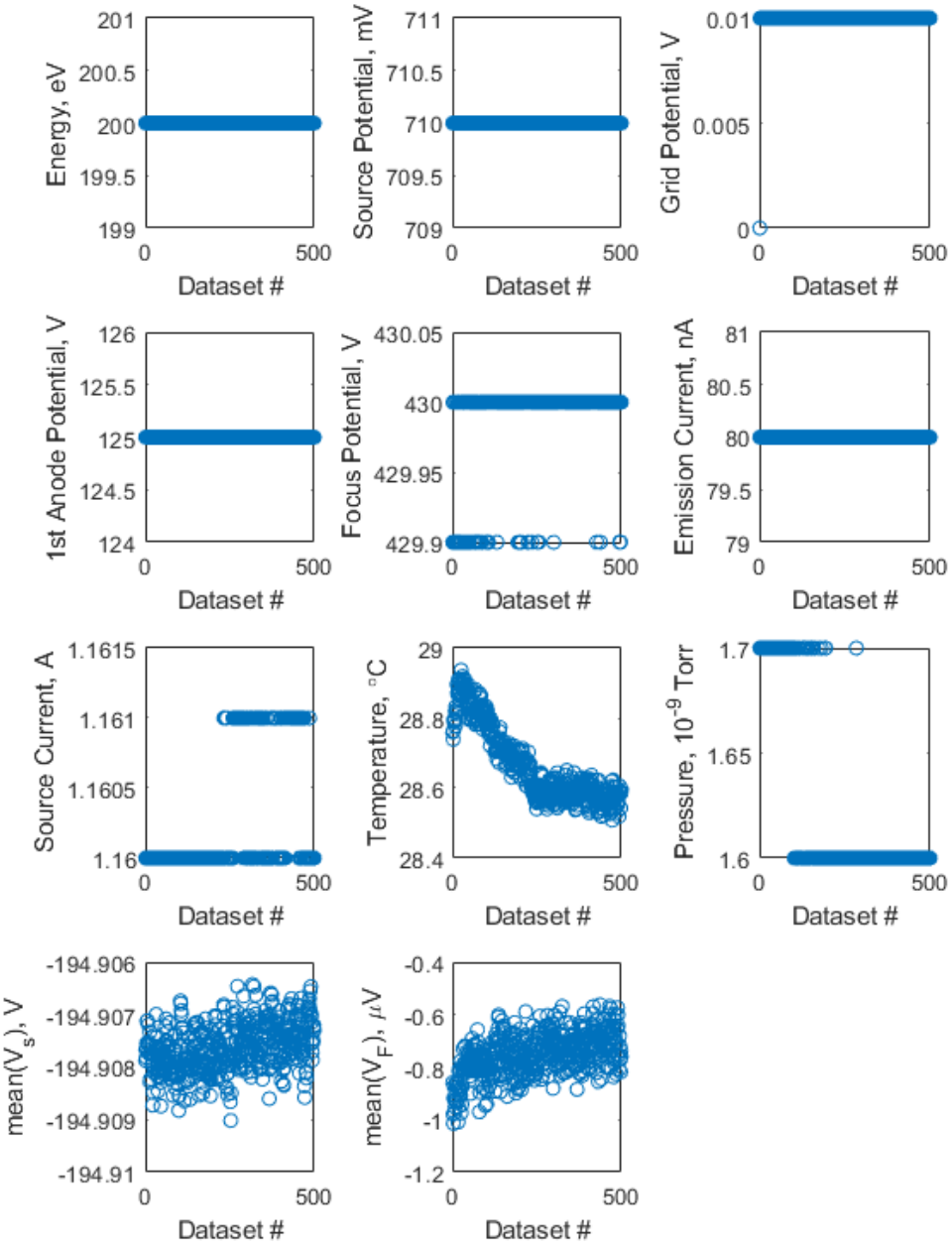


Figure 87: Graph containing plots of 11 additional parameters measured during each dataset.

For this research, the pulser and capacitive pulsing options are not used. The 1st anode potential, $V_{FA}$, and focus potential, $V_{FO}$, are measured with respect to the cathode. However, the grid is negatively biased with respect to the cathode by the grid potential, $V_{VG}$.

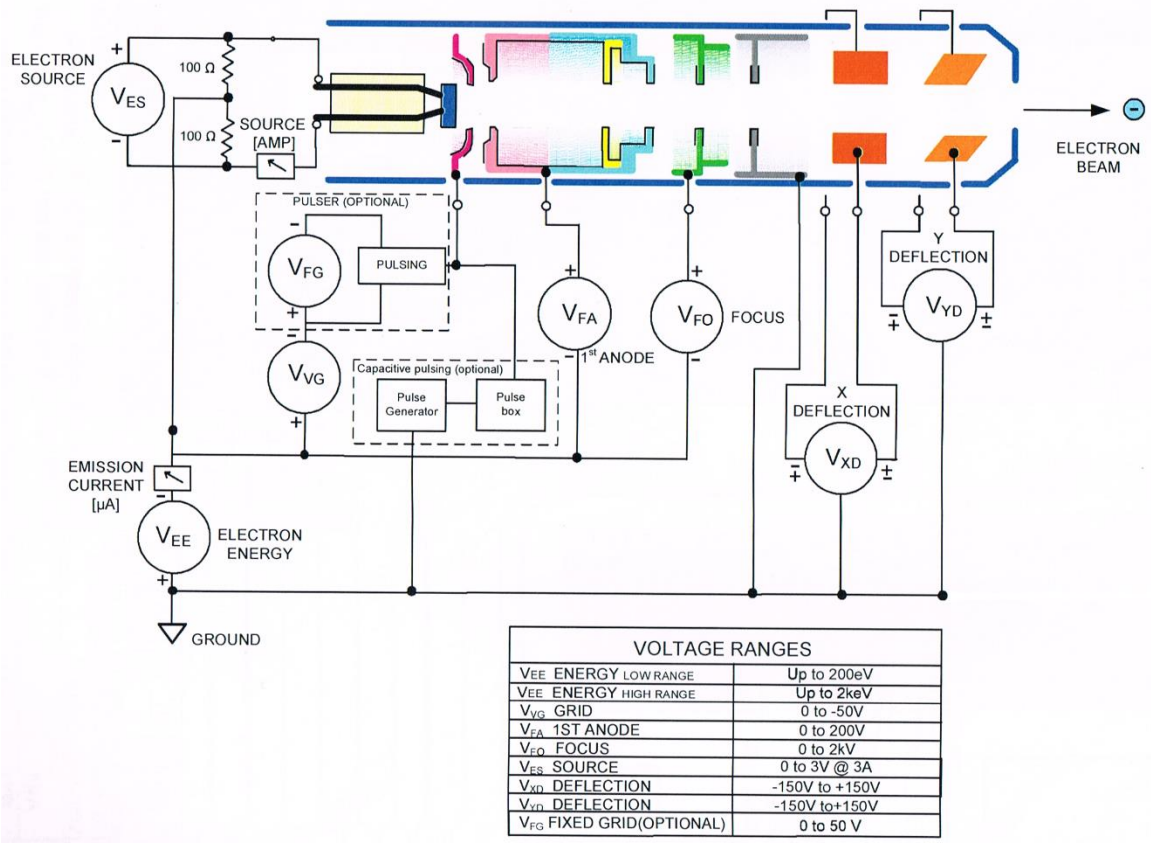


| VOLTAGE RANGES | |
|---|---|
| $V_{EE}$ ENERGY LOW RANGE | Up to 200eV |
| $V_{EE}$ ENERGY HIGH RANGE | Up to 2keV |
| $V_{VG}$ GRID | 0 to -50V |
| $V_{FA}$ 1ST ANODE | 0 to 200V |
| $V_{FO}$ FOCUS | 0 to 2kV |
| $V_{ES}$ SOURCE | 0 to 3V @ 3A |
| $V_{XD}$ DEFLECTION | -150V to +150V |
| $V_{YD}$ DEFLECTION | -150V to+150V |
| $V_{FG}$ FIXED GRID(OPTIONAL) | 0 to 50 V |

Figure 88: ELG-2A electron gun block diagram [136].

The emission current is the net electron current leaving the cathode, grid, 1st anode, and focus. This current is not useful when measurements are performed in the pA range and routinely registers a leakage current even when the cathode is not heated. According to the manufacturer of the electron gun, the expected error associated with these measurements is ±1 for the least significant digit recorded. These errors are listed in Table 4.

The temperature of the vacuum chamber is measured using a K Type thermocouple taped to the outside of the vacuum chamber. A National Instruments™ temperature input device (USB-TC01) is used to measure the voltage produced by the thermocouple and communicate the temperature to the laptop over USB. The manual for the temperature input device indicates that the error associated with temperature measurements is approximately ±1.1 °C when the device is operating at room temperature and approximately ±2.5 °C over the full operating temperature range [138]. This device routinely measured a higher temperature than the room temperature measured by other thermometers.

Table 4: Error associated with e-gun parameters.

| Measured parameter | Associated error |
|---|---|
| $V_{EE}$ (for low energy range) | ±0.01 V |
| $V_{EE}$ (for high energy range) | ±0.1 V |
| $V_{VG}$ | ±0.01 V |
| $V_{FA}$ | ±0.1 V |
| $V_{FO}$ | ±0.1 V |
| $V_{ES}$ | ±0.001 V |
| Source Current | ±0.001 A |
| Emission Current | ±0.01 μA |

The pressure of the load lock chamber and main chamber are measured using a Kurt J. Lesker® IG6600 dual ionization gauge controller and two G100F ion gauges. The pressures are measured in Torr and are recorded in scientific notation with two significant digits. The error associated with these measurements is not listed and is assumed to be ±1 for the least significant digit recorded [139].

The aforementioned parameters are measured once per dataset after the electron gun stabilizes following being turned on by adjusting the grid potential. The mean sample

voltage and mean Faraday cup voltage however are calculated from voltage measurements taken over the same period as the current measurements and synchronized with the current measurements. The voltage measurements occasionally show transient behavior in the first few samples of each dataset. Like the current measurements, this is a nuance of the measurement system, and these samples are ignored when calculating the mean voltage. Appendix C provides details on the file formats used to store the measured data.

### 3.1.16 Complete Circuit Model

Based on the electrical characteristics of the measurement circuit and the results of the dose and recovery study, the circuit model shown in Figure 89 was created to capture all the transient effects that had been observed in experimentation and provide an additional explanation for the systematic shift discussed previously.

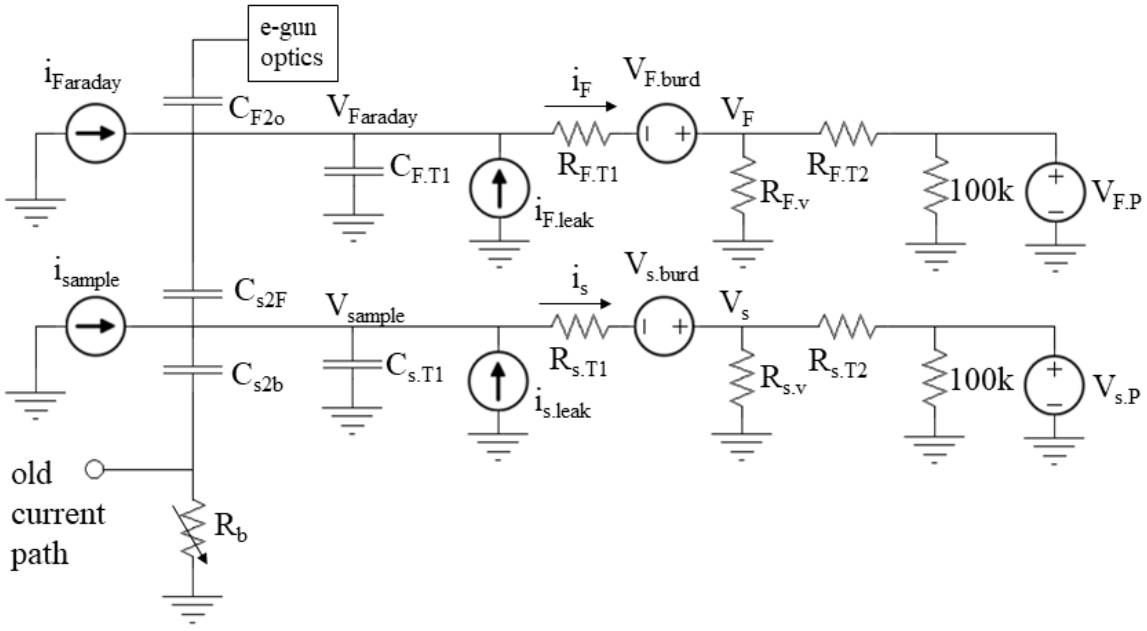


Figure 89: Model of complete electrical circuit. The conventional current standard is not followed.

$i_{Faraday}$ is the current through the Faraday cup, and $i_{sample}$ is the current through the sample puck. $R_b$ is the leakage resistance of the dielectric ball bearings. $C_{s2b}$ represents the capacitive coupling between upper and lower halves of the modified sample puck. $C_{s2F}$ represents the capacitive coupling between the sample puck and Faraday cup. $C_{F2o}$ represents the capacitive coupling between the Faraday cup and electron gun optics. $C_{F.T1}$ and $R_{F.T1}$ are respectively the capacitance and resistance of the transmission lines between the voltmeter in the Faraday cup circuit and Faraday cup. $C_{s.T1}$ and $R_{s.T1}$ are respectively the capacitance and resistance of the transmission lines between the voltmeter in the sample circuit and sample puck. $C_{F.T1}$, $R_{F.T1}$, $C_{s.T1}$, and $R_{s.T1}$ are used to model the long settling time of the circuit, which was discussed in a previous section. $i_F$ and $i_s$ are the currents measured by the electrometers in the Faraday cup and sample circuits, respectively. $R_{F.T2}$ and $R_{s.T2}$ are the resistances of the transmission lines between the power supplies and voltmeters in the Faraday cup and sample circuits, respectively. $V_{F.P}$ and $V_{s.P}$ are the voltages of the power supplies in the Faraday cup and sample circuit, respectively. $V_F$ and $V_s$ are the voltages measured by the voltmeters with respect to ground, and $R_{F.v}$ and $R_{s.v}$ are the input impedances of the voltmeters. $V_{Faraday}$ and $V_{sample}$ are the voltages of the Faraday cup and sample puck with respect to ground.

In Figure 89, $V_{F.burd}$ and $V_{s.burd}$ are the input voltage burdens of the electrometers. The voltage burden varies depending on the range the electrometer is operating in and the amount of current flowing through the electrometer [140]. When operating in the 20-pA, 2-nA, 20-nA, 2μA, and 20μA ranges, the burden is within ±20 μV. When operating in the 200-pA, 200-nA, and 200-μA ranges, the burden is within ±100 μV. Throughout this

document, $V_s$ and $V_F$ are considered the sample voltage and Faraday cup voltage respectively since they differ by less than 100 μV in most cases.

In the figure, $i_{s.leak}$ and $i_{F.leak}$ are the leakage currents that were measured and subtracted before calculating the ratios in Section 3.1.14. They have been referred to as leakage currents. However, in addition to leakage currents, these currents are also the result of the input bias current of the electrometers, which is discussed in the electrometer instruction manual and low level measurements handbook [135, 140]. The specifications for the electrometers indicate that the magnitude of the input bias current is less than 3 fA when operating at room temperature.

The capacitors $C_{F.T1}$ and $C_{s.T1}$ are not only responsible for long setting times but are also likely responsible for the systematic shift discussed previously. The currents $i_F$ and $i_s$ are dependent on the charged state of these capacitors in addition the currents $i_{Faraday}$ and $i_{sample}$. When $i_{Faraday}$ and $i_{sample}$ equal zero and the circuit has stabilized, $V_{sample} \approx V_s$, and $V_{Faraday} \approx V_F$. When $i_{Faraday}$ and $i_{sample}$ are nonzero and the circuit has stabilized, $V_{sample} \approx V_s - i_s R_{s.T1}$, and $V_{Faraday} \approx V_F - i_F R_{F.T1}$. Increasing $i_{Faraday}$ and $i_{sample}$ increases the voltage different between the two stable states. This also causes a larger difference in the amount of charge stored in the capacitors between the two states. The systematic shift was likely due to these capacitors charging and discharging as $i_{Faraday}$ and $i_{sample}$ were repeatedly altered with each transition of the Faraday cup. By reducing the currents $i_{Faraday}$ and $i_{sample}$ and using small doses with long recovery times, the voltages across the capacitors remain near $V_{Faraday} \approx V_F$ and $V_{sample} \approx V_s$ across multiple datasets leading to a reduction in the amount of shift observed in the data.

In addition to $V_{sample}$ and $V_{Faraday}$ varying when the currents $i_{Faraday}$ and $i_{sample}$ are altered, $V_s$ and $V_F$ also vary. Figure 90 shows $V_s$ varying as the current $i_s$ is intermittently disrupted by moving the Faraday cup between the opened and closed position. For this experiment, the sample power supply was disconnected, and the circuit was grounded. This is equivalent to setting $V_{s.P}$ to zero in the circuit above. The measured current, $i_s$, varied between 0 nA for the cup in the closed position and -26 nA for the cup in the open position. This figure demonstrates that the resistance of the transmission lines can produce measurable voltage drops across the transmission lines when current is flowing. This resistance is often considered negligible in literature; however, given the low noise associated with the equipment, the voltage drops across the transmission lines can produce an appreciable effect on measurements when $i_s$ and $i_F$ are greater than 1 nA.

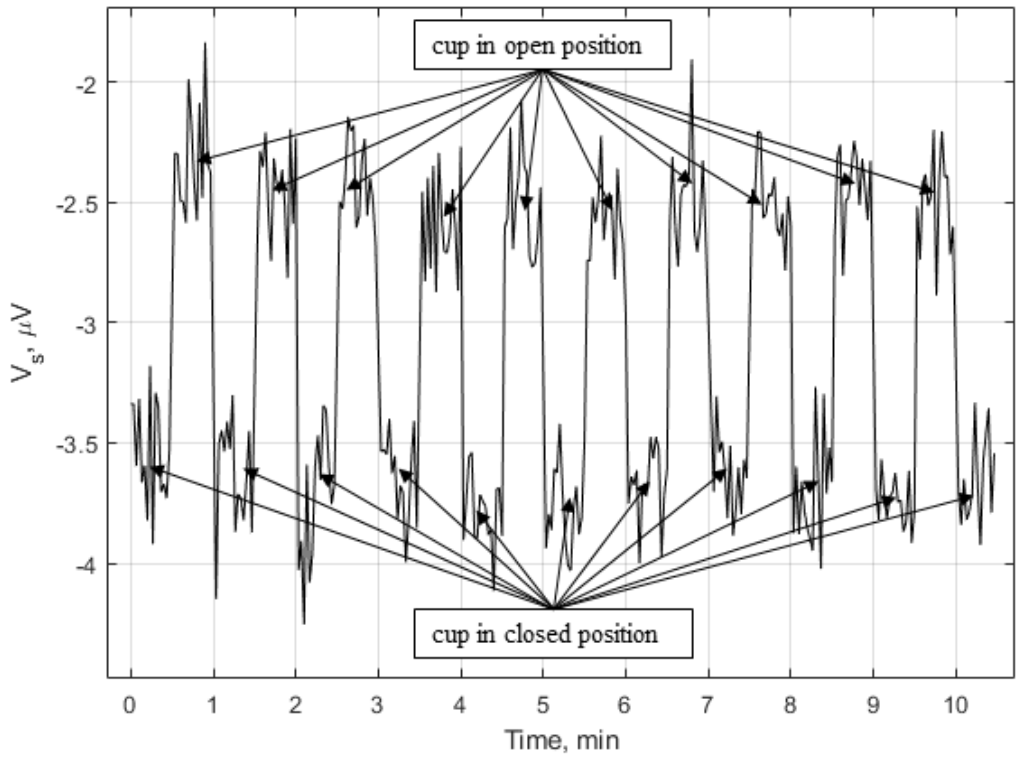


Figure 90: Fluctuations in $V_s$ due to voltage drop across $R_{s.T2}$.

## 3.2 Development of Simulation Model

In the initially purposed research, all simulations were to be performed using the VSim® software by the Tech-X corporation. However, due to computational hardware limitations and research constraints, simulations were instead performed using the SIMION® simulator by Scientific Instrument Services, Inc. Unlike VSim®, SIMION® does not provide a model for secondary electron emission nor the capability to simulate a heavily space charged environment [141]. This limited the scope of this research while still providing valuable insight into the trajectories of the primary electron during SEE experiments. The following two sections will discuss the progress and problems faced during modelling using both VSim® and SIMION®. The later sections describe how this model was calibrated based on experimental measurements.

### 3.2.1 VSim®

VSim® has the capability to create 3D CAD models using its VSimComposer interface or import existing 3D models using geometry files, such as STL files. For this research, a 3D model of the electron gun and sample puck were created using VSimComposer due to author's familiarity with VSimComposer and ease with which the geometry could be altered between simulations. Parts of the electron gun, such as the optics, are created by combining basic geometries (e.g. cylinders, spheres, and cones) using Boolean operations. The first problem faced during the construction of the model was that the parts created using Boolean operations would split back into basic geometries upon closing and reopening the simulation files. In the first attempt to create a model of the electron gun, the names that were automatically assigned to the basic geometries, constants,

and parameters were not overwritten. However, it was observed that these names would be altered when closing and reopening the simulation files, and this may have caused the splitting problem. In the second attempt to create a model of the electron gun, the automatically assigned names were manually overwritten. This appeared to fix the splitting issue. However, it was later observed that the sample puck would split apart when attempting to move its location by adjusting a numerical constant that defines its location along the z-axis of the simulation space. In order to reassemble the sample puck, the corrupted sample puck geometry had to be first deleted. Then, the simulation had to be closed and then reopened, which updated the location of all the geometries which made up the sample puck. Finally, the sample puck was recreated by combining the geometries.

The final model created in VSim® is shown in Figure 91. This research focused on the electron beam's interaction with the sample, so the Faraday cup was only modeled in the open position. The Faraday cup is connected to a wire that contains a coiled section as previously shown in Figure 64. However, in the VSim® model, this wire is approximated using a straight wire due to the complexity associated with creating the coiled section. Furthermore, the exact dimensions of the coiled section are unknown, and it could not be measured while in the UHV chamber. The model contains dielectric materials. However, these had to be removed when using the electrostatic field solver. In addition to the dielectrics identified in Figure 91, additional dielectrics are present within the electron gun. These dielectrics were included in the simulation to absorb any electrons that made contact with the dielectrics removing them from the simulation. The internal features of the Faraday cup were not included in the model because they have a negligible effect on the

electrostatic field in the region through which the electron beam travels when the cup is in the open position.

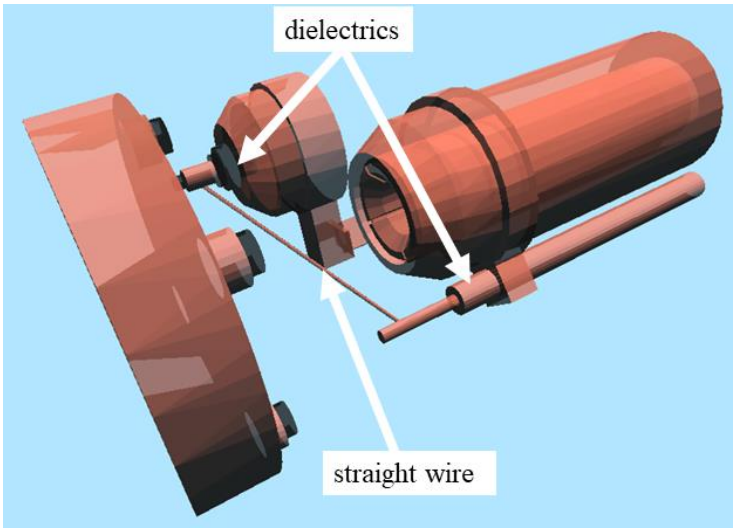


Figure 91: Final VSim® model of electron gun and sample puck.

The location of the sample puck with respect end of the gun barrel was measured using a laser level, painter's tape, and a Vernier caliper as shown in Figure 92. The surface of the sample puck which faces the electron gun is 45.37 mm from the end of the gun barrel when the sample manipulator's Y-axis micrometer is set to zero. The maximum error associated with this measurement is estimated to be ± 1 mm, which was approximately the width of the laser beam. Increasing the Y-axis micrometer brings the sample puck closer to the electron gun.

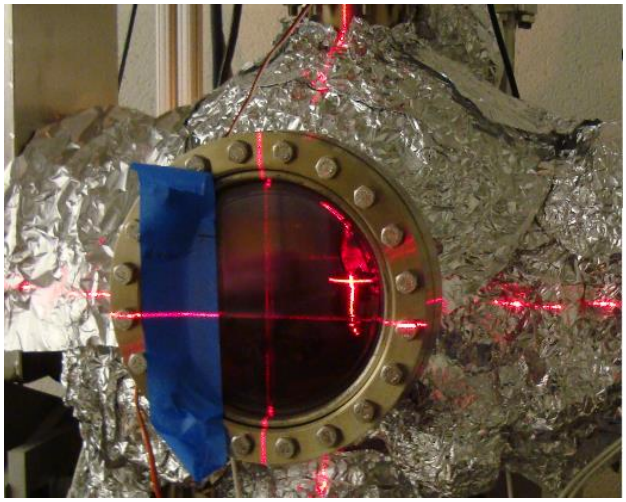

Figure 92: Measurement of sample puck location.

With the model completed, the electrostatic field within and around the electron gun was solved using electrostatic field solver of VSim® for a set of electrode potentials that had been used during experimentation. Figure 93 shows the resulting electric field potential.

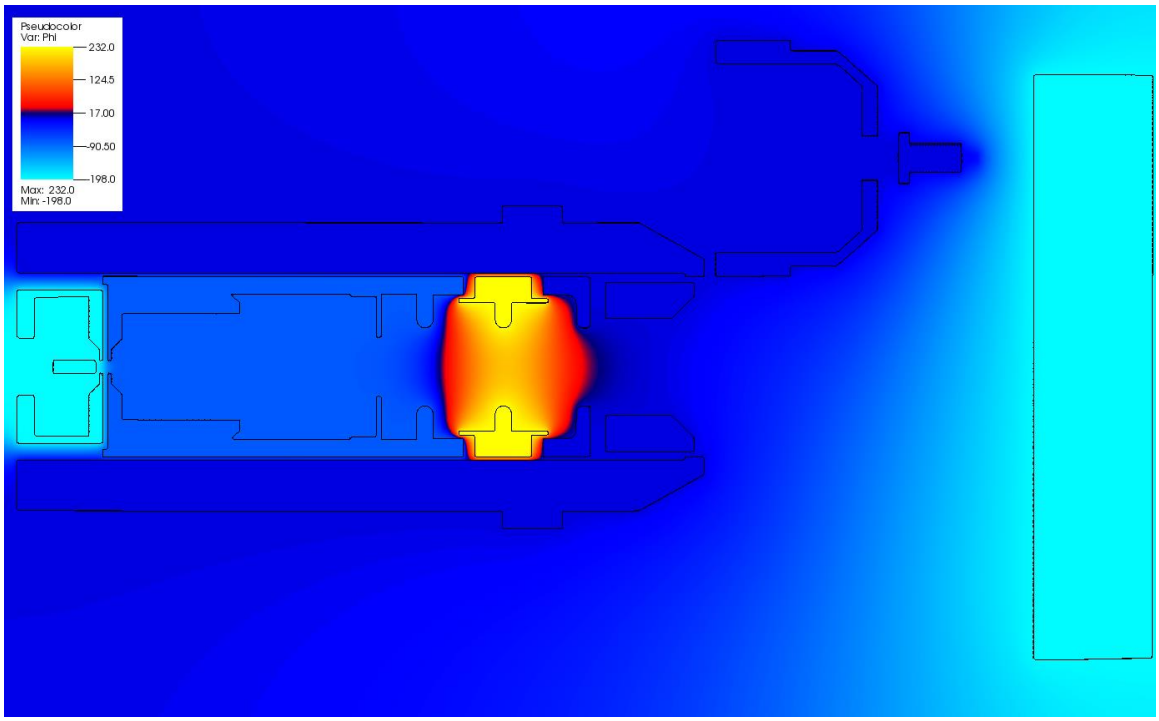


Figure 93: Colormap of electric field potential generated using VSim®. Units are in volts.

A second problem however arose when attempting to import the electrostatic field into a simulation which caused the simulation to abort. Upon solving the electrostatic fields, VSim® creates an HDF file containing the electric field intensity at each grid point. This HDF file can be imported into a particle simulation, and the force on each particle is then calculated using this field. After spending several weeks on this problem, the software developer indicated that the problem arises when VSim® attempts to extrapolate the electrostatic field to the surface of a part. This extrapolation is performed across a few grid cells. If the part occupies less space than these grid cells, an error will occur, and the simulation will abort. In order to fix this problem, the part which occupies less space than these grid cells must be removed, or the size of the grid cells decreased. It was found that nearly all of the parts making up the model had to be removed in order for the simulator to successfully operate. Since electrons may interact with all of the parts in the simulation, it is not feasible to remove any of the parts. Therefore, the only option is to decrease the size of the grid cells. Unfortunately, decreasing the grid size requires more than the 64 GB of RAM currently available on the desktop licensed to run VSim®. Due to budget and time constraints, the RAM on this desktop could not be increased during this research. Additionally, there was the risk that the VSim® simulation might continue to fail even after the grid cells were decreased resulting in further loss of research time. Thus, the research effort shifted to developing a SIMION® model since SIMION® was readily available and Sattler was previously successful in using the software to perform simulations of the electron gun used in this research [4].

### 3.2.2 SIMION®

Shortly after the problem with importing electrostatic fields in VSim® was discovered, a large effort was undertaken to both learn how to use SIMION® and create a new model of the electron gun and sample puck. The manufacturer had previously provided Sattler with a 2D cylindrical model of the electron gun [4]. A cross-sectional view of the original model is shown in 3D in Figure 94.

The original model was overly simplified and unable to predict many of the experimental observations.

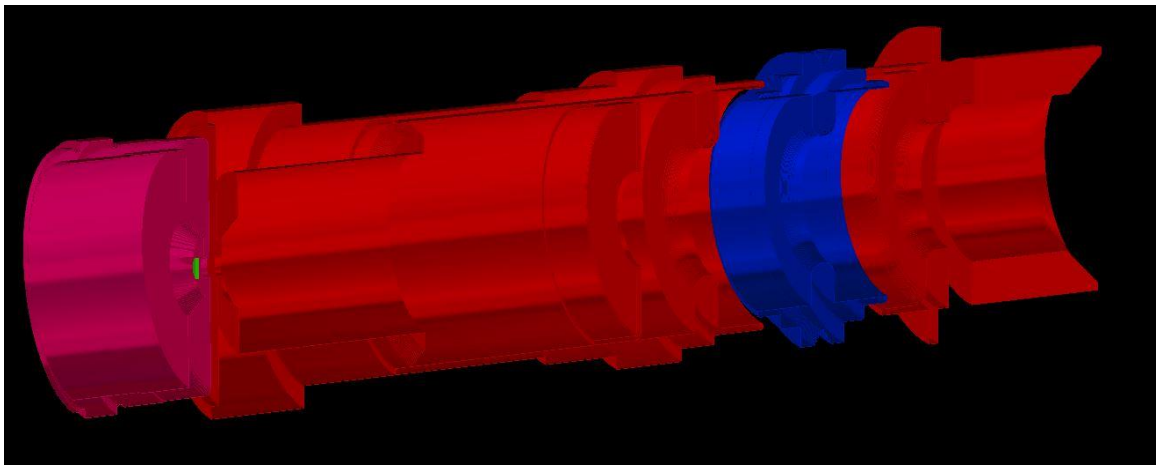

Figure 94: Original SIMION® model provided by manufacturer.

Firstly, the sample puck does not appear in this model, so it is not possible to account for the nonzero electric field between the electron gun and sample puck. Secondly, Earth's magnetic field, though small, does become significant at low primary electron energies and is not accounted for in this model. Thirdly, experimental observations proved that biasing the Faraday cup has a significant effect on the trajectories of electrons as they leave the electron gun. Since the Faraday cup does not appear in the model, the effect of the cup on electron trajectories cannot be predicted. Finally, this model assumes all the electrons leave the cathode within the same plane and with the same velocity vector as shown in Figure

95. This model is inappropriate when considering the asymmetries in the magnetic and electric fields. Earth's magnetic is not cylindrically symmetric about the axis of the electron gun, and electric field is not cylindrically symmetric because the electron gun with attached Faraday cup and sample puck are not cylindrically symmetric. Furthermore, given the low primary electron energies involved in this research, the assumption that all the electrons leave the cathode in the same direction with same velocity will lead to significant errors in the prediction of the trajectories and energy distribution of the primary electrons.

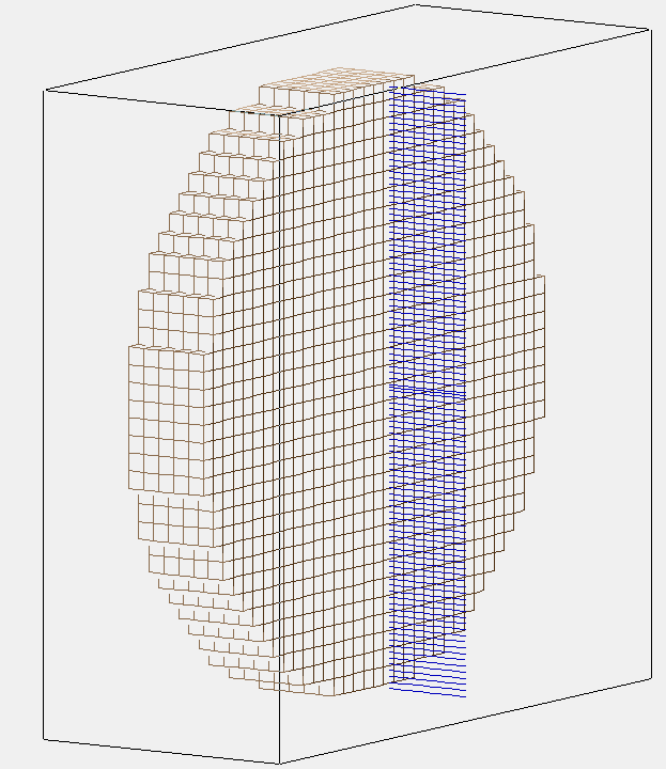

Figure 95: Original emission distribution of electrons from the circular cathode. The electron trajectories are shown as blue lines oriented normal to cathode surface.

In order to partially account for the shortcomings of the original model, this model was first updated to include the sample puck and gun barrel as shown in Figure 96. This provided the means to calculate the electrostatic field between the gun and sample puck.

Next, Earth's magnetic field was added to the simulation by creating an empty basic potential array (PA) of magnetic type along with a user program in the SIMION® workbench. This procedure followed the instructions provided in the online SIMION® 2019 supplemental documentation [142]. Though this 2D cylindrical model provided valuable SIMION® experience, it was later discovered that a more accurate 3D SIMION® model could be easily created using the model previously developed in VSim®.

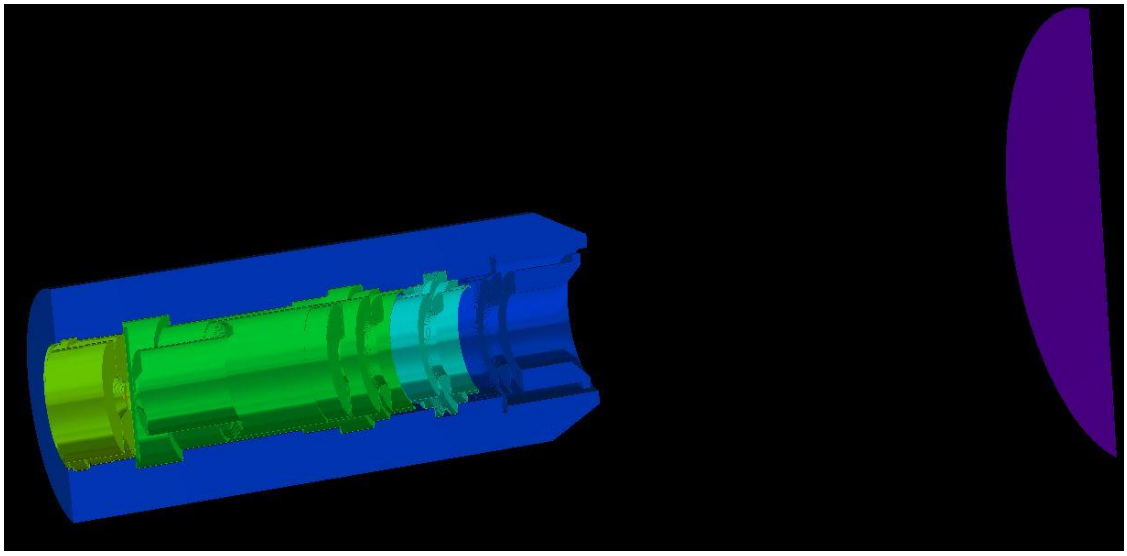

Figure 96: Cross-sectional view of updated electron gun model with a purple disk acting as the sample puck.

Whenever a part is assigned a material in VSim®, VSim® creates a STL file for the part within the same directory as the simulation files. The STL files for each part can be imported into SIMION® by using the SIMION SL™ Tools and individually numbering the STL files as described in the online SL Tools tutorial [143]. This allowed the model which was developed in VSim® to be easily converted into a SIMION® model. SIMION® uses a basic PA to define the geometry of each electrode making up the model [141]. These electrodes are numbered based on the number appended to the end of the STL filename. Simulating the sample puck at different distance from the electron gun required separate

basic PAs. These PAs were created for the sample puck at several distances from the electron gun by generating separate STL files for the sample puck at different distance using VSim®. Earth's magnetic field was again added to the simulation using an empty basic PA of magnetic type following the instructions provided in the SIMION® 2019 supplemental documentation [142]. The PAs are able to account for the effects of the sample puck, Faraday cup, and Earth's magnetic field. Dielectric materials were not included in this model because of their negligible effect on the electric field in the region the primary electron beam traverses.

### 3.2.3 Calibration of Magnetic Field

The magnetic field in the SIMION® model is homogeneous vector field which is defined in cartesian coordinates based on the reference frame of the magnetic PA. In order to properly assign the appropriate vector components to the magnetic field, the magnetic field within the vacuum chamber had to first estimated. Ideally, the magnetic field within chamber should be measured directly; however, the experimental system does not provide the capability to do so. Instead, the magnetic field was measured external to the chamber, and it was assumed that there is a negligible difference between the magnetic field internal and external to the chamber.

For comparison, the magnetic field was both calculated using the World Magnetic Model (WMM) and measured using a magnetometer. The magnetic field was calculated by first determining the location of the experimental system using Google Earth and then entering the location information in the online magnetic field calculator provided by the National Oceanic and Atmospheric Administration [144]. The calculated magnetic field

information is shown in Table 5. Measurements of the magnetic field in the area surrounding the chamber varied greatly due to presence of ferrous materials. In order to avoid distortions in Earth's magnetic field, measurements were performed near the vacuum chamber and a few feet away from any ferrous materials, and the results are shown in Table 5.

Table 5: Measured and calculated magnetic field at experimental system location.

| | North Component | West Component | Vertical Component |
|---|---|---|---|
| Calculated | 20.1794 μT | 2.2125 μT | -48.2119 μT (downward) |
| Measured | 28.0522 μT | 5.10211 μT | -34.6884 μT (downward) |

The measured results agree reasonably well with the WMM. Since Earth's magnetic field is distorted within the lab due to the presence of ferrous materials, the results obtained by measurement were considered more accurate because the WMM is unable to account for these distortions. Therefore, the measured results were entered as the magnetic field components of the model after the appropriate translation into reference frame of the magnetic PA. The effect of this magnetic field on the electron trajectories is significant for low energy primary electrons as shown in Figure 97 and is discussed in greater detail in Chapter IV.

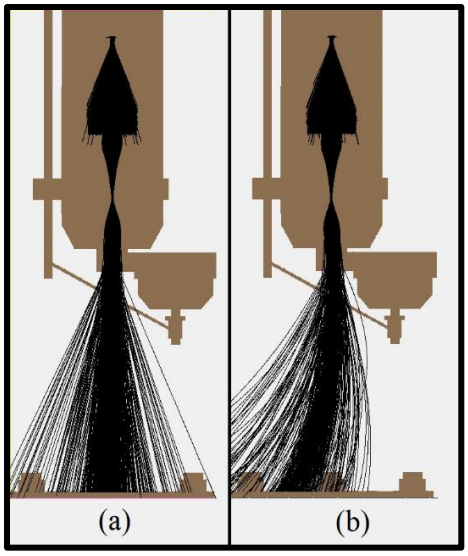

Figure 97: Comparison of low-energy primary electron trajectories (shown in black) with the magnetic field disable (a) and enabled (b).

### 3.2.4 Calibration of Thermionic Emission Distribution

The one of the most challenging tasks in the creation of the simulation model was the calibration of the thermionic emission energy distribution. Normally, the energy distribution can be calculated if both the work function and temperature of the cathode are known [145, 146]. The electron gun has a tantalum cathode, and work function for tantalum is 4.22 eV [146, 147]. However, the experimental system does not have a means to measure the temperature of the cathode directly. A second approach is to determine the current density of the electrons leaving the cathode and use this density to solve for the temperature using the work function of the cathode [145, 146]. Unfortunately, the experimental system is unable to measure the current leaving the cathode and is only able to measure the current leaving the electron gun. These currents differ because many of the electrons emitted by the cathode are absorbed within the electron gun. Thus, a new method for calibrating the energy distribution was required.

The energy distribution can be estimated in a similar fashion to using a retarding electric field to determine the energy distribution of the secondary electrons, which was discussed in Section 2.3.1. In this case, a negative bias is applied to the sample to retard the primary electrons from reaching the sample. This method is complicated by the fact that the sample may reflect some of the primary electrons rather than absorbing all the electrons. Furthermore, this approach assumes that the energy distribution of electrons emitted from the cathode only shifts in energy while the shape of the distribution curve remains constant as the electrons pass from the cathode to the sample. Based on simulation results, this assumptions in approximately valid and discussed more detail in Section 4.4.

The fundamentals of this estimation procedure are best explain using the energy band diagram shown in Figure 98. An electron is emitted from the cathode after first overcoming the work function of tantalum, $\Phi_{Ta}$, with a kinetic energy, $E_c$. It is then accelerated by the accelerating potential, $V_{EE}$, of the electron gun (see Section 3.1.15). The total kinetic energy gained during this acceleration is also dependent on the work function, $\Phi_{316SS}$, of the opening of the 316SS electron gun barrel. The gun barrel is held at ground potential. After passing through the opening, the electron is slowed by the retarding electric field created by biasing the sample by $V_{sample}$ (see Section 3.1.16). The sample for this measurement is the 316SS sample puck that was discussed previously, and the work function of the gold-plated fasteners is ignored in this analysis. The electrons arrive at the sample with the kinetic energy, $E_p$.

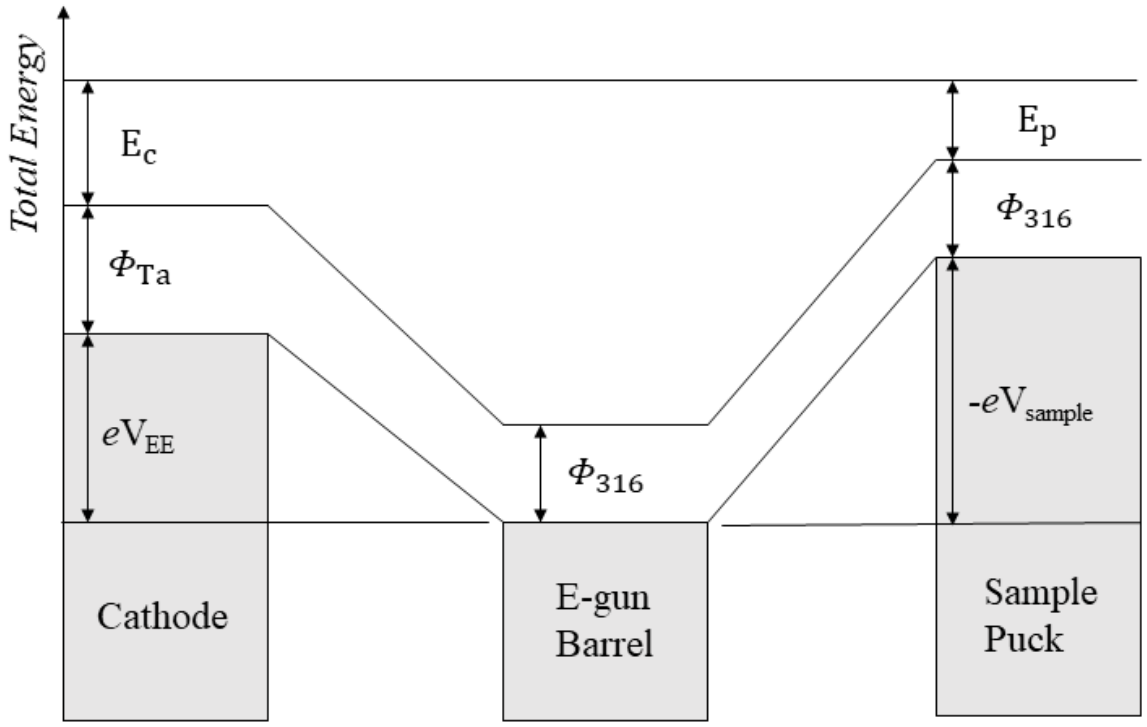

Figure 98: Energy band diagram of experiment setup for measuring the energy distribution of the electrons emitted from the cathode. *e* is the charge of an electron.

In order for electrons to reach the sample, their $E_c$ must exceed $\Phi_{316SS} - \Phi_{Ta} - eV_{EE} - eV_{sample}$. Since these energies are distributed, the number of electrons capable of reaching the sample is reduced as $V_{sample}$ becomes more negatively bias. This distribution has sometimes been approximated using a Gaussian distribution [7]. However, it better approximated with chi-squared distribution, which has the same form as a Maxwell-Boltzmann or Maxwellian energy distribution [146]. For this research, the energy distribution will be defined using the chi-squared distribution as defined in the following equation.

$$f(E_c) = \frac{1}{\alpha}\sqrt{\frac{E_C}{2\pi\alpha}}e^{-\frac{E_c}{2\alpha}} \tag{12}$$

The scaling factor, α, is used to adjust the distribution based on experimental measurements. This corresponds to the Maxwell-Boltzmann energy distribution with *k*T replaced by 2α [16]. The Figure 99 shows the form of the of the distribution. The maximum of this distribution is located at $E_c = \alpha$.

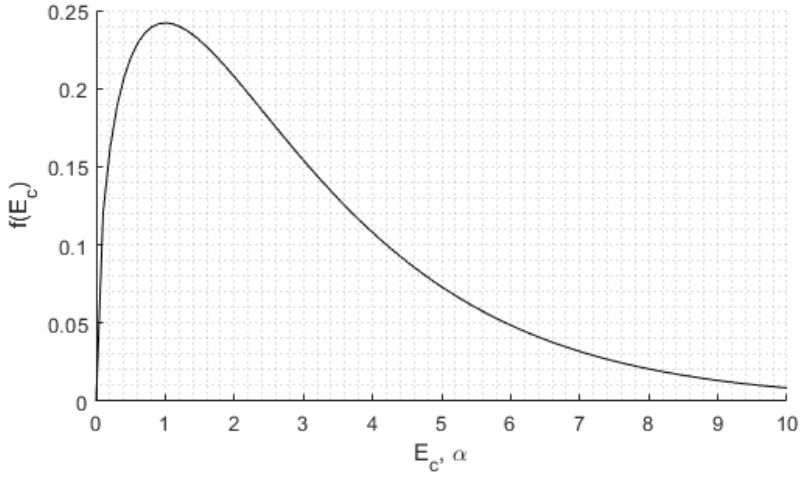


Figure 99: Chi-squared distribution for approximating the thermionic emission energy distribution.

Figure 100 shows the current through the sample, $i_{sample}$, as the accelerating potential, $V_{EE}$, was increased. For these measurements, the $V_{sample}$ maintained at -1.14 V. The low sample bias was chosen to reduce the effects of the asymmetric electric field created by the Faraday, which is discussed in a later section. An alternative approach to this measurement is to maintain the accelerating potential and increase the sample bias; however, this requires more time to perform since altering the sample bias requires waiting for the sample circuit to settle as discussed in Section 3.1.12. The focus potential, $V_{FO,}$ was adjusted to maximize $i_{sample}$ at $V_{EE}$ = 1.10 V. The 1$^{st}$ anode potential, $V_{FA}$, was 10.0 V. The source potential, which dictates the temperature of the cathode, was 710 mV. A 10$^{th}$ order polynomial was fit to the data, and the derivative of the polynomial was used to locate the point where the $i_{sample}$ is increasing most rapidly marked by dashed lines in Figure 100.

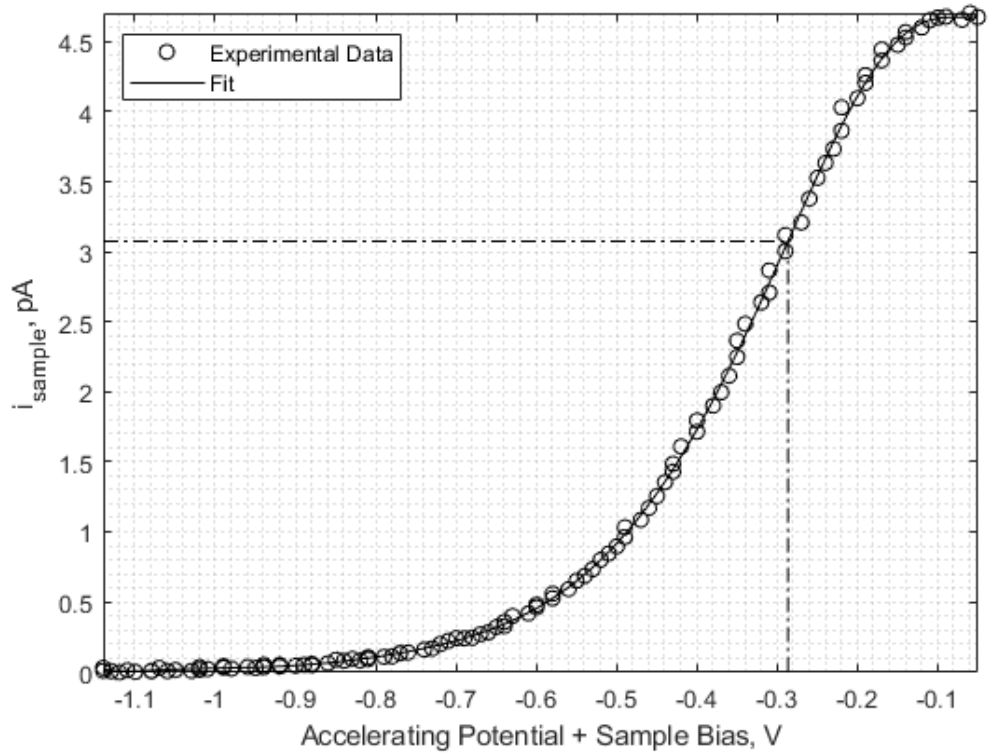


Figure 100: Sample current measured while varying the accelerating potential and maintaining a -1.14V sample bias. The dashed lines mark the location of maximum slope.

The $i_{sample}$ is equal to the primary current, $i_{pri}$, minus the secondary electron current, $i_{sec}$. Thus, the slope is dependent on both $i_{pri}$ and $i_{sec}$ as defined by the following equation.

$$\text{slope} = \frac{d\mathrm{i}_{\mathrm{sample}}}{d(\mathrm{V}_{\mathrm{EE}} + \mathrm{V}_{\mathrm{sample}})} = \frac{d\mathrm{i}_{\mathrm{pri}}}{d(\mathrm{V}_{\mathrm{EE}} + \mathrm{V}_{\mathrm{sample}})} - \frac{d\mathrm{i}_{\mathrm{sec}}}{d(\mathrm{V}_{\mathrm{EE}} + \mathrm{V}_{\mathrm{sample}})} \qquad (13)$$

Since more electrons are able to make it to the sample as $\mathrm{V}_{\mathrm{EE}} + \mathrm{V}_{\mathrm{sample}}$ increases, the derivative of $i_{pri}$ is equal to or greater than zero. The secondary electron current however may increase or decrease as $\mathrm{V}_{\mathrm{EE}} - \mathrm{V}_{\mathrm{sample}}$ increases [54]. In order to make this approximation possible, it is assumed that the derivative of $i_{sec}$ is equal zero at the point where the slope is maximum. Ideally, the primary electron beam would enter a device containing a suppression grid instead of being incident on the sample puck so that $i_{sec}$ is truly negligible compared to $i_{pri}$. Based on this assumption,

$$max\left(\frac{d\mathrm{i}_{\mathrm{sample}}}{d(\mathrm{V}_{\mathrm{EE}}+\mathrm{V}_{\mathrm{sample}})}\right)\approx max\left(\frac{d\mathrm{i}_{\mathrm{pri}}}{d(\mathrm{V}_{\mathrm{EE}}+\mathrm{V}_{\mathrm{sample}})}\right) \quad (14)$$

The $\mathrm{V}_{\mathrm{EE}}-\mathrm{V}_{\mathrm{sample}}$ is then related to α by

$$\alpha=-e\left(\mathrm{V}_{\mathrm{EE}}+\mathrm{V}_{\mathrm{sample}}\right)_{@max\ slope}-\Delta\Phi \quad (15)$$

where $\Delta\Phi=\Phi_{\mathrm{Ta}}-\Phi_{316}$ and $e$ is the charge of an electron. Since the energy distribution in equation 12 is a probability density function, its associated cumulative distribution function, $F(\mathrm{E_c})$ is related to the $\mathrm{i_{pri}}$ by

$$\mathrm{i}_{\mathrm{pri}}=\mathrm{I}_{\mathrm{p}}\times\left[1-F\left(-e\left(\mathrm{V}_{\mathrm{EE}}+\mathrm{V}_{\mathrm{sample}}\right)-\Delta\Phi\right)\right] \quad (16)$$

where $\mathrm{I_p}$ is the total current leaving the electron gun, which is 6.5 pA. This current was measured by positively biasing the sample to +200 V while keep the electron gun setting the same. In Figure 101, the primary current using equation 16 is plotted against the measured sample current for different values of $\Delta\Phi$. The red curve indicates that the sample current is more than the primary current, which violates the law of charge conservation. The green curve indicates that a rather large number of backscattered primary electrons with the SEY approaching 95% when the accelerating potential plus sample voltage is -1.11 V, which is much larger than any of the measurements made by Fowler and Farnsworth [54]. The blue curve indicates that the number of backscattered primary electrons decreases towards zero as the primary electron energy is decreased, which is consistent with a polycrystalline metal that has not undergone a thermal anneal while in vacuum [54]. The sample puck is made from polycrystalline metal and was not thermal annealed to remove surface impurities due to atmospheric exposure. Thus, the blue curve appears to be the most reasonable fit.

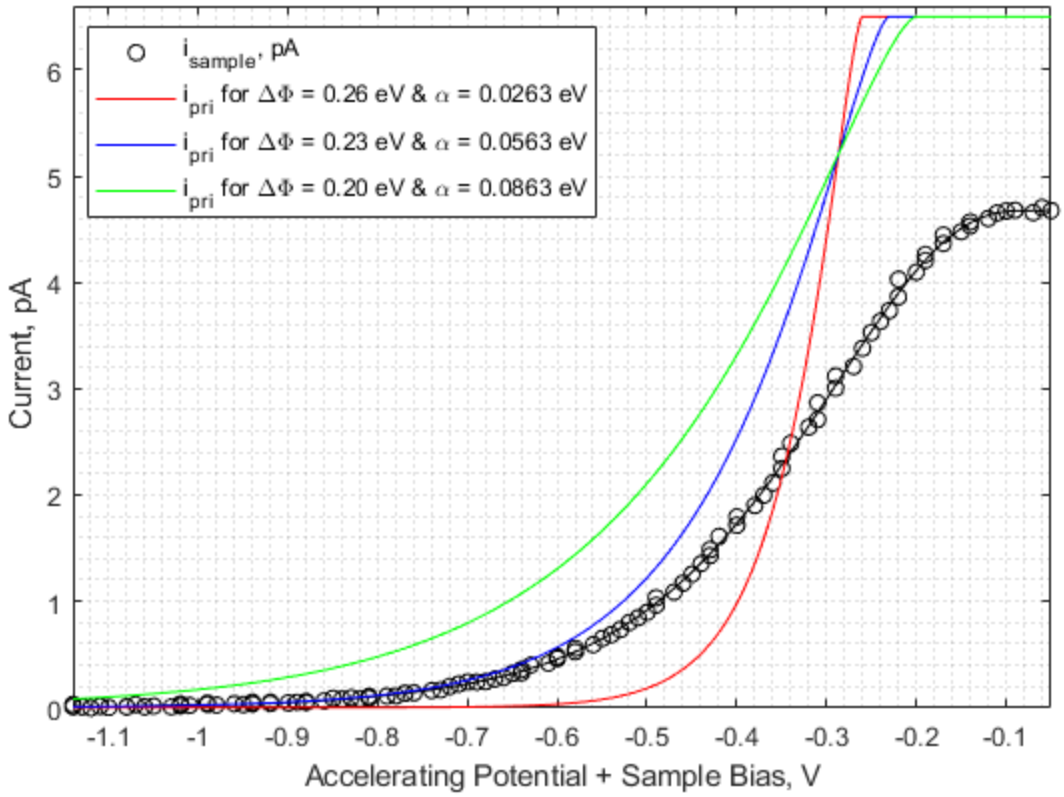


Figure 101: Comparison of $i_{pri}$ given by equation 16 to $i_{sample}$ for $\Delta\Phi$ = 0.20 eV, 0.23 eV, and 0.26 eV.

For an α = 0.0563 eV, the full width at half maximum (FWHM) of $f(E_c)$ is 0.202 eV. Since $2\alpha = kT$, where $k$ is the Boltzmann constant, the temperature of the cathode is approximately 1307 K. The current density, J, from the cathode can then be calculated using the Richardson-Dushman equation [146].

$$J = \frac{55 \times 10^4 \mathrm{A}}{\mathrm{m}^2\mathrm{K}^2} 1307^2 \exp\left(-\frac{4.22eV}{\left(\frac{8.617 \times 10^{-5}eV}{\mathrm{K}}\right)1307\mathrm{K}}\right) = 2.97 \times 10^{-11}\,\mathrm{A/m^2} \qquad (17)$$

The cathode is a disk with a radius between 0.400 mm and 0.424 mm. Thus, the calculated current leaving the cathode is between 25.0 pA and 28.2 pA. Since this current is greater

than the total current leaving the electron gun, the result is valid and indicates a reasonable efficiency in transporting the electrons through the electron gun.

Cimino *et al*. measured a 0.85-eV FWHM for the same electron gun with a tantalum cathode [7]. However, they were preforming measurements with a thousand times greater primary electron current than that involved in this research. To produce higher currents requires increasing the cathode's temperature causing thermal broadening of the energy distribution. In addition, they used a different method of measuring the FWHM which did not account for backscatter primary electrons. At the 3123-K melting point of tantalum, the FWHM is only 0.483 eV for the Maxwell-Boltzmann energy distribution, and the current leaving the calculated cathode is between 417 mA and 471 mA which is much greater than the low nA primary current used during their measurements and the maximum rated current of the electron gun (10 μA). Alternatively, Thong stated that the FWHM is approximately 2.45$kT$; however, the FWHM does not exceed 0.659 eV below the melting point of tantalum [146]. The manufacturer of the electron gun calculated a 0.3-eV FWHM within the rated current range of the electron gun (1nA to 10 μA) [136]. Therefore, it is unlikely that their measured FWHM is correct. Since the primary currents used in this research are well below the rated current range, it is reasonable to infer that the FWHM will be less than the 0.3-eV FWHM calculated by the manufacturer lending greater credence to the approximation performed in this research.

The approximated energy distribution is shown in Figure 102. A set of one million random energy values were generated in accordance with this distribution using the custom MATLAB script found in Appendix D.

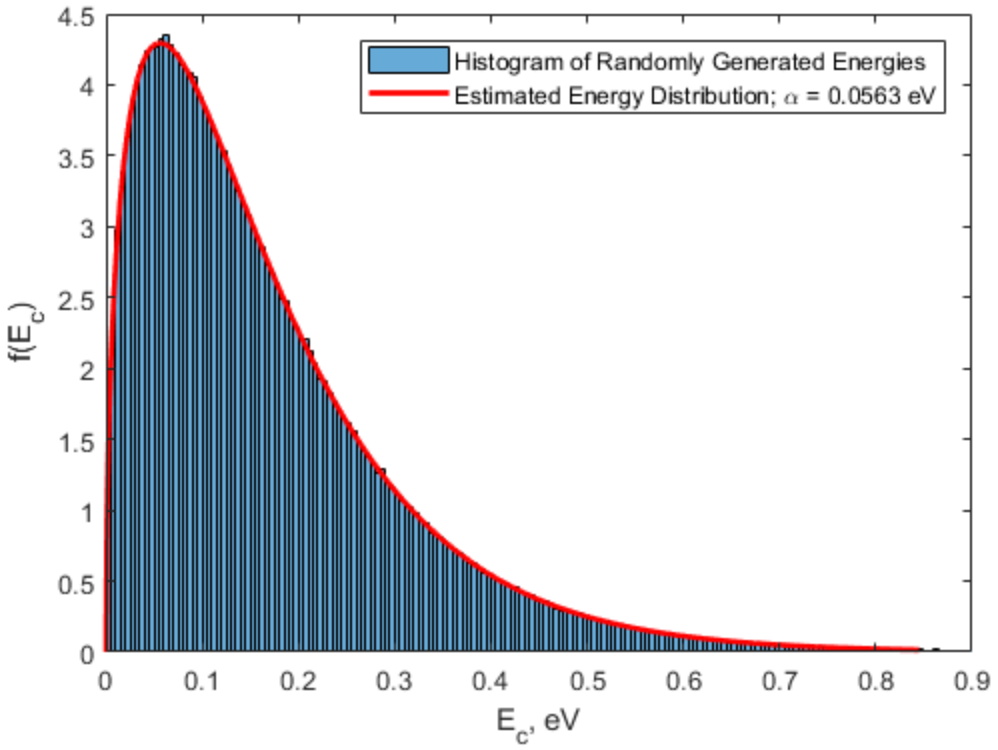


Figure 102: Estimated energy distribution of electrons emitted from the cathode. The distribution function $f(E_c)$ is overlaid on the histogram of the randomly generated energies.

The data generated by MATLAB for the emitted electrons was imported into SIMION® using the procedure outline in Appendix D. The simulated electrons are emitted uniformly across the surface of the cathode. Their angular distribution follows Lambert's cosine law in accordance with Thong [146]. The distribution of elevation angles is shown in Figure 103.

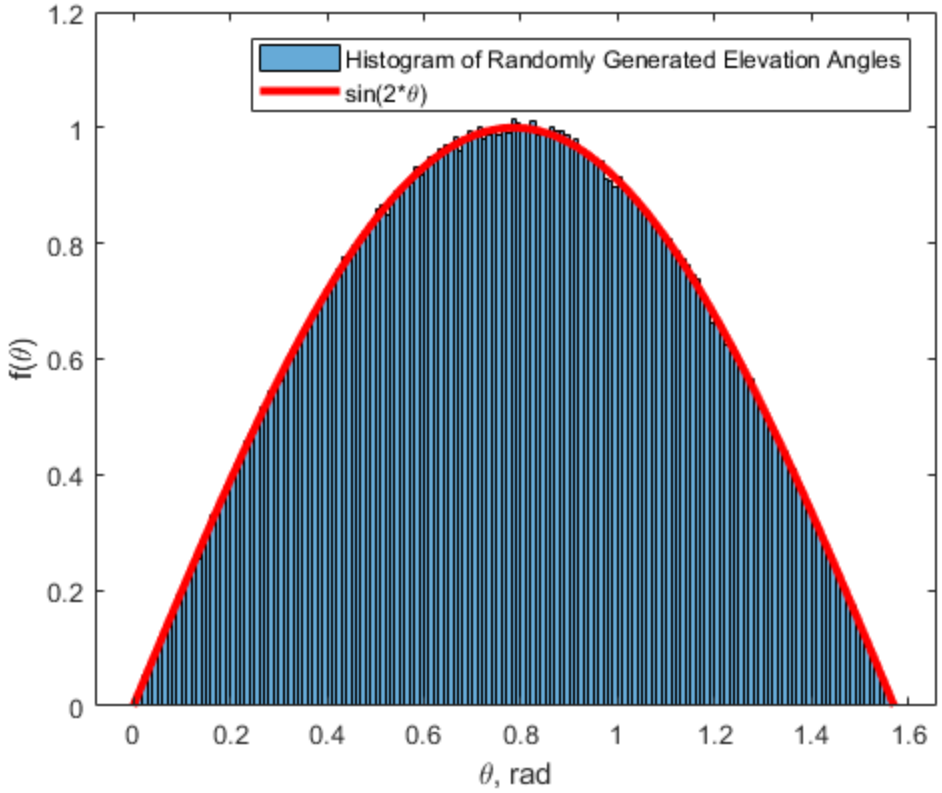


Figure 103: Histogram of randomly generated elevation angles following Lambert's cosine law.

Based on this approximation, the work function of 316SS is then $\Phi_{316} = \Phi_{\mathrm{Ta}} - \Delta\Phi$=3.99 eV. However, Cieślik *et al.* have reported that the work function for 316SS is 4.6 eV [148]. If their value is correct, then more electrons must be emitted with higher kinetic energies than that predicted here. The deviation from their reported value may be due to contaminants on the surface. However, being unable to measure the work function by other means, this cannot be confirmed. This work function is applied when setting the potentials of the electrodes in the SIMION® model. Since the electrodes are composed of 316SS, the work function is applied to all of the electrodes with the exception of the cathode, where a work function of 4.22 eV is applied.

### 3.3 Summary

In this chapter, the iterative process of experimentation, modeling and simulation, and theoretical refinement was introduced as a necessary approach to determining when and to what extent the assumptions listed in Chapter II are violated. In order to implement this process, an experimental system was developed to autonomously perform a large number of SEE experiments under varying conditions. During this development, several important discoveries were made that enabled better repeatability in experiments. The first discovery was the rather lengthy time required for the cathode output to stabilize. Allowing the cathode to remain on for at least three hours prior to measurements reduces the repeatability problems caused by a drifting primary electron current. The second discovery was the unexpected transitions or discontinuities in the sample and Faraday cup currents. These transitions were the precursors to burst noise which severely degraded the repeatability of measurements. This noise may have been caused by the dielectric breakdown of the insulators within the chamber after exposure to electrons from the electron gun and secondary electrons from the sample. These transitions and the burst noise were eliminated by reducing the current output of the cathode and minimizing the duration over which the chamber was exposed to electrons during each measurement. The third discovery was the large settling time associated with varying the sample and Faraday cup voltage. The results showed that altering these voltages by 100 V required a settling time of one hour before measurements are performed in the pA range. The fourth discovery was the capacitive coupling between the electron gun optics and the Faraday cup. When the potentials of the optics are varied between measurements, the system should be allowed 30 seconds to stabilize before beginning measurements to avoid the transient behavior

associated with the coupling. Since other researchers commonly use similar systems to the one developed in this chapter, the discoveries made in the development of this system may be applied to systems used by others in the research community.

The implementation of the iterative process also required the development of a simulation model. Problems regarding the VSim® software ultimately led to the use of SIMION® in this research. SIMION® lacks the capabilities of VSim® which limited the scope of this research. Though not the focus of this research, it was necessary to develop a new model for thermionic emission in order to complete the simulation model. This model was calibrated using a new method which was developed in this chapter. It also provides a new means of estimating the work function of the sample. The calibrated model was validated by comparison with the results obtained by other researchers and the manufacturer of the electron gun. Using the Richardson-Dushman equation, the cathode temperature estimated from this model provided an emission current prediction that was reasonably consistent with experimental measurements. With the development of the experimental system and simulation model complete, the second and third objectives of this research were fulfilled, and the focus shifted toward performing measurements and analyzing experimental data.

# IV. Results and Analysis

In Chapter II, a list of common assumptions made during SEY measurements were given. Violations of these assumptions may lead to variations in the measured SEY for different test conditions. In order to better understand when these assumptions are violated and the effect of these violations on measurements, several tested were devised in which specific parameters of the tests were varied. The results of these tests are summarized in Sections 4.1 through 4.4. In Section 4.5, a magnetized sample is investigated to determine if placing magnets on the vacuum chamber walls will suppress tertiary electrons during SEY measurements. For the results of this chapter, the estimated SEY can be obtained by substituting the Faraday cup current, $i_{Faraday}$, for $i_{pe}$ and the sample current, $i_{sample}$, for $i_s$ in the second equation listed in Table 1 of Section 2.2.1 as shown below.

$$\sigma_{est.2} = 1 - \frac{i_s}{i_p} = 1 - \frac{i_{sample}}{i_{Faraday}} \tag{18}$$

In this chapter, $i_{sample}$ and $i_{Faraday}$ will be looked at individually; and, in some cases, the ratio of $i_{sample}$ to $i_{Faraday}$ will be discussed.

### 4.1 Comparison of Measurements at Different Primary Currents

As discussed in Section 2.6.4, the ratio between any two currents measured within the chamber should remain constant since SEY is independent of current. To test the validity of this assertion, measurements were performed with several emission currents while the potentials listed in Table 6 remained constant.

Table 6: Potentials used in tests performed using different emission currents.

| $V_G$, V | $V_{FO}$, V | $V_{FA}$, V | $V_s$, V | $V_F$, μV |
|---|---|---|---|---|
| 0.00 | 429.95±0.05 | 125.0 | -194.910±0.002 | -0.1±0.3 |

The accelerating potential was varied between 193.1 and 213.0 V. The spacing between the end of the electron gun and sample puck was 45.37 mm. The emission current was varied by adjusting the source potential, $V_{ES}$. The chamber pressure for these measurements was between $3.1 \times 10^{-9}$ and $3.4 \times 10^{-9}$ Torr. The ratio between the sample current, $i_{sample}$, in the open position and the Faraday cup current, $i_{Faraday}$, in the closed position is plotted in Figure 104.

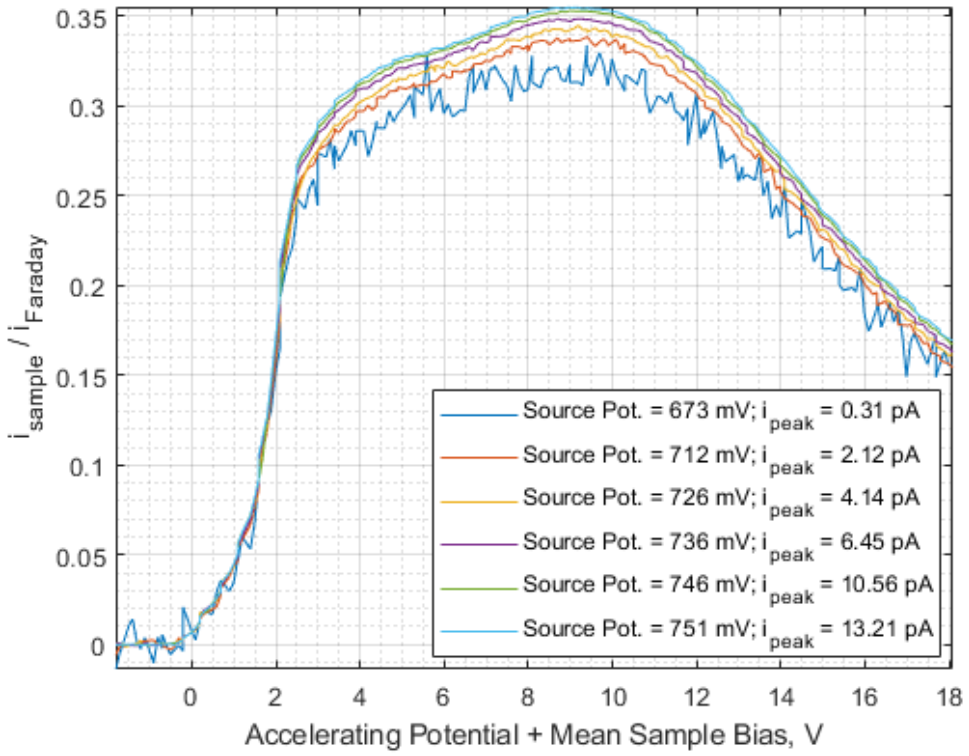


Figure 104: Ratio of the sample current in the open position to the Faraday cup current in the closed position for different source potentials and zero grid potential. The maximum sample current is listed as $i_{peak}$.

The results in Figure 104 indicate that the ratio is not constant and increases with increasing cathode temperature. This deviation from a constant ratio may be due to space charge, a variation in energy distribution of the electrons emitted from the cathode as the cathode

temperature is varied, or a nonlinearity in the current measurements made by the electrometers. Unfortunately, to better determine cause of this deviation, a simulation model capable of modeling space charge effects must be used, and SIMION® is not capable of performing this modelling. These results show that under certain conditions the ratio between two currents may not remain constant, and the estimated SEY may also vary based on equation 18. Thus, when preforming comparative tests not regarding changes in emission current, care must be exercised to ensure the emission current is consistent between the tests.

The grid potential, $V_G$, provides another means of adjusting the emission current. Increasing $V_G$ decreases the emission current. It also decreases the diameter of electron beam entering the 1st anode as shown Figure 105, which may lead to a smaller spot size on the sample.

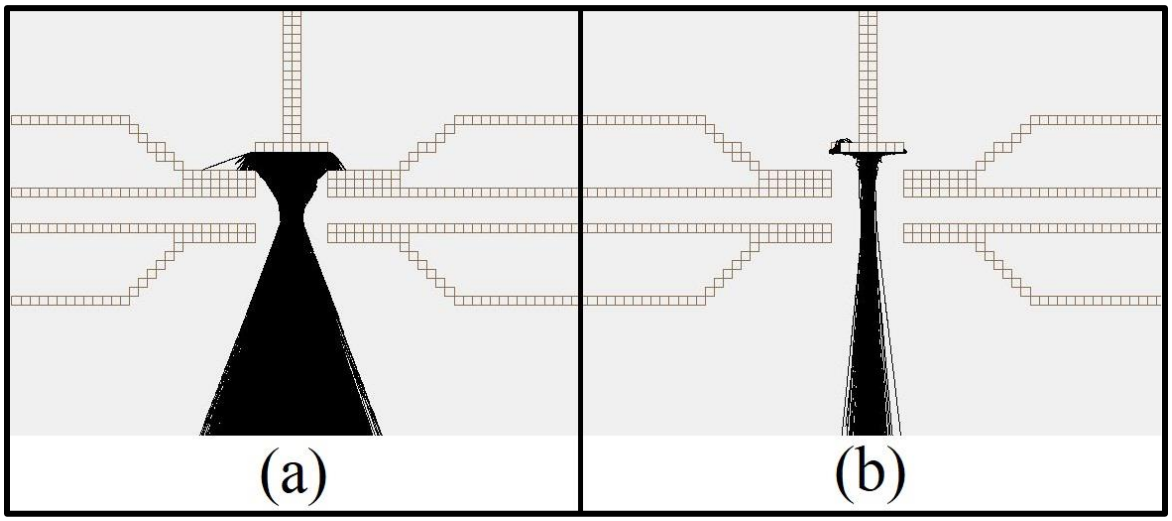


Figure 105: Electron trajectories from cathode into 1st Anode with no grid potential applied (a) and with grid potential applied (b). Electron trajectories are shown in black. The electrons are moving in the downward direction.

Unfortunately, the electron trajectories predicted by SIMION® are questionable when a grid bias is applied due the increased likelihood of space charge in front of the cathode

since SIMION® was not designed to model a heavily space charged environment [141]. For this reason, the grid potential is zero throughout all the tests in the sections that follow.

Using the grid potential to reduce the primary current alters the ratio between the sample current, $i_{sample}$, in the open position and the Faraday cup current, $i_{Faraday}$, in the closed position between currents as shown in Figure 106. The potentials for the results shown in this figure were the same as those listed in Table 6 with the exception of the grid potential. The red curve in this graph is from the same data as the red curve in Figure 104. The chamber pressure during these tests was between $3.2 \times 10^{-9}$ and $3.5 \times 10^{-9}$ Torr, and the spacing between the end of the electron gun and sample puck was 45.37 mm. The blue curve shows a ratio greater than the red curve and any of the curves shown previously in Figure 104. These results indicate that altering the grid potential may also cause SEY measurements to vary.

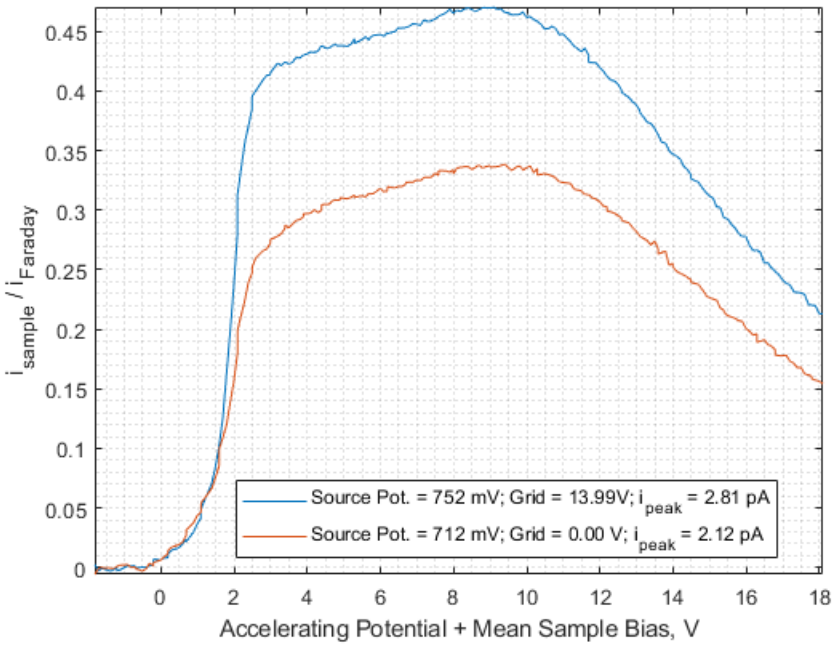


Figure 106: Ratio of the sample current in the open position to the Faraday cup current in the closed position for a biased and unbiased grid. The maximum sample current is listed as $i_{peak}$.

Increasing the grid bias also leads to a smaller beam diameter entering the Faraday cup. Since the Faraday cup was not biased for these tests due to beam deflection (see Section 3.1.6), the Faraday cup is primarily dependent on its geometry to prevent secondary electrons from leaving the Faraday cup. In the Faraday cup, electrons from the electron gun enter a hollow cylinder which is blocked on one end. A narrow beam of electrons will produce more secondary electrons towards the center of the blocked end. Since secondary electrons are generally emitted following a cosine angular distribution, more secondary electrons are likely to escape from the Faraday cup when the beam is narrower which reduces the amount of current measured by the Faraday cup. Thus, the amount of current measured by the Faraday cup depends not only on the amount of current entering the cup but also on the characteristics of the beam, such as the energy and diameter. These characteristics change based on the optical setting of the electron gun. This may lead to large variations in the current measured by the Faraday cup as the optical setting vary as shown in Figure 107. This figure was created from the data discussed previously in this section with a source potential equal to 751 mV and following the setting shown in Table 6. It is unlikely that less electrons are entering the cup as the accelerating potential is increased. Therefore, it is likely that more secondary electrons are escaping the Faraday cup as the accelerating potential is increased. This behavior is important to mitigate by positively biasing the Faraday cup if attempting to determine the primary electron current using the Faraday cup. Furthermore, when performing comparative tests not regarding changes in the potentials of the electron gun optics, the potentials of the optics must remain consistent between tests in order for comparisons to be reasonable.

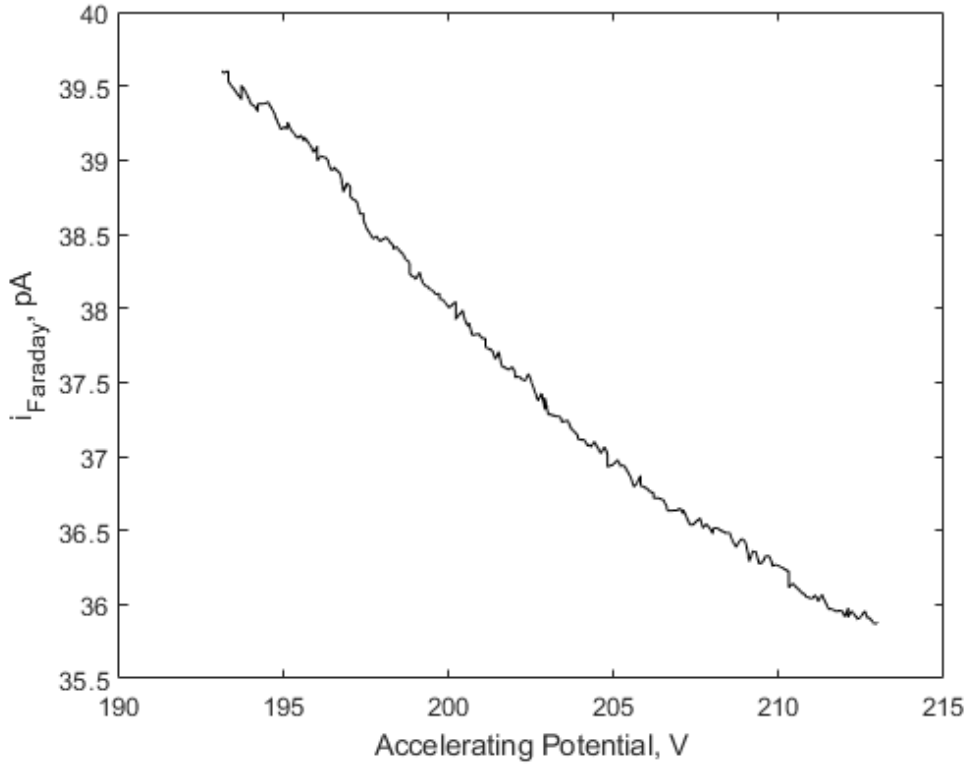

Figure 107: Plot of Faraday cup current in the closed position versus accelerating potential for the potentials specified in Table 6 and a 751-mV source potential.

Reducing the emission current of the cathode reduces the likelihood of space charge effects and the thermal broadening of the thermionic emission energy distribution. However, measurements become increasing noisy for currents below 140 fA as shown in Figure 108. Averaging may be used to reduce this noise and allow operation down to about 20 fA. Measurements below 20 fA are not practical due to the noise associated with the current measurements as discussed in Section 3.1.4. The blue curve measured with a 643-mV source voltage was measured by extending the duration in which the electron gun is on (i.e. no grid bias) from that shown in Figure 83 of Section 3.1.14. This allowed averaging of the currents when the gun is on over more samples. The duration of each dataset remained 2 minutes.

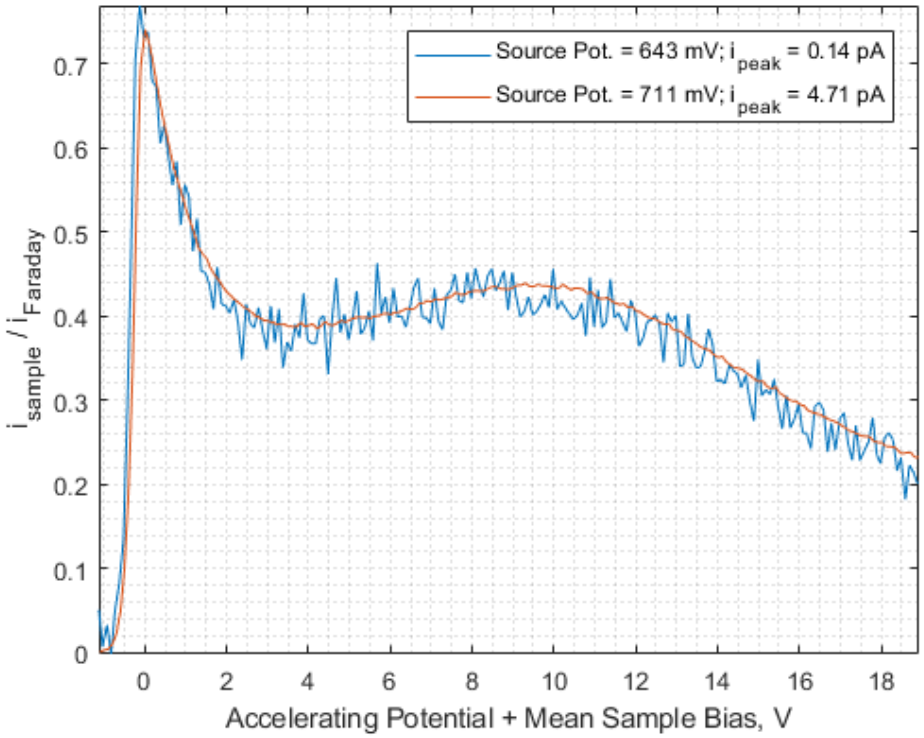

Figure 108: Ratio of the sample current in the open position to the Faraday cup current in the closed position for different source potentials and zero grid potential. The maximum sample current is listed as $i_{peak}$.

In conclusion, the results of this section indicate that SEY measurements are sensitive to the current involved in the measurement and the optical setting of the electron gun. Thus, when performing SEY measurements on different samples for comparison, both the current and optical settings must remain consistent between measurements in order for the comparison to be reasonable. To the author's knowledge, this is a common practice observed by researchers throughout the scientific community. Though this does allow qualitative comparison, it does not guarantee that the measurements are of the true SEY.

### 4.2 Electron Gun to Sample Spacing

In addition to the potentials and currents chosen when performing measurements, the geometries within the chamber may also affect the outcome of a SEY measurement. To

determine the sensitivity of measurements to changes in geometry, measurements were performed for different spacings between the end of the electron gun and the sample puck. For all the measurements, the potentials listed in Table 7 were maintained. The source potential was near the source potential used to calibrate the SIMION® model, which was 710 mV. The accelerating potential was varied between 193.1 and 213.0 V. The chamber pressure for these measurements was between $3.1 \times 10^{-9}$ and $3.3 \times 10^{-9}$ Torr. Figure 109 indicates that electrons reach the sample at lower energies when the spacing is increased.

Table 7: Potentials used in measurements with different spacings.

| $V_{ES,}$ V | $V_G$, V | $V_{FO}$, V | $V_{FA}$, V | $V_s$, V | $V_F$, μV |
|---|---|---|---|---|---|
| 709 mV | 0.00 | 429.95±0.05 | 125.0 | -194.909±0.0025 | 0.79±0.24 |

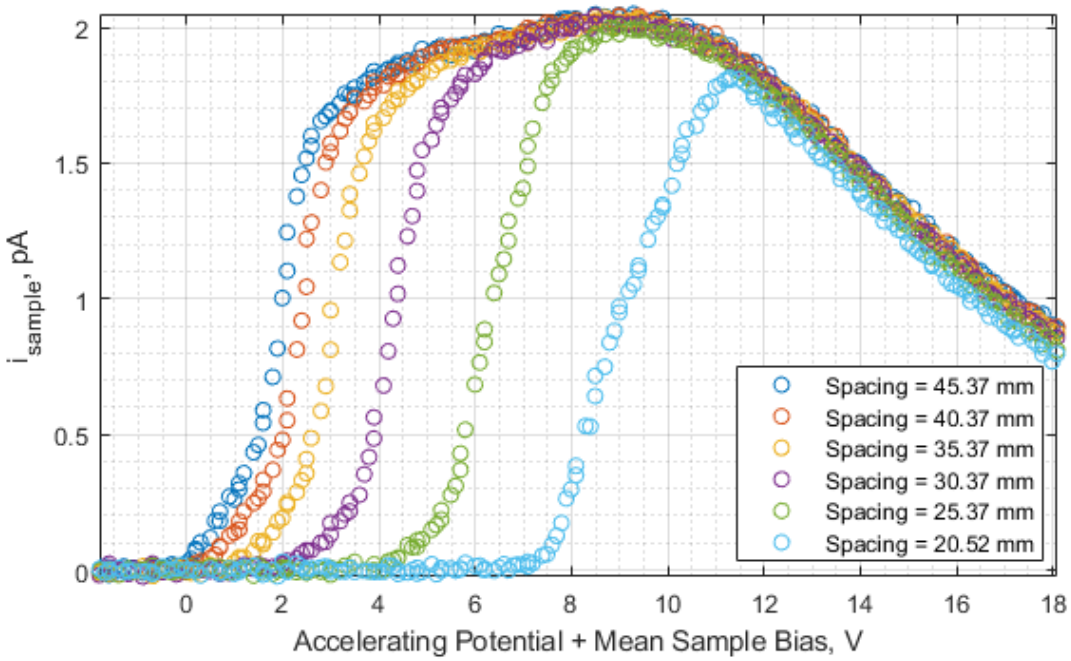


Figure 109: Sample current measured for the open position for different spacings between the end of the electron gun and the sample puck. The sample bias was -195 V.

This behavior is counterintuitive since one would expect that more electrons would reach the sample as the spacing is decreased. The SIMION® model developed in Chapter III indicates that this behavior is due to deflection caused by the asymmetric electric field

between the sample and Faraday cup. Figure 110 demonstrates this deflection for a spacing of 45.37 mm. At the accelerating potential of 195 V, the electron beam does not intercept the sample as indicated by the large number of electron trajectories leaving the sample moving upward and to the right in the Figure 110(a). Though the electrons do have sufficient energy to reach the sample when exiting the electron gun, they fail to do so because of the asymmetric electric field between the sample and Faraday cup.

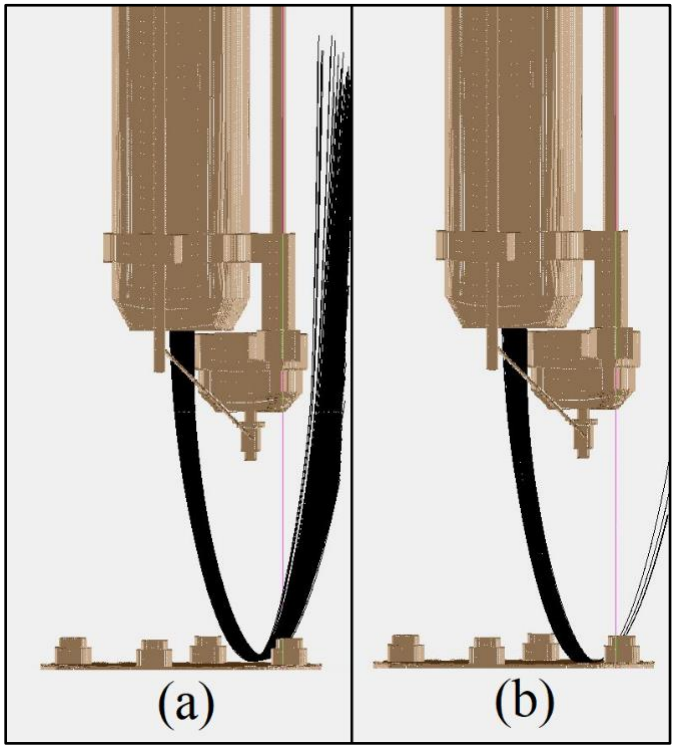


Figure 110: Electron trajectories (shown in black) for a spacing of 45.37 mm. The accelerating potentials were 195V (a) and 200V (b). All other potentials were set in accordance with Table 7.

For this spacing, the simulation model indicates that electrons will start interacting with the sample between an accelerating potential of 197 and 198 V. Measurements however indicate that this interaction begins at 195 V. The disagreement between the simulation and experimental results may be due to inaccuracies in the model or electron-electron interactions, which SIMION® is not designed to simulate.

As the spacing between the electron gun and sample is reduced, the asymmetric field is enhanced increasing the deflection as shown in Figure 111 for a spacing of 20.52 mm. For this spacing, the simulation model indicates that electrons will start intercepting the sample between an accelerating potential of 205 and 206 V. However, the experiment results indicate that electrons begin arriving at the sample at an accelerating potential of 203 V.

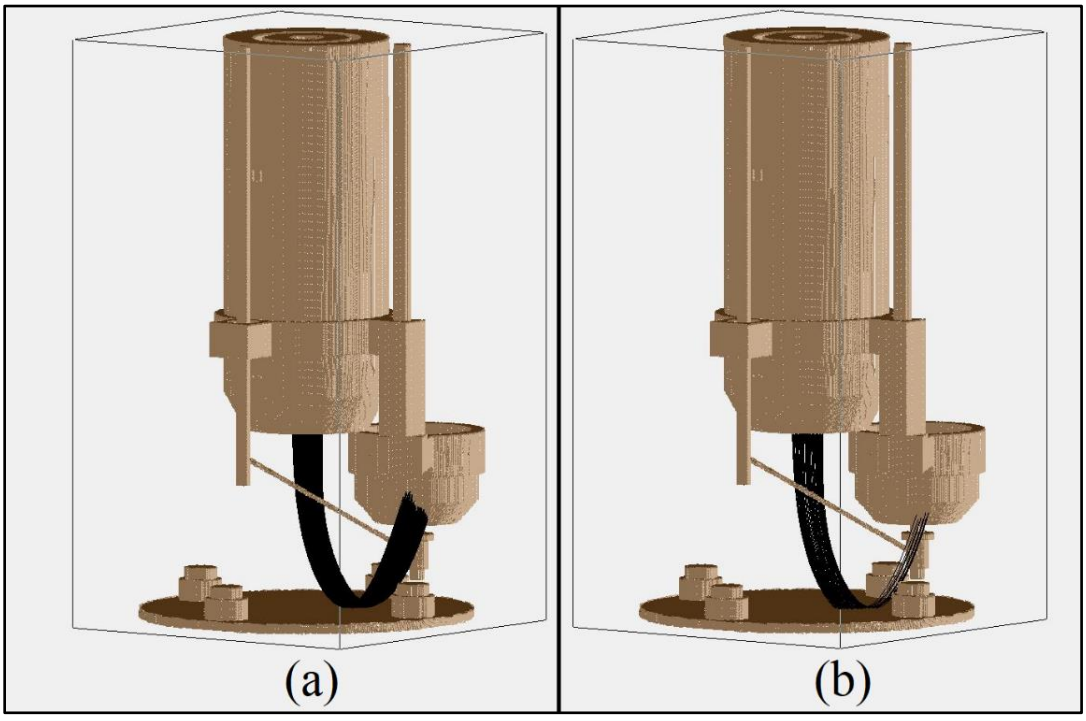


Figure 111: Electron trajectories (shown in black) for a spacing of 45.37 mm. The accelerating potentials were 202V (a) and 210V (b). All other potentials were set in accordance with Table 7.

If the electron beam is broadened as show in Figure 112, electrons are able to arrive at the sample at a lower accelerating potential as indicated by the plot of the sample current in Figure 113. The simulation model predicted that electrons would begin interacting with the sample when the accelerating potential was between 194 and 195 V, and measurements indicate that interactions began at an accelerating potential of 194 V.

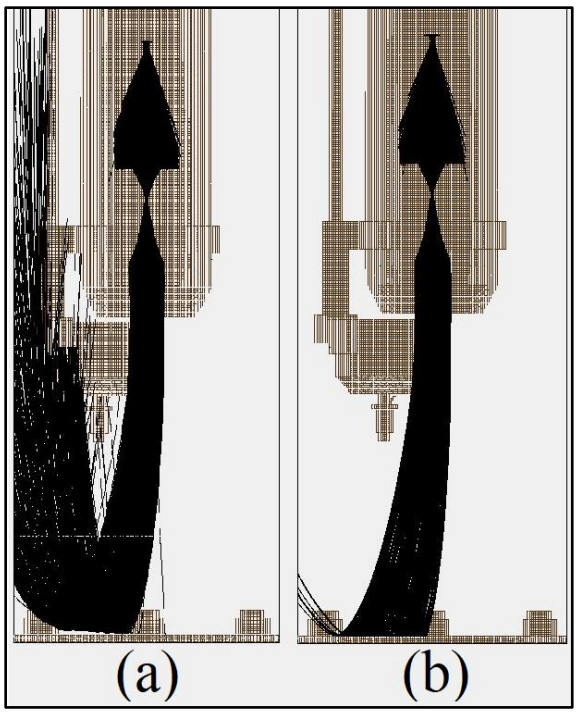

Figure 112: Electron trajectories (shown in black) for a spacing of 45.37 mm. The accelerating potentials were 195 V (a) and 204 V (b). All other potentials were set in accordance with Table 8.

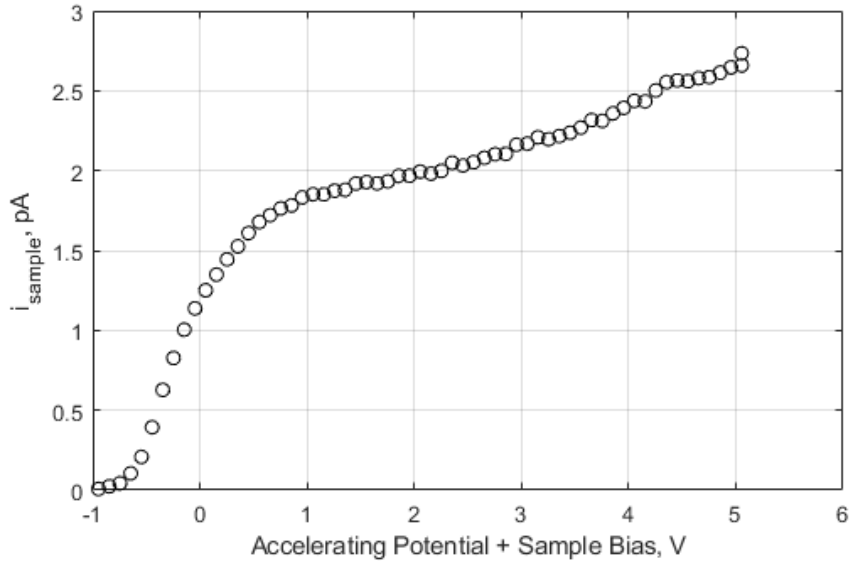

Figure 113: Sample current measured for the open position for a spacing of 45.37 mm and optimized for maximum sample current at an accelerating potential of 195 V. Plot corresponds with potentials listed in Table 8.

The potentials corresponding to this test are shown in Table 8. The chamber pressure for test was between $3.2 \times 10^{-9}$ and $3.4 \times 10^{-9}$ Torr, and the spacing was 45.37 mm.

The test was performed by adjusting the focus potential until highest sample current was measured for an accelerating potential of 195 V; however, this sample current is small compared to the current leaving the electron gun, which is around 6.5 pA.

Table 8: Potentials used to maximize sample current for $V_{EE}$ = 195 V and $V_s$ = -195 V.

| $V_{ES,}$ V | $V_G$, V | $V_{FO}$, V | $V_{FA}$, V | $V_s$, V | $V_F$, μV |
|---|---|---|---|---|---|
| 711 mV | 0.00 | 1560.0 | 10.0 | -195.016±0.001 | 0.0 ±0.2 |

The sample bias for the aforementioned test was -195 V. This high negative potential prevents many electrons from reaching the sample even when the electrons have sufficient energy to reach the sample due to the deflection caused by the asymmetric electric field between the Faraday cup and sample. When attempting make SEY measurements with primary electron energies below 12 eV, a large negative sample bias will lead to incorrect assessment of the primary current. In addition, the primary electrons will not be normally incident on the sample. Furthermore, using these measurements to estimate the thermionic emission energy distribution and the work function of the sample as described in Section 3.2.4 will lead to significant errors in the model. In order to perform this estimation, the sample bias must be reduced as much as possible to avoid the deflection of the primary electron while still being negatively biased enough to prevent electrons from reaching the sample when the accelerating potential is zero.

By reducing the negative bias of the sample, more electrons are able to reach the sample at lower primary electron energy as shown in Figure 114. These measurements were conducted using the potentials listed in Table 9. The chamber pressure for these measurements was between $3.3x10^{-9}$ and $3.7x10^{-9}$ Torr. The measurements were performed with a spacing of 25.37 mm and 45.37 mm.

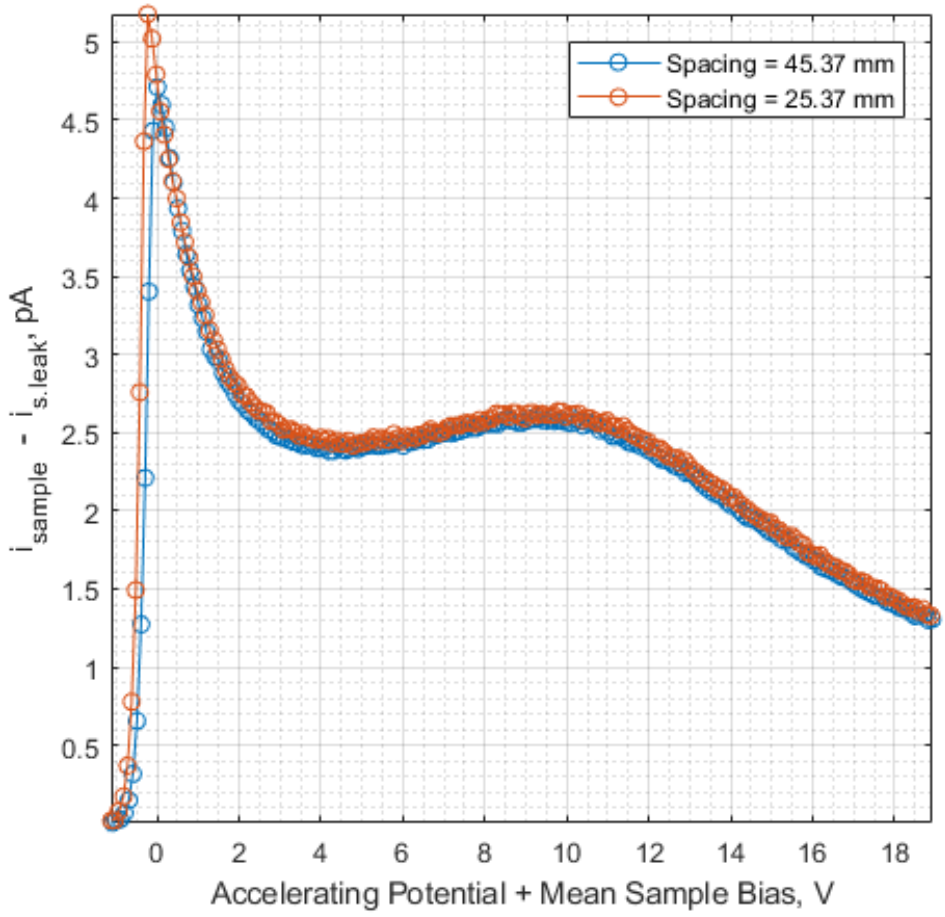


Figure 114: Sample current measured for the open position for different spacings between the end of the electron gun and the sample puck. The sample bias was -1.1 V.

Table 9: Potentials used to maximize sample current for $V_{EE}$ = 1.1 V and $V_s$ = -1.1 V.

| $V_{ES}$, V | $V_G$, V | $V_{FO}$, V | $V_{FA}$, V | $V_s$, V | $V_F$, μV |
|---|---|---|---|---|---|
| 711 mV | 0.00 | 147.0 | 10.0 | -1.0902±0.0002 (blue curve)<br>-1.1205±0.0003 (red curve) | -0.1 ±0.3 |

The sample bias was slightly different between measurements due to the challenge associated with precisely adjusting the power supply which has a readout resolution of 0.1 V. The maximum sample current measured when the spacing was 25.37 mm was about 0.47 pA more than when the spacing was 45.37 mm. This difference is caused by the electron beam spreading out more and missing the sample when the spacing is larger as shown in Figure 115.

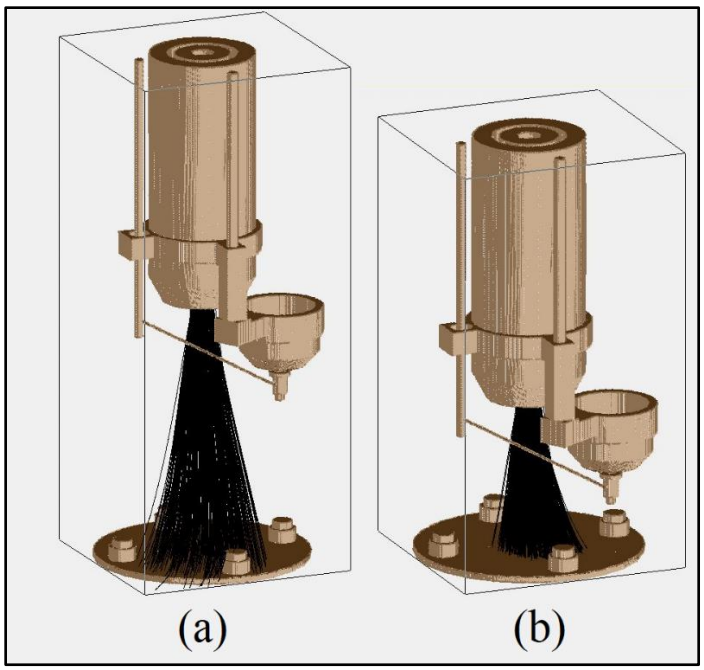

Figure 115: Electron trajectories (shown in black) for a spacing of 25.37 mm (a) and 45.37 mm (b). The accelerating potentials was 1.1 V. All other potentials were set in accordance with Table 9.

In conclusion, the primary electron beam is significantly affected by the spacing between the electron gun and sample at low primary electron energies. This effect is minimized by reducing the sample bias as much as possible. The sample bias may be increased as the primary electron energy is increased in order to prevent tertiary electrons from returning to the sample. At low primary electron energies, the primary electron beam is asymmetrically misshapen, and this cannot be corrected without grounding the sample or removing the Faraday cup from the electron gun.

### 4.3 Dependency of First Crossover on E-gun Optics

The first crossover, which was discussed in Section 2.2.3, is an important feature of the SEY curve. The measurement of the primary electron energy at the crossover does not require measuring or assessing the primary current. Instead, it requires only

determining the energy at which the sample current reverses directions. This measurement is sensitive to the optical settings of the electron gun as shown in Figure 116. These measurements were performed at different 1st anode potentials. The potentials for these measurements are shown in Table 10. The chamber pressure was between $3.4 \times 10^{-9}$ and $3.6 \times 10^{-9}$ Torr during these tests, and the spacing was 45.37 mm. A linear fit was used to estimate the location were the sample current reverses directions. The energy at the first crossover was determined by adding the accelerating potential to the sample bias. A plot of the first crossover energies for different 1st anode potentials is show in Figure 117.

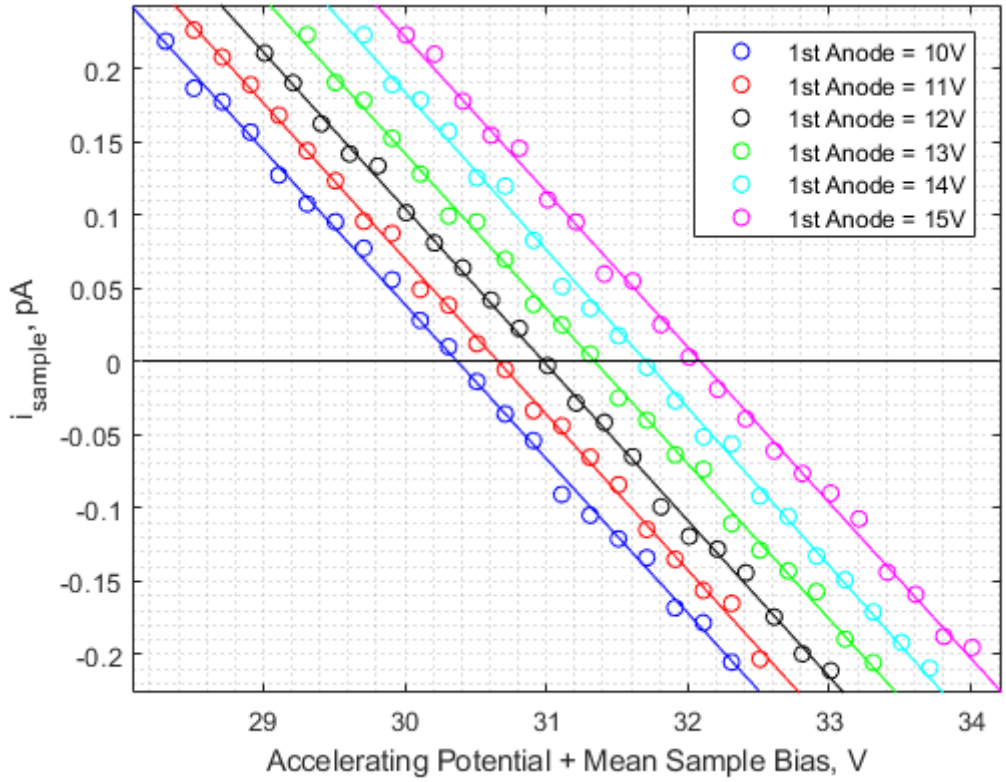


Figure 116: Sample current measured around the 1st crossover for different 1st anode potentials.

Table 10: Potentials used in measurements of first crossover energy.

| $V_{ES}$, V | $V_G$, V | $V_{FO}$, V | $V_s$, V | $V_F$, µV |
|---|---|---|---|---|
| 711 mV | 0.00 | 500.0 | -20.0112±0.0005 | -0.1 ±0.3 |

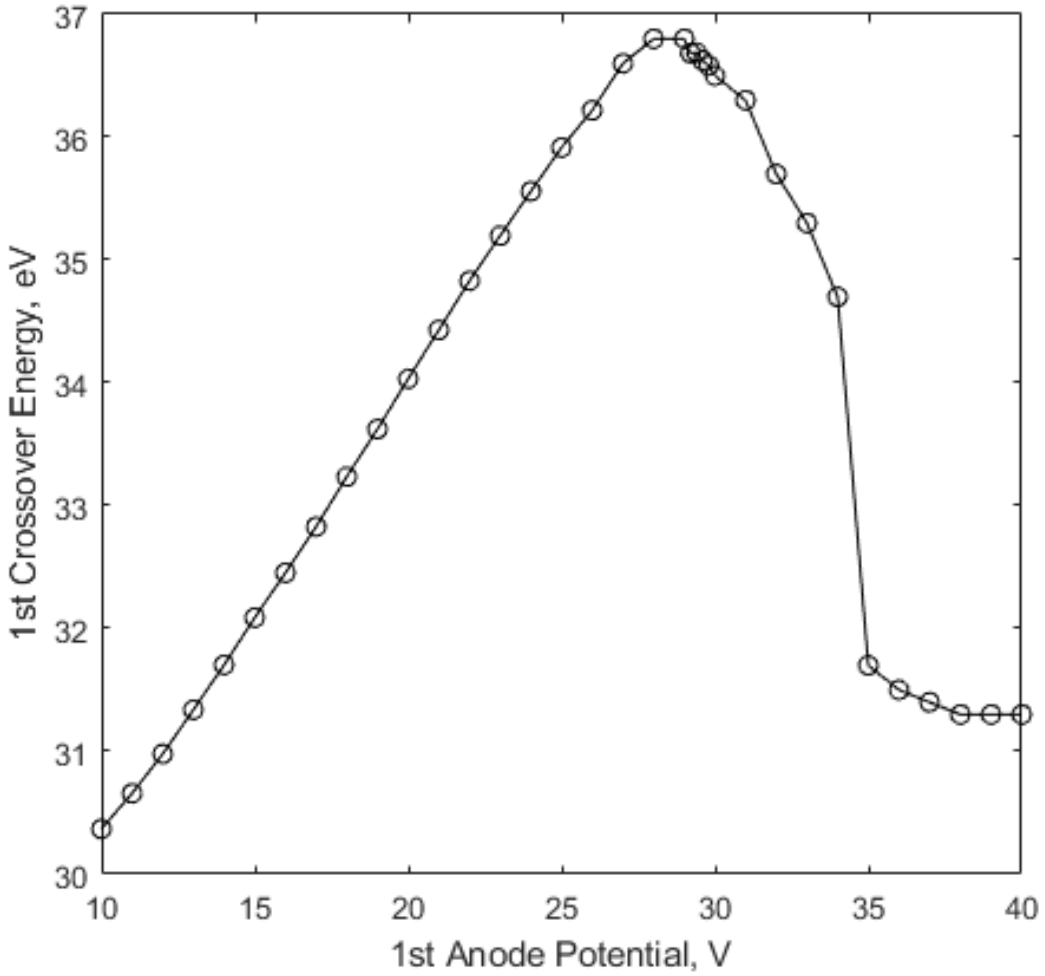


Figure 117: First crossover energy versus 1st anode potential. Data corresponds to potentials listed in Table 10.

The results shown in Figure 117 indicates that measurements of the first crossover energy are sensitive to the settings of the electron gun optics. These results are due to changes in shape of the primary electron beam as shown in Figure 118 for different 1st anode potentials. The sensitivity of these measurements to the shape of the primary electron beam highlights the need for a metric for comparing the quality of different primary electron beams and developing techniques to optimize the quality of the electron beam, which is the focus of the following section.

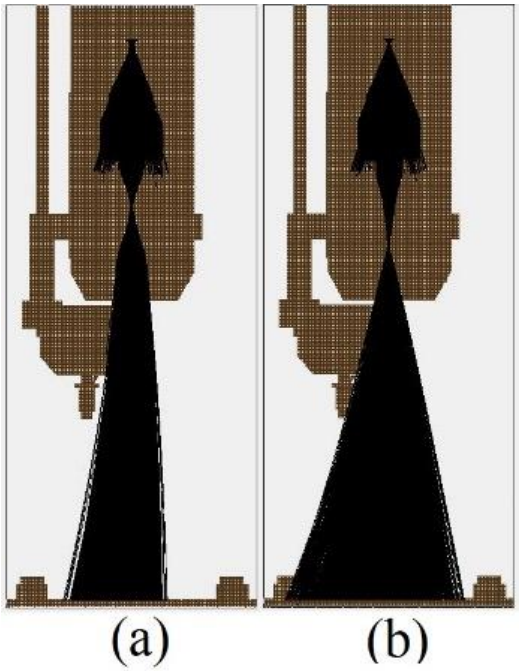


Figure 118: Electron trajectories (shown in black) for 1st anode potential of 10 V (a) and 40 V (b). The accelerating potentials was 51 V. All other potentials were set in accordance with Table 10. The spacing was 45.37 mm.

### 4.4 Scanned Focus Measurements

In Chapter II, the assumption that all electrons arrive at the same incidence angle was identified in Assumption 3. The extent to which this assumption is violated is central to determining the quality of the primary electron. In addition, the primary electron should land within the area normally occupied by a sample mounted on the sample puck. Based on these two factors, the following beam quality factor (BQF) equation was developed.

$$\mathrm{BQF} = \frac{100}{\mathrm{N}} \sum_{\mathrm{n}=1}^{\mathrm{N}} H(\mathrm{r_w} - \mathrm{r_i(n)})\,(1 - |\theta_i(\mathrm{n}) - \theta_d|/90) \tag{18}$$

where N is the number of primary electrons interacting with the sample puck based on a SIMION® simulation with a million electrons emitted from the cathode. *H* is the Heaviside function, and $r_w$ is radius occupied by a sample measured from the center of the sample puck. The value of $r_w$ varies with the sample being tested; however, it should be less than

10 mm to avoid having the electrons interact with the fasteners of the sample puck. Each individual electron will intercept the sample puck at a distance $r_i(n)$ from center of the sample puck. The desired incidence angle in degrees is $\theta_d$, and the incidence angle in degrees associated with each electron impacting the sample puck is $\theta_i(n)$. Each electron may add a maximum value of one to the summation. If the electron lands outside $r_w$, zero is added to the summation for that electron. If the electron lands within $r_w$, it receives value based on the difference between its incidence angle and the desired incidence angle. If all the electrons hit the sample puck at the desired incidence angle and within $r_w$, then the BQF will be 100%. Otherwise, the BQF will be less than 100%. Equation 18 provides a simple metric for comparing beam quality and may be used in an optimization routine to determine the optimum electron gun settings and sample bias for any primary electron energy.

As an example of this equation being used, consider the electron trajectories shown in Figure 119.

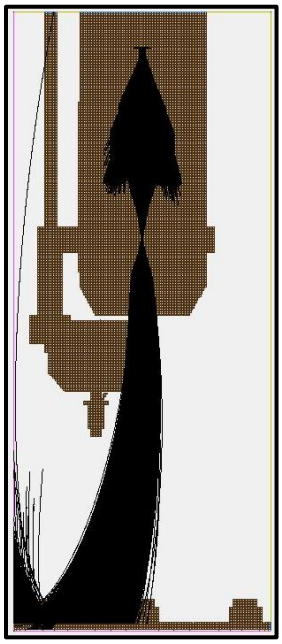

Figure 119: Electron trajectories (shown in black) for a spacing of 45.37 mm and the potentials listed in Table 11.

Table 11: Potentials used in simulation corresponding to Figure 119.

| $V_{EE}$, V | $V_G$, V | $V_{FO}$, V | $V_{FA}$, V | $V_s$, V | $V_F$, μV |
|---|---|---|---|---|---|
| 5 | 0 | 210.1 | 10 | -5 | 0 |

The potentials for this simulation are listed in Table 11. The electrons are deflected from the center of the sample puck by the electric field between the sample puck and Faraday cup. Each of the electrons that is "flown" through the simulation space will terminate when colliding with an obstacle or reaching the boundaries of the simulation space, which the developers of SIMION® refer to as a "splat" [141]. SIMION® was configured to record the location, elevation angle, and energy during each "splat" to a text file. This text was then imported into MATLAB for analysis (see Appendix E).

Figure 120 shows the 3D histogram based on the number of electrons impacting at each location on the sample puck.

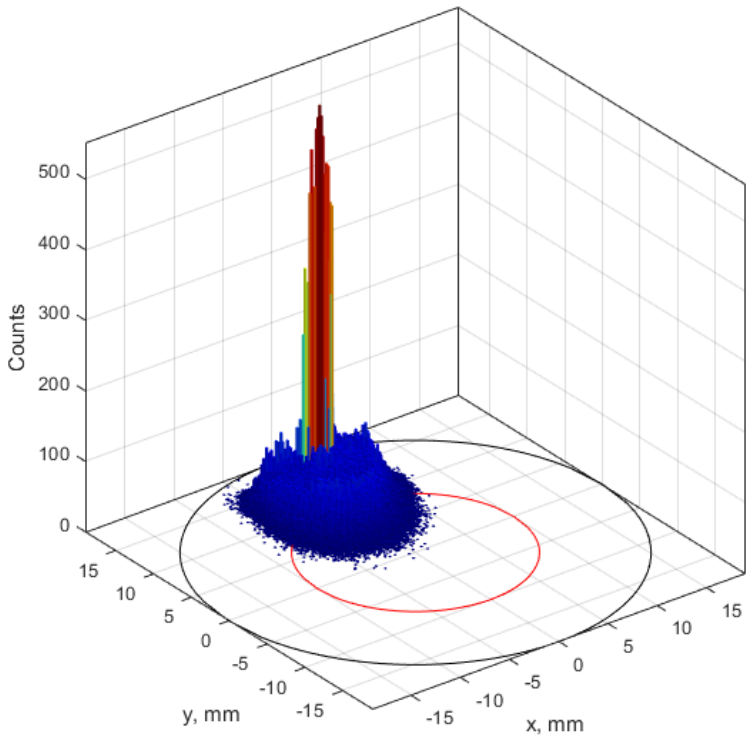


Figure 120: Histogram of x.y-coordinates for primary electrons of example.

The black circle designates the edge of the sample puck, and the red circle designates 10 mm from the center of the sample puck. A large number of electrons interact with one of the fasteners causing a large number of counts to appear near the point x = 0 mm, y = 12.6 mm.

The angular distribution of the incidence angles is shown in Figure 121. Normal incidence is indicated by an incidence angle of 90°. The electrons do not hit the sample puck normally which agrees with Figure 119.

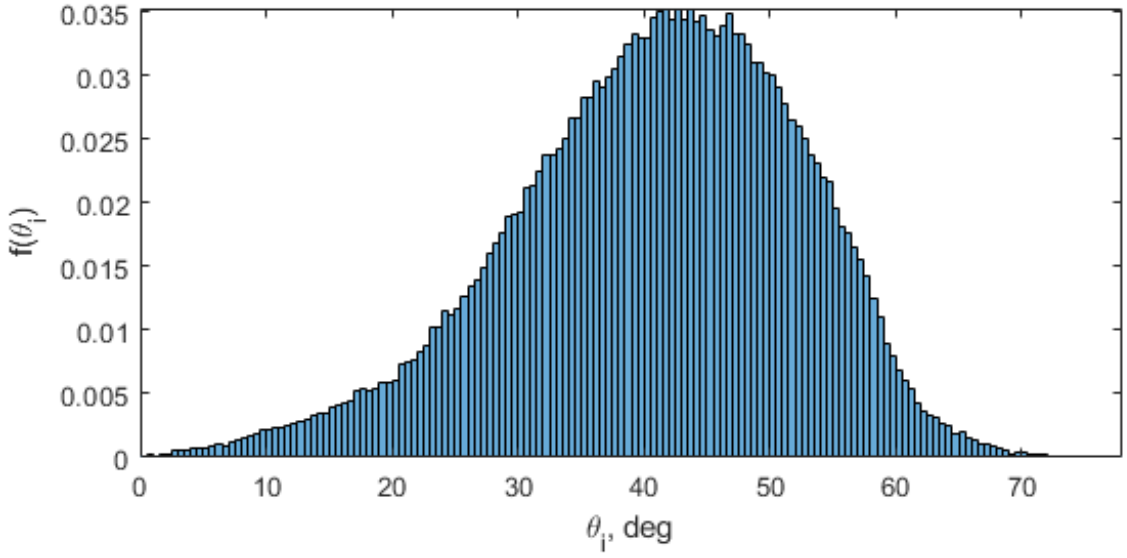


Figure 121: Angular distribution of primary electrons of example.

The energy distribution of the primary electrons is shown in Figure 122. The cathode emission energy distribution developed in Section 3.2.4 is overlaid on this distribution. The cathode emission energy distribution was shifted in energy based on the accelerating potential, sample bias, and work functions of the cathode and sample puck. The shape of the energy distribution of the primary electrons is approximately the same as the cathode emission energy distribution. It was assumed when calibrating the thermionic

emission model in Section 3.2.4 that these would have the same shape, and Figure 122 lends validity to this assumption.

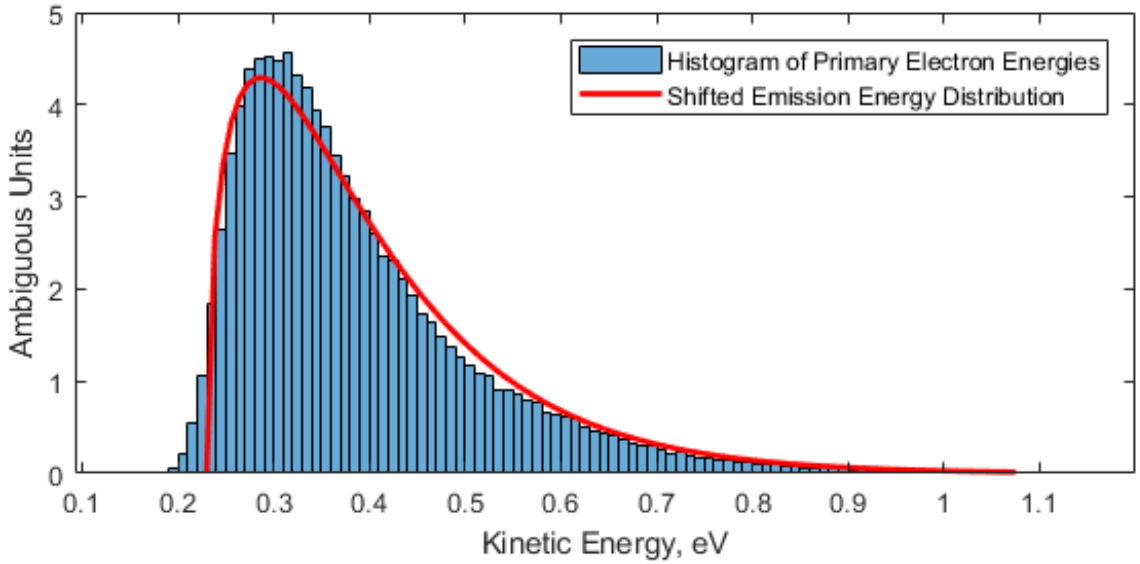


Figure 122: Energy distribution of primary electrons of example.

The BQF for this electron beam is 20.8%, which indicates that measurements performed using this beam largely violate Assumption 3. This example highlights the importance of including the sample puck and Faraday cup in the model. Without them, the simulation would yield a much higher BQF since the electrons would not be deflected by the asymmetric electric field between sample puck and Faraday cup. Thus, assessments made regarding the primary electron beam without including them are inaccurate, especially at low primary electron energies.

In addition to performing simulations to determine the optimum electron gun settings, the dependence of SEY on incidence angle may be utilized to optimize the primary beam experimentally for normal incidence. For amorphous and polycrystalline material, the SEY increases as the incidence angle decreases from 90° as discussed in Section 2.2.7. Thus,

the sample current is maximized when electrons are normally incident on the surface. The optimal electron gun settings are found by adjusting the optics of the electron gun until the sample current is maximized.

Implementing this technique comes with two challenges. The first challenge is specific to the ELG-2A electron gun. Adjustments to the 1st anode and grid potentials effect the primary electron current in addition the shape of the primary electron beam. Increasing the 1st anode potential increases the number of electrons pulled from the cathode and through the pre-focus beam stop aperture identified in Figure 123, and increasing the grid potential reduces the number of electrons entering the 1st anode. For this technique to be used, the primary current must remain constant. Therefore, the potentials of the 1st anode and grid must not be altered when using this technique, and only the focus potential may be varied in order to optimize the beam for each accelerating potential.

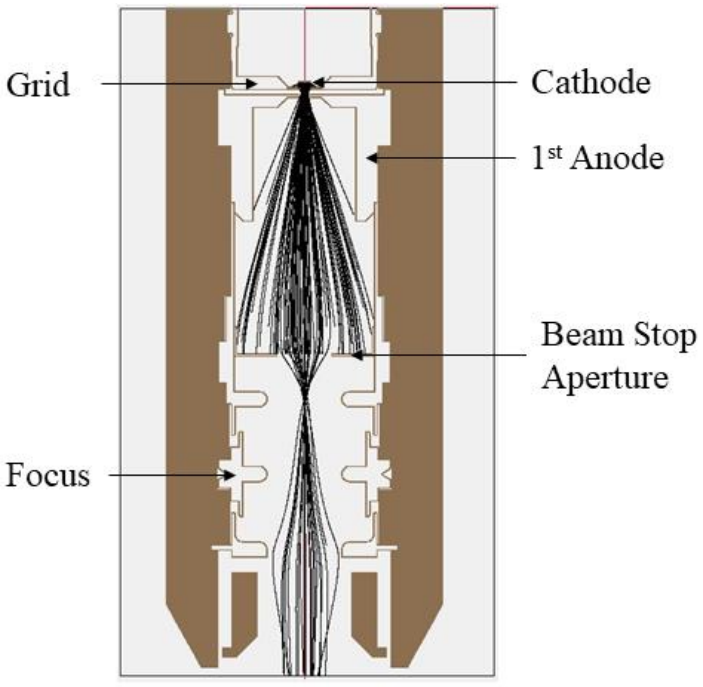


Figure 123: Diagram identifying location of pre-focus beam stop aperture. Electron trajectories are shown in black.

The second challenge is that the sample current may appear to maximize for more than one focus potential. In this case, the simulation model must be used in conjunction with experimental results to determine the optimum electron gun settings.

The technique is implemented in practice by sweeping the focus potential, $V_{FO}$, for each accelerating potential, $V_{EE}$. Initially, this process may require a large amount of time if there is no a priori knowledge regarding the range of focus potentials the optimal value lies within. The results from performing this technique are shown in Figure 124. The results correspond to primary electron impact energies between 21 and 31 eV.

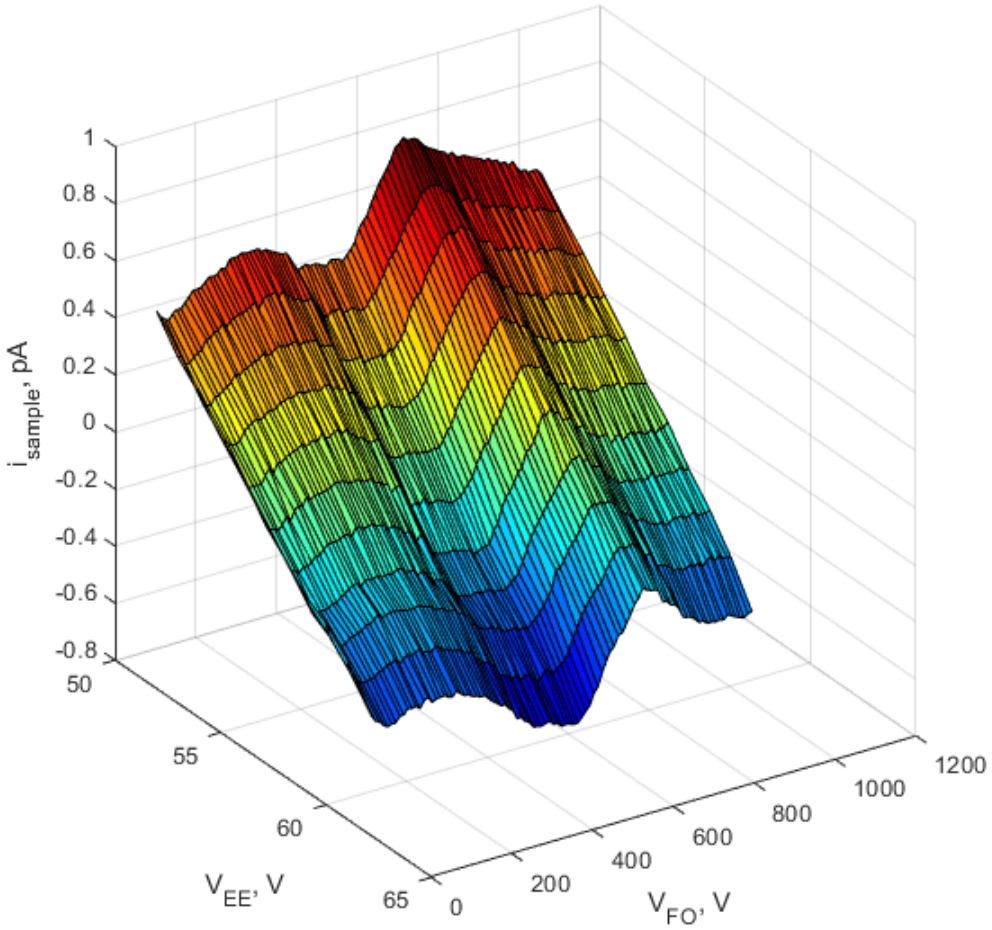


Figure 124: Surface plot of the sample current, $i_{sample}$, versus accelerating potentials, $V_{EE}$, and focus potentials, $V_{FO}$. The sample bias was -30 V for these measurements. The other potentials involved in these measurements are listed in Table 12.

The plot is made up of 1056 measurements at different accelerating and focus potentials. The potentials listed in Table 12 were held constant during these measurements. The chamber pressure was between $2.5 \times 10^{-9}$ and $5.8 \times 10^{-9}$ Torr. During these measurements which lasted 45 hours and 51 minutes, the temperature measured on the chamber increased from 28°C to 33°C which led to the large range of chamber pressures observed in the data but does not appear to have negatively impacted the measurement. The cause of this large rise in temperature is unknown. The sample current, $i_{sample}$, reverses directions in these measurements indicating that these measurements are near the first crossover energy. This data is also shown in the form of a contour plot in Figure 125.

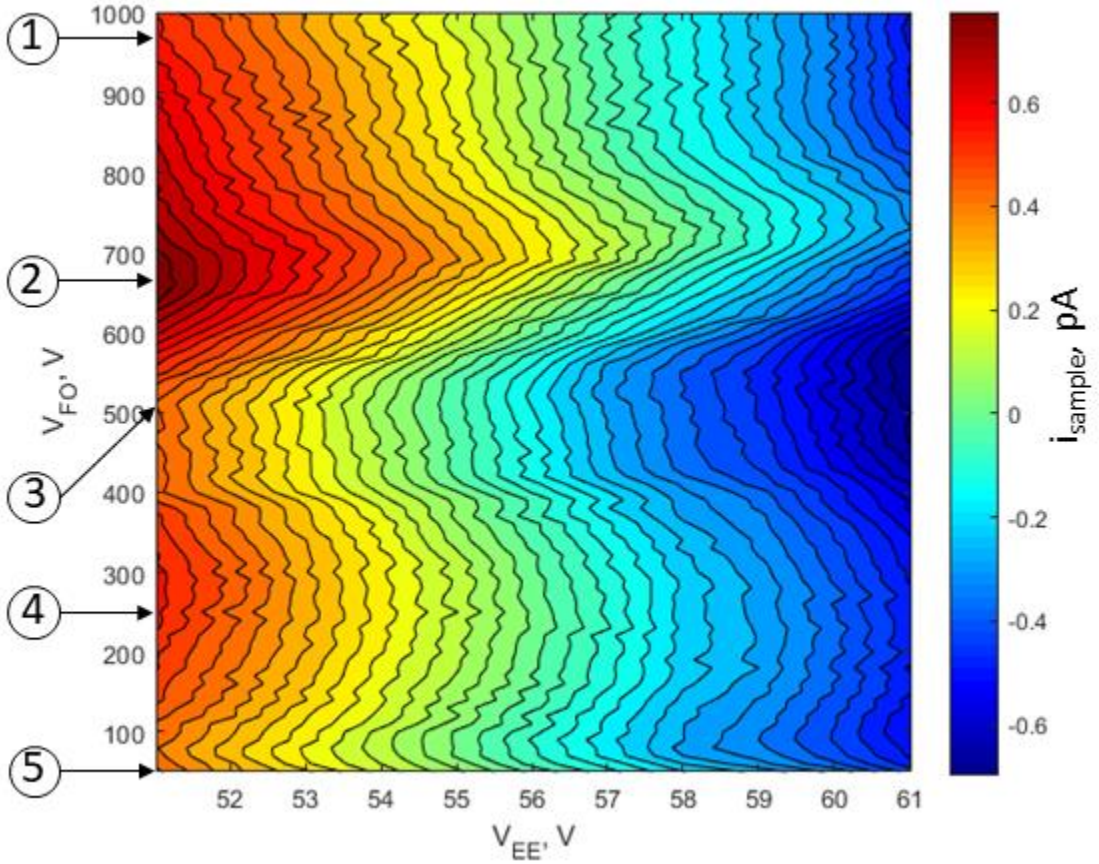


Figure 125: Contour plot of the sample current, $i_{sample}$, versus accelerating potentials, $V_{EE}$, and focus potentials, $V_{FO}$. The sample bias was -30 V for these measurements. Five locations are identified for further analysis.

Each accelerating potential appears to have maxima and minima near the same focus potentials. The maxima and minima identified in Figure 125 for an accelerating potential of 51 V will now be investigated individually.

Table 12: Potentials used in measurements involve primary electron energies between 21 and 31 eV.

| $V_{ES,}$ V | $V_G$, V | $V_{FA}$, V | $V_s$, V | $V_F$, μV |
|---|---|---|---|---|
| 711 mV | 0.00 | 10.0 | -30.018±0.004 | -0.3±0.3 |

At location 1, the focus potential is 980.9 V, and the beam diverges near the opening of the electron gun as shown in Figure 126.

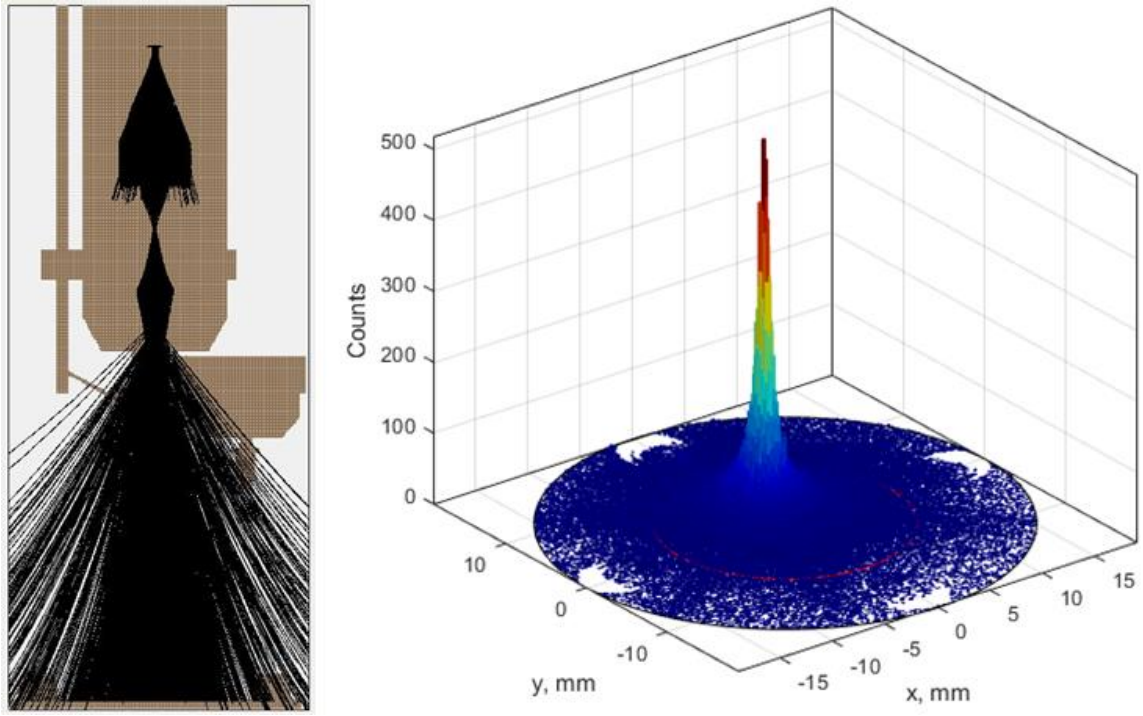


Figure 126: Electron trajectories (left) and histogram of incident locations on the sample surface (right) for location 1.

Despite this divergence, a large number of electrons land within the radius $r_w$ as shown in the histogram. The angular distribution is spread between 52.5° and 90°. The BQF is 68.5%.

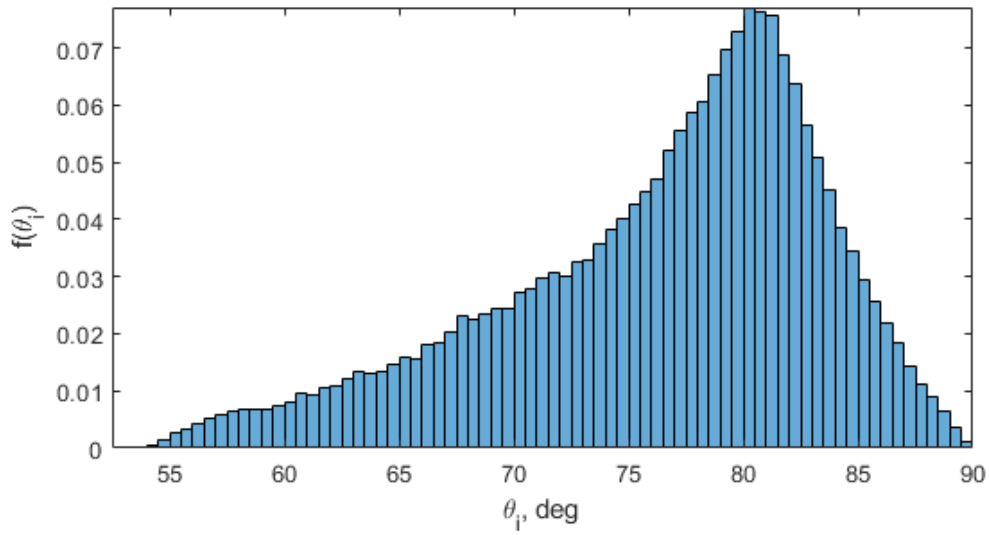


Figure 127: Angular distribution of primary electrons for location 1.

At location 2, the focus potential is 680 V, and the beam exhibits spreading after passing the Faraday cup as shown in Figure 128.

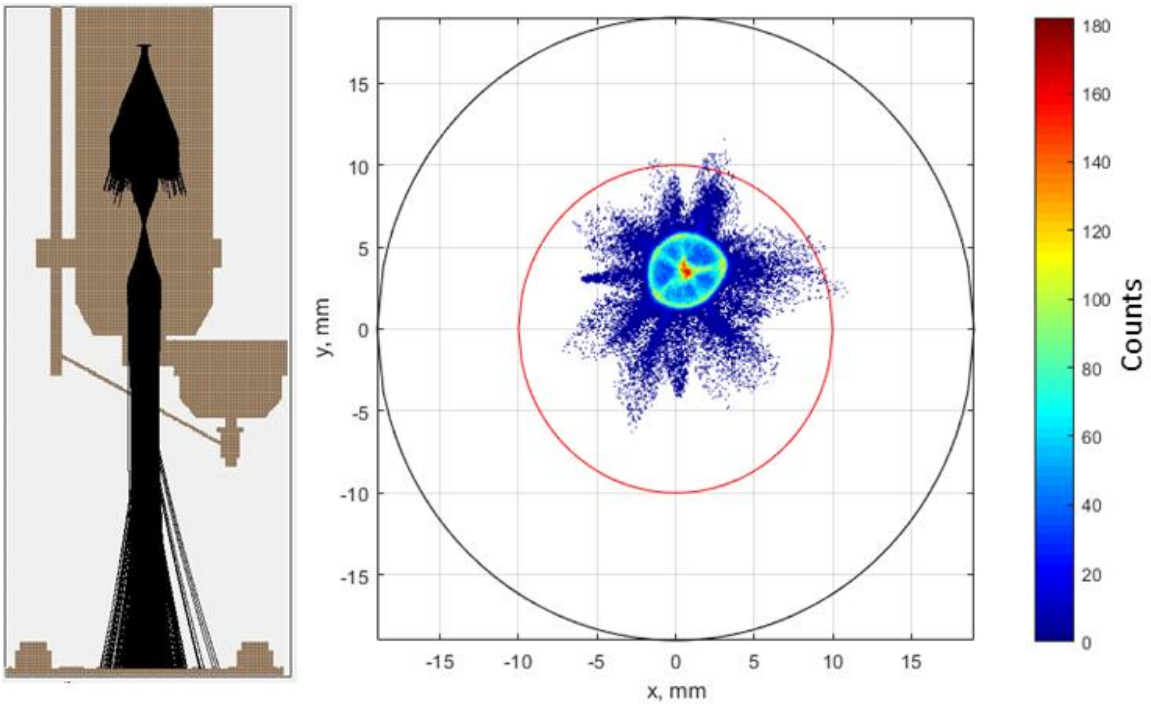


Figure 128: Electron trajectories (left) and histogram of incident locations on the sample surface (right) for location 2.

A large number of the electrons land within the radius $r_w$. The angular distribution is also much narrower than the previous location as shown in Figure 129. The BQF is 89.5%.

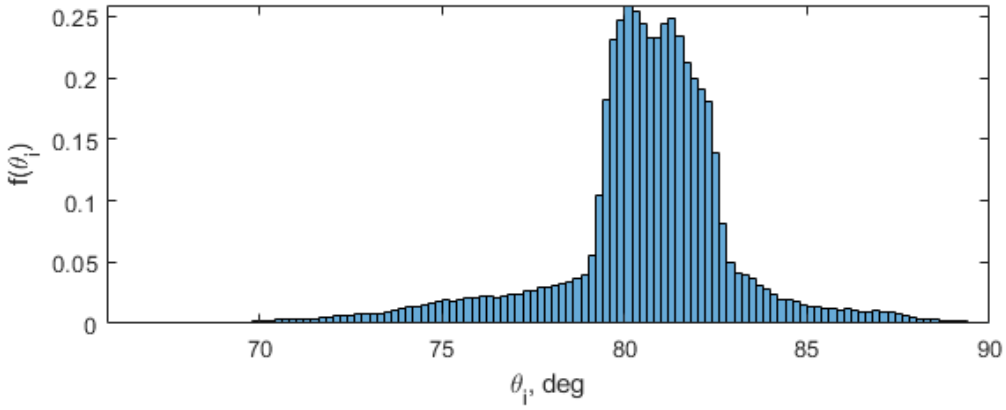


Figure 129: Angular distribution of primary electrons for location 2.

At location 3, the beam begins to diverge near the focus optic and appears to have fewer electrons in the center than on the perimeter of the beam as shown in Figure 130. The angular distribution is spread between 70° and 90°, the BQF is 82.2 %.

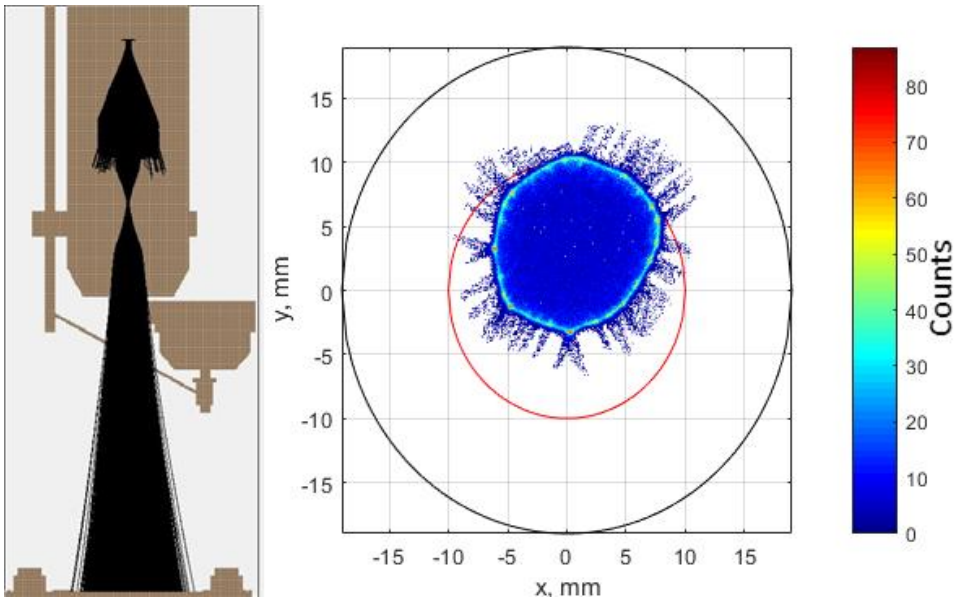


Figure 130: Electron trajectories (left) and histogram of incident locations on the sample surface (right) for location 3.

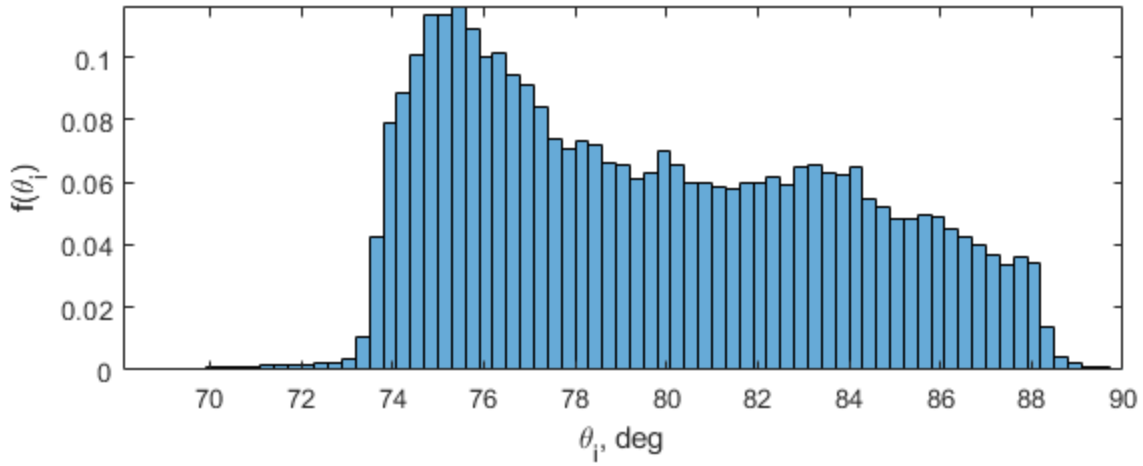


Figure 131: Angular distribution of primary electrons for location 3.

At location 4, the focus potential is 250.1 V, and the beam begins to diverge at the location of the focus optic as shown in Figure 132. A large number of the electron interact with the fasteners of the sample as indicated by the peaks in the histogram.

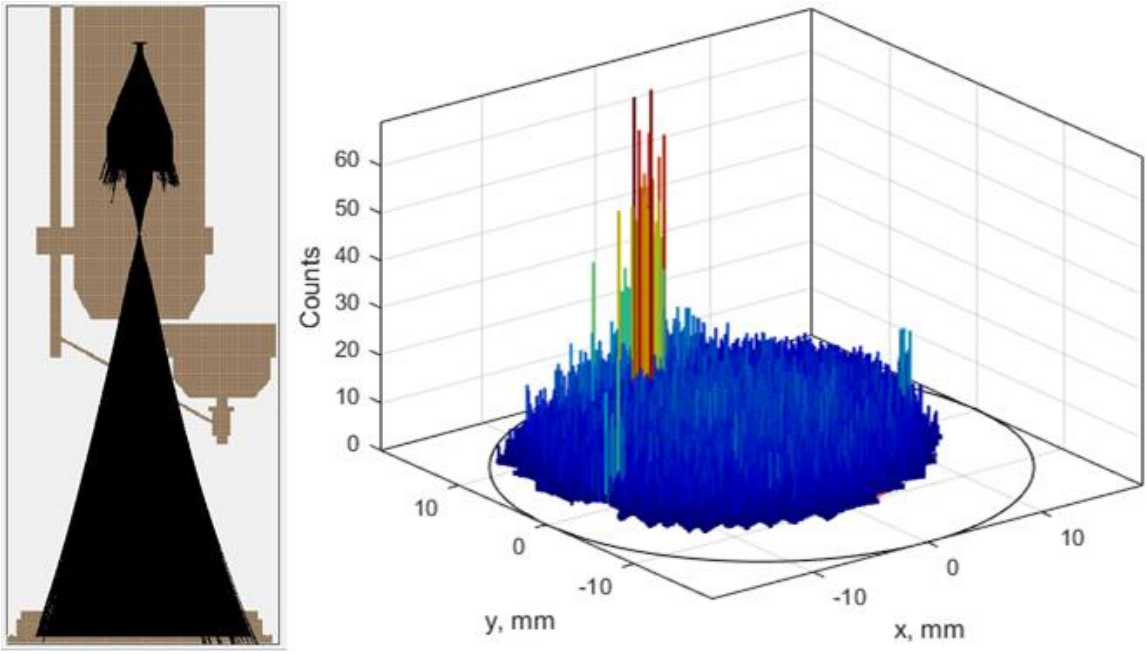


Figure 132: Electron trajectories (left) and histogram of incident locations on the sample surface (right) for location 4.

The angular distribution is spread between 58° and 90° as shown in Figure 133. Despite this location being a local maximum, the BQF is only 48.4%, and sample current is likely greater due to the interaction of the electrons with the fasteners.

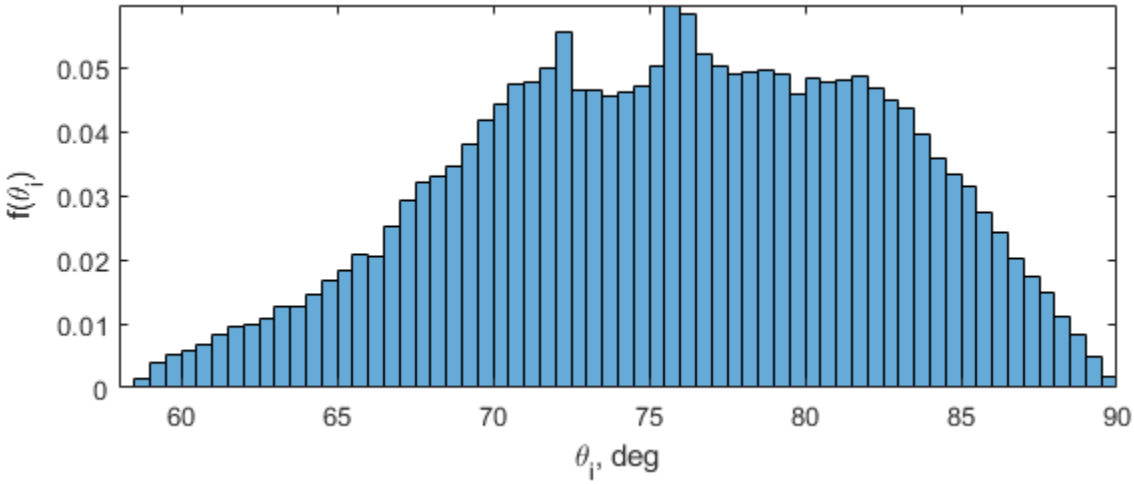


Figure 133: Angular distribution of primary electrons for location 4.

At location 5, the spot size on the sample puck is the smallest as indicated in Figure 134. The angular distribution is also the narrowest spanning approximately 8°. However, the BQF is 87.1% which is lower than that obtained for location 2. This location has a lower BQF because its angular distribution is centered around 78.5°. Whereas, the distribution for location 2 is centered around 81°, which is closer to the desired incidence angle of 90°. Since the angular distribution of location 5 deviates further from normal incidence, more secondary electrons will be emitted from the sample compared to location 2 decreasing the sample current.

In summary, the maximum sample current does correspond with the maximum BQF for the locations discussed. It was also shown that the sample current may have other maxima due to the interaction of the electrons with the fasteners and these maxima do not correspond to a high BQF. Furthermore, the results also indicate that the minimum spot

size does not guarantee the maximum BQF, and that the BQF is a better metric than spot size in determining the extent to which Assumption 3 is violated.

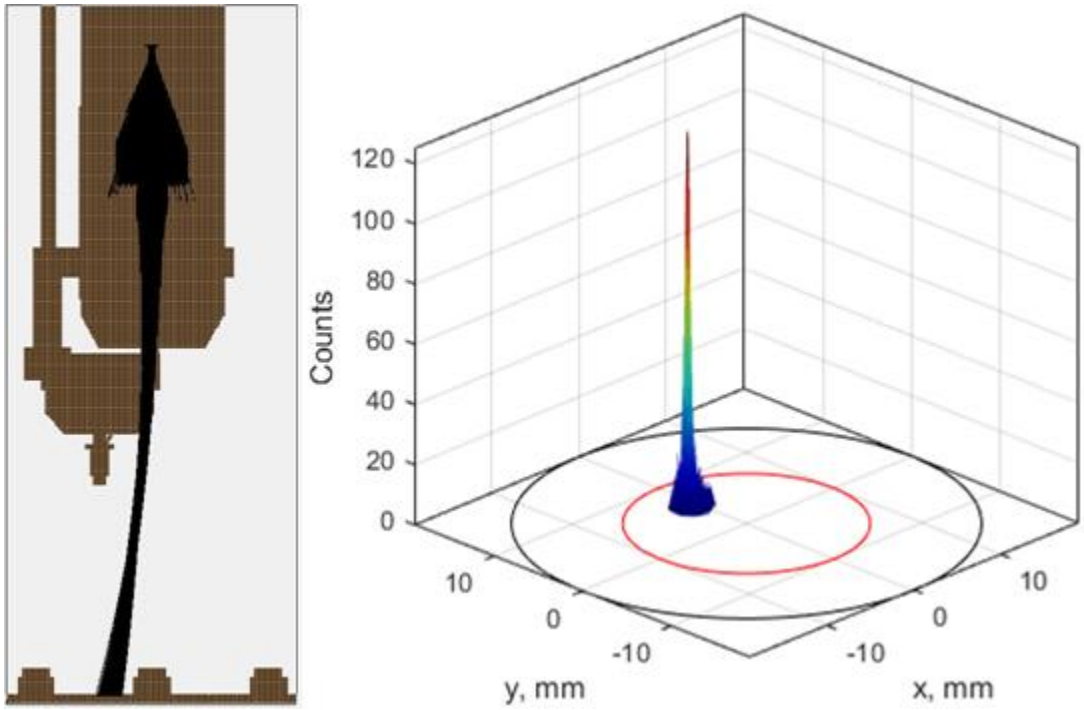


Figure 134: Electron trajectories (left) and histogram of incident locations on the sample surface (right) for location 5.

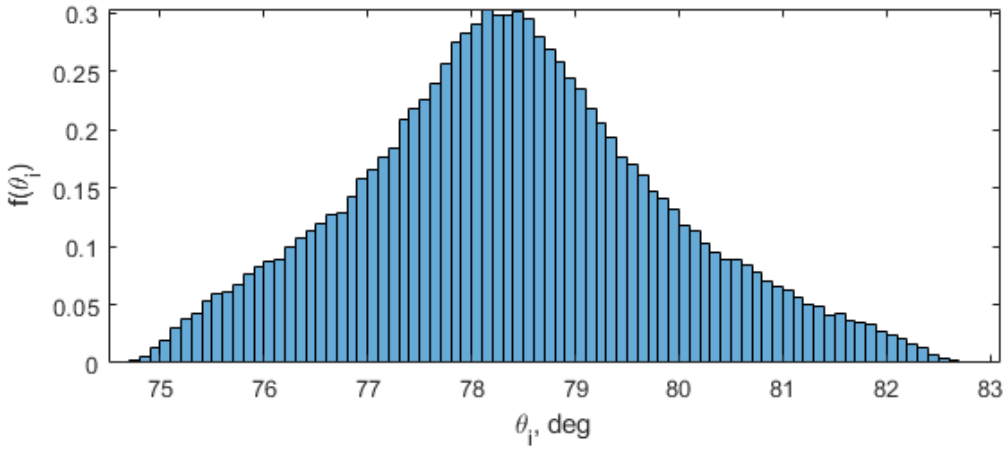


Figure 135: Angular distribution of primary electrons for location 5.

At lower primary electron energies, the shape of the curve for sample current versus accelerating potential and focus is similar to Figure 124 as shown in Figure 136, and the sample current may be used to determine the optical settings which produce the maximum

BQF. Figure 136 is made up of 506 measurements with the accelerating potential and sample bias decreased from those used in the aforementioned measurements. The measurements correspond to primary electron impact energies between 10 and 20 eV. The potentials listed in Table 13 were held constant during these measurements. The chamber pressure was between $2.3 \times 10^{-9}$ and $3.4 \times 10^{-9}$ Torr.

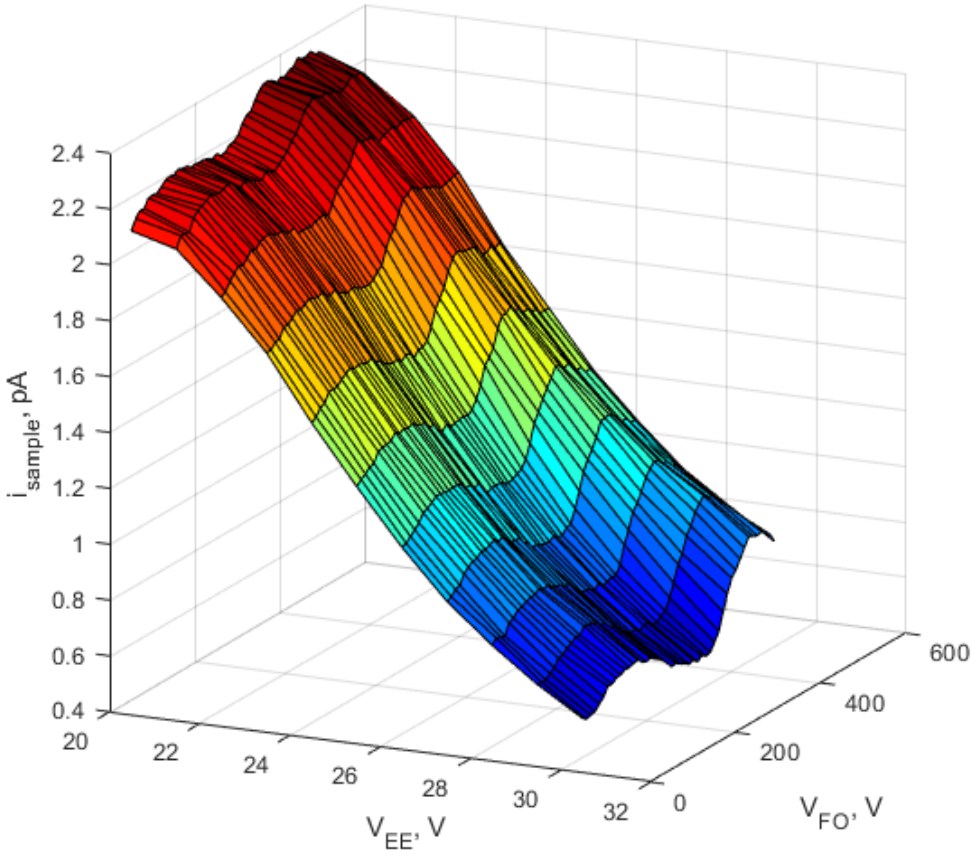


Figure 136: Surface plot of the sample current, $i_{sample}$, versus accelerating potentials, $V_{EE}$, and focus potentials, $V_{FO}$. The sample bias was -10 V for these measurements. The other potentials involved in these measurements are listed in Table 13.

Table 13: Potentials used in measurements involve primary electron energies between 10 and 20 eV.

| $V_{ES,}$ V | $V_G$, V | $V_{FA}$, V | $V_s$, V | $V_F$, μV |
|---|---|---|---|---|
| 711 mV | 0.00 | 10.0 | -9.99235±0.00025 | -0.15±0.25 |

At even lower primary electron energies, the maxima and minima for a given accelerating potential become less distinguishable as shown in Figure 137. At an accelerating potential of 5 V, the maximum occurs at a focus potential of 201.1 V, which is identified in Figure 137. The simulated example at the beginning of this section was based on the potentials associated with this maximum. Though the sample current is highest at this point, the BQF is only 20.8%. Using the sample current to determine the optimal electron gun settings is more difficult at low energy since the maxima and minima for a given accelerating potential are more difficult to locate.

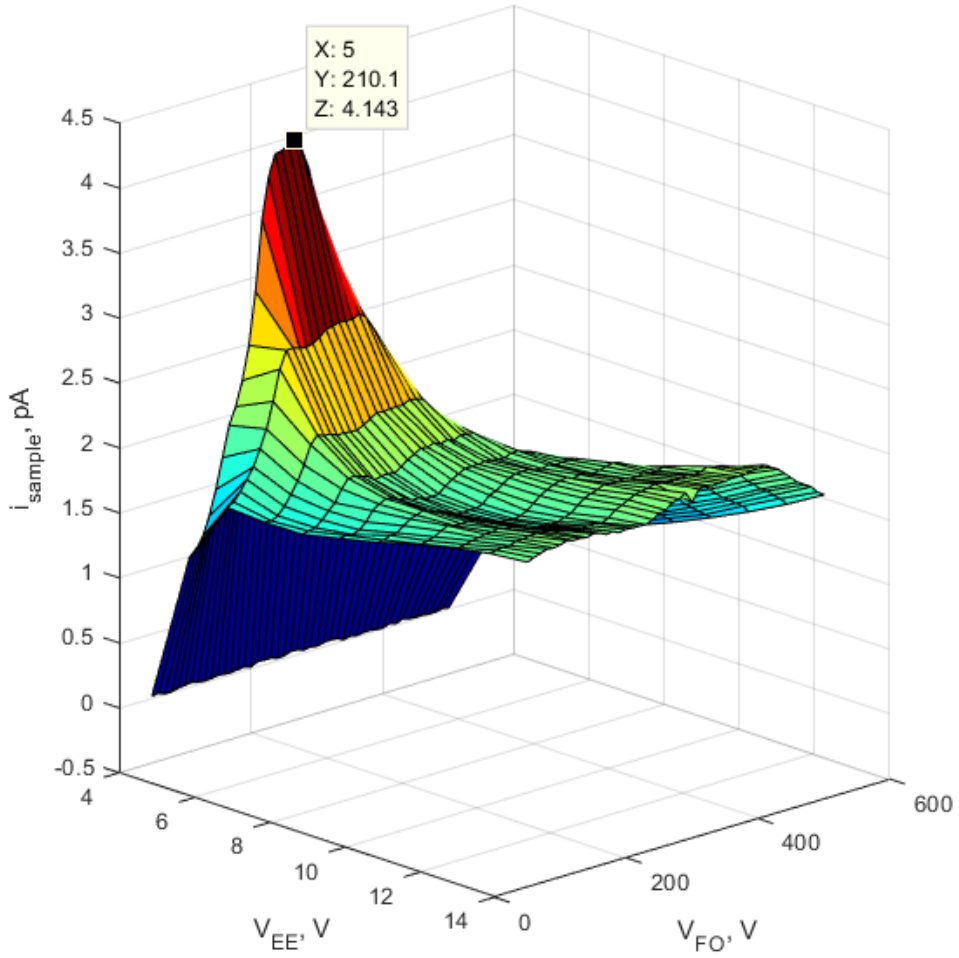


Figure 137: Surface plot of the sample current, $i_{sample}$, versus accelerating potentials, $V_{EE}$, and focus potentials, $V_{FO}$. The sample bias was -5 V for these measurements. The other potentials involved in these measurements are listed in Table 15.

Table 14: Potentials used in measurements involve primary electron energies between 0 and 9 eV.

| $V_{ES,}$ V | $V_G$, V | $V_{FA}$, V | $V_s$, V | $V_F$, μV |
|---|---|---|---|---|
| 710 mV | 0.00 | 10.0 | -5.017±0.0002 | -0.25±0.25 |

### 4.5 Magnetic Type I Contrast Sample

In the previous section, the maximum BQF listed is 89.5% for an acceleration potential of 51 V and a sample bias of -30 V. The BQF is degraded from 100% by the deflection due to the asymmetric field caused by biasing the sample. In order to prevent this deflection, the sample bias must be removed. However, in the experimental system, the sample was negatively biased in order to prevent tertiary electrons from reaching the sample. Thus, another method is needed to suppress the tertiary electrons without having to negatively bias the sample.

Magnetic materials are known to alter the trajectories of secondary electrons creating a contrast in SEM images known as a magnetic contrast type I [149, 150]. Yuan *et al.* indicated that with strong magnetic fields the secondary electrons could be confined to the sample [150]. In order to determine, if this effect could be used to prevent tertiary electrons from leaving the walls of the chamber, neodymium magnets were attached in a checkerboard pattern of north and south polarities to the back of a 316SS disk as shown in Figure 138. The magnets were alternated in polarity to provide cancellation of the magnetic field far from the magnets in order to prevent disturbing the primary electron beam. It is easier for the secondary electrons to leave the sample along the magnetic field lines which extend further above the sample as shown in Figure 139. This leads to brighter pixels in SEM image above the center of the magnets as shown in Figure 140. The region of the disk

containing magnets underneath appears darker in SEM images than the region without as shown in Figure 141, which indicates fewer secondary electrons are escaping this magnetized region of the disk.

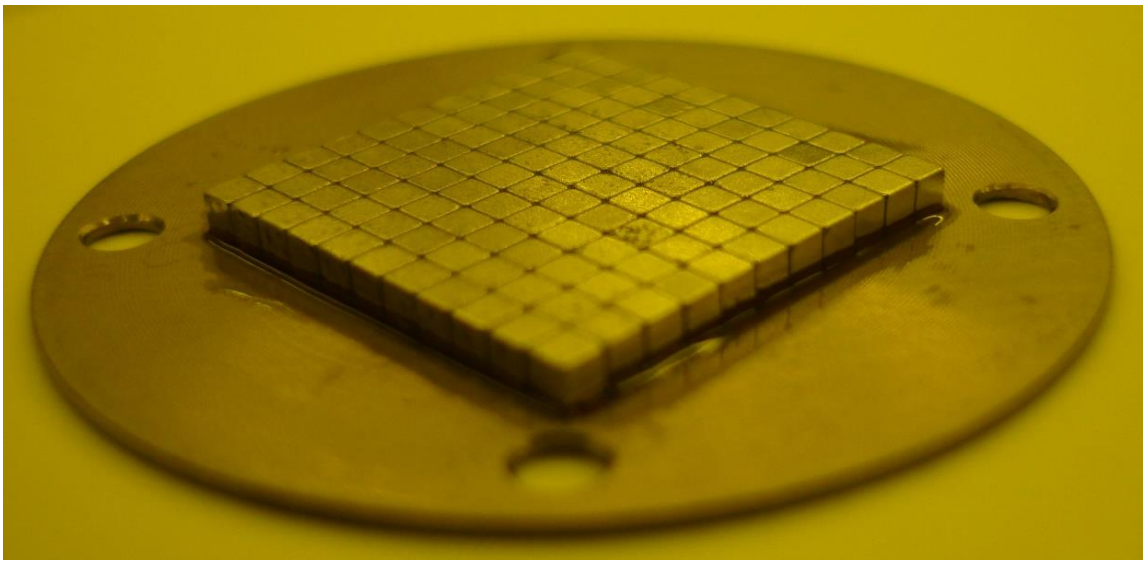

Figure 138: Checkboard pattern of magnets attached to the back of a 316SS disk.

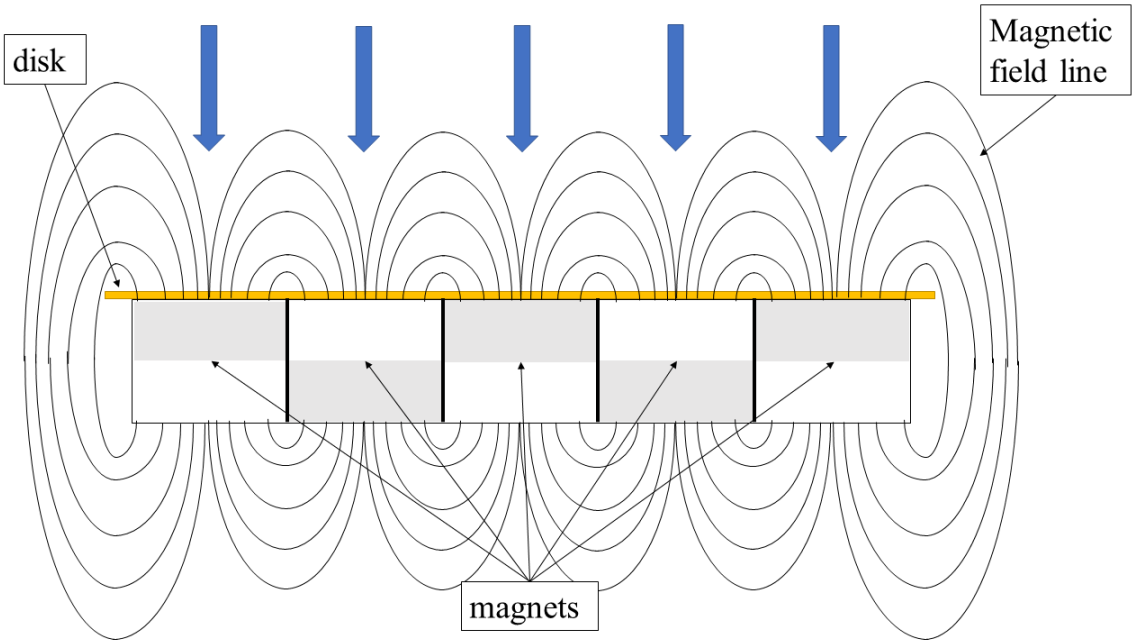


Figure 139: Cross-sectional drawing of magnetic field lines for magnetized 316SS disk. The blue arrows indicated the locations where secondary electrons can more easily escape from the surface of the disk.

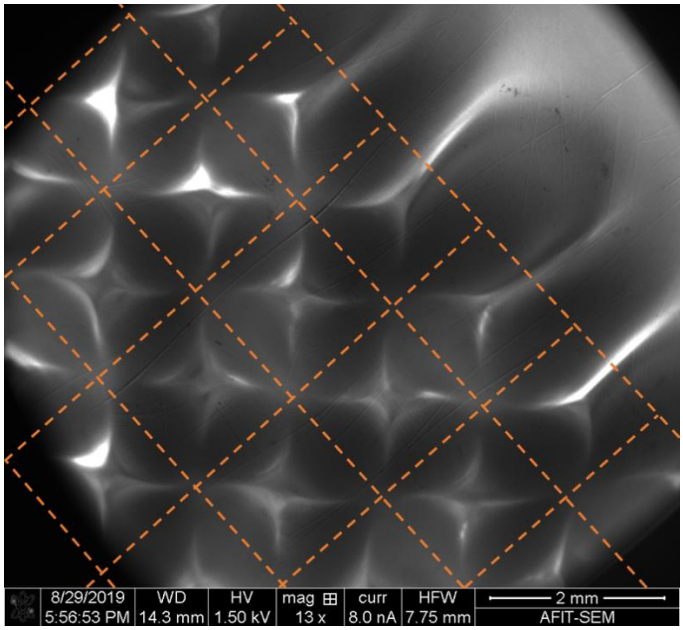

Figure 140: SEM image of the top 316SS disk with magnets underneath. The orange dashed lines correspond to the edges of the magnets.

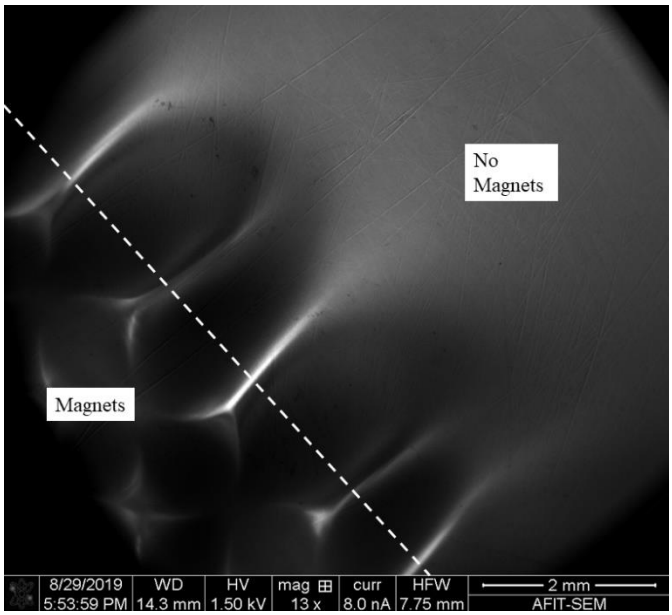

Figure 141: SEM image comparing magnetized and non-magnetized region of the 316SS disk.

This disk was first tested with primary electrons of low energy. The potentials used in this test are shown in Table 15. The chamber pressure was between $3.8 \times 10^{-9}$ and $4.0 \times 10^{-9}$ Torr. At an accelerating potential of 0 V, electrons were still able to reach the magnetized

disk when the sample was biased to -10 V. In the previous results for the sample puck, electrons were unable to reach the sample when the accelerating potential was 0 V and the sample bias was decreased to less than -1.1 V.

Table 15: Potentials for testing magnetized sample at low primary electron energies.

| $V_{ES,}$ V | $V_G$, V | $V_{FA}$, V | $V_s$, V | $V_F$, μV |
|---|---|---|---|---|
| 710 mV | 0.00 | 10.0 | -9.9725 ±0.0003 | -0.25±0.35 |

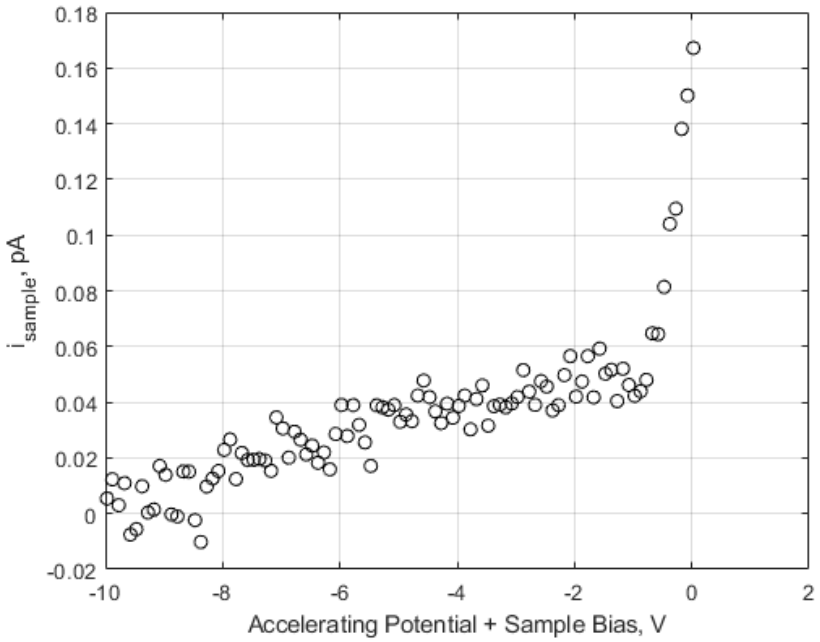


Figure 142: Sample current for magnetized sample at low primary electron energies.

This difference may be a result of two possibilities. The first is that the thermionic energy distribution contains electrons with more energy than was previously estimated (i.e. the energy distribution shown in Figure 102 should span over 10 eV). However, this is very unlikely since the simulation results agree well with the experimental data previously presented and the cathode would exceed the melting point of tantalum in order to produce a detectible number of electrons with more than 10 eV of kinetic energy. The second is that the electron-electron interactions (i.e. space charge effects) allow some of the electrons to

overcome the energy barrier posed by the negatively biased sample. The magnetic field acts like funnels which channel electrons down towards the center of each magnet increasing the likelihood of these interactions occurring. It is more likely that this possibility is true, but it cannot be varied with SIMION® due the its limitations regarding space charge.

The primary electron beam is distorted by the magnetic field surrounding the disk making it difficult to determine how the primary electrons are interacting with the sample. In order to determine if the disk was successful at retaining the secondary electrons, the disk was tested at several focus potentials for each accelerating potential. The disk was biased to -10 V in order to reduce the number of tertiary electrons reaching the disk from the chamber walls. Since negatively biasing the sample reduces the ability of the magnetic field to retain secondary electrons, the bias on the disk was not decreased from -10 V. The potentials used in this test are shown in Table 16. The chamber pressure was between $3.2x10^{-9}$ and $3.6x10^{-9}$ Torr.

Table 16: Potentials used in testing magnetized sample while varying the accelerating and focus potentials.

| $V_{ES,}$ V | $V_G$, V | $V_{FA}$, V | $V_s$, V | $V_F$, μV |
|---|---|---|---|---|
| 711 mV | 0.00 | 10.0 | -9.9874 ±0.0004 | -0.2±0.2 |

The results of these test are shown in Figure 143. When the focus potential, $V_{FO}$, equals 100 V, the sample current remains positive. Previously, the sample current for sample puck alone became negative when $V_{EE} + V_{ss}$ exceeded approximately 30 V. This indicates that secondary electrons are being retained at the disk by the magnetic field preventing the sample current from reversing directions. Thus, the SEY remains less than one. However, the sample current remained small (<1.5 pA) compared to the primary electron current

which was approximately 6.5 pA based on previous measurements. The current may be small due to the current limiting effect of space charge or the deflections of primary electrons away from the disk by the magnetic field. This reduction in current indicates that the magnetized sample may not function well when used as an electron absorber.

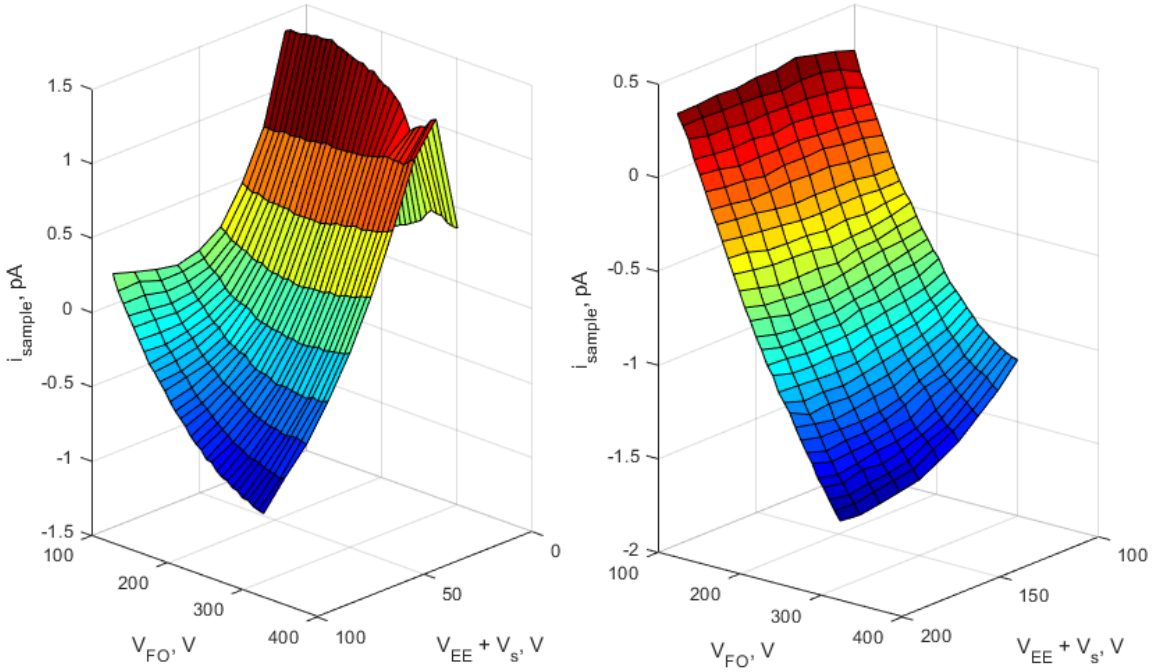


Figure 143: Surface plot of the sample current, $i_{sample}$, versus accelerating potentials, $V_{EE}$, plus sample bias, $V_s$, and focus potentials, $V_{FO}$ from measurements involving magnetized sample. The other potentials involved in these measurements are listed in Table 16.

When the focus potential is increased from 100 V, the sample current is able to reverse directions. This reversal may be caused by primary electrons interacting with the regions of the disk which are not magnetized or the unsuccessful retention of secondary electrons. In order to determine that the magnetized sample is successful at retaining a majority of the secondary electrons under all conditions, the magnetic checkboard must be extended to encompass the entire back of the disk. This was not accomplished due to the time constraints of this research. In summary, this research indicates that it may be possible to reduce secondary electron emission using a checkboard pattern of magnets under a

conductive surface; however, additional testing is necessary to confirm that secondary electron emission will be reduced for all test conditions.

### 4.6 Summary

In this chapter, several discoveries were made that may enable greater accuracy and repeatability in SEY measurements. First, it was discovered that measurements of SEY are sensitive to the primary electron current involved in the measurements. This does not indicate that the SEY is current dependent, which would be in opposition to the belief currently held by the scientific community. Rather, it indicates that other factors, such as space charge or variations in the energy distribution of the primary electrons, may cause the measurements of the SEY appear current dependent. Second, it was discovered the shape of the primary electron beam is more sensitive to the spacing between the sample and electron gun when the negative bias of the sample is large. Thus, it is important to reduce this bias as much as possible to prevent the distortion of the primary electron beam. Third, it was found the first crossover is sensitive to the electron gun settings, and it varied by over 6 eV for the tests performed in this chapter. This sensitivity highlighted the need for a new metric for defining the quality of the primary electron beam hence the BQF metric was developed. Fourth, it was discovered that the BQF is a better metric for determining beam quality than spot size since the BQF takes into consideration the incidence angle of the primary electrons. Fifth, it was found that a relationship exists between the maximum sample current and the BQF. This relationship may be used to fine-tune the primary electron beam experimentally. Sixth, it was discovered that under certain conditions the magnetic type I contrast may be used to reduce the SEY to less than one,

which warrants further investigation to determine if secondary electron emission can be reduced for all conditions. Lastly, it was found that the magnetized sample appears to limit the primary electron current reaching the sample which reduces its usefulness as an electron absorber.

# V. Conclusions and Recommendations

This chapter summarizes the finding of this research and provides guidance for improving the accuracy of SEE measurements. Section 5.1 answers the research questions identified in the objectives of Chapter I. Section 5.2 provides guidance for improving the accuracy of measurements based on this research. Section 5.3 provide a roadmap of the continuing research effort. Section 5.4 lists the key contributions of this research.

## 5.1 Answers to Research Questions

In Chapter I, eight objectives for this research were specified. Six of those objectives were directed towards answering the following questions.

1) What are the factors, excluding sample composition, which may lead to measurement discrepancies?

In Chapter II, it was determined that seven assumptions are commonly made during SEY measurement as well as other types of SEE measurement. These assumptions are

1. The measured SEY at one location on a sample's surface is applicable to the entire surface.
2. The effects of contact potential difference are negligible.
3. The primary electrons impact the sample surface at the desired incidence angle and energy.
4. Space charge is negligible.
5. Earth's magnetic field is negligible.
6. The primary electron current can be accurately measured using a Faraday cup or by positively biasing the sample.
7. The measurement results are solely due to the SEE interaction taking place on the sample's surface involving primary and secondary electrons and all other interactions occurring in the vacuum chamber are negligible.

The violation of these assumptions is the factor that will lead to measurement discrepancies. Therefore, it is important to either minimize these violations or

assume some of the assumptions listed are non-negligible and appropriately correct for them in the measurements.

2) How are SEY measurements affected by the use of different primary electron currents?

In Chapter IV, it was shown that differences in the primary electron current altered the ratio between the sample current and Faraday cup current, which leads to an SEY estimate that varies with the primary current. This result does not indicate that the SEY is current dependent. Instead, it indicates that measurements of SEY may be current dependent due to factors such as space charge, the energy distribution of the primary electrons, and nonlinearities in the measurement system. Furthermore, it indicates that assumptions 3 and 4 may have been violated.

3) How does the spacing between the electron gun and sample effect SEY measurements?

In Chapter IV, it was discovered that the primary electron energy associated with the electrons beginning to interact with the sample is sensitive to the spacing between the electron gun and sample when a large negative bias (-195 V) is applied to sample. It was determined that this sensitivity is due to the deflections of electrons by the asymmetric electric field between the sample and Faraday cup. These results indicated severe violations of Assumption 3. Reducing the sample bias decreases the deflection. However, the deflection cannot be eliminated entirely without properly biasing the sample to eliminate the electric field between the sample and Faraday cup based on their CPD or removing the Faraday cup from the end of the electron gun.

4) How is the first crossover of the SEY curve altered by changing the potential of the electron gun optics?

Though in principle the primary electron energy associated with the first crossover is easy to measure, the results shown in Chapter IV indicate that this energy is sensitive to the electron gun's optical settings. For the settings which were tested, this energy varied by more than 6 eV. This variation was due to changes in the shape of the primary electron beam, which led to violations of Assumption 3.

5) How can the electron gun's optics be adjusted in order to reduce SEY measurement errors?

In order to reduce SEY measurement errors, the electron gun's optics must be adjusted to minimize the violation of Assumption 3. A new metric, called BQF, was developed in Chapter IV which provides a quantitative means of determining how well the primary electron beam satisfies Assumption 3. The optimal electron gun settings may be found by calculating the BQF for different electron gun settings using the simulation model. The settings which produce the highest BQF best satisfy Assumption 3. In addition, measurements of the sample current may be used to determine the optimal electron gun settings for measurements performed at normal incidence as described in Chapter IV. This method requires varying the focus potential of the electron gun until the sample current is maximized for a given $1^{st}$ anode, grid, and accelerating potential.

6) Can the magnetic type I contrast effect be used to reduce secondary emission from the vacuum chamber walls during SEY measurements?

The results shown in Chapter IV indicate that it may be possible to reduce secondary electron emission using the magnetic type I contrast effect. Unfortunately, the results of the measurements performed on the magnetized 316SS disk did not confirm that the SEY would remain below one for all focus potentials of the electron gun, and it is unknown if the electron beam may have been interacting with the unmagnetized portion of the disk. Additional testing is necessary to confirm that secondary electron emission is indeed reduced for all variations in the primary electron beam. The magnetic field appears to limit the primary electron current reaching the surface of the disk. This diminishes its usefulness as an electron absorber. Ideally, the vacuum chamber walls will absorb all the secondary electrons from sample during SEY measurements. Thus, the current limiting effect of the magnetic type I contrast may prohibit its use in reducing secondary electron emission from the vacuum chamber walls.

## 5.2 Guidance for Improving Measurement Accuracy

Throughout this research, the challenges associated with performing SEE measurements have become increasing apparent, especially in the case of low energy SEY measurements. The highest accuracy is obtained by satisfying all the assumptions listed in the previous section. However, this is impossible to achieve in practice. In most cases, the first assumption can be readily satisfied by increasing the diameter of the primary electron beam. However, if the sample has large features, measurements should be performed at several locations and averaged. This is accomplished by translating the sample rather than

scanning the electron beam since scanning the electron beam leads to a variation in the incidence angle.

Since materials often have different work functions, Assumption 2 cannot be satisfied in many cases. For low energy measurements, this assumption should be avoided since the CPD may be of the same order of magnitude as the primary electron energies. The CPD must be determined in situ because exposure to the atmosphere will alter the surface chemistry of the sample leading to a change in the sample's work function. The method developed in Section 3.2.4 may be used in estimating the work function of the sample. However, measurements of the work function using the Kelvin probe method or the photoelectric effect will provide addition additional information that will aid in better determining the work functions that should be applied to each electrode within the measurement system. Since the electric field within the system is determined based on both the measured potential and work function of each electrode, the simulation model will provide the most accurate results when both are incorporated into the model.

Much of this research focused on satisfying the incidence angle aspect of Assumption 3. The methods developed in this research involving the BQF may be used in determining the electron gun settings that best satisfy the incidence angle requirement. As observed in the results section of this research, an asymmetric electric field should be avoided due the deflecting effect this has on the primary electrons. This requires either eliminating the electric field entirely between the electrodes that are causing the asymmetry or redesigning the measurement system without these electrodes. Assumption 3 also requires that all the primary electrons arrive at the sample with the same energy. In practice, this is impossible. The cathode temperature may be decreased to reduce thermal spreading

(see Section 3.2.4). However, this also reduces the currents being measured which leads to a lower SNR. Alternatively, a different cathode may be selected, or an energy analyzer may be used to filter out electrons that do not have the desired energy. In any case, the primary electrons can never be made to arrive at the sample with precisely the same energy. Nevertheless, the energy distribution for the primary electrons may be determined and then deconvolved with the measured SEY curve to yield the true SEY curve [7].

Assumption 4 becomes increasing challenging as the primary electron energy is reduced since electrons are traveling more slowly and have more opportunities to interact with each other. Space charge effects are mitigated by reducing the currents involved in measurement. However, reducing the current also creates additional challenges caused by the reduction in the SNR. To fully examine this problem will require the aid of simulation models which are capable of simulating electron-electron interactions. In general, scenarios that confine electrons to a small volume should be avoided whenever possible when performing measurements.

Assumption 5 may be satisfied by shielding the vacuum chamber from external magnetic fields using a material with high permeability, such as mu-metal, or by negating the magnetic field with a second magnetic field. One of the challenges observed in this research is determining the magnetic field within the vacuum chamber and near the electron gun. Assuming that the magnetic field within the chamber is same as the magnetic field outside the chamber is prone to error since the chamber is composed of materials that are slightly magnetic. Placing a magnetometer within the chamber and near the electron gun is the best way to determine if Assumption 5 is satisfied. If Assumption 5 is not satisfied, the

incidence angle of the primary electron beam may be shifted from the desired incidence angle as the primary electron's energy is decreased.

Satisfying Assumption 6 presents two challenges. The first challenge is capturing all of the electrons leaving the electron gun in order measure the current associated with the primary electron beam. By increasing the positive bias of the sample or Faraday cup, progressively more electrons are captured and the measured current increases as indicated by Figure 144. The positive bias may be increased to the limits of the measurement apparatus and still not capture all of the electrons leaving the electron gun.

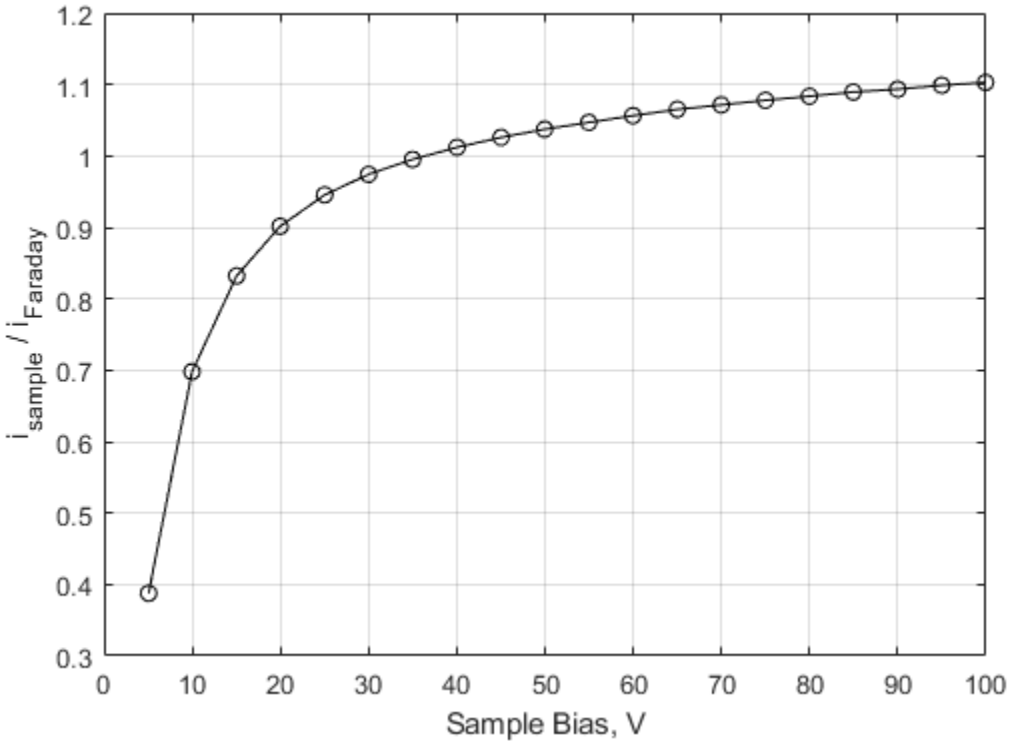


Figure 144: Ratio of the sample current in the open position to the Faraday cup current in the closed position versus sample bias. This figure is an adaptation of Figure 67. The Faraday cup bias and electron gun settings were held constant for these measurements.

The largest permissible positive bias should be used in order to measure this current, and the geometry of the Faraday cup also helps to capture more of these electrons providing a

more accurate measurement of this current. However, this current is not the primary electron current that reaches the sample surface since not of all electrons which leave the electron gun may reach the sample surface. The second challenge is determining the primary current based on the current leaving the electron gun. For higher primary electron energies (>10 eV), most of the electrons leaving the electron gun can be directed into the sample. Thus, the primary current and current leaving the electron gun are approximately equal. For lower energies (<10 eV), directing the electrons into the sample becomes more challenging due to beam defocusing and possibly space charge effects. In this case, simulation models in addition to measurements should be used to assess the primary current.

Proving that Assumption 7 has been satisfied or the extent to which it has been violated is more difficult compared to the other assumptions. Given the nature of this assumption, it is not directly measurable. Thus, it requires the iterative process discussed in the beginning of Chapter III. Unfortunately, literature regarding this topic is scarce. This research originally set out to investigate this topic in greater detail but was prohibited due to software problems and time constraints. Based on literature, the biggest challenge to overcome in order to satisfy this assumption is suppressing tertiary electrons while simultaneously avoiding defocusing of the primary electron beam [56].

In addition to attempting to satisfy the assumptions, these measurements are considered low-level measurements requiring additional considerations to perform accurately and with low noise. The discussion regarding the development of the experiment system used in this research provides insight into these considerations when developing an experimental system to measure SEE. Perhaps, the most critical factor learned from the developed of the

system was the timing of measurements in order to avoiding transients, which allowed measurements of currents in the fA range.

### 5.3 Roadmap of Future Research

This research was a first step in trying to improve the accuracy of SEE measurements with a focus on SEY measurements. The following steps listed below are the planned future research.

**1) Replacement of Faraday cup with a horn-shaped collector**

Due primarily to the asymmetric electric field created by the Faraday cup, the cup will be replaced by a horn-shaped collector as shown in Figure 145 and Figure 146. The updated design will provide the following benefits:

a) No asymmetric electric field to cause primary electron beam deflection

b) Faster measurements since measurements do not involve the step of moving the Faraday cup and waiting for the associated transient to settle

c) No repetitious movement of mechanical parts during measurements which could eventually lead to a mechanical failure

d) Greater accuracy in determining thermionic emission distribution since secondary emission from the sample can be suppressed by negatively biasing the collector during measurements of the distribution

e) Higher BQF due to less beam defocusing with the removal of the negative sample bias

f) Simplification of the simulation model to 2D since the apparatus is approximately cylindrically symmetric when the Faraday cup is removed

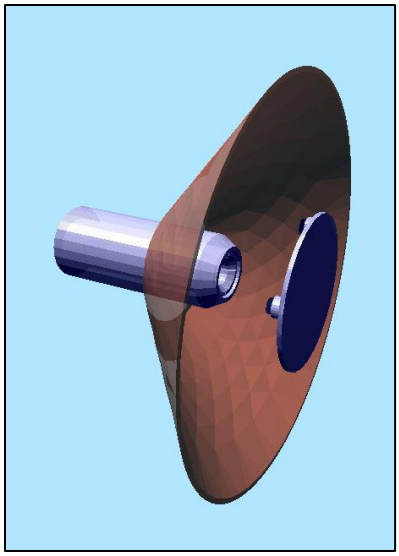

Figure 145: Horn-shaped collector mounted at end of electron gun.

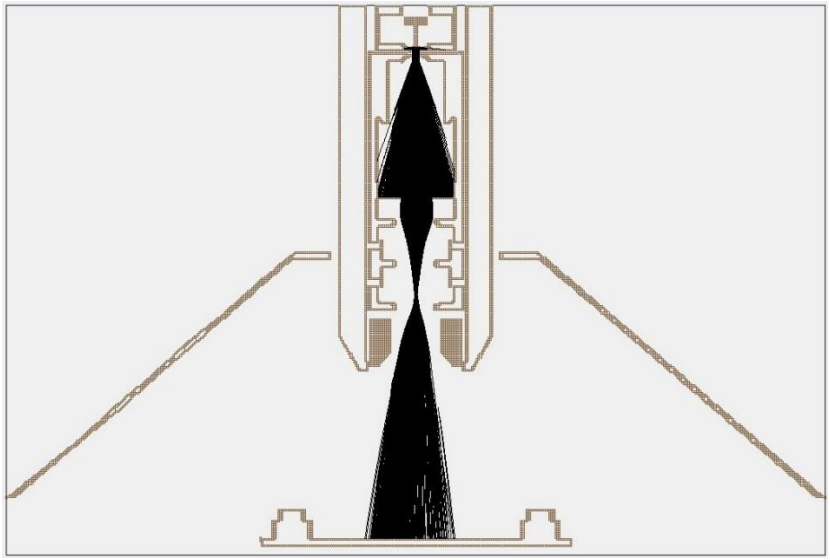

Figure 146:Cross-sectional view of electron gun with horn-shaped collector.

**2) Development of a feedback control system to mitigate the magnetic field near the electron gun**

This system will be implemented with a magnetometer within the chamber on the electron gun. Electromagnetics will be mounted outside the chamber to provide a

counteracting magnetic field. This will alleviation the effect the magnetic field has on the primary and secondary electrons.

**3) Extend simulation model to include secondary electron emission and space charge effects using VSim**

In order to determine the validity of assumption 7, a simulation model capable of modelling both SEE and space charge is required. VSim has the necessary capabilities. However, a computer with more RAM than the one used in this research, which had 64 GB, is required. An additional software package, called Charge Particle Optics (CPO), will also be investigated for its suitability in performing these simulations [151].

**4) Develop a sensor for measuring the work function of the sample in situ**

The ability to measure the work function of a sample will aid in determining the thermionic emission energy distribution and provide a means of validating the method which was develop in Section 3.2.4.

**5) Provide access to measured data for use by outside organizations**

Once the accuracy of the experimental system has been determined, then the measurements produced by the system will be made readily available to outside organizations for use in modelling and simulation and scientific research. Since the system is and will continue to be automated, large amount of data can be easily generated for use by others throughout the scientific and engineering communities.

## 5.4 Key Contributions

This research effort produced several key contributions which will benefit both the ongoing effort at AFIT and those performing experimental research regarding secondary electron emission.

### 5.4.1 Automated experimental system

` In addition to the hardware modifications and the repairs performed during this research, the system was automated to perform a countless number of tests under varying test conditions based on a tab-delimited text file. This significantly reduces the number of research hours that would be spent otherwise manually controlling the system. With the modifications to the hardware and programming, the system is capable of performing measurements in the fA range. The system is beneficial to the continuing research at AFIT, and others performing SEE measurements outside AFIT may find the information regarding the development of this system useful.

### 5.4.2 High-fidelity simulation model

The development of a high-fidelity model of the experimental apparatus is critical to the ongoing study of SEE at AFIT. This model has already proven its value in this research in providing predictions for the primary electron trajectories and explaining experimental data. The model will continue to be added to and used in future research.

### 5.4.3 Thermionic emission energy distribution model

A new model of the thermionic emission energy distribution was developed that allowed calibration without knowledge of the cathode's temperature. This model also provides a means of estimating the work function of the sample being tested and is critical in predicting the trajectories of the primary electrons at low energy. It may be used in the deconvolution of the measured SEY curve to obtain the true SEY curve. This model will continue to be tested in ongoing research following the replacement of the Faraday cup with a horn-shaped collector.

### 5.4.4 New metric for characterizing primary electron beam

Previous research at AFIT based the quality of the primary electron beam on the spot size created at the sample [4]. The electron beam was considered the best for SEY measurement when the spot size was minimized. However, Assumption 1 indicates that a larger spot size may actually be better in provide an average SEY for the entire surface. Furthermore, the SEY is dependent on the incidence angle, and the spot size does not take this factor into account. A new metric, called the BQF, was developed in order to quantify how well the primary electron beam achieved the desired incidence angle and landed within the desired sample area.

### 5.4.5 Discovery of relationship between BQF and sample current

During this research, it was discovered that a relationship exists between the BQF and the measured sample current. The relationship may be used in order to determine the optimal electron gun settings when measurements are performed at normal incidence.

Since the sample current is maximized when the primary electrons are normally incident on the sample surface, the optimal electron gun settings may be found by adjusting the optics of the electron gun until the sample current is maximized. This method may be used in addition to the predictions by the simulation model to fine-tune the primarily electron beam and correct for deficiencies in the model.

## Appendix A. Communication and Timing Connections

The experimental system is controlled by a single laptop running LabVIEW as shown in Figure 147. The waveform generator provides the timing source for the electrometers and digital multimeters (DMMs). The electrometers are maintained in the "Trigger Layer" during measurements to provide the quickest response to the timing signal [140].

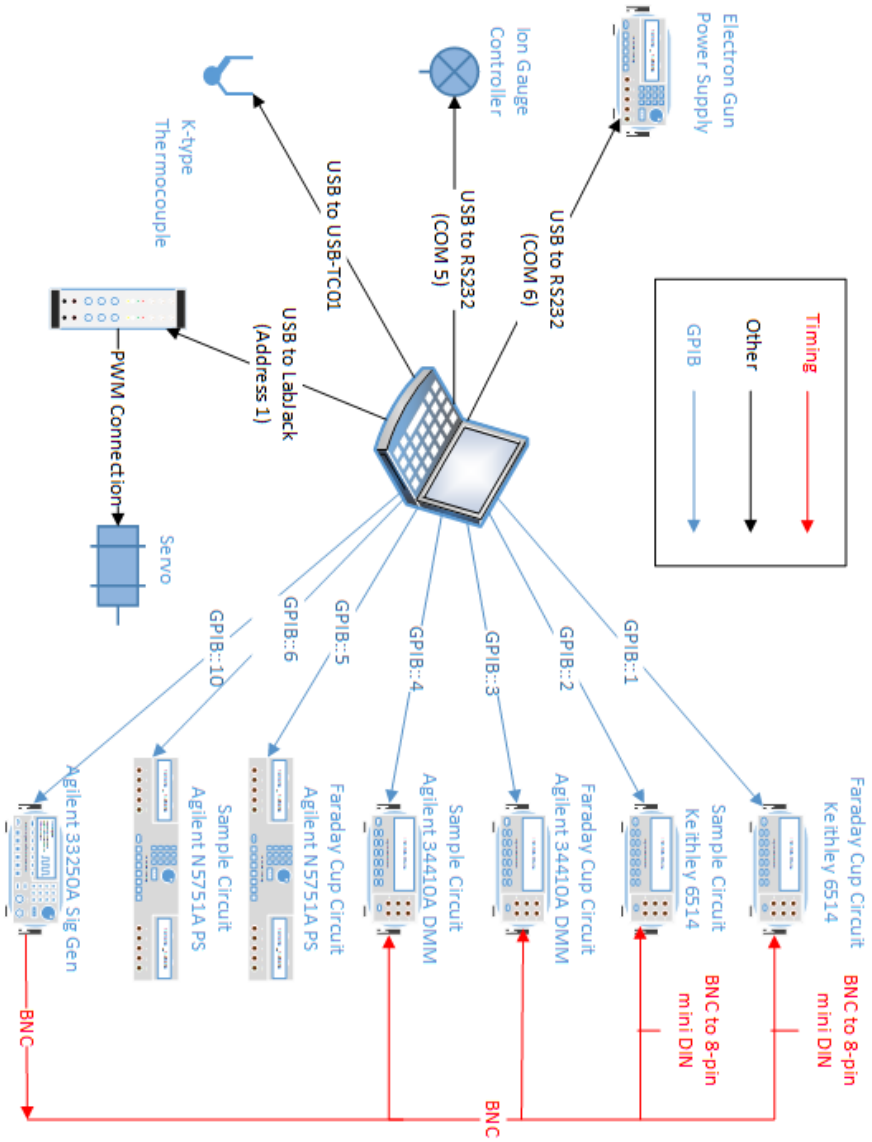


Figure 147: Communication and Timing Connections.

## Appendix B. Measurement Procedures

The following procedure provides the steps involved in setting up the experimental system to perform measurements. It is assumed that the chamber has already been pumped down to less than $1.0x10^{-8}$ Torr and the sample has been properly positioned.

1. Energize electron gun cathode to begin three-hour warmup period.
    a. Turn on the electron gun power supply using the green rocker switch.
    b. Turn on the high voltage supply using the red rocker switch.
    c. Set the grid potential to 50 V to prevent electrons from leaving the cathode.
    d. Set the source potential to the desired value.
    e. Start three-hour warm up period.
2. Turn on meters, power supplies, and signal generator.
3. After allowing one hour for the meters to warmup, perform input bias current and offset voltage calibration on the Keithley electrometers following the procedure listed on page 2-17 of the Model 6514 System Electrometer Instruction Manual. This will require disconnecting the electrometers from the rest of the measurement circuit.
4. Reconnect electrometers to the measurement circuit.
5. Set electrometers to measure current.
6. Set the power supplies to the appropriate voltage. Depending on the voltage, it may require over an hour for the circuit to settle after applying a new voltage to the circuit.
7. Set the electrometers to 10 PLCs and the smallest current range possible depending on the expected amount of current to be measured. Do not use auto range. You will be performing a zero correct for this range in a later step.
8. Create a tab-delimited text file containing the desired electron gun settings for each measurement following the format shown in Figure 148. Figure 149 shows an example

MATLAB script for creating this text file. There is not a limit on the number of rows contained within the text file. The experimental system will perform measurements starting from the top row and conclude with the last row. This step may be accomplished at any time prior to measurements.

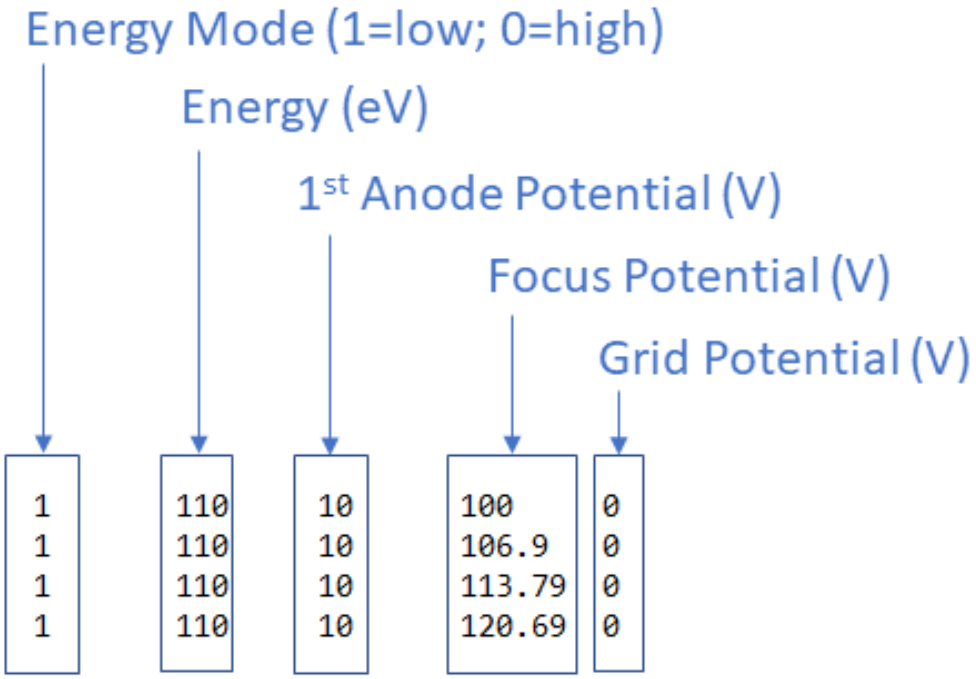


Figure 148: Identification of columns in tab-delimited text file for configuring electron gun.

```
Mode=ones(300,1);
Grid=zeros(300,1);
Anode=10*ones(300,1);
Energy=linspace(110,200,10);
Focus=linspace(100,300,30);
[Energy,Focus]=meshgrid(Energy,Focus);
output=[Mode,Energy(:),Anode,Focus(:),Grid];
dlmwrite('config4.txt',output,'delimiter','\t','newline','pc')
```

Figure 149: Example MATLAB script for generating tab-delimited text file for configuring electron gun.

9. Configure laptop

    a. Connect laptop to external power.

b. Connect all USB cables to the appropriate locations identified on the laptop.

c. Power up laptop and login to “jsattler” account.

10. Create a folder for measured data.

11. Open “File_Driven_Measurment.vi” on desktop.

12. Enter the file path to the text file containing the desired electron gun settings as shown in Figure 150.

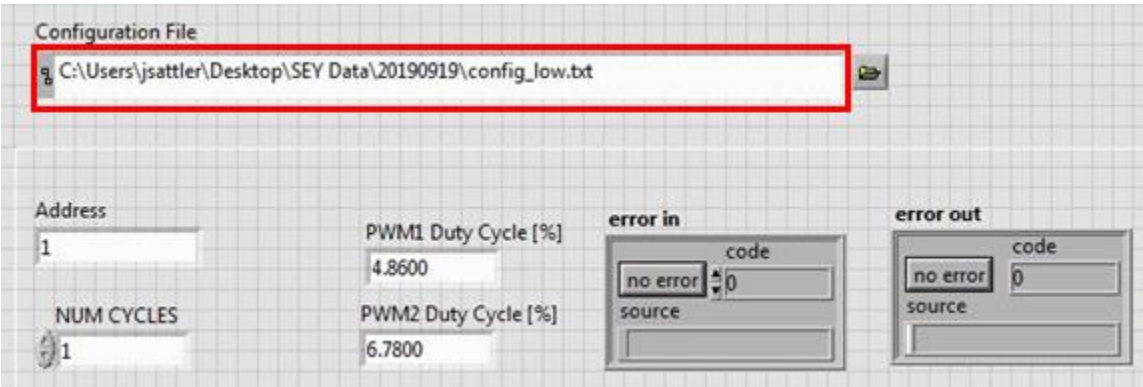


Figure 150: Box on LabVIEW front panel for specifying the file path of text file containing electron gun settings.

13. Enter the file path for the input and output files produced during measurements as shown in Figure 151. Each measurement will produce an input and output file, and the files will be automatically indexed starting from one.

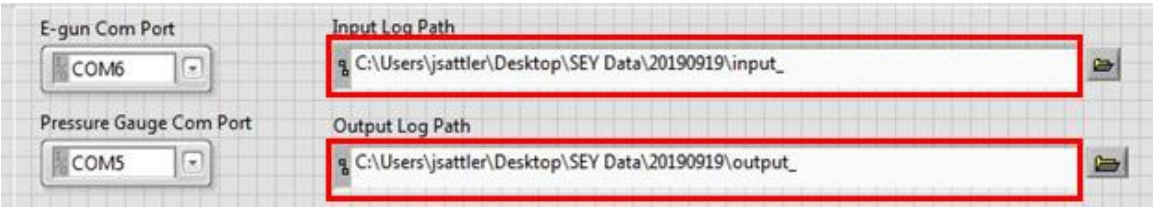


Figure 151: Boxes on LabVIEW front panel for specifying the file path of the input and output files.

14. Enter information regarding the sample being tested and the sample’s location in the chamber as shown in Figure 152. This data will be stored in each input file.


Figure 152: Boxes on LabVIEW front panel containing information regarding sample type and location within chamber.

15. Ensure that the front panel is set to the values shown in the following figures. The front panel should default to the correct settings.

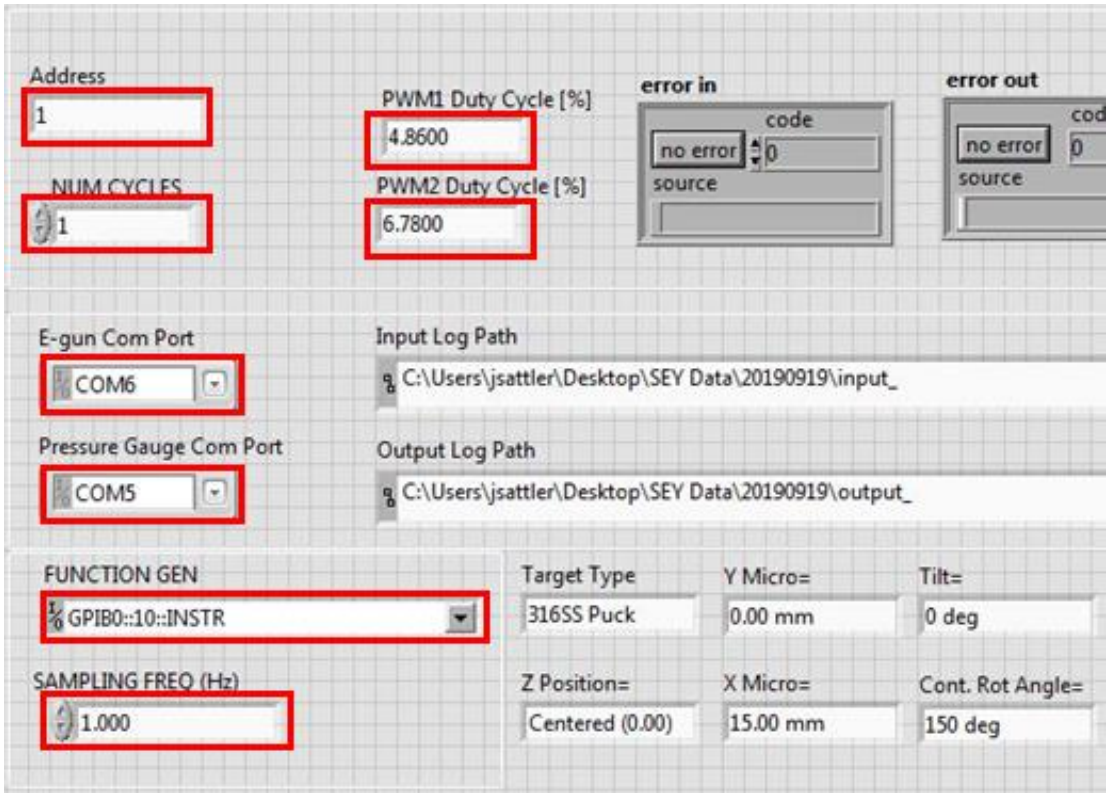


Figure 153: Settings on LabVIEW front panel for servo, electron gun, pressure gauge, and function generator (a.k.a. signal generator) configuration.

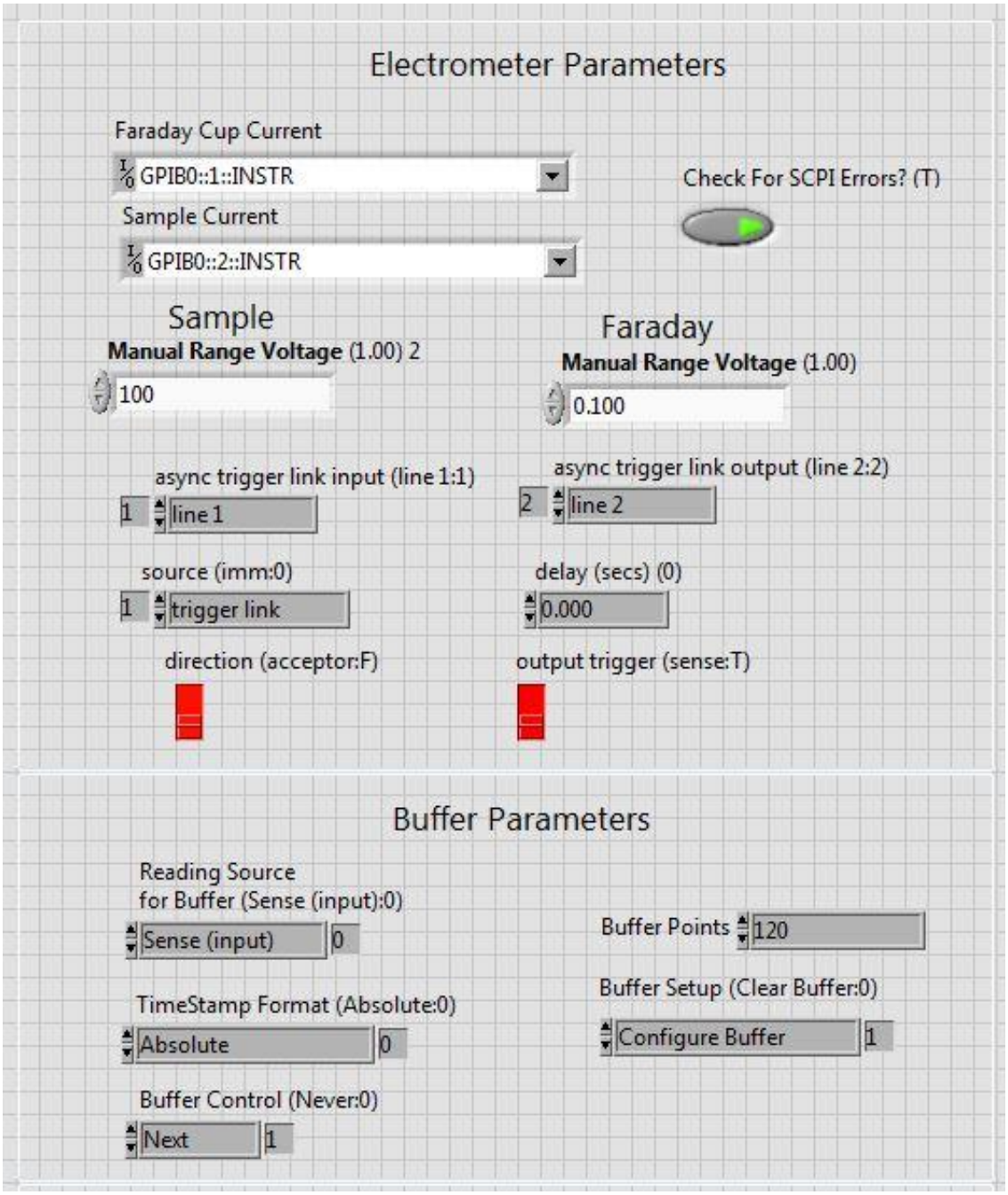

Figure 154: Settings on LabVIEW front panel for configuration of Keithley electrometers and Agilent DMMs.

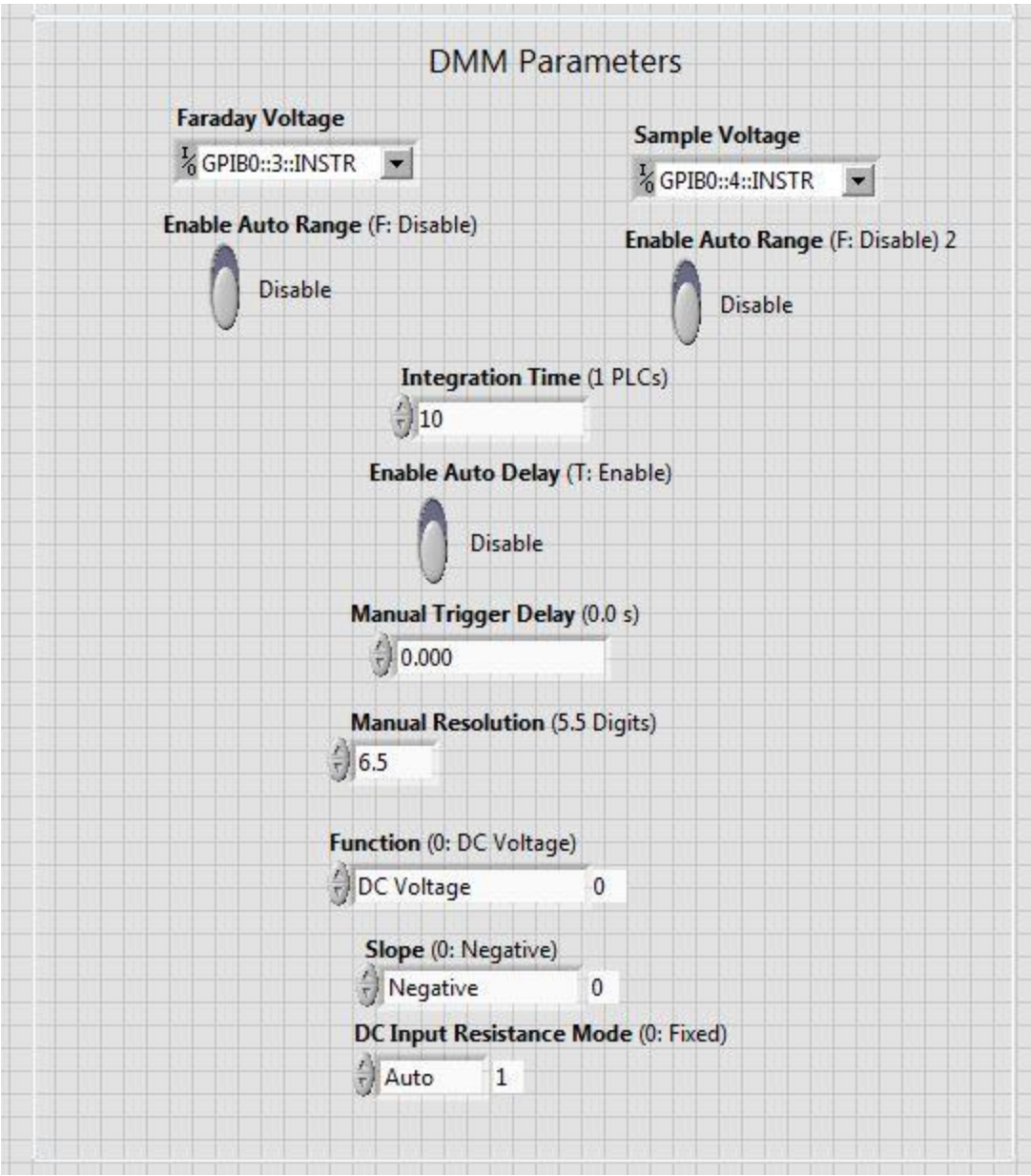

Figure 155: More settings on LabVIEW front panel for configuration of Agilent DMMs.

16. Ensure that the electrometers do not display FAST, MED, SLOW, REL, or FILT.

17. Enable zero check on the electrometers and perform a zero correct.

18. Disable zero check on the electrometers.

19. After the three-hour warmup time has been fulfilled, click the run icon on LabVIEW to begin measurements. LabVIEW's front panel will display data from the most recent

dataset acquired. If the data does not appear correct, measurements can be stopped using the stop button under the loop index. It may require that the system cycles through another measurement before stopping. It is a good idea to make sure that the input and output files are being properly stored in the desired folder and the data within the files appear correct before leaving the system to perform a large number of measurements autonomously.

## Appendix C. File Formats and Data Analysis Scripts

Measurements are stored in an input and output file. The input file stores information regarding the measurement conditions, and the output file stores the currents measured by the Keithley electrometers and voltages measured by the Agilent DMMs. The format for the input file is shown in Figure 156.

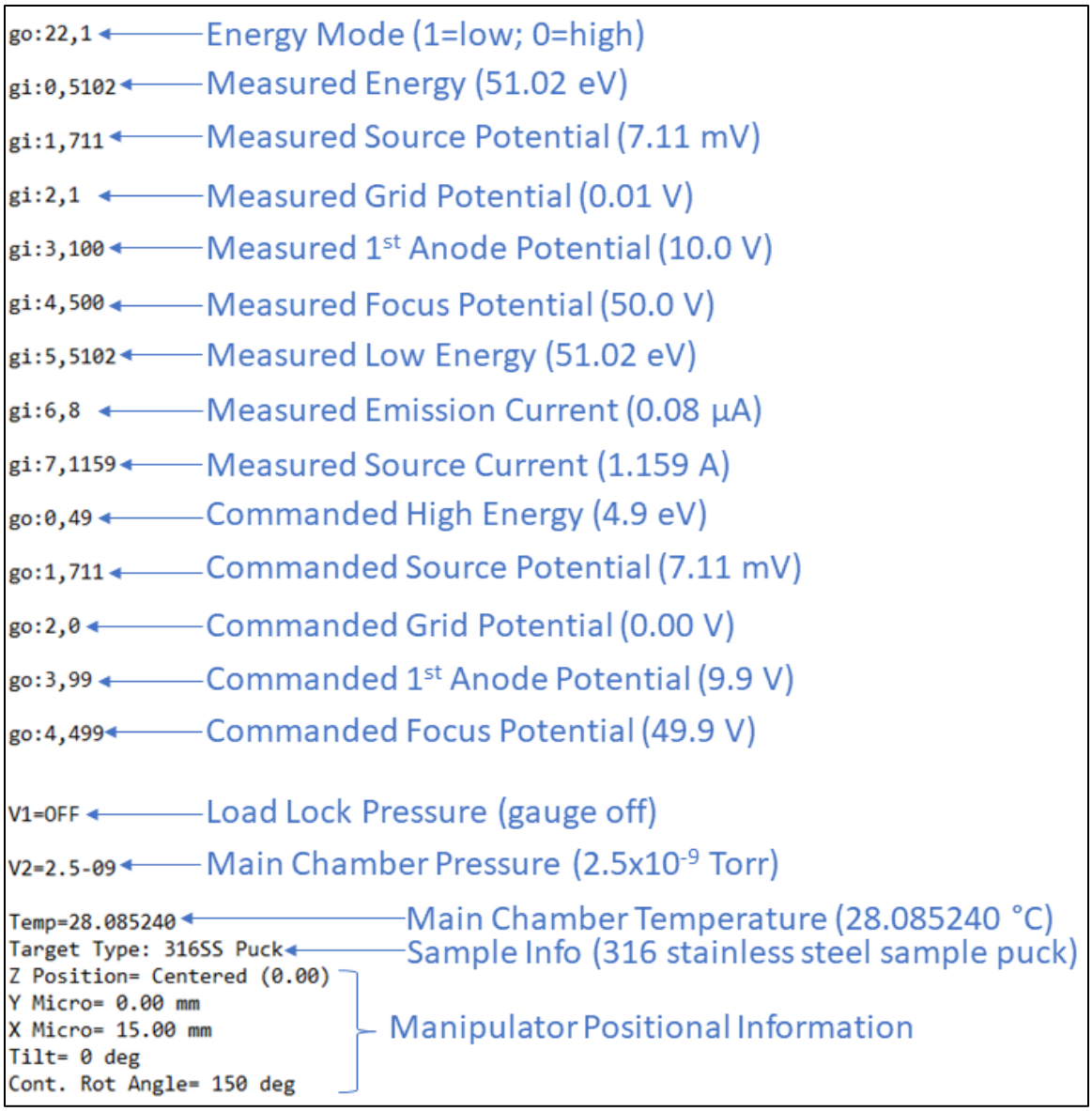


Figure 156: Input file format.

For more information regarding the electron gun related parameters, consult section 4.4.2 of the ELG-2/EGPS-1022 Electron Gun and Power Supply System manual.

The format for the output file is shown in Figure 157. Each column is associated with a variable or parameter.

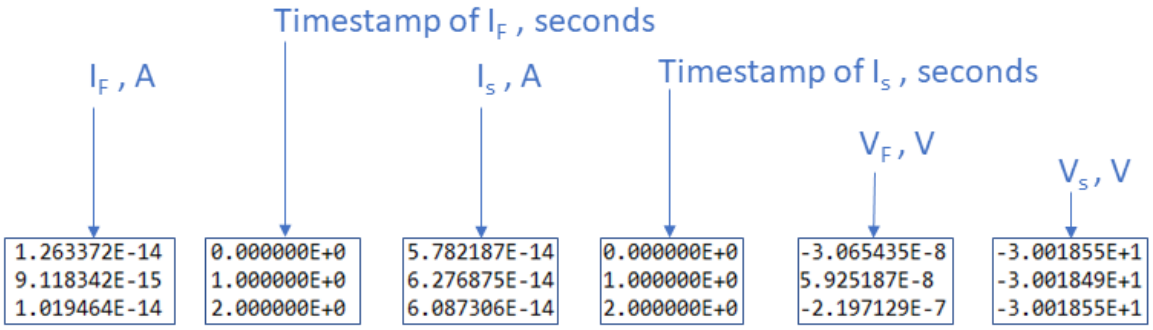


Figure 157: Output file format.

Before data is extracted from the input and output files. The plots of the currents $i_s$ and $i_F$ for multiple datasets should be created using the following MATLAB script. This script is used to determine the appropriate locations to extract samples from when using the Multiple Dataset Analysis script.

```
%%%%%%%%%%%%%%%%%%%%%%%%%%%%%%%%%%%%%%%%%%%%%%%%%%%%%%%%%%%%%%%%%%%%%%%%%%%%%%%%
% Title: Overlap Datasets
% Author: Matthew Vincie
% Organization: Air Force Institute of Technology
% Date: 27 Oct 2019
% Description: This script is used to plot the current signals from
%              multiple datasets on top of one another. Markers are used to
%              identify the locations where data will be extracted using
%              the Multiple_Dataset_Analysis script.
%%%%%%%%%%%%%%%%%%%%%%%%%%%%%%%%%%%%%%%%%%%%%%%%%%%%%%%%%%%%%%%%%%%%%%%%%%%%%%%%

%% Clear
close all;
clear
clc
%% Setup
Number_Files=1056; %Number of files to read
%% Plot Sample Current from Multiple Datasets
figure('units','normalized','outerposition',[0 0 1 1])
for i=1:Number_Files
filename = sprintf('output_%d.txt',i);
D = dlmread(filename);
plot(-D(:,3)*10^12)%,'.black');
ylabel('i_s, pA');
xlabel('Sample Number');
```

```
hold on
end

% The following code places markers on the plots to identify the beginning
and
% end of the regions where data will be extracted from.
dline=linspace(-3,3,10);
plot(6*ones(10,1),dline,'k-.')%Plot vertical line through sample number 6
plot(41*ones(10,1),dline,'k-.')%Plot vertical line through sample number 41
plot(63*ones(10,1),dline,'k-.')%Plot vertical line through sample number 63
plot(64*ones(10,1),dline,'k-.')%Plot vertical line through sample number 64
plot(74*ones(10,1),dline,'k-.')%Plot vertical line through sample number 74
plot(76*ones(10,1),dline,'k-.')%Plot vertical line through sample number 76
plot(84*ones(10,1),dline,'k-.')%Plot vertical line through sample number 84


%% Plot Faraday Cup Current from Multiple Datasets
figure('units','normalized','outerposition',[0 0 1 1])
for i=1:Number_Files
filename = sprintf('output_%d.txt',i);
D = dlmread(filename);
plot(-D(:,1)*10^12)%,'.black');
ylabel('i_F, pA');
xlabel('Sample Number');
hold on
end
axis([0,120,-1,7])

% The following code places markers on the plots to identify the beginning
and
% end of the regions where data will be extracted from.
dline=linspace(-10,10,10);
plot(6*ones(10,1),dline,'k-.')%Plot vertical line through sample number 6
plot(41*ones(10,1),dline,'k-.')%Plot vertical line through sample number 41
plot(63*ones(10,1),dline,'k-.')%Plot vertical line through sample number 63
plot(64*ones(10,1),dline,'k-.')%Plot vertical line through sample number 64
plot(74*ones(10,1),dline,'k-.')%Plot vertical line through sample number 74
plot(76*ones(10,1),dline,'k-.')%Plot vertical line through sample number 76
plot(84*ones(10,1),dline,'k-.')%Plot vertical line through sample number 84
```

The following MATLAB script is an example of a MATLAB script used to extract data from each dataset and produce a variety of plots including surface and contour plots. The "Read Output File and Extract Data" and "Read Input File" sections of the script were routinely used to extract data from datasets regardless of the type of measurements being performed and the plots being created.

```
%%%%%%%%%%%%%%%%%%%%%%%%%%%%%%%%%%%%%%%%%%%%%%%%%%%%%%%%%%%%%%%%%%%%%%%%%%%%%%%%
% Title: Multiple Dataset Analysis
% Author: Matthew Vincie
```

```
% Organization: Air Force Institute of Technology
% Date: 27 Oct 2019
% Description: This script is used is extract and display data from
%              multiple datasets.
%%%%%%%%%%%%%%%%%%%%%%%%%%%%%%%%%%%%%%%%%%%%%%%%%%%%%%%%%%%%%%%%%%%%%%%%%%%%%%%

%% Clear
close all;
clear
clc
%% Setup
Number_Files=1056;% Number of files to read
%% Extract Data From Multiple Datasets
for i=1:Number_Files
%% Read Output File and Extract Data
filename = sprintf('output_%d.txt',i);
DO = dlmread(filename);
MEAN_Sample_Leakage_fA(i)=mean(-DO([6:41,84:120],3)*10^15);
MEAN_Faraday_Leakage_fA(i)=mean(-DO([6:41,84:120],1)*10^15);
MEAN_Sample_CLOSED_fA(i)=mean(-DO(63:64,3)*10^15);
MEAN_Faraday_CLOSED_pA(i)=mean(-DO(63:64,1)*10^12);
MEAN_Sample_OPEN_pA(i)=mean(-DO(74:76,3)*10^12);
MEAN_Faraday_OPEN_fA(i)=mean(-DO(74:76,1)*10^15);

MEAN_Sample_Voltage(i)=mean(DO(4:120,6));
STD_Sample_Voltage(i)=std(DO(4:120,6));

MEAN_Faraday_Voltage(i)=mean(DO(4:120,5));
STD_Faraday_Voltage(i)=std(DO(4:120,5));
%% Read Input File
filename = sprintf('input_%d.txt',i);
fname = fopen(filename);
myline = fgetl(fname);
mygoindex = 1;
mygiindex = 1;
while ischar(myline)
    %myline = "go: #,####"
    if uint8(myline)==9
        % Do Nothing - Blank line
    elseif length(myline)==0
    else
        % Do something
        if myline(1:2) == 'go'
            mycommas=strfind(myline,',');
            go(mygoindex,i) =
str2double(myline(mycommas(1)+1:length(myline)));
            mygoindex = mygoindex+1;
        elseif myline(1:2) == 'gi'
            mycommas=strfind(myline,',');
            gi(mygiindex,i) =
str2double(myline(mycommas(1)+1:length(myline)));
            mygiindex = mygiindex+1;
        elseif myline(1:4) == 'Temp'
            Temp(i) = str2double(myline(6:length(myline)));
        elseif myline(1:2) == 'V2'
            Pressure(i) = str2double(myline(4:6))*10^(-
str2double(myline(8:9)));
        end
    end
    myline = fgetl(fname);
end
```

```
fclose(fname);
end
%% Plot Input Factors
figure
subplot(3,4,1)
plot(gi(6,:)/100,'o')
ylabel('Energy, eV')
xlabel('Measurement Number')
subplot(3,4,2)
plot(gi(2,:),'o')
ylabel('Source Potential, mV')
xlabel('Measurement Number')
subplot(3,4,3)
plot(gi(3,:)/100,'o')
ylabel('Grid Potential, V')
xlabel('Measurement Number')
subplot(3,4,4)
plot(gi(4,:)/10,'o')
ylabel('1st Anode Potential, V')
xlabel('Measurement Number')
subplot(3,4,5)
plot(gi(5,:)/10,'o')
ylabel('Focus Potential, V')
xlabel('Measurement Number')
subplot(3,4,6)
plot(gi(7,:)/100,'o')
ylabel('Emission Current, \muA')
xlabel('Measurement Number')
subplot(3,4,7)
plot(gi(8,:)/1000,'o')
ylabel('Source Current, A')
xlabel('Measurement Number')
subplot(3,4,8)
plot(Temp,'o')
ylabel('Temperature, \circC')
xlabel('Measurement Number')
subplot(3,4,9)
plot(Pressure*1e9,'o')
ylabel('Pressure, 10^-^9 Torr')
xlabel('Measurement Number')
subplot(3,4,10)
plot(MEAN_Sample_Voltage,'o')
ylabel('Mean Sample Voltage, V')
xlabel('Measurement Number')
subplot(3,4,11)
plot(MEAN_Faraday_Voltage*1e6,'o')
ylabel('Mean Faraday Voltage, \muV')
xlabel('Measurement Number')
%% Plot sample current versus accelerating potential
figure
plot(gi(6,:)/100,MEAN_Sample_OPEN_pA-MEAN_Sample_Leakage_fA/1e3,'o')
ylabel('i_s_a_m_p_l_e, pA')
xlabel('Accelerating Potential, V')
grid
%% Contour plot of sample current versus focus potential and accelerating
% potential
X=vec2mat(gi(6,:)/100,96)';
Y=vec2mat(gi(5,:)/10,96)';
Z=vec2mat(MEAN_Sample_OPEN_pA-MEAN_Sample_Leakage_fA/1e3,96)';
figure
contourf(X,Y,Z,40)
```

```
colormap jet
c = colorbar;
c.Label.String = 'i_s_a_m_p_l_e, pA';
xlabel('V_E_E, V')
ylabel('V_F_O, V')
%% Surf plot of sample current versus focus potential and accelerating
%  potential
figure
surf(X,Y,Z)
colormap jet
xlabel('V_E_E, V')
ylabel('V_F_O, V')
zlabel('i_s_a_m_p_l_e, pA')
%% Plot maximum current for a given accelerating potential
z=zeros(1,size(MEAN_Sample_OPEN_pA,2));
i_max=zeros(1,11);
energy=zeros(1,11);
for i=0:10
    maximum=max(MEAN_Sample_OPEN_pA(96*i+1:96*(i+1)));
    i_max(i+1)=maximum;
    energy(i+1)=gi(6,96*i+1)/100+MEAN_Sample_Voltage(96*i+1);
    z(96*i+1:96*(i+1))=(MEAN_Sample_OPEN_pA(96*i+1:96*(i+1))-...
        MEAN_Sample_Leakage_fA(96*i+1:96*(i+1))/1e3)/maximum;
end
figure
plot(energy,i_max,'k')
ylabel('i_s_a_m_p_l_e, pA')
xlabel('Accelerating Potential, V')
```

# Appendix D. Simulating Thermionic Emission

Thermionic emission is simulated in SIMION® by appropriately defining the initial conditions of each electron. These initial conditions can be defined for each electron using a .ion file or for a group of electrons using a .fly or .fly2 file. Defining the initial conditions using a .ion file allows the user to create custom distributions for the electrons. The custom distributions used in this research required the use of a .ion file. This file was generated through a two-step process. First, the following MATLAB script was used to generate the initial conditions for electrons following the distributions outlined in Section 3.2.4.

```
%%%%%%%%%%%%%%%%%%%%%%%%%%%%%%%%%%%%%%%%%%%%%%%%%%%%%%%%%%%%%%%%%%%%%%%%%%%%%%%%
% Title: Thermionic Emission Distribution
% Author: Matthew Vincie
% Organization: Air Force Institute of Technology
% Date: 27 Oct 2019
% Description: This script is used is generate the initial conditions of
%              the electrons used by SIMION(R).
%%%%%%%%%%%%%%%%%%%%%%%%%%%%%%%%%%%%%%%%%%%%%%%%%%%%%%%%%%%%%%%%%%%%%%%%%%%%%%%%
clear
close all
format long
%% Setup
alpha=0.056332160160160;% Alpha of associated with energy distribution
inv_alpha=1/alpha;% Inverse of Alpha
Duration=4e-4; % Duration of emission (s)
Q_e=1.60217662e-19; % Charge of an electron (C)
NUM=1e2; % Number of electrons to generate
R_mm=0.425; % Radius of cathode
y=-5.1; % y coordinate of starting position in simulation space
x_c=19; % x coordinate of cathode center in simulation space
z_c=19; % z coordinate of cathode center in simulation space
m_e=0.00054857990946; % Mass of an electron in amu
q_e=-1; % Charge of an electron in e
CWF=1; % Charge Weighting Factor
COLOR=0; % Color using by SIMION to display the particles trajectory 0=black
%% Create Uniform Distribution for Time of Birth
TOB=Duration*rand(NUM,1)*1e6; % Time of Birth (microsecond)
%% Generate theta direction angles following Lambert's cosine law and plot
%  results
X=rand(NUM,1);
theta_rad=0.5*acos(1-2*X);% Random theta distribution in radians
%% Generate uniformly distributed azimuth direction angles
azimuth=360*rand(NUM,1);
%% Generate  energy distribution
X=randn(NUM,3);
Y=X(:,1).^2+X(:,2).^2+X(:,3).^2;
energy=Y/inv_alpha;
%% Generate Starting Positions using a circular uniform distribution
%  See https://stackoverflow.com/questions/5837572/generate-a-random-point-
%  within-a-circle-uniformly
```

```
r_0=R_mm*sqrt(rand(NUM,1));
theta_0=2*pi*rand(NUM,1);
x=x_c+r_0.*cos(theta_0);
z=z_c+r_0.*sin(theta_0);
%% Convert theta_rad into SIMION coordinate frame
elevation=theta_rad-pi/2;
elevation=elevation*180/pi;
%% Generate temp.txt file with initial conditions
M=[TOB,m_e*ones(NUM,1),q_e*ones(NUM,1),x,y*ones(NUM,1),z,azimuth,elevation,...
    energy,CWF*ones(NUM,1),COLOR*ones(NUM,1)];
dlmwrite('temp.txt',M,'delimiter',',','newline','pc')
```

Next, the file “temp.txt” was opened, and “;0” was added above the first line in the file. The file was then saved in the simulation program directory along with the potential arrays with the .txt file extension replaced by .ion.

## Appendix E. Script for Analyzing Data Produced by SIMION

SIMION® is configured to record the location, elevation angle, and kinetic energy associated with a "splat" (i.e. final position of an electron within the simulation space). This information is stored in text file, which can be imported into MATLAB for analysis. The following MATLAB script was used in this research to analyze the simulation data.

```
%%%%%%%%%%%%%%%%%%%%%%%%%%%%%%%%%%%%%%%%%%%%%%%%%%%%%%%%%%%%%%%%%%%%%%%%%%%%%%%%
% Title: Analysis of SIMION(R) Output File
% Author: Matthew Vincie
% Organization: Air Force Institute of Technology
% Date: 27 Oct 2019
% Description: This script is used to analyze the location, energy, and
%              elevation angle of the electrons at their final position
%              within the SIMION(R) simulation space.
%%%%%%%%%%%%%%%%%%%%%%%%%%%%%%%%%%%%%%%%%%%%%%%%%%%%%%%%%%%%%%%%%%%%%%%%%%%%%%%%
clear
close all
%% Setup
Sample_Bias=-30;% Sample Bias (V)
Energy=51;% Accelerating Potential (V)
theta_d=90;% Desired Incidence Angle (deg)
position_bins=200;% Number of bins used in 2D histogram of positions
DATA=dlmread('E21F50.txt','\t',1,0);% Import simulation output
work_radius=10;% Radius of working area in mm
sample_radius= 19; % Radius of sample puck in mm
sample_uppermost= -86; % Uppermost point of sample puck in workbench (mm)
hits=0;% Initialization: number of electrons intercepting the sample puck
BQF_sum=0;% Initialization: Beam Quality Factor Summation
%% Analysis of Simulation Data
NUM=size(DATA,1);
for i=1:NUM
    if ((DATA(i,2)-19)^2+(DATA(i,4)-19)^2)<sample_radius^2 && DATA(i,3)<sample_uppermost
        hits=hits+1;% Add one to the number of electrons intercepting the sample puck
        x(hits)=DATA(i,2)-19;% Record x location of hit with respect to sample puck center
        y(hits)=DATA(i,4)-19;% Record y location of hit with respect to sample puck center
        angle(hits)=-DATA(i,5);% Record elevation angle of hit
        energy(hits)=DATA(i,6);% Record energy of hit
        BQF_sum=BQF_sum+(1-abs(-DATA(i,5)-theta_d)/90)*...
            heaviside(work_radius^2-(DATA(i,2)-19)^2-(DATA(i,4)-19)^2);
    end
end
BQF=100*BQF_sum/hits% Calculate Beam Quality Factor
%% Histogram of Primary Electron Energies
alpha=0.056332160160160;% Alpha of associated with thermionic emission energy distribution
Work_Function_delta=0.23;% Work function difference (cathode - sample)
offset=Work_Function_delta+Energy+Sample_Bias;
histogram(energy,'Normalization','pdf')
hold on
E=linspace(0,1,1000);
Y=(1/alpha)*sqrt(E/(2*pi*alpha)).*exp(-E/(2*alpha));% Thermionic Energy Distribution
E=E+offset;% Offset distribution for sample bias, accelerating potential, and work function
difference
plot(E,Y,'r','LineWidth',2)
legend('Histogram of Primary Electron Energies','Shifted Thermionic Emission Energy Distribution')
xlabel('Kinetic Energy, eV')
ylabel('Ambiguous Units')
%% Histogram of Incident Elevation Angles
figure
histogram(angle,'Normalization','pdf')
ylabel('f(\theta_i)')
xlabel('\theta_i, deg')
axis tight
%% 2D Histogram of Incident Positions on Sample Puck
figure
histogram2(x,y,position_bins,'FaceColor','flat')
colormap jet
```

```
hold on
y_c=sqrt(sample_radius^2-x_c.^2);
plot(x_c,y_c,'k')
y_c=-sqrt(sample_radius^2-x_c.^2);
plot(x_c,y_c,'k')
x_c=linspace(-work_radius,work_radius,100);
y_c=sqrt(work_radius^2-x_c.^2);
plot(x_c,y_c,'r')
y_c=-sqrt(work_radius^2-x_c.^2);
plot(x_c,y_c,'r')
xlabel('x, mm')
ylabel('y, mm')
zlabel('Counts')
```

# VI. Bibliography


[1] L. Austin and H. Starke, "Ueber die Reflexion der Kathodenstrahlen und eine damit verbundene neue Erscheinung secundärer Emission," *Annalen der Physik,* vol. 314, no. 10, pp. 271-292, 1902.

[2] Y. Lin and D. Joy, "A new examination of secondary electron yield data," *Surface and Interface Analysis,* vol. 37, no. 11, pp. 895-900, 2005.

[3] D. C. Joy, "A Database of Electron-Solid Interactions," April 2008. [Online]. Available: http://studylib.net/doc/5878300/. [Accessed 2018].

[4] J. M. Sattler, Engineered Surfaces to Control Secondary Electron Yield for Multipactor Suppression, PhD dissertation, AFIT-ENG-DS-17-S-018. School of Engineering and Management, Air Force Institute of Technology (AU), Wright-Patterson AFB OH, 2017(AD-1051603).

[5] T. P. Graves, "Standard/Handbook for Multipactor Breakdown Prevention in Spacecraft Components," Aerospace Corporation Report No. TOR-2014-02198, El Segundo, CA, 2014.

[6] S. A. Rice and J. P. Verboncoeur, "A Comparison of Multipactor Predictions Using Two Popular Secondary Electron Models," *IEEE Transactions on Plasma Science,* vol. 42, no. 6, pp. 1484-1487, 2014.

[7] R. Cimino, L. Gonzalez, R. Larciprete, A. Di Gaspare, G. Iadarola and G. Rumolo, "Detailed investigation of the low energy secondary electron yield of technical Cu and its relevance for the LHC," *Physical Review Special Topics-Accelerators and Beams,* vol. 18, no. 051002, pp. 1-10, 2015.

[8] K. G. McKay, "Secondary Electron Emission," *Advances in Electronics and Electron Physics,* vol. 1, pp. 65-130, 1948.

[9] H. Bruining, Physics and Applications of Secondary Electron Emission, 2nd ed., D. W. F. (Harwell), Ed., London: Pergamon Press LTD, 1954.

[10] A. W. Hull, "Negative Resistance". US Patent 1387984, 16 August 1921.

[11] A. W. Hull, "The Dynatron: A Vacuum Tube Possessing Negative Electric Resistance," *Proceedings of the Institute of Radio Engineers,* vol. 6, no. 1, pp. 5-34, February 1918.

[12] J. E. Brittain, "Electrical Engineering Hall of Fame: Albert W. Hull [Scanning Our Past]," *Proceedings of the IEEE,* vol. 98, no. 4, pp. 635-637, April 2010.

[13] The Editors of Encyclopaedia Britannica, "Auger effect," Encyclopaedia Britannica, Inc., 19 September 2016. [Online]. Available: https://www.britannica.com/science/Auger-effect. [Accessed 15 November 2017].

[14] A. Carlson, "Schematic Drawing of the Auger Effect," 15 October 2007. [Online]. Available: https://commons.wikimedia.org/wiki/File:Auger_Process.svg. [Accessed 16 July 2018].

[15] H. Seiler, "Secondary electron emission in the scanning electron microscope," *Journal of Applied Physics,* vol. 54, no. 11, pp. R1-R18, 1983.

[16] J. P. McKelvey, Solit state phyiscs for engineering and materials science, Malabar, Florida: Krieger Publishing Company, 1993.

[17] I. J. Blanken, "Scanning our past from the Netherlands: Bernard Tellegen and the pentode valve," *Proceedings of the IEEE,* vol. 91, no. 1, pp. 238-239, 2003.

[18] J. L. H. Jonker, "Phenomena in Amplifier Valves Caused by Secondary Emission," *Philips Tech. Rev.,* vol. 3, pp. 211-216, 1938.

[19] G. Holst and B. D. H. Tellegen, "Means for Amplifying Electric Oscillations". US Patent 1945040, 30 January 1934.

[20] R. A. Kishek and e. al., "Multipactor discharge on metals and dielectrics: Historical review and recent theories," *Physics of Plasmas,* vol. 5, no. 5, pp. 2120-2126, 1998.

[21] C. Gutton, "Sur la décharge électrique à fréquence très élevée," *Comptes-Rendus Hebdomadaires des Séances de l'Académie des Sciences,* vol. 178, pp. 467-470, 1924.

[22] M. H. Gutton, "Recherches sur les propriétés diélectriques des gaz ionisés et la décharge en haute fréquence," *Annales de Physique,* vol. 10, no. 13, pp. 63-130, 1930.

[23] Y. Blanchard, "Maurice Ponte and Henri Gutton, pioneers of early French studies on resonant magnetron (1932–1940)," *2010 International Conference on the Origins and Evolution of the Cavity Magnetron,* pp. 5-10, 2010.

[24] C. Gutton and H. Gutton, "Sur la décharge électrique en haute fréquence," *Comptes-Rendus Hebdomadaires des Séances de l'Académie des Sciences,* vol. 186, pp. 303-305, 1928.

[25] P. T. Farnsworth, "Television by electron image scanning," *J. Franklin Inst.,* vol. 218, pp. 411-444, 1934.

[26] P. T. Farnsworth, "Multipactor Osicallator and Amplifier". US Patent 2091439, 31 August 1937.

[27] S. Anza and e. al., " Prediction of multipactor breakdown for multicarrier applications: The quasi-stationary method," *IEEE Transactions on Microwave Theory and Techniques,* vol. 60, no. 7, pp. 2093-2105, 2012.

[28] J. R. M. Vaughan, "Multipactor," *IEEE Transactions on Electron Devices,* vol. 35, no. 7, pp. 1172-1180, 1988.

[29] Y. Li, W.-Z. Cui and H.-G. Wang, "Simulation investigation of multipactor in metal components for space application with an improved secondary emission model," *Physics of Plasmas,* vol. 25, no. 4, pp. 417-423, 2015.

[30] A. J. Hatch and H. B. Williams, "The Secondary Electron Resonance Mechanism of Low-Pressure High-Frequency Gas Breakdown," *Journal of Applied Physics,* vol. 25, pp. 417-423, 1954.

[31] G. August and J. B. Chown, "Reduction of gas-discharge breakdown thresholds in the ionosphre due to multipacting," *Proceedings of the Second Workshop on Voltage Breakdown in Electronic Equipment at Low Air Pressure,* pp. 193-201, 1969.

[32] I. Ben-Zvi, J. F. Crawford and J. P. Turneaure, "Electron Multiplication in Cavities," *IEEE Transactions on Nuclear Science,* vol. 20, no. 3, pp. 54-58, 1973.

[33] C. M. Lyneis, H. A. Schwettman and J. P. Turneaure, "Elimination on electron multipacting in superconducting structures for electron accelerators," *Applied Physics Letters,* vol. 31, no. 8, pp. 541-543, 1977.

[34] A. Vikharev, E. Ilyakov, S. Kuzikov and I. Kulagin, "Multipactor discharge in crossed fields in a cylindrical cavity for the 3-cm wavelength band," *Radiophysics and Quantum Electronics,* vol. 54, no. 12, pp. 820-827, 2012.

[35] C. Lingwood, G. Burt, A. Dexter, J. Smith, P. Goudket and P. Stoltz, "Phase space analysis of multipactor saturation in rectangular waveguide," *Physics of Plasmas,* vol. 19, no. 032106, pp. 1-9, 2012.

[36] J. M. Dawson, "Partilce simulation of plasmas," *Reviews of modern physics,* vol. 55, no. 2, pp. 403-447, 1983.

[37] N. G. Rogers, *Electron multipactor: theory review, comparison and modeling of mitigation techniques in ICEPIC,* MS thesis, AFIT/GE/ENP/09-M02. School of Engineering and Management, Air Force Institute of Technology (AU), Wright-Patterson AFB OH, 2009 (AD-A495885).

[38] R. Lloyd, *Multipactor Discharge in High Power Microwave Systems: Analyzing Effects and Mitigation through Simulation in ICEPIC,* MS thesis, AFIT/ENP/13-M22. School of Engineering and Management, Air Force Institute of Technology (AU), Wright-Patterson AFB OH, 2013 (AD-A580743).

[39] R. Warnecke, "Émission secondaire de métaux purs," *Journal de Physique et le Radium,* vol. 7, no. 6, pp. 270-280, 1938.

[40] H. Bruining, "Secondary Electron Emission," *Philips technical review,* vol. 3, no. 3, pp. 80-86, 1938.

[41] J. F. Marshall and M. A. Pomerantz, "Fundamentals of Secondary Electron Emission," *Proceedings of the IRE,* vol. 39, no. 11, pp. 1367-1373, 1951.

[42] A. Shih and C. Hor, "Secondary Emission Properties as a Function of the Electron Incident Angle," *IEEE Transactions on Electron Devices,* vol. 40, no. 4, pp. 824-829, 1993.

[43] W. Yardley, "Willis Whitfield, Inventor of Clean Room That Purges Tiny Particles, Dies at 92," *The New Your Time,* p. B17, 5 December 2012.

[44] C. J. Powell, N. E. Erickson and T. E. Madey, "Results of a joint auger/esca round robin sponsored by astm committee E-42 on surface analysis. Part II. Auger results," *Journal of Electron Spectroscopy and Related Phenomena,* vol. 25, pp. 87-118, 1982.

[45] C. J. Powell, R. Shimizu, K. Yoshihara and S. Ichimura, "Development of standards for reliable surface analyses by ISO technical committee 201 on surface chemical analysis," *Surf. Interface Anal.,* vol. 47, no. 1, pp. 127-134, 2014.

[46] C. K. Birdsall and W. B. Bridges, Electron Dynamics of Diode Regions, New York: Academic Press, 1966.

[47] M. Pivi, F. K. King, R. E. Kirby, T. O. Raubenheimer, G. Stupakov and F. Le Pimpec, "Sharp reduction of the secondary electron emission yield from grooved surfaces," *Journal of Applied Physics,* vol. 104, no. 104904, pp. 1-10, 2008.

[48] M. Ye, Y. N. He, S. G. Hu, J. Yang, R. Wang, T. C. Hu, W. B. Peng and W. Z. Cui, "Investigation in anomalous total secondary electron yield for micro-porous Ag surface under oblique incidence conditions," *Journel of Applied Physics,* vol. 114, no. 104905, pp. 1-8, 2013.

[49] N. D. Zameroski, P. Kumar, C. Watts, T. Svimonishvili, M. Gilmore, E. Schomiloglu and J. Gaudet, "Secondary Electron Yield Measurements From Materials With Application to Collectors of High-Power Microwave Devices," *IEEE Transactions on Plasma Science,* vol. 34, no. 3, pp. 642-651, 2006.

[50] D. J. Scott, D. Capista, K. L. Duel, R. M. Zwaska, S. Greenwald, W. Hartung, Y. Li, T. P. Moore and M. A. Palmer, "Secondary Electron Yield Measurements of Fermilab's Main Injector Vacuum Vessel," National Accelerator Laboratory Report No. FERMILAB-CONF-12-196-AD, 2013.

[51] O. Hachenberg and W. Brauer, "Secondary Electron Emission from Solids," *Advances in electronics and electron physics,* vol. 11, pp. 413-499, 1959.

[52] A. N. Andronov, "Secondary Electron Emission at Very Low Electron Energy," *St. Petersburg State Polytechnical University J. Phys. Math,* pp. 67-78, 2014.

[53] J. Roupie, O. Jbara, T. Tondu, M. Belhaj and J. Puech, "The study of electron emission from aluminum in the very low primary energy range using Monte Carlo simulations," *Journal of Physics D: Applied Physics,* vol. 46, no. 12, 2013.

[54] H. A. Fowler and H. E. Farnsworth, "Reflection of Very Slow Electrons," *Physical Review,* vol. 111, no. 1, pp. 103-112, 1958.

[55] H. Heil and J. V. Hollweg, "Electron reflection coefficient at zero energy. I. Experiments," *Physical Review,* vol. 164, no. 3, pp. 881-886, 1967.

[56] J. W. P. Wang, M. Belhaj and J.-C. M. Velez, "Modeling facility effects on secondary electron emission experiment," *IEEE Transactions on Plasma Science,* vol. 40, no. 10, pp. 2773-2780, 2012.

[57] C. C. Chang, "Auger electron spectroscopy," *Surface Science,* vol. 25, no. 1, pp. 53-79, 1971.

[58] I. F. Patai and M. A. Pomerantz, "Contact Potential Difference," *Journal of the Franklin Institute,* vol. 252, no. 3, pp. 239-260, 1951.

[59] H. E. Farnsworth, "Energy Distribution of Secondary Electrons from Copper, Iron, Nickel and Silver," *Physical Review,* vol. 31, no. 3, pp. 405-413, 1928.

[60] J. L. H. Jonker, "On the Theory of Secondary Emission of Metals," *Philips Res. Rep.,* vol. 12, pp. 249-258, 1957.

[61] C. Herring and M. H. Nichols, "Thermionic emission," *Review of Modern Physics,* vol. 21, no. 2, pp. 185-271, 1949.

[62] A. J. Dekker, "Secondary Electron Emission," *Solid State Physics,* vol. 6, pp. 251-311, 1958.

[63] E. M. Baroody, "A Theory of Secondary Electron Emission from Metals," *Physical Review,* vol. 78, no. 6, pp. 780-787, 1950.

[64] S. C. Brown, "Basic Data of Plasma Physics," MIT Press and John Wiley & Sons, Inc., New York, 1959.

[65] J. Cazaux, "About the charge compensation of insulating samples in XPS," *Journal of Electron Spectroscopy and Related Phenomena,* vol. 113, no. 1, pp. 15-33, 2000.

[66] J. Cazaux, "Mechanisms of Charging in Electron Spectroscopy," *Journal of Electron Spectroscopy and Related Phenomena,* vol. 105, no. 2, pp. 155-185, 1999.

[67] R. E. Bunney, "Review of Liturature: Secondary Electron Emission," NASA, 1964.

[68] A. Shih, J. Yater, C. Hor and R. Abrams, "Secondary electron emission studies," *Applied surface science,* vol. 111, pp. 251-258, 1997.

[69] H. Bruining, J. H. De Boer and W. G. Burgers, "Secondary Electron Emission of Soot in Valves with Oxidecathode," *Physica ,* vol. 4, no. 4, pp. 267-275, 1937.

[70] J. L. H. Jonker, "On the Theory of Secondary Electron Emission," *Philips Research Reports,* vol. 7, pp. 1-20, 1952.

[71] R. Valizadeh and e. al., "Low secondary electron yield engineered surface for electron cloud mitigation," *Applied Physics Letters,* vol. 105, no. 231605, pp. 1-5, 2014.

[72] H. Bruining, "The depth at which secondary electrons are liberated," *Physica,* vol. 3, no. 9, pp. 1046-1052, 1936.

[73] A. B. Laponsky and N. Rey Whetten, "Dependence of secondary electron emission on crystal orientation," *Physical Review Letters,* vol. 3, no. 11, pp. 510-512, 1959.

[74] V. Malát and J. Horáček, "Space-charge limitation of secondary electron emission," *Czechoslovak Journal of Physics,* vol. 28, pp. 1246-1259, 1978.

[75] M. D. Hare, "The effects of initial electron velocities and space charge in secondary emission," *IRE Transactions on Electron Devices,* vol. 6, no. 4, pp. 397-404, 1959.

[76] G. F. Dionne, "Origin of secondary electron emission yield curve parameters," *Journal of Applied Physics,* vol. 46, no. 8, pp. 3347-3351, 1975.

[77] R. G. Lye and A. J. Dekker, "Theory of secondary emission," *Physical Review,* vol. 107, pp. 977-, 1957.

[78] J. F. Marshall, "The Theory of Secondary Emission," *Physical Review,* vol. 88, no. 2, pp. 416-417, 1952.

[79] H. Salow, "Sekündarelektronen-Emission," *Phys. Z.,* vol. 41, pp. 434-442, 1940.

[80] D. E. Woolridge, "Theory of Secondary Emission," *Physical Review,* vol. 56, no. 6, pp. 562-578, 1939.

[81] A. J. Dekker and A. van der Ziel, "Theory of the Production of Secondary Electrons in Solids," *Physical Review,* vol. 86, no. 5, pp. 755-760, 1952.

[82] J. Devooght, A. Dubus and J. C. Dehaes, "Improved age-diffusion model for low-energy electron transport in solids. I. Theory," *Phys. Rev. B,* vol. 36, no. 10, pp. 5093-5109, October 1987.

[83] E. J. Sternglass, "Secondary Electron Emission and Atomic Shell Structure," *Physical Review,* vol. 80, no. 5, pp. 925-926, 1950.

[84] R. M. Vaughan, "Secondary emission formulas," *IEEE Transactions on Electron Devices,* vol. 40, no. 4, p. 830, 1993.

[85] J. R. M. Vaughan, "A new formula for secondary emission yield," *IEEE Transactions on Electron Devices,* vol. 36, no. 9, pp. 1963-1967, 1989.

[86] C. Vicente, M. Mattes, D. Wolk, H. L. Hartnagel, J. R. Mosig and D. Raboso, "FEST3D: A simulation tool for multipactor prediction," *Workshop on Multipactor, RF and DC Corona and Passive Intermodulation in Space RF Hardware,* pp. 11-17, 2005.

[87] Computer Simulation Technology (CST(R)), "Multipactor & Breakdown Analysis of RF Components," Dassault Systèmes Simulia Corp, 2017. [Online]. Available: https://www.cst.com/solutions/article/multipactor--breakdown-analysis-of-rf-components. [Accessed 2017].

[88] P. Vempati, J. Ludwick, M. Cahay, S. B. Fairchild, T. C. Back and P. T. Murray, "A new formula for secondary emission yield in the low voltage region: An improvement of Vaughan's expression," *2017 30th International Vacuum Nanoelectronics Conference (IVNC),* pp. 214-215, 2017.

[89] M. A. Furman and M. T. F. Pivi, "Probabilistic model for the simulation of secondary electron emission," *Phys. Rev. ST Accel. Beams,* vol. 5, no. 12, pp. 1-18, 2002.

[90] Z. J. Ding, X. D. Tang and R. Shimizu, "Monte Carlo study of secondary electron emission," *Journal of Applied Physics,* vol. 89, no. 1, pp. 718-726, 2001.

[91] D. C. Joy, Monte Carlo Modeling for Electron Microscopy and Microanalysis, New York: Oxford University Press, 1995.

[92] Z. Insepov, V. Ivanov, S. Jokela, I. Veryovkin, A. Zinovev and H. Frisch, "Comparison of secondary electron emission simulation to experiment," *Nuclear Instruments and Methods in Physics Research A,* vol. 639, no. 1, pp. 155-157, 2011.

[93] J. M. Millet and J. P. J. Lafon, "Secondary-electron emission from porous solids," *Physical Review A,* vol. 52, no. 1, pp. 433-438, 1995.

[94] J. Tückmantel and e. al., "Improvements to power couplers for the LEP2 superconducting cavities," in *Proceedings Particle Accelerator Conference.,* Dallas, TX, vol. 3, pp. 1642-1644, 1995.

[95] A. J. Hatch, "Suppression of multipacting in particle accelerators," *Nuclear Instruments and Methods,* vol. 41, pp. 261-271, 1966.

[96] R. Cimino, M. Commisso, D. R. Grosso, T. Demma, V. Baglin, R. Flammini and R. Larciprete, "Nature of the Decrease of the Secondary-Electron Yield by Electron Bombardment and its Energy Dependence," *Phys. Rev. Lett.,* vol. 109, no. 064801, pp. 1-5, 2012.

[97] F. Le Pimpec, R. E. Kirby, F. K. King and M. Pivi, "Electron conditioning of technical aluminium surfaces: Effect on the secondary," *Journal of Vacuum Science & Technology A,* vol. 23, pp. 1610-1618, 2005.

[98] S. Wang, O. Malyshev, R. Valizadeh, E. Seddon and M. Cropper, "The secondary electron yield from transition metals," in *Proc. of IPAC2014,* Dresden, Germany, 2014.

[99] L. A. Gonzalez, M. Angelucci, R. Larciprete and R. Cimino, "The secondary electron yield of noble metal surfaces," *AIP Advances,* vol. 7, no. 115203, 2017.

[100] V. Nistor, L. A. González, L. Aguilera, I. Montero and L. Galán, "Multipactor suppression by micro-structured gold/silver coatings for space applications," *Applied Surface Science,* vol. 315, pp. 445-453, 2014.

[101] V. C. Nistor, *New approaches to anti-multipactor coatings for space applications,* Madrid: PhD Thesis, Autonomous University of Madrid, 2015.

[102] J. J. Scholtz, D. Dijkkamp and R. W. A. Schmitz, "Secondary electron emission properties," *Philips journal of research,* vol. 50, no. 3, pp. 375-289, 1996.

[103] G. A. Harrower, The Energy Spectra of Secondary Electrons from Copper and Silver, 1952.

[104] G. A. Harrower, "Electron Spectra of Secondary Electrons from Mo and W for Low Primary Energies," *Physical Review,* vol. 104, no. 1, pp. 52-56, 1956.

[105] R. Kollath, "Sekundärelektronen-emission fester körper bei bestrahlung mit elektronen," *Electron-Emission Gas Discharges I/Elektronen-Emission Gasentladungen I,* pp. 232-303, 1956.

[106] R. Kollath, "Zur Energieverteilung der Sekundärelektronen II. Meßergebnisse und Diskussion," *Annalen der Physik,* vol. 436, no. 7-8, pp. 357-380, 1947.

[107] J. Petillo and e. al., "The MICHELLE Three-Dimensional Electron Gun and Collector Modeling Tool: Theory and design," *IEEE Transactions on Plasma Science,* vol. 30, no. 3, pp. 1238-1264, 2002.

[108] A. Van der Ziel, Solid State Physical Electronics, Englewood Cliffs, NJ: Prentice-Hall, 1968.

[109] M. A. Furman and M. T. F. Pivi, "Simulation of Secondary Electron Emission Based on a Phenomenological Probabilistic Model," SLAC-PUB-9912, 2003.

[110] J. L. H. Jonker, "The Angular Distribution of the Secondary Electrons of Nickel," *Philips Res. Rep.,* vol. 6, pp. 372-387, 1951.

[111] J. Burns, "Angular distribution of secondary electrons from (100) faces of copper and nickel," *Physical Review,* vol. 119, no. 1, pp. 102-114, 1960.

[112] J. L. H. Jonker, "The Angular Distribution of the Secondary Electrons of Soot," *Philips Res. Rep.,* vol. 8, pp. 434-440, 1953.

[113] W. Doliński, J. Palczyński, P. Mazur and L. Gieniec, "Angular Distributions of Secondary Electrons Emitted from the Polycrystalline Silver," *Acta Physica Polonica A,* vol. 81, no. 2, pp. 211-222, 1992.

[114] A. Telang, *Efficient Method for Geometry Independent Multipactor Modeling. MS thesis,* University of Waterloo, 2009.

[115] F. L. Krawczyk, "Status of Multipacting Simulation Capabilities for SCRF Applications," Los Alamos National Lab, New Mexico, 2001.

[116] AURORASAT, "FEST3D," Aurora Software and Testing, S.L., 2017. [Online]. Available: http://www.fest3d.com/spark3d.php. [Accessed 2017].

[117] AURORASAT, "FEST3D User Manual," Aurora Software and Testing, S.L., [Online]. Available: http://www.fest3d.com/Online_Help/FEST3D/index8.html#material. [Accessed 2017].

[118] AURORASAT, "SPARK3D Online Help," Aurora Software and Testing, S.L., [Online]. Available: http://www.fest3d.com/Online_Help/SPARK3D/Spark_index.html. [Accessed 2017].

[119] T. Pinheiro-Ortega, J. Armendáriz, S. Anza, J. Gil, C. Vincente, B. Gimeno and V. Boria, "A new general RF breakdown simulation tool," in *ESA ESTEC 7th Int. Workshop on Multipactor Corona and Passive Intermodulation in Space RF Hardware*, 2011.

[120] CST AG, "Press Release: CST Announces Acquisition of AURORASAT," Computer Simulation Technology, Darmstadt, Germany, 2016.

[121] Dassault Systèmes, "SIMULIA REALISTIC SIMULATION SOLUTIONS," SIMULIA, 2019. [Online]. Available: https://www.3ds.com/products-services/simulia/products/. [Accessed 24 September 2019].

[122] Tech-X, "Tech-X Products," Tech-X Corporation, 2017. [Online]. Available: https://www.txcorp.com/. [Accessed 2017].

[123] J. W. Eastwood and R. W. Hockney, Computer Simulation Using Particles, New York: Mc Grawhill, 1981.

[124] C. K. Birdsall and A. B. Langdon, Plasma Physics via Computer Simulation, CRC Press, 2004.

[125] Tech-X, *VSim Reference Manual. Release 8.2.0*, Boulder, CO: Tech-X Corporation, 2017.

[126] C. Nieter, P. H. Stoltz, C. Roark and S. Mahalingam, "Modeling of Multipacting in RF Structures Using VORPAL," in *AIP Conference Proceedings*, 2010.

[127] D. J. Amdahl, R. E. Peterkin Jr., J. D. Blahovec, L. A. Bowers, J. W. Luginsland and J. J. Watrous, "Virtual Prototyping of RF Weapons," in *38th Aerospace Sciences Meeting & Exhibit, AIAA*, Reno, NV, 2000.

[128] E. B. Hooper and e. al., "Modeling Results for a Linear Simulator of a Divertor. UCRL-ID-114517," Lawrence Livermore National Laboratory, 1993.

[129] P. Mardahl, A. Greenwood, T. Murphy and K. Cartwright, "Parallel performance characteristics of ICEPIC," in *IEEE User Group Conference*, 2003.

[130] P. J. Mardahl, K. L. Cartwright, A. D. Greenwood, T. Murphy, M. D. Haworth and M. Lopez, "High Power Microwave Tube Verification and Design Using the ICEPIC 3D Parallel, Electromagnetic PIC Code," in *18th International Conference on Numerical Simulation of Plasmas*, Cape Code, 2003.

[131] C. Fichtl, K. Cartwright, P. Mardahl and J. Verboncoeur, "Self-consistent simulation of multipactor discharge at HPM dielectric windows," *The 31st IEEE International Conference on Plasma Science, IEEE Conference Record - Abstracts*, p. 126, 2004.

[132] I. Gimpel and O. Richardson, "The secondary electron emission from metals in the low primary energy region," *Proceedings of the Royal Society of London. Series A. Mathematical and Physical Sciences*, vol. 182, pp. 17-47, 1942.

[133] M. Ye, D. Wang, L. Yun, Y.-n. He, W.-z. Cui and M. Daneshmand, "Positive bias and vacuum chamber wall effect on total electron yield measurement: A re-consideration of the sample current method," *Journal of Applied Physics*, vol. 121, no. 074902, pp. 1-7, 2017.

[134] Office of Nuclear Energy, "Role of Modeling and Simulation in Scientific Discovery," 29 January 2013. [Online]. Available: https://www.energy.gov/ne/articles/role-modeling-and-simulation-scientific-discovery. [Accessed 3 October 2019].

[135] Keithley, "Low Level Measurements Handbook - 7th Edition," [Online]. Available: https://www.tek.com/document/handbook/low-level-measurements-handbook.

[136] Kimball Physics, Inc., "ELG-2/EGPS-1022 Electron Gun and Power Supply System Manual," Wilton, NH, 2016.

[137] Atlas Specialty Metals, "Magnetic Response of Stainless Steels," December 2008. [Online]. Available: http://www.atlassteels.com.au/documents/TN11-Magnetic%20response%20rev%20Dec%202008.pdf.

[138] National Instruments, "Specifications USB-TC01 1-Channel Temperature Input Device," 31 October 2017. [Online]. Available: http://www.ni.com/pdf/manuals/374918b.pdf.

[139] Kurt J. Lesker, "KJL6600 Instruction Manual," [Online]. Available: https://www.lesker.com/newweb/gauges/pdf/manuals/kjl6600%20instruction%20manual.pdf. [Accessed 24 August 2019].

[140] Keithley, "Model 6514 System Electrometer Instruction Manual Manual," 17 September 2015. [Online]. Available: https://www.tek.com/low-level-sensitive-and-specialty-instruments/high-resistance-low-current-electrometers-series-650-5#. [Accessed 26 August 2019].

[141] D. A. Dahl and D. J. Manura, SIMION(R) Version 8.0/8.1 User Manual, Ringoes, NJ: Scientific Instrument Services, Inc., 2011.

[142] Scientific Instrument Services, Inc., "Magnets," Adaptas Solutions, 2019. [Online]. Available: https://simion.com/info/magnets.html. [Accessed 25 August 2019].

[143] Scientific Instruments Services, Inc., "SL Tools Tutorial," Adaptas Solutions, 2019. [Online]. Available: https://simion.com/info/sltoolstut.html. [Accessed 2 12 2019].

[144] National Oceanic and Atmospheric Administration, "Magnetic Field Calculator," [Online]. Available: https://www.ngdc.noaa.gov/geomag/calculators/magcalc.shtml?model=wmm#igrfwmm. [Accessed June 2019].

[145] P. T. McCarthy, R. G. Reifenberger and T. S. Fisher, "Thermionic and photo-excited electron emission for energy-conversion processes," *Frontiers in Energy Research,* vol. 2, no. 54, pp. 1-15, 2014.

[146] J. T. L. Thong, Electron beam testing technology, New York: Plenum Press, 1993.

[147] J. A. Dean, "Properties of Atoms, Radicals, and Bonds," in *Lange's Handbook of Chemistry, 15th Edition*, New York, McGraw-Hill, Inc., 1999, p. 4.81.

[148] M. Cieślik, W. Reczyński, A. Janus, K. Engvall, R. Socha and A. Kotarba, "Metal release and formation of surface precipitate at stainless steel grade 316 and Hanks solution interface–Inflammatory response and surface finishing effects," *Corrosion Science,* vol. 51, pp. 1157-1162, 2009.

[149] T. Yamamoto and K. Tsuno, "Magnetic contrast in secondary electron images of uniaxial ferromagnetic materials obtained by scanning electron microscopy," *physica status solidi,* vol. 28, pp. 479-487, 1975.

[150] J. Yuan, R. Senkel and L. & Reimer, "Recording of magnetic contrast type I by a two-detector system," *Scanning,* vol. 9, no. 6, pp. 249-256, 1987.

[151] Scientific Instrument Services, Inc., "Charge Particle Optics Software," Adaptas Solutions, [Online]. Available: https://simion.com/cpo/. [Accessed October 2019].

[152] H. Fransworth, "Electronic bombardment of metal surfaces," *Physical Review,* vol. 25, no. 1, pp. 41-57, 1925.

[153] J. R. Michael, "High Resolution at Low Beam Energy in the SEM: Resolution Measurement of a Monochromated SEM," *Wiley Periodicals,* vol. 33, pp. 147-154, 2011.

[154] J. M. Sattler, R. A. Coutu, R. Lake, T. Laurvick, T. Back and S. Fairchild, "Modeling micro-porous surfaces for secondary electron emission control to suppress," *Journal of Applied Physics,* vol. 122, no. 055304, pp. 1-9, 2017.

# REPORT DOCUMENTATION PAGE

*Form Approved*
*OMB No. 074-0188*



**PLEASE DO NOT RETURN YOUR FORM TO THE ABOVE ADDRESS.**

| **1. REPORT DATE** *(DD-MM-YYYY)* | **2. REPORT TYPE** | **3. DATES COVERED** *(From – To)* |
|---|---|---|
| 25-11-2019 | Doctoral Dissertation | Sep 2017 - Nov 2019 |

**TITLE AND SUBTITLE**

The Challenges of Low-Energy Secondary Electron Emission Measurement

**5a. CONTRACT NUMBER**

**5b. GRANT NUMBER**

**5c. PROGRAM ELEMENT NUMBER**

**6. AUTHOR(S)**

Vincie, Matthew, Capt, USAF

**5d. PROJECT NUMBER**

**5e. TASK NUMBER**

**5f. WORK UNIT NUMBER**

**7. PERFORMING ORGANIZATION NAMES(S) AND ADDRESS(S)**

Air Force Institute of Technology
Graduate School of Engineering and Management (AFIT/EN)
2950 Hobson Way, Building 640
WPAFB OH 45433-7765

**8. PERFORMING ORGANIZATION REPORT NUMBER**

AFIT-ENG-DS-19-D-007

**9. SPONSORING/MONITORING AGENCY NAME(S) AND ADDRESS(ES)**

Intentionally left blank

**10. SPONSOR/MONITOR'S ACRONYM(S)**

**11. SPONSOR/MONITOR'S REPORT NUMBER(S)**

**12. DISTRIBUTION/AVAILABILITY STATEMENT**

DISTRUBTION STATEMENT A:
APPROVED FOR PUBLIC RELEASE; DISTRIBUTION UNLIMITED.

**13. SUPPLEMENTARY NOTES**

This material is declared a work of the U.S. Government and is not subject to copyright protection in the United States.

**14. ABSTRACT**

The phenomena known as secondary electron emission was discovered over a century ago. Yet, it remains very difficult to model accurately due to the limited availability of reliable experimental data. With the growing use of computer simulations in hardware development, the need for accurate models has increased. This research focused on determining what factors may be causing measurement discrepancies and methods for increasing the accuracy of measurements. It was found that several assumptions are commonly invoked when these measurements are performed that may not always be consistent with reality. The violation of these assumptions leads to measurement bias that is contingent upon the apparatus and the voltages used during the measurement. This research showed that secondary electron yield measurements are sensitive to changes in the apparatus geometry, the current level, and the electron gun settings. New techniques, hardware, and models were developed in order facilitate greater measurement repeatability and accuracy.

**15. SUBJECT TERMS**

Multipactor, Secondary Electron Emission, Secondary Electron Yield, Angular Distribution of Secondary Electrons, Secondary Electron Energy Distribution

| **16. SECURITY CLASSIFICATION OF:** | | | **17. LIMITATION OF ABSTRACT** | **18. NUMBER OF PAGES** | **19a. NAME OF RESPONSIBLE PERSON** |
|---|---|---|---|---|---|
| **a. REPORT** | **b. ABSTRACT** | **c. THIS PAGE** | | | Dr. Tod Laurvick, Major (AFIT/ENG) |
| **U** | **U** | **U** | **UU** | 265 | **19b. TELEPHONE NUMBER** *(Include area code)* (937) 255-3636, x4382 Tod. Laurvick@afit.edu |

**Standard Form 298 (Rev. 8-98)**
Prescribed by ANSI Std. Z39-18